# Microenvironmental Control of Epigenetic Transitions during Human Somatic Cell Reprogramming

by

Ty Harkness

A dissertation submitted in partial fulfillment of the requirements for the degree of

Doctor of Philosophy

(Biomedical Engineering)

at the

UNIVERSITY OF WISCONSIN-MADISON

2016

Date of final oral examination: 05/04/2016

The dissertation is approved by the following members of the Final Oral Committee:
Krishanu Saha, Assistant Professor, Biomedical Engineering
William L. Murphy, Professor, Biomedical Engineering
Aseem Z. Ansari, Professor, Biochemistry
Randolph S. Ashton, Assistant Professor, Biomedical Engineering
Rupa Sridharan, Assistant Professor, Cell and Regenerative Biology

## Abstract

Somatic cell reprogramming enables the generation of self-renewing and patient-specific cell sources for drug discovery, cell therapies, and tissue engineering. The ability to faithfully and efficiently reprogram cells to uniform target populations could have far-reaching consequences in biomedical research and patient care. Reprogramming cell cultures, however, are notoriously multivariate, asynchronous, and inefficient. Thus far, studies undertaken to improve reprogramming methods have largely relied on onerous optimization and guesswork focused on genetic manipulation or addition of soluble factors to overcome epigenetic barriers. These challenges motivate the mechanistic study of reprogramming processes under conditions allowing for precise and independent control of signaling inputs. This thesis aimed to combine rational engineering of the reprogramming microenvironment with innovative materials science, biological, and engineering techniques to collect large, high quality, reproducible data sets that could be analyzed and understood through multivariate computational modeling. Using this basic strategy we were able to generate testable hypotheses to understand and engineer epigenetic transitions. The resulting studies represent tangible steps toward a mechanistic understanding of human somatic cell reprogramming, which is critical to the rapid clinical adaption of reprogramming technologies.

## Acknowledgements

Nobody accomplishes anything of worth alone, and this thesis would not have been possible without the support, guidance, and contributions of a great many people. I would like to first thank my Ph.D. advisor, Krishanu Saha, for providing me the opportunity to learn and grow as a scientist under your supervision. Your encouragement, insights, and passion have constantly inspired me. Thank you to my committee members, Professors William Murphy, Aseem Ansari, Randolph Ashton, and Rupa Sridharan. Your input, feedback, and guidance have been invaluable to the completion of this thesis. I would also like to thank my previous advisors, Professors Wen-Rong Jiang, Brenda Ogle, David Kaplan, and Zhenkun Lou for their guidance and the opportunities afforded to me on this path.

Thank you to all of the members of the Saha lab for your collaboration and scientific advice, and for making the long days and nights in lab bearable. Thank you to my friends in Madison, and especially my roommates who have made the past five years more fun than I would have imagined graduate school to be. To my family and especially my parents, Ed and Laurie, thank you for your constant support and for instilling a love of learning in me from a young age, even if I didn't appreciate it then.

Finally, to Mary, thank you for your constant and overwhelming encouragement and support, even though it meant us being a thousand miles apart. I couldn't have done it without you.

# Table of Contents

## List of Figures

## List of Tables

# Chapter 1. Thesis Overview

## 1.1 Introduction and Motivation

Somatic cell reprogramming encompasses both generation of induced pluripotent stem cells (iPSCs) and direct conversion of one mature cell type to another. Reprogramming is achieved at the epigenetic level, in other words in heritable covalent modifications to DNA or proteins surrounding DNA[1]. Reprogramming and direct conversion enable the generation of self-renewing and patient-specific cell sources for drug discovery, cell therapies, and tissue engineering[2]. Accordingly, the ability to faithfully and efficiently reprogram cells to uniform target populations could have far-reaching consequences in biomedical research and patient care.

Cultures containing reprogramming cells, however, are notoriously multivariate, asynchronous, and inefficient, with complex signaling occurring among cells, soluble factors in the media, and the surrounding proteinaceous matrix[3]. In our view, progress in the reprogramming field has been hindered both by an inability to uncouple and rationally control distinct signaling inputs and an under-emphasis on biophysical cues. Thus far, studies undertaken to improve reprogramming methods have largely relied on onerous optimization and guesswork focused on genetic manipulation or addition of soluble factors to overcome epigenetic barriers[4]. Furthermore, chemical and physical signals in the cellular microenvironment are often interdependent, complicating mechanistic studies of cell fate decisions[5]. These challenges motivate the mechanistic study of reprogramming processes under conditions allowing for precise and independent control of signaling inputs. This thesis aims to meet this need through

rational engineering of both the genome and the microenvironment. By combining classical materials science and engineering techniques with recent advances in molecular and cell biology and high content imaging, we strove to collect large, high quality data sets that could be analyzed and understood through multivariate computational modeling. Using this basic strategy we were able to generate testable hypotheses to understand and engineer epigenetic transitions. The resulting studies represent tangible steps toward a mechanistic understanding of how human cells integrate biochemical and biophysical cues during reprogramming, which is critical to the clinical adaption of reprogramming technologies.

## 1.2 Key results of individual studies

**1. Nanofibrous electrospun polymers for reprogramming human cells.** In this study it was shown for the first time that engineering the biophysical cellular microenvironment could increase the efficiency of reprogramming human fibroblasts to iPSCs. By empirically testing a library of electrospun polymers, it was found that reprogramming on certain nanofibrous substrates enhanced reprogramming efficiency by over 500% compared to standard tissue culture plastic. Establishment of a novel antibody labeling system allowed for the tracking of intermediate cell types throughout reprogramming and loss of CD44 expression during the first 10 days of reprogramming proved to be highly predictive of iPSC generation. The beneficial effects of nanofibrous substrates were also limited to the first 17 days of reprogramming. Further, multivariate computational analysis identified individual microenvironmental stimuli that were key drivers of reprogramming outcomes.

**2. Effects of regulating cytoskeletal and nuclear morphology via micropatterned multiwell plates.** Here we created the Microcontact Printed Well Plate (μCP Well Plate), a versatile cell culture platform capable of independent presentation of biochemical and biophysical cues and enabling both high-throughput and high-resolution imaging and analyses of live human cells. Classical microcontact printing techniques were adapted to produce large single-cell arrays of precisely patterned human cells in the format of standard multiwell plates. A new cell line was engineered to express fluorescent labels identifying nuclear and cytoskeletal morphology in live cells, revealing the interplay of cell geometry, cytoskeletal organization, and epigenetics. This work was the first to describe the regulation of a core nucleosome member, Histone 2B, by cell geometry alone.

**3. Tracking and predicting reprogramming from a biophysical perspective.** In our final study we showed that the progression of somatic cell reprogramming through intermediate states can be studied via high-content analysis of nuclear biophysical characteristic alone. A set of eight nuclear measurements was sufficient to separate multiple cell types, as well as to distinguish both reprogramming and differentiating intermediates. Computation models of biophysical characteristics were used to predict reprogramming efficiency and generate new hypotheses regarding reprogramming. Insights gained from this analysis led us to investigate the role of mechanotransductors during reprogramming and suggested a novel role for YAP as a regulator of MET during early stages of reprogramming.

## References


1 Mattout, A., Biran, A. & Meshorer, E. Global epigenetic changes during somatic cell reprogramming to iPS cells. *Journal of molecular cell biology* **3**, 341-350 (2011).

2 Saha, K. & Jaenisch, R. Technical Challenges in Using Human Induced Pluripotent Stem Cells to Model Disease. *Cell Stem Cell* **5**, 584-595, doi:10.1016/j.stem.2009.11.009 (2009).

3 Hanna, J. H., Saha, K. & Jaenisch, R. Pluripotency and cellular reprogramming: facts, hypotheses, unresolved issues. *Cell* **143**, 508-525 (2010).

4 Feng, B., Ng, J.-H., Heng, J.-C. D. & Ng, H.-H. Molecules that promote or enhance reprogramming of somatic cells to induced pluripotent stem cells. *Cell Stem Cell* **4**, 301-312 (2009).

5 Kilian, K. A., Bugarija, B., Lahn, B. T. & Mrksich, M. Geometric cues for directing the differentiation of mesenchymal stem cells. *Proceedings of the National Academy of Sciences* **107**, 4872-4877 (2010).

# Chapter 2. Background

## 2.1 Mechanisms of Cellular Reprogramming

Reprogramming of mature cells into an induced pluripotent state was first described in mouse cells in 2006[1]. The next year, overexpression of one of two distinct combinations of transcription factors was shown to accomplish this feat in human cells: Oct4, Sox2, Klf4, and c-Myc (OSKM), termed the Yamanaka factors[2]; or Oct4, Sox2, Nanog, and Lin28 (OSNL), termed the Thomson factors[3]. These studies, while revolutionary, reported that <0.1% of the starting cell population reached a stable pluripotent state after approximately one month of factor expression. Since this point, thousands of studies have focused on understanding how concerted action of these transcription factors transforms cells to a pluripotent state and how this process can be engineered to improve reprogramming speed and efficiency.

The consistency and reproducibility of reprogramming studies was significantly enhanced by establishing chemically defined, xeno-free culture conditions for deriving and maintaining iPSCs[4,5] as well as more controlled delivery and expression of the reprogramming factors[6-9]. The derivation of “secondary” fibroblast lines with reprogramming factors integrated into the host genome eliminated variability based on viral transduction[10]. A variety of small molecules have been used to enhance cellular transitions during reprogramming[11-15], even completely replacing exogenous transcription factors in one report[16], but efficiencies still generally hover below 2%. Multiple studies have suggested that low efficiencies are not due to the presence of “elite” starting cell populations that are more amenable to reprogramming than

others[7,17-19], but instead derive from a series of stochastic epigenetic transitions throughout the reprogramming process[7,20-26]. Several recent studies have reported reprogramming that more closely resembles a deterministic process after genetic or chemical modifications[27-30], but these have been conducted in mouse cells – which bear important differences from human cells in the context of pluripotency[31] – and have yet to be widely replicated.

The number of epigenetic transitions required for reprogramming is unclear, but it is generally agreed that successful reprogramming requires both loss of initial somatic identity and establishment of target identity[31]. Work in the 1990s and early 2000s suggested that activation of transcription factors could also facilitate direct conversion of one mature cell type to another[32-34], but interest was initially tempered due to incomplete erasure of somatic identity. After the Yamanaka and Thomson studies, however, renewed attention led to reports of direct conversion of mature fibroblasts into induced neurons[35], blood progenitors[36], cardiomyocytes[37], and hepatocyte-like cells[38] that stably activate native transcriptional networks and display functional characteristics of the target cell type without passing through a pluripotent “ground” state[31].

While many direct conversion studies induced epigenetic transitions through expression of lineage-specific transcription factors, conversion of mouse fibroblasts to both neural and cardiac lineages has also been reported via transient (<7 days) expression of the classical Yamanaka (OSKM) factors followed by exposure to lineage-specific media conditions[13,39,40]. Using this strategy, the traditional time-consuming steps of isolating and differentiating pure pluripotent populations are eliminated. This “OSKM conversion” strategy has proven useful in human somatic cell reprogramming

by conversion of patient fibroblasts to neural lineages to create disease models for the study of amyotrophic lateral sclerosis[41,42]. While recent evidence suggests that successful conversion using the “OSKM conversion” method may involve passage through a transient Nanog$^{+}$ pluripotent state[43,44], cells will rapidly revert to a fibroblast phenotype after similarly transient OSKM expression even when kept in pluripotent media conditions[20], suggesting that some memory of initial somatic state is retained at this point.

Comprehensive studies of iPSC generation performed on the mRNA[22,45], protein[46,47], and epigenetic[48,49] levels also report that loss of somatic identity occurs within the first ~7 days of reprogramming. For example, a majority of the physical changes apparent in reprogramming (discussed in greater detail below) occur within the first week[21], contemporaneous with large shifts in the repressive histone marker H3K27me3 that safeguard fibroblast-like expression patterns[48]. In contrast, expression of members of the pluripotency transcription network such as Oct4 and Sox2 is upregulated only after ten days of OSKM expression[45], and large scale changes in DNA methylation also occur only late in the reprogramming process[45].

Despite many detailed and comprehensive studies, the precise path reprogramming intermediates take to reach a target identity (pluripotent or otherwise) remains unclear. iPSC reprogramming alone can result in at least two distinct pluripotent cell types[25]. Various intermediate states have been described, including a pre-implantation “naïve” state[50] and an extra-embryonic-like state[51]. Further confounding efforts towards straightforward, uniform characterization of reprogramming intermediates is the observation that these intermediate states may shift dramatically

based on the reprogramming system of choice, even if the same four Yamanaka factors are expressed throughout[52].

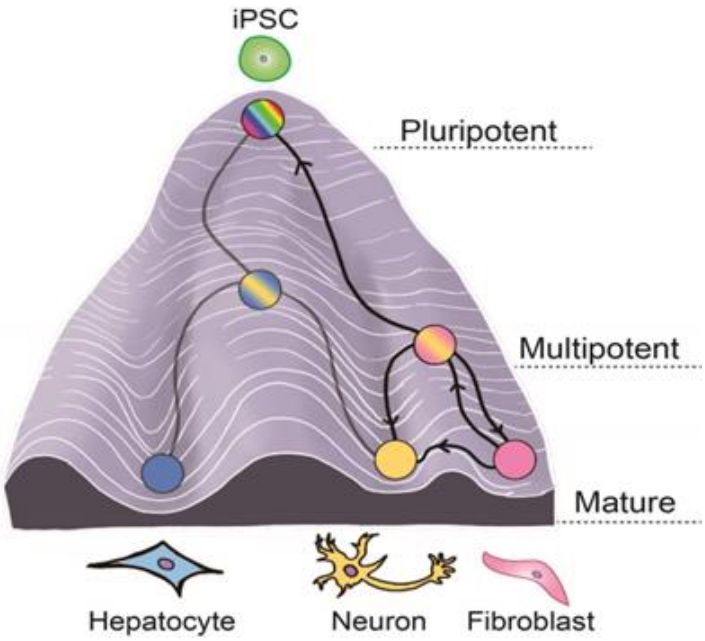


**Figure 2-1. Waddington's epigenetic landscape depicting potential reprogramming pathways.**

Taken together, however, these experimental data support a model in which erasure of somatic identity and establishment of target identity occur sequentially – each over 1-2 weeks – rather than simultaneously. In this model, OSKM expression results in rapid loss of somatic identity and transit through a temporary and unstable multi- or pluripotent "intermediate" state. Intermediates occupying this epigenetic space revert to their initial state in the absence of additional inputs, but can be driven to pluripotency by continued factor expression or induced to adapt a distinct epigenetic state through microenvironmental cues (Figure 2-1). This late-stage establishment of new target cell identity seems to be less efficient and require longer time scales than erasure of initial somatic identity[22,24].

## 2.2 Influence of Biophysical Cues on Cell Fate Decisions

The phrase “cell fate” is often used to refer to the terminal state of an undifferentiated stem cell[53]. Here, we use “cell fate decision” as an umbrella term incorporating any change to the identity or activity of a particular cell, including among others differentiation, reprogramming, proliferation, apoptosis, and senescence. Controlling human cell fate remains an important goal for many in the regenerative medicine, cancer, and stem cell biology fields[54]. There is a growing appreciation that microenvironmental factors play a major role in these decision processes, including key biophysical cues that can be transmitted from the cell exterior to interior in a variety of ways. At the cell surface, integrins and cadherins project from both sides of the lipid membrane, binding various extracellular matrix (ECM) and cell-surface proteins in the microenvironment and initiating signaling cascades in the cytoplasm[55]. These signaling cascades are complex, involving both force-sensitive compounds and transcription factors. Talin[56,57], p130CAS[58], and focal adhesion kinase[59] are force-sensitive molecules that form at sites of clustered integrin binding and link integrins to the actin cytoskeleton[55], which is then connected to the nucleoskeleton via linker of nucleoskeleton and cytoskeleton (LINC) complexes that extend through the nuclear lamina[60,61]. By way of this connection, the cytoskeleton has a direct impact on the morphology and composition of the nuclear lamina[62-64]. The nuclear lamina, in turn, has a significant role in determining chromatin organization, chromatin dynamics, and ultimately gene expression[62,65-68]. Finally, transcription factors such as YAP/TAZ can also translocate to the nucleus and activate expression of specific gene subsets under

mechanical stress[69,70]. The mechanisms by which these processes are coordinated and can be engineered within human cells are still incompletely understood.

Of particular interest to this thesis is the influence of geometry on cellular behavior. This relationship was first described in seminal studies in the late 1990s[60,71] and has since been an active area of research[72]. Geometry has been shown to influence many cell fate decisions, including proliferation[71,73], apoptosis[71,74], differentiation[75,76], and epigenetic reprogramming[77,78], and imprecise control of cell shape and area during the study of these processes can lead to noisy or misleading data[54,79-81]. For example, constraining single cells to uniform micropatterns greatly reduces the intrinsic cell-to-cell variability of mRNA transcript abundance[82], and inconsistent differentiation of mesenchymal stem cells has been traced back to variations in cell shape and cytoskeletal tension inherent in standard cell culture methods[75,76].

## 2.3 Evidence of Biophysical Influence in Somatic Cell Reprogramming

Dramatic biophysical changes are inherent in many cellular transitions, including that of mature fibroblast to pluripotent stem cells. Fibroblasts typically assume an elongated morphology with low levels of cell-cell contacts and highly developed cytoskeletal network, while pluripotent stem cells pack tightly together in a compact circular morphology with relatively little cytoplasm and a less developed cytoskeleton[1,83,84] (Figure 2-2).

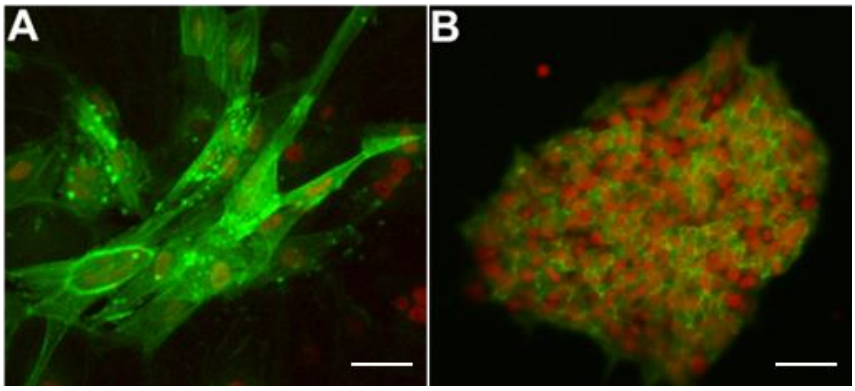


**Figure 2-2. Biophysical changes inherent in reprogramming.** C1.2 reprogrammable line expressing H2B-mCherry and LifeAct-GFP in Fibroblast **(A)** and iPSC **(B)** state. 50 µm scale bars.

Live imaging of reprogramming cells has identified early-stage reduction of cell size as a critical event for successful reprogramming[85]. Nuclear geometry is also altered during this transition, with iPSCs typically harboring nuclei half the size of their fibroblast counterparts[86]. These biophysical changes have traditionally been studied in the context of the mesenchymal-to-epithelial transition (MET) which occurs relatively early in the reprogramming process[20,21,87], concurrent to epigenetic changes indicating loss of somatic identity[49]. MET is repressed by transforming growth factor β (TGF-β) signaling[21], and is characterized by dramatic reorganization of the actin cytoskeleton, silencing of mesenchymal markers such as Snail, Slug, and N-cadherin, and expression of epithelial markers such as Ep-CAM, β-catenin, and E-cadherin. Altering the biophysical environment through culturing cells on soft hydrogels encourages MET and promotes reprogramming[88].

While more detailed studies suggest iPSC reprogramming does not follow a smooth and linear progression of mesenchymal to epithelial characteristics[89-91], large physical changes are required for both cell bodies and nuclei in the course of reprogramming, and these changes are associated with specific patterns of gene

expression and epigenetic status[87,91]. The very survival and self-renewal of pluripotent cells depends upon long-term activation of classical mechanotransduction molecules Rho GTPase and YAP/TAZ and their maintenance of actin dynamics[92] – a relationship that is not required in differentiated cells. Although yet to be studied in detail, similar biophysical transitions would be expected to occur during direct conversion of fibroblasts to other epithelial lineages.

Few reports have directly assessed the influence of biophysical inputs on reprogramming kinetics. Elongating cells via culture on PDMS microchannels or aligned nanofibers has been reported to increase efficiency of both iPSC reprogramming[77] and direct fibroblast-to-neuron conversion[93]. These effects are thought to be mediated through increased concentration of “open” chromatin markers such as Histone H3 acetylation (AcH3) in elongated nuclei and/or initiation of MET[77]. In a three-dimensional context, PEG-based hydrogels have been used to enhance iPSC reprogramming efficiency through similar means (encouraging MET and epigenetic plasticity). By employing a systematic strategy that varied both biophysical and biochemical cues, the authors of this report were able to enhance reprogramming efficiency by 300-400%[94]. Recent reports also described the critical importance of kinases that activate cytoskeletal remodeling[95] on iPSC generation and increased actomyosin tension and induction of Oct4 and Nanog expression after culturing human cells on soft PDMS substrates[96]. These biophysical cues have yet to be used to systematically drive cell fate choice during reprogramming, but become even more interesting when considering recent studies describing the pivotal importance of overall chromatin organization and

dynamics on reprogramming and pluripotent state[97-100] and the relative ease of altering chromatin state through controlling cell geometry[62-64].

## 2.4 High-Content Imaging Technologies

High-content imaging has been defined as any optical assay enabling parallel monitoring of multiple cell phenotypes[101]. While high-throughput screens typically measure a signal averaged over all cells within a microplate well and are limited to one or two measurements in parallel, high-content screens are often conducted at the single-cell level and can take tens or hundreds of measurements simultaneously[101]. Microscopy-based high-content imaging has become widely available only in the last decade, enabled by concurrent advances in several technologies. A microscopy-based high content screen requires, minimally, a microscope capable of visualizing subcellular features in detail, automation of imaging (often through use of an automated microscope stage with efficient autofocus capabilities) and software capable of extracting information from the resulting images. Additional tools often include an incubation chamber to keep cells under optimal atmospheric conditions during live-cell imaging, fluorescent probes, and fluorescent imaging capabilities.

Advances in the range and stability of fluorescent probes[102], in combination with the rise of advance genetic engineering technologies such as CRISPR/Cas9[103] to fluorescently tag virtually any molecule in live cells, has greatly expanded the targets available for analysis. Automated microscopes have become commonplace[104-108] and several sophisticated software suites capable of powerful standardized image processing and analysis have become freely available[109-112]. As a result, high-content

imaging is now within the reach of most academic laboratories. These techniques have been used to assay markers of stem cell maintenance and differentiation to identify compounds regulating stem cell self-renewal[113], classify large libraries of drugs and small molecules based on cell morphology[114,115], and even to measure the subcellular localization of nearly the entire proteome of single yeast cells[116], among many other applications. To date, high content imaging has been used sparingly, but effectively, in reprogramming studies[20,23].

## 2.5 Reprogramming Standardization, Scale-up, and Clinical Viability

Reprogramming studies are notoriously variable, labor intensive, and system-dependent[52], leading to a severe lack of standardization in the field[117]. These studies are typically performed in standard tissue culture plates that are unsuitable for high-resolution imaging and offer little to no control of biophysical cues. As a result, high-content data that could illuminate the progression of reprogramming cells is lacking. Without a mechanistic understanding of reprogramming progression, the efficiency of iPSC generation remains low. However, enthusiasm in the reprogramming field remains high and progress is rapid.

After years of debate, a recent study revealed that previously reported differences between ESCs and iPSCs could be attributed almost entirely to variations in genetic backgrounds[118]. If genetically matched ESCs and iPSCs are indeed virtually identical, long-standing concerns about the inherent “artificial” nature of iPSCs should be eased. Computational tools that both model and predict reprogramming transitions and other cell fate decisions have emerged to help make sense of the massive amounts

of genetic, mRNA, and protein-level data available from mostly population-based studies[119-121]. Additionally, CRISPR/Cas9 technology has now enabled simultaneous gene correction and reprogramming of patient cells, which could enable one-step creation of unlimited cell sources for patient-specific corrective cell therapies[122].

While these advances are exciting, regulatory hurdles need to be cleared if reprogramming techniques are to become clinically widespread. After the first clinical trial utilizing iPSCs as a cell therapy in humans was suspended due to regulatory changes and possible genetic aberrations[123], these regulatory concerns have only been heightened. Progress on this front has been made by establishing protocols for the creation of Good Manufacturing Practice (GMP)-grade iPSCs[124], optimizing and standardizing the workflow of large-scale technician-based iPSC generation[125], and even nearly completely automating the iPSC reprogramming process through the use of robotics[126]. All these efforts have resulted in improved consistency and efficiency of iPSC generation and many employ non-integrative reprogramming vectors that avoid altering the patient genome. Once iPSCs have been generated, there are several methods available for clinical-grade scale-up of pluripotent cells[127].

Although many challenges remain, the rapid progress since the first report of iPSC generation only a decade ago is quite encouraging. These challenges can be met and overcome through a marriage of traditional biological techniques with the recent advances described above to advance a mechanistic understanding of reprogramming processes, and by a continued emphasis on standardization and reproducibility when eyeing clinical applications.

## References


1 Takahashi, K. & Yamanaka, S. Induction of pluripotent stem cells from mouse embryonic and adult fibroblast cultures by defined factors. *cell* **126**, 663-676 (2006).

2 Takahashi, K. *et al.* Induction of pluripotent stem cells from adult human fibroblasts by defined factors. *cell* **131**, 861-872 (2007).

3 Yu, J. *et al.* Induced pluripotent stem cell lines derived from human somatic cells. *Science* **318**, 1917-1920 (2007).

4 Chen, G. *et al.* Chemically defined conditions for human iPSC derivation and culture. *Nature methods* **8**, 424-429 (2011).

5 Beers, J. *et al.* Passaging and colony expansion of human pluripotent stem cells by enzyme-free dissociation in chemically defined culture conditions. *Nature protocols* **7**, 2029-2040 (2012).

6 Hanna, J. *et al.* Metastable pluripotent states in NOD-mouse-derived ESCs. *Cell stem cell* **4**, 513-524 (2009).

7 Hanna, J. *et al.* Direct cell reprogramming is a stochastic process amenable to acceleration. *Nature* **462**, 595-601 (2009).

8 Carey, B. W. *et al.* Reprogramming factor stoichiometry influences the epigenetic state and biological properties of induced pluripotent stem cells. *Cell stem cell* **9**, 588-598 (2011).

9 Kim, S.-I. *et al.* KLF4 N-Terminal Variance Modulates Induced Reprogramming to Pluripotency. *Stem cell reports* (2015).

10 Hockemeyer, D. *et al.* A drug-inducible system for direct reprogramming of human somatic cells to pluripotency. *Cell stem cell* **3**, 346-353 (2008).

11 Ichida, J. K. *et al.* A small-molecule inhibitor of Tgf-β signaling replaces Sox2 in reprogramming by inducing Nanog. *Cell stem cell* **5**, 491-503 (2009).

12 Shi, Y. *et al.* Induction of pluripotent stem cells from mouse embryonic fibroblasts by Oct4 and Klf4 with small-molecule compounds. *Cell stem cell* **3**, 568-574 (2008).

13 Kim, J. *et al.* Direct reprogramming of mouse fibroblasts to neural progenitors. *Proceedings of the National Academy of Sciences* **108**, 7838-7843 (2011).

14 Ichida, J. K. *et al.* Notch inhibition allows oncogene-independent generation of iPS cells. *Nature chemical biology* **10**, 632-639 (2014).

15 Tran, K. A. *et al.* Collaborative rewiring of the pluripotency network by chromatin and signalling modulating pathways. *Nature communications* **6** (2015).

16 Hou, P. *et al.* Pluripotent stem cells induced from mouse somatic cells by small-molecule compounds. *Science* **341**, 651-654 (2013).

17 Hanna, J. *et al.* Direct reprogramming of terminally differentiated mature B lymphocytes to pluripotency. *Cell* **133**, 250-264 (2008).

18 Staerk, J. *et al.* Reprogramming of peripheral blood cells to induced pluripotent stem cells. *Cell stem cell* **7**, 20 (2010).

19 Loh, Y.-H. *et al.* Generation of induced pluripotent stem cells from human blood. *Blood* **113**, 5476-5479 (2009).

20 Samavarchi-Tehrani, P. *et al.* Functional genomics reveals a BMP-driven mesenchymal-to-epithelial transition in the initiation of somatic cell reprogramming. *Cell stem cell* **7**, 64-77 (2010).

21 Li, R. *et al.* A mesenchymal-to-epithelial transition initiates and is required for the nuclear reprogramming of mouse fibroblasts. *Cell stem cell* **7**, 51-63 (2010).

22 Buganim, Y. *et al.* Single-cell expression analyses during cellular reprogramming reveal an early stochastic and a late hierarchic phase. *Cell* **150**, 1209-1222 (2012).

23 Golipour, A. *et al.* A late transition in somatic cell reprogramming requires regulators distinct from the pluripotency network. *Cell stem cell* **11**, 769-782 (2012).

24 Tanabe, K., Nakamura, M., Narita, M., Takahashi, K. & Yamanaka, S. Maturation, not initiation, is the major roadblock during reprogramming toward pluripotency from human fibroblasts. *Proceedings of the National Academy of Sciences* **110**, 12172-12179 (2013).

25 Tonge, P. D. *et al.* Divergent reprogramming routes lead to alternative stem-cell states. *Nature* **516**, 192-197 (2014).

26 Armond, J. W. *et al.* A stochastic model dissects cell states in biological transition processes. *Scientific reports* **4** (2014).

27 Di Stefano, B. *et al.* C/EBP [agr] poises B cells for rapid reprogramming into induced pluripotent stem cells. *Nature* **506**, 235-239 (2014).

28 Bar-Nur, O. *et al.* Small molecules facilitate rapid and synchronous iPSC generation. *Nature methods* **11**, 1170-1176 (2014).

29 Guo, S. *et al.* Nonstochastic reprogramming from a privileged somatic cell state. *Cell* **156**, 649-662 (2014).

30 Rais, Y. *et al.* Deterministic direct reprogramming of somatic cells to pluripotency. *Nature* **502**, 65-70 (2013).

31 Hanna, J. H., Saha, K. & Jaenisch, R. Pluripotency and cellular reprogramming: facts, hypotheses, unresolved issues. *Cell* **143**, 508-525 (2010).

32 Weintraub, H. *et al.* Activation of muscle-specific genes in pigment, nerve, fat, liver, and fibroblast cell lines by forced expression of MyoD. *Proceedings of the National Academy of Sciences* **86**, 5434-5438 (1989).

33 Xie, H., Ye, M., Feng, R. & Graf, T. Stepwise reprogramming of B cells into macrophages. *Cell* **117**, 663-676 (2004).

34 Tachibana, M. *et al.* Ectopic expression of MITF, a gene for Waardenburg syndrome type 2, converts fibroblasts to cells with melanocyte characteristics. *Nature genetics* **14**, 50-54 (1996).

35 Vierbuchen, T. *et al.* Direct conversion of fibroblasts to functional neurons by defined factors. *Nature* **463**, 1035-1041 (2010).

36 Szabo, E. *et al.* Direct conversion of human fibroblasts to multilineage blood progenitors. *Nature* **468**, 521-526 (2010).

37 Ieda, M. *et al.* Direct reprogramming of fibroblasts into functional cardiomyocytes by defined factors. *Cell* **142**, 375-386 (2010).

38 Sekiya, S. & Suzuki, A. Direct conversion of mouse fibroblasts to hepatocyte-like cells by defined factors. *Nature* **475**, 390-393 (2011).

39 Efe, J. A. *et al.* Conversion of mouse fibroblasts into cardiomyocytes using a direct reprogramming strategy. *Nature cell biology* **13**, 215-222 (2011).

40 Thier, M. *et al.* Direct conversion of fibroblasts into stably expandable neural stem cells. *Cell stem cell* **10**, 473-479 (2012).

41 Meyer, K. *et al.* Direct conversion of patient fibroblasts demonstrates non-cell autonomous toxicity of astrocytes to motor neurons in familial and sporadic ALS. *Proceedings of the National Academy of Sciences* **111**, 829-832 (2014).

42 Liu, M.-L., Zang, T. & Zhang, C.-L. Direct Lineage Reprogramming Reveals Disease-Specific Phenotypes of Motor Neurons from Human ALS Patients. *Cell reports* **14**, 115-128 (2016).

43 Maza, I. *et al.* Transient acquisition of pluripotency during somatic cell transdifferentiation with iPSC reprogramming factors. *Nature biotechnology* **33**, 769-774 (2015).

44 Bar-Nur, O. *et al.* Lineage conversion induced by pluripotency factors involves transient passage through an iPSC stage. *Nature biotechnology* **33**, 761-768 (2015).

45 Polo, J. M. *et al.* A molecular roadmap of reprogramming somatic cells into iPS cells. *Cell* **151**, 1617-1632 (2012).

46 Hansson, J. *et al.* Highly coordinated proteome dynamics during reprogramming of somatic cells to pluripotency. *Cell reports* **2**, 1579-1592 (2012).

47 Zunder, E. R., Lujan, E., Goltsev, Y., Wernig, M. & Nolan, G. P. A Continuous Molecular Roadmap to iPSC Reprogramming through Progression Analysis of Single-Cell Mass Cytometry. *Cell Stem Cell* **16**, 323-337 (2015).

48 Hussein, S. M. *et al.* Genome-wide characterization of the routes to pluripotency. *Nature* **516**, 198-206 (2014).

49 Koche, R. P. *et al.* Reprogramming factor expression initiates widespread targeted chromatin remodeling. *Cell stem cell* **8**, 96-105 (2011).

50 Cacchiarelli, D. *et al.* Integrative analyses of human reprogramming reveal dynamic nature of induced pluripotency. *Cell* **162**, 412-424 (2015).

51 Zhao, Y. *et al.* A XEN-like state bridges somatic cells to pluripotency during chemical reprogramming. *Cell* **163**, 1678-1691 (2015).

52 Chantzoura, E. *et al.* Reprogramming Roadblocks Are System Dependent. *Stem cell reports* **5**, 350-364 (2015).

53 Wagers, A., Christensen, J. & Weissman, I. Cell fate determination from stem cells. *Gene therapy* **9** (2002).

54 Iskratsch, T., Wolfenson, H. & Sheetz, M. P. Appreciating force and shape [mdash] the rise of mechanotransduction in cell biology. *Nature Reviews Molecular Cell Biology* (2014).

55 Giancotti, F. G. & Ruoslahti, E. Integrin signaling. *Science* **285**, 1028-1033 (1999).

56 Lee, S. E., Kamm, R. D. & Mofrad, M. R. Force-induced activation of talin and its possible role in focal adhesion mechanotransduction. *Journal of biomechanics* **40**, 2096-2106 (2007).

57 Vogel, V. & Sheetz, M. Local force and geometry sensing regulate cell functions. *Nature reviews molecular cell biology* **7**, 265-275 (2006).

58 Sawada, Y. *et al.* Force sensing by mechanical extension of the Src family kinase substrate p130Cas. *Cell* **127**, 1015-1026 (2006).

59 Mitra, S. K., Hanson, D. A. & Schlaepfer, D. D. Focal adhesion kinase: in command and control of cell motility. *Nature reviews Molecular cell biology* **6**, 56-68 (2005).

60 Maniotis, A. J., Chen, C. S. & Ingber, D. E. Demonstration of mechanical connections between integrins, cytoskeletal filaments, and nucleoplasm that stabilize nuclear structure. *Proceedings of the National Academy of Sciences* **94**, 849-854 (1997).

61 Starr, D. A. & Fridolfsson, H. N. Interactions between nuclei and the cytoskeleton are mediated by SUN-KASH nuclear-envelope bridges. *Annual review of cell and developmental biology* **26**, 421 (2010).

62 Toh, K. C., Ramdas, N. M. & Shivashankar, G. Actin cytoskeleton differentially alters the dynamics of lamin A, HP1α and H2B core histone proteins to remodel chromatin condensation state in living cells. *Integrative Biology* **7**, 1309-1317 (2015).

63 Versaevel, M. *et al.* Super-resolution microscopy reveals LINC complex recruitment at nuclear indentation sites. *Scientific reports* **4** (2014).

64 Kim, D.-H. & Wirtz, D. Cytoskeletal tension induces the polarized architecture of the nucleus. *Biomaterials* **48**, 161-172 (2015).

65 Bronshtein, I. *et al.* Loss of lamin A function increases chromatin dynamics in the nuclear interior. *Nature communications* **6** (2015).

66 Guelen, L. *et al.* Domain organization of human chromosomes revealed by mapping of nuclear lamina interactions. *Nature* **453**, 948-951 (2008).

67 Peric-Hupkes, D. *et al.* Molecular maps of the reorganization of genome-nuclear lamina interactions during differentiation. *Molecular cell* **38**, 603-613 (2010).

68 Kind, J. *et al.* Genome-wide maps of nuclear lamina interactions in single human cells. *Cell* **163**, 134-147 (2015).

69 Low, B. C. *et al.* YAP/TAZ as mechanosensors and mechanotransducers in regulating organ size and tumor growth. *FEBS letters* **588**, 2663-2670 (2014).

70 Aragona, M. *et al.* A mechanical checkpoint controls multicellular growth through YAP/TAZ regulation by actin-processing factors. *Cell* **154**, 1047-1059 (2013).

71 Chen, C. S., Mrksich, M., Huang, S., Whitesides, G. M. & Ingber, D. E. Geometric control of cell life and death. *Science* **276**, 1425-1428 (1997).

72 Dalby, M. J., Gadegaard, N. & Oreffo, R. O. Harnessing nanotopography and integrin-matrix interactions to influence stem cell fate. *Nature materials* **13**, 558-569 (2014).

73 Qutub, A. A. & Popel, A. S. Elongation, proliferation & migration differentiate endothelial cell phenotypes and determine capillary sprouting. *BMC systems biology* **3**, 13 (2009).

74 Wang, D. *et al.* Tissue-specific mechanical and geometrical control of cell viability and actin cytoskeleton alignment. *Scientific reports* **4** (2014).

75 McBeath, R., Pirone, D. M., Nelson, C. M., Bhadriraju, K. & Chen, C. S. Cell shape, cytoskeletal tension, and RhoA regulate stem cell lineage commitment. *Developmental cell* **6**, 483-495 (2004).

76 Kilian, K. A., Bugarija, B., Lahn, B. T. & Mrksich, M. Geometric cues for directing the differentiation of mesenchymal stem cells. *Proceedings of the National Academy of Sciences* **107**, 4872-4877 (2010).

77 Downing, T. L. *et al.* Biophysical regulation of epigenetic state and cell reprogramming. *Nature materials* **12**, 1154-1162 (2013).

78 Cordie, T. *et al.* Nanofibrous electrospun polymers for reprogramming human cells. *Cellular and Molecular Bioengineering* **7**, 379-393 (2014).

79 Discher, D. E., Janmey, P. & Wang, Y.-l. Tissue cells feel and respond to the stiffness of their substrate. *Science* **310**, 1139-1143 (2005).

80 Trappmann, B. *et al.* Extracellular-matrix tethering regulates stem-cell fate. *Nature materials* **11**, 642-649 (2012).

81 Han, S. J., Bielawski, K. S., Ting, L. H., Rodriguez, M. L. & Sniadecki, N. J. Decoupling substrate stiffness, spread area, and micropost density: a close spatial relationship between traction forces and focal adhesions. *Biophysical journal* **103**, 640-648 (2012).

82 Battich, N., Stoeger, T. & Pelkmans, L. Control of transcript variability in single mammalian cells. *Cell* **163**, 1596-1610 (2015).

83 Høffding, M. K. & Hyttel, P. Ultrastructural visualization of the Mesenchymal-to-Epithelial Transition during reprogramming of human fibroblasts to induced pluripotent stem cells. *Stem cell research* **14**, 39-53 (2015).

84 Boraas, L. C., Guidry, J. B., Pineda, E. T. & Ahsan, T. Cytoskeletal Expression and Remodeling in Pluripotent Stem Cells. *PLoS One* **11** (2016).

85 Smith, Z. D., Nachman, I., Regev, A. & Meissner, A. Dynamic single-cell imaging of direct reprogramming reveals an early specifying event. *Nature biotechnology* **28**, 521-526 (2010).

86 Mattout, A., Biran, A. & Meshorer, E. Global epigenetic changes during somatic cell reprogramming to iPS cells. *Journal of molecular cell biology* **3**, 341-350 (2011).

87 Liao, B. *et al.* MicroRNA cluster 302–367 enhances somatic cell reprogramming by accelerating a mesenchymal-to-epithelial transition. *Journal of Biological Chemistry* **286**, 17359-17364 (2011).

88 Choi, B. *et al.* Stiffness of Hydrogels Regulates Cellular Reprogramming Efficiency Through Mesenchymal-to-Epithelial Transition and Stemness Markers. *Macromolecular bioscience* (2015).

89 Liu, X. *et al.* Sequential introduction of reprogramming factors reveals a time-sensitive requirement for individual factors and a sequential EMT–MET mechanism for optimal reprogramming. *Nature cell biology* **15**, 829-838 (2013).

90 Unternaehrer, J. J. *et al.* The Epithelial-Mesenchymal Transition Factor SNAIL Paradoxically Enhances Reprogramming. *Stem cell reports* **3**, 691-698 (2014).

91 Gingold, J. A. *et al.* A genome-wide RNAi screen identifies opposing functions of Snai1 and Snai2 on the Nanog dependency in reprogramming. *Molecular cell* **56**, 140-152 (2014).

92 Ohgushi, M., Minaguchi, M. & Sasai, Y. Rho-signaling-directed YAP/TAZ activity underlies the long-term survival and expansion of human embryonic stem cells. *Cell stem cell* **17**, 448-461 (2015).

93 Kulangara, K. *et al.* The effect of substrate topography on direct reprogramming of fibroblasts to induced neurons. *Biomaterials* **35**, 5327-5336 (2014).

94 Caiazzo, M. *et al.* Defined three-dimensional microenvironments boost induction of pluripotency. *Nature materials* (2016).

95 Sakurai, K. *et al.* Kinome-wide functional analysis highlights the role of cytoskeletal remodeling in somatic cell reprogramming. *Cell stem cell* **14**, 523-534 (2014).

96 Guo, J., Wang, Y., Sachs, F. & Meng, F. Actin stress in cell reprogramming. *Proceedings of the National Academy of Sciences* **111**, E5252-E5261 (2014).

97 Huang, K. *et al.* Dynamically reorganized chromatin is the key for the reprogramming of somatic cells to pluripotent cells. *Scientific reports* **5** (2015).

98 Cheloufi, S. *et al.* The histone chaperone CAF-1 safeguards somatic cell identity. *Nature* **528**, 218-224 (2015).

99 Ishiuchi, T. *et al.* Early embryonic-like cells are induced by downregulating replication-dependent chromatin assembly. *Nature structural & molecular biology* (2015).

100 Huynh, L. M., Shinagawa, T. & Ishii, S. Two Histone Variants TH2A and TH2B Enhance Human Induced Pluripotent Stem Cell Generation. *Stem cells and development* **25**, 251-258 (2015).

101 Boutros, M., Heigwer, F. & Laufer, C. Microscopy-Based High-Content Screening. *Cell* **163**, 1314-1325 (2015).

102 Zhang, J., Campbell, R. E., Ting, A. Y. & Tsien, R. Y. Creating new fluorescent probes for cell biology. *Nature reviews Molecular cell biology* **3**, 906-918 (2002).

103 Hsu, P. D., Lander, E. S. & Zhang, F. Development and applications of CRISPR-Cas9 for genome engineering. *Cell* **157**, 1262-1278 (2014).

104 Perlman, Z. E. *et al.* Multidimensional drug profiling by automated microscopy. *Science* **306**, 1194-1198 (2004).

105 Mitchison, T. J. Small-molecule screening and profiling by using automated microscopy. *Chembiochem* **6**, 33-39 (2005).

106 Yarrow, J. C., Totsukawa, G., Charras, G. T. & Mitchison, T. J. Screening for cell migration inhibitors via automated microscopy reveals a Rho-kinase inhibitor. *Chemistry & biology* **12**, 385-395 (2005).

107 Conrad, C. & Gerlich, D. W. Automated microscopy for high-content RNAi screening. *The Journal of cell biology* **188**, 453-461 (2010).

108 Wang, M. *et al.* Novel cell segmentation and online SVM for cell cycle phase identification in automated microscopy. *Bioinformatics* **24**, 94-101 (2008).

109 Eliceiri, K. W. *et al.* Biological imaging software tools. *Nature methods* **9**, 697-710 (2012).

110 Schneider, C. A., Rasband, W. S. & Eliceiri, K. W. NIH Image to ImageJ: 25 years of image analysis. *Nat methods* **9**, 671-675 (2012).

111 Carpenter, A. E. *et al.* CellProfiler: image analysis software for identifying and quantifying cell phenotypes. *Genome biology* **7**, R100 (2006).

112 Schindelin, J. *et al.* Fiji: an open-source platform for biological-image analysis. *Nature methods* **9**, 676-682 (2012).

113 Desbordes, S. C. *et al.* High-throughput screening assay for the identification of compounds regulating self-renewal and differentiation in human embryonic stem cells. *Cell stem cell* **2**, 602-612 (2008).

114 Loo, L.-H., Wu, L. F. & Altschuler, S. J. Image-based multivariate profiling of drug responses from single cells. *Nature methods* **4**, 445-453 (2007).

115 Young, D. W. *et al.* Integrating high-content screening and ligand-target prediction to identify mechanism of action. *Nature chemical biology* **4**, 59-68 (2008).

116 Chong, Y. T. *et al.* Yeast proteome dynamics from single cell imaging and automated analysis. *Cell* **161**, 1413-1424 (2015).

117 Robinton, D. A. & Daley, G. Q. The promise of induced pluripotent stem cells in research and therapy. *Nature* **481**, 295-305 (2012).

118 Choi, J. *et al.* A comparison of genetically matched cell lines reveals the equivalence of human iPSCs and ESCs. *Nature biotechnology* (2015).

119 Ashwin, S. & Sasai, M. Effects of Collective Histone State Dynamics on Epigenetic Landscape and Kinetics of Cell Reprogramming. *Scientific reports* **5** (2015).

120 Rackham, O. J. *et al.* A predictive computational framework for direct reprogramming between human cell types. *Nature genetics* (2016).

121 Trapnell, C. *et al.* The dynamics and regulators of cell fate decisions are revealed by pseudotemporal ordering of single cells. *Nature biotechnology* **32**, 381-386 (2014).

122 Howden, S. E. *et al.* Simultaneous Reprogramming and Gene Correction of Patient Fibroblasts. *Stem cell reports* **5**, 1109-1118 (2015).

123 Garber, K. RIKEN suspends first clinical trial involving induced pluripotent stem cells. *Nature biotechnology* **33**, 890-891 (2015).

124 Durruthy-Durruthy, J. *et al.* Rapid and efficient conversion of integration-free human induced pluripotent stem cells to GMP-grade culture conditions. *PloS one* **9**, e94231 (2014).

125 Beers, J. *et al.* A cost-effective and efficient reprogramming platform for large-scale production of integration-free human induced pluripotent stem cells in chemically defined culture. *Scientific reports* **5** (2015).

126 Paull, D. *et al.* Automated, high-throughput derivation, characterization and differentiation of induced pluripotent stem cells. *Nature methods* **12**, 885-892 (2015).

127 Chen, K. G., Mallon, B. S., McKay, R. D. & Robey, P. G. Human pluripotent stem cell culture: considerations for maintenance, expansion, and therapeutics. *Cell Stem Cell* **14**, 13-26 (2014).

# Chapter 3. Nanofibrous electrospun polymers for reprogramming human cells

Elements of this work have been published as:

**Cordie, T., Harkness, T., Jing, X., Carlson-Stevermer, J. et al., Nanofibrous electrospun polymers for reprogramming human cells. *Cell and Molecular Bioengineering.* 2014, *7*, 379–393.**

## 3.1 Introduction

Dramatic changes in cell fate and function can be achieved via forced expression of transcription factors[1]. These changes are coordinated by particular combinations of factors (e.g., Oct4, Sox2, Klf4 and c-Myc, or Oct4, Sox2, Nanog and Lin28[2,3]) and are molecularly encoded at the epigenetic level. Such epigenetic reprogramming processes are typically multi-step and noisy, generating many intermediate, partially reprogrammed cell types during the process[4,5]. Improving methods to accelerate reprogramming and generate high quality, fully reprogrammed cells would advance the field and open up new applications in disease modeling[6], tissue engineering[7] and drug discovery[8].

While extensive studies have been conducted on the roles of transcription factors, miRNA, small molecules and other soluble factors[9,10], very little is known about how biophysical properties of cell culture substrates influence somatic cell

reprogramming. Recent work with mouse fibroblasts indicated that altering the biophysical microenvironment through the use of microgroove channels and electrospun fibers induced hyperacetylation of histones that synergized with Oct4, Sox2, Klf4 and c-Myc reprogramming factors[11]. Hyperacetylation of histones has been shown to prevent chromatin from compacting into a 30-nm fiber[12]. Such hyperacetylation could promote promiscuous transcription by favoring a more open chromatin conformation that permits binding of the reprogramming factors and transcriptional machinery. Indeed, an open chromatin structure induced by two histone variants, TH2A and TH2B, was linked to enhanced reprogramming[13]. Further, hyperacetylation of specific sites in the genome or at specific lysines on histone 3 could directly serve as recognition sites for factors that promote transcription[14]. For instance, acetylation of lysine 27 on histone 3 (H3K27ac), an enhancer mark, was increased in MBD3-depleted cells that had accelerated reprogramming kinetics[15]. Acetylation machinery could complex with other cofactors (e.g., WDR5) and reprogramming factors to hyperacetylate chromatin at specific loci to locally enhance transcription[14,16] to enhance reprogramming[11,17]. Together, these results suggests that materials that force nuclei to have a more open chromatin environment by increasing acetylation both globally and at specific sites in the genome could synergize with reprogramming factors to drive epigenetic reprogramming.

Because nanofibrous materials were successful in mouse reprogramming[11] and may be able to perturb nuclei to adopt a more open conformation amenable to reprogramming, we have taken an empirical approach to identifying nanofibrous materials that could promote human reprogramming. Synthetic polymers - PCL, PLA, PPC, and TPU - are commonly used in manufacturing and polymer processing to

produce highly-aligned scaffolds that may be able to alter nuclear shape. Furthermore, these materials can be synthesized to mimic the fibrous nature of native extracellular matrix (ECM), which has been shown to change the degree of cellular adhesion to substrates (e.g., through variations in ligand density, integrin clustering and cytoskeletal organization[18]).

Here we describe the synthesis and characterization of a material library of nanofibrous substrates generated by electrospinning PCL, PLA, PPC, and TPU. Reprogramming of human fibroblasts by transcription factors was performed on this library to identify substrates that enhanced factor-mediated reprogramming. We found that nuclear shape can be perturbed on these nanofibrous substrates, but reprogramming factors rapidly erase these perturbations and induce a circular shape early in the process. Several nanofibrous substrates promoted reprogramming, and elevated reprogramming did not correlate with materials-induced global hyperacetylation of histone 3. Regression of our experimental dataset indicated a multivariate response of cells to the biochemical and biophysical properties of their microenvironment during reprogramming. We expect this work to inform the development of design rules for materials that can drive the epigenetic reprogramming of patients' cells.

## 3.2 Materials and Methods

### *3.2.1 Materials*

Polylactic acid (PLA, 2002 D) and poly(propylene carbonate) (PPC, QPAC® 40) were purchased from Natureworks LLC and Empower Materials Inc., respectively.

Medical grade thermoplastic polyurethane (TPU ,Texin® Rx85A) was generously donated by Bayer Material Science Inc. Polycaprolactone (PCL, $M_n$=80,000 g/mol), polyacrylic acid (PAA, Mn=50,000g/mol), chloroform (CF, ACS regent), N,N-dimethyl formamide (DMF, ACS regent) and pentyl acetate were all purchased from Sigma-Aldrich (Milwaukee, WI, USA). Manufacturers for all other reagents are listed below within the text.

*3.2.2 Substrate Preparation*

Each polymer solution was prepared at various concentrations as described in Table 3-1. Electrospinning was carried out using a custom-built electrospinning device as previously described[19]. The prepared solution was loaded in a plastic syringe connected to an 18-gauge blunt-end needle and then mounted on a digital syringe pump (Harvard Bioscience Company). Spinning conditions consisted of a voltage of 18 kV, a 15 cm needle-to-target distance, and a 0.5 mL/h flow rate. Two parallel steel plates separated by a 3 cm distance were used to collect the aligned fibers. Fibers were then applied to the sterilized, round stainless steel washers (inner diameter of 8.33 mm, McMaster-Car; Part C0532R) to maintain structural integrity for cell culture applications. Random fibers were spun directly onto the washers.

**Table 3-1. Composition of polymer solutions used in substrate synthesis.**

| Sample | Solute Concentration | Solvent Composition |
|---|---|---|
| PLA | 9% wt. | CF/DMF (w/w=4/1) |
| PPC | 10% wt. | CF/DMF (w/w=4/1) |
| PCL | 12% wt. | CF/DMF (v/v=3/2) |
| TPU | 11% wt. | DMF |

Because we were unable to make aligned TPU fibers without the addition of PAA, 1 wt% PAA was added to the TPU solution before electrospinning to improve conductivity. However, dense fiber mats of random TPU fibers could be created for water contact angle and BET assay without the addition of PAA. To prepare the PCL nanofibrous substrates with a “shish kebab” structure (PCL-SK), 30 µL of 0.8% PCL in the pentyl acetate was dropped onto the prepared PCL nanofibers and the samples were placed in the fume hood to let solvents evaporate overnight.

### *3.2.3 Scanning Electron Microscopy Imaging and Analysis*

Each nanofibrous substrate was imaged by scanning electron microscopy (SEM, JEOL 6500, Nikon) using an accelerating voltage of 10 kV. The electrospun substrates were cut with a scalpel and sputter-coated with gold for 40 seconds before imaging. Images were converted to binary format using ImageJ, where the fibers appeared black and the pores white. Fiber alignment, fiber diameter and substrate porosity were determined by ImageJ software analysis. The percentage of the white pixels relative to the total scaffold surface area in each image was defined as the percent porosity[20]. For alignment and diameter measurements, fifty fibers were profiled for each sample from three images. The fiber diameter was the average value of at least fifty fibers measured using three images.

### *3.2.4 Water Contact Angle*

Water contact angle (WCA) was calculated for each substrate in the random orientation and before protein adsorption. Each polymer sample was electrospun for up

to 3 hours in order to create the proper thickness to support a water droplet. Each sample was tested using the sessile drop method during atmospheric conditions using a video contact angle instrument (Dataphysics OCA 15) and a droplet size setting of 4 µL. Three samples for each substrate were tested.

### *3.2.5 Mechanical Properties and Flexibility*

Electrospun membranes and TCPS were configured into a rectangular shape, with the dimensions of 50×10 $mm^2$. Tensile tests were performed on an Instron 5565 universal testing machine using a 250 N load cell with a crosshead speed of 5 mm/min. At least four samples were tested for each type of electrospun fibrous membrane. The Young's modulus and elongation-at-break were obtained from the stress–strain curves.

### *3.2.6 BET Surface Area*

Surface areas of PLA, PCL and TPU substrates were measured by a Brunauner-Emmett-Teller (BET) instrument (Gemini VII Version 2.00) using a nitrogen gas physical adsorption method. The instrument accuracy had a lower limit of 0.1 $m^2$ and therefore only randomly oriented substrates, which could be synthesized at large scale, were measured. Prior to the BET measurement, samples were degassed in a vacuum oven at 45$^oC$ for 24 hours. A relative pressure range, $P/P_o$, of 0.05-0.25 was used for calculating the BET surface area using the Gemini VII software. The individual mass of each substrate (used in surface area per substrate calculations) was assayed by measuring the mass of each polymer (n=15) with washer and then subtracting the washer's mass.

*3.2.7 Protein Adsorption*

The amount of protein adsorbed to each substrate was calculated using the Pierce BCA Protein Assay Kit and protocol (Thermo Fisher Scientific Inc., 2013) per manufacturer's instructions. Proteins were allowed to adsorb onto the materials overnight, using the same media conditions that were used when seeding cells. A standard graph was made following the BCA standard kit protocol using bovine serum albumin (BSA) as standards. Absorbance at 560 nm of each sample (n=3) was measured using a plate reader (Promega GloMax®-Multi Microplate Multimode Reader), and protein content was inferred from the standard graph.

*3.2.8 Substrate Processing For Cell Culture*

After electrospinning, each fiber substrate was allowed to air dry in a fume hood for at least 24 hours, to allow full dissipation of any residual solvents. Samples were sterilized via ultraviolet light from the biosafety cabinet (Baker Company) for 20 minutes on each side of the scaffold. All cell culture experiments were conducted in 24 well plates that were pre-treated with poly-HEMA (Sigma) to prevent cell attachment to culture wells. Poly-HEMA, 2 wt% solution was made with 100% ethanol (Pharmco-AAPER, ACS/USP Grade). Each scaffold was immersed in a protein solution to allow for protein adsorption before cells were seeded. The protein solution contained the following components: DMEM-high glucose (Life Technologies), supplemented with 5% FBS (Life Technologies), 2% Penicillin/Streptomycin (Life Technologies) and growth-factor-reduced Matrigel (BD) coated at a concentration of 0.02 mg per well, for a minimum of 1 hour inside an incubator at 37$^{o}$C.

*3.2.9 Media Conditions*

Fibroblast cells were maintained in a "fibroblast medium" consisting of DMEM-high glucose (Life Technologies), supplemented with 10% FBS (Life Technologies), 1 mM L-glutamine (Life Technologies), 1% nonessential amino acids (Life Technologies) and Penicillin/Streptomycin (Life Technologies). Fibroblast medium was used during routine maintenance of the cells as well as during seeding onto the scaffolds.
"E8 medium" was made in house following the previously published protocol[21]. E8 medium was then modified by excluding TGF-β, which is then referenced as "E7 medium." Both E8 and E7 are a defined, xeno-free human pluripotent stem cell culture media and do not contain serum. Both E8 and E7 were used to culture human embryonic stem cell (hESC) lines, WA01 and WA01+H2B-mCherry cells, as well as the C1.2 iPSC line.

*3.2.10 Generation of H2B-mCherry Transgenic Cells*

hESC line WA01 (WiCell Research Institute) underwent genome modification to create an H2B-mCherry positive stem cell line via CRISPR/Cas9 gene editing. The H2B-mCherry plasmid was generated by cloning the H2B-mCherry sequence (Addgene # 20972) into the GFP sequence of the AAV-CAGGS-EGFP plasmid (Addgene #22212). This plasmid was electroporated with Cas9 plasmids as described previously[22,23]. Isolated cell lines retained constitutive expression during culture and differentiation into HEF1 (fibroblast) cells (see next section). The hESC WA01+H2B-mCherry cell line was used for cell attachment and proliferation data. The cells were maintained on 6 well plates coated with Matrigel at a concentration of 8.6 μg/cm$^2$. All

stem cell lines were maintained with E8 medium, fed on a daily basis and typically passaged every four days using EDTA (Versene, Life Technologies)[21]. Before seeding the hESCs onto the corresponding substrates the cells were pretreated with a ROCK inhibitor (Y-27632, Selleck Chemical) at a 10 μM concentration in water for a minimum of two hours. ROCK inhibition prevents apoptosis of single cells during passaging of human pluripotent stem cells[24-27]. The passaged cells were seeded at a density of 4 $x10^4$ cells per well with E8 medium for attachment and proliferation studies. Cells were fed on a daily basis and cultured at incubator settings of 5% $CO_2$ and 37°C.

*3.2.11 Fibroblast Differentiation*

WA09+H2B-mCherry hESCs and C1.2 iPSCs were made into embryoid bodies via the Aggrewell method (Stem Cell Technologies) per manufacturer's instructions and cultured in non-adherent cell culture plates (Corning Inc.) to form aggregates in "differentiation medium" comprised of 80% knockout Dulbecco's modified Eagle's medium (KO-DMEM) (Invitrogen), 1 mM L-glutamine, 20% FBS, and 1% nonessential amino acids. After 4 days in suspension, aggregates were transferred onto matrigel-coated plates and cultured for an additional 9 days. After three passages in differentiation medium, cells were transitioned to fibroblast media. Most cells in culture appeared fibroblast-like after three to five passages. To confirm a fibroblast phenotype after differentiation, cells were stained with anti-proly1-4 hydroxylase beta (mouse monoclonal clone #3-2B12A, Acris Antibodies) as described previously[28].

*3.2.12 Fibroblast Reprogramming*

C1.2 fibroblasts contain the doxycycline (DXC)-inducible transcription factors Oct4, Sox2, Klf4 and c-Myc[28]. The C1.2 cell line was prepared by infecting C1 fibroblasts with a inducible c-Myc virus[28] to generate a C1.2 iPSC line that could be differentiated into “secondary” fibroblasts as described previously[28]. C1.2 fibroblasts were cultured in fibroblast medium. Cells were maintained between 5-15 passages with media changes every 2 days and passaged every 6-7 days with TrypLE (Invitrogen) on TCPS plates or flasks.

Cells were seeded at a density of $4x10^4$ per well of a 24-well plate (BD) for reprogramming experiments. DXC-treated cells were cultured with doxycycline hyclate (Sigma Cat. D9891) at a final concentration of 2 µg/mL. During reprogramming, cells were fed daily with fibroblast medium with DXC and 1 µM hydrocortisone[21] (Sigma). The DXC stock concentration of 2 mg/mL solution was typically vortexed prior to addition.

*3.2.13 Immunofluorescence*

Samples were washed with PBS, fixed with 4% paraformaldehyde in PBS for 15 min, and permeabilized with 0.5% Triton X-100 in PBS for 30 min. Primary antibodies were allowed to bind overnight at 4°C in a 5% donkey serum blocking buffer. Secondary antibodies were obtained from Life Technologies and used at a 1:400 dilution in 5% donkey serum for an incubation period of one hour at 4°C. Primary antibody dilutions are listed in Table 3-2. Imaging was performed using a Nikon Eclipse Ti.

**Table 3-2. Antibodies and stains used for immunocytochemistry.**

| Target | Vendor/Cat# | Dilution |
|---|---|---|
| **TRA-1-60** | Millipore MAB4360 | 1:100 |
| **CD44** | BD 560531 | 1:200 |
| **Nanog** | R&D Systems AF1997 | 1:200 |
| **SSEA-4** | Millipore MAB4304 | 1:50 |
| **Oct3/4** | BD 560186 | 1:10 |
| **Sox2** | BD 560531 | 1:40 |
| **F-Actin** | Sigma P1951 | 1:400 |
| **Nuclei** | Life Technologies H1399 | 1:10,000 |

*3.2.14 Flow Cytometry*

Data was acquired with an Accuri C6 (BD Biosciences) and analyzed using FlowJo (TreeStar). Samples that were antibody-stained were detached from substrates by two incubations of 10 min each in Accutase (Life Technologies) at 37$^{o}$C followed by immunofluorescence staining protocol as described above. For attachment and proliferation studies, flow cytometry data were collected 24 hours post-seeding for initial cell attachment data (n=3), and again 72 hours post seeding for proliferation data (n=3). Each well containing the substrate was initially washed twice with PBS to ensure that the cells collected were not growing in suspension within the poly-HEMA coated well. For cell counting, TrypLE (Life Technologies) was used to detach the cells for 5 minutes at 37$^{o}$C. After incubation the cells were collected and centrifuged at 200x*g* for five minutes. The supernatant was then aspirated, and the cells were resuspended in 600 uL of PBS and filtered through a 100 µm mesh (BD) prior to analysis.

*3.2.15 Nuclear Shape and Size Analysis*

Nuclear size and shape index was calculated by manually tracing ellipses around individual Hoescht-stained nuclei. Nuclear shape index is given by the formula

$$NSI = \frac{4\pi A}{P^2}$$

where *A* and *P* represent the area and perimeter of a nuclei, respectively. Analysis was performed using Fiji software[29].

*3.2.16 Statistics*

Statistical analysis was performed using Microsoft Excel via an unpaired, 2-tailed student's t-test for single-variable analysis and a two-factor ANOVA test with replicates for two-variable analysis.

*3.2.17 Partial Least Squares Regression*

Analysis was performed in MATLAB using the SIMPLS method[30]. The model was analyzed for goodness of fit ($R^2Y$) as well as goodness of prediction ($Q^2$). $Q^2$ was validated by 14-fold cross validation so that each observation was left out exactly once[31]. Inputs to the model consisted of an explanatory matrix. Columns in the matrix represented biochemical and biophysical cues. Each row represented a different combination of cues. A response matrix was generated from experimental data with columns representing different cellular responses and rows corresponding to the above cue combinations. Raw explanatory and response values were mean centered and variance scaled prior to analysis.

## 3.3 Results

### *3.3.1 Materials library characteristics*

A biomimetic substrate library with ECM-like nanofibrous structure was successfully generated through electrospinning[32]. Synthetic polymers PCL, PLA, PPC and TPU were individually electrospun as a membrane onto electrically conductive parallel plates to align fibers.

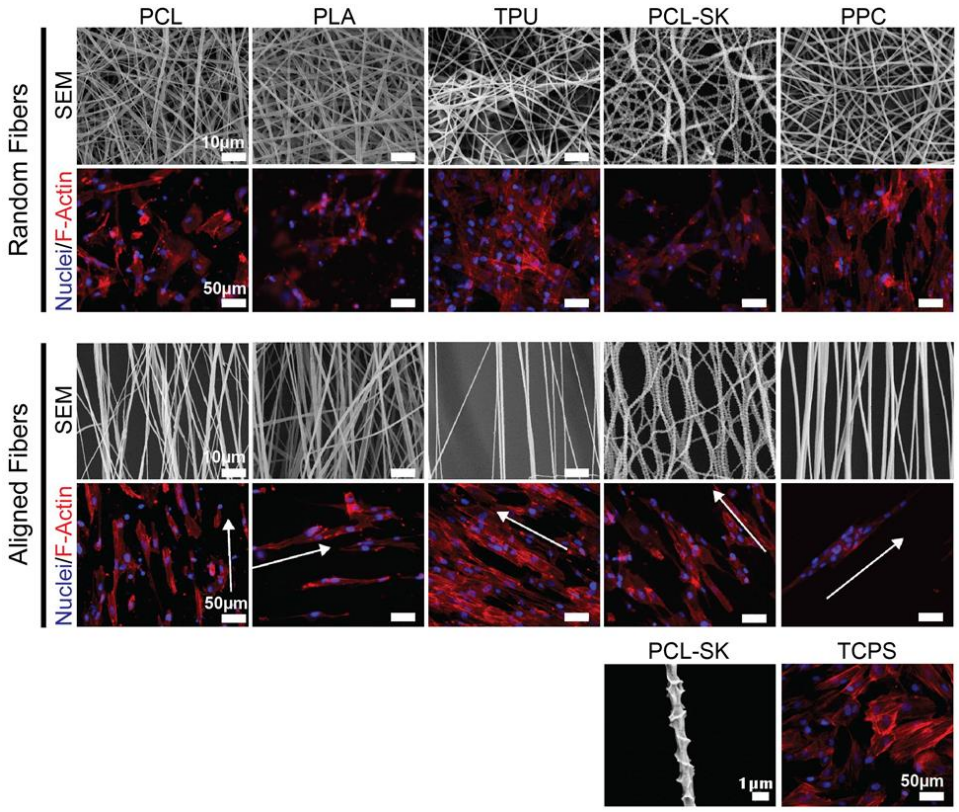


**Figure 3-1. Nanofibrous substrate library with attached fibroblasts.** Electron microscopy images of each polymer substrate [polylactic acid (PLA), polycaprolactone (PCL), thermoplastic polyurethane (TPU)]. Below each image is an immunocytochemistry image of HEF1 fibroblasts grown on each substrate. Cells were fixed after five days in culture. Nuclei and F-actin were stained by Hoechst dye and phalloidin, respectively. Arrows indicate fiber orientation. TCPS: tissue culture polystyrene.

Electrospinning without an organized electric field at the collector plate created substrates that were not aligned in a particular direction, termed “random” substrates (Figure 3-1). Scanning electron microscope (SEM) analysis confirmed a nanofibrous

structure with fiber diameters of 500-1000 nm within the range of native ECM[33] (Table 1). For the aligned substrates, the distribution of fiber diameter of TPU, PPC and PCL fibers were fairly concentrated within ten degrees of the desired direction of alignment (Table 3-3 and Figure 3-2). Aligned substrates also differed from randomly spun substrates in porosity (Table 3-3). Finally, a "shish kebab" structure was prepared with PCL nanofibrous substrates (PCL-SK) to produce a variant topology compared to standard PCL substrates[34] (Figure 3-1 and Table 3-3).

**Table 3-3. Properties of nanofibrous substrate library.** Mean values ± 95% confidence intervals are listed for all values except fiber alignment which is listed as mean values ± standard deviation. All TCPS data refers to 24 well plate dimensions. A fiber alignment of zero degrees would indicate perfect alignment. The average fiber diameter is not applicable to TCPS. We were unable to fabricate aligned fibers with the proper requirements for water contact angle, surface area analysis and tensile testing.

| | TCPS | PLA-R | PLA-A | PCL-R | PCL-A | TPU-R | TPU-A | PPC-R | PPC-A | PCL-SK -R | PCL-SK -A |
|---|---|---|---|---|---|---|---|---|---|---|---|
| Fiber Diameter (nm) | N/A | 960 ±76 | 788 ±93 | 617 ±84 | 537 ±59 | 594 ±29 | 669 ±59 | 829 ±50 | 794 ±66 | 980 ±80 | 990 ±63 |
| % Porosity | N/A | 38±6 | 65±4 | 49±4 | 84±3 | 43±5 | 73±9 | 45±0.16 | 75±15 | 26.71±5 | 38±10 |
| BET Surface Area ($m^2/g$) | N/A | 4.168 | 4.168 | 2.201 | 2.201 | 2.129 | 2.129 | N/A | N/A | N/A | N/A |
| Surface area per substrate ($cm^2$) | 1.9 | 1724 ±355 | 1690 ±5 | 808 ±107 | 684 ±5 | 26 ±7 | 6 ±2 | N/A | N/A | N/A | N/A |
| Elastic Modulus (MPa) | 533 ±47 | 40 ±1.5 | N/A | 10.2 ±1.5 | N/A | 7.4 ±0.1 | N/A | 432.3 ±15.4 | N/A | 10.5 ±1.7 | N/A |
| Elongation at break (%) | 5.1 ±2.0 | 71.7 ±9.3 | N/A | 148.6 ±3.8 | N/A | 150.9 ±11.2 | N/A | 1285.8 ±240.8 | 1197.9 ±142.6 | N/A | N/A |
| Protein Adsorption ($\mu g/cm^2$) | 21.2 ±4.0 | 1.33 ±0.2 | 0.779 ±0.1 | 2.03 ±0.3 | 1.77 ±0.1 | 71.3 ±11.3 | 192.3 ±9.5 | 1285 ±240 | 1197 ±142 | N/A | N/A |
| Fibroblast Proliferation Index | 1.29 ±0.56 | 2.19 ±1.26 | 1.55 ±0.59 | 2.01 ±1.19 | 0.78 ±0.28 | 1.61 ±1.15 | 1.89 ±1.96 | 1.59 ±1.27 | 2.52 ±1.38 | 3.79 ±2.85 | 1.01 ±0.54 |
| Fibroblasts Attachment Day 1 (total cells) | 28,907 ±3098 | 10,927 ±5,186 | 8,077 ±2,162 | 12,289± 5,531 | 12,717± 3,401 | 16,111± 4,645 | 14,103±1 0,600 | 13,183 ±7,285 | 14,340 ±6,196 | 14,659 ±6282 | 7,929 ±3,486 |
| Stem Cell Proliferation Index | 8.81 ±1.71 | 3.34 ±1.87 | 2.47 ±1.14 | 3.14 ±1.32 | 6.72 ±4.22 | 3.54 ±0.38 | 4.61 ±2.74 | 2.83 ±1.28 | 3.01 ±1.49 | 3.49 ±1.14 | 3.72 ±0.96 |
| Stem Cell Attachment Day 1 (total cells) | 7,246 ±233 | 5,052 ±2,664 | 4,844 ±1,882 | 8,768 ±2,264 | 4,782 ±2,664 | 7,724 ±811 | 7,416 ±3,697 | 7,483 ±1,268 | 8,386 ±2,611 | 5,551 ±1704 | 5,758 ±1,396 |
| Water Contact Angle (Degrees) | 65 ±6.1 | 116 ±6.5 | N/A | 127 ±1.1 | N/A | 111 ±1.3 | N/A | 112 ±0.2 | N/A | 128 ±0.4 | N/A |

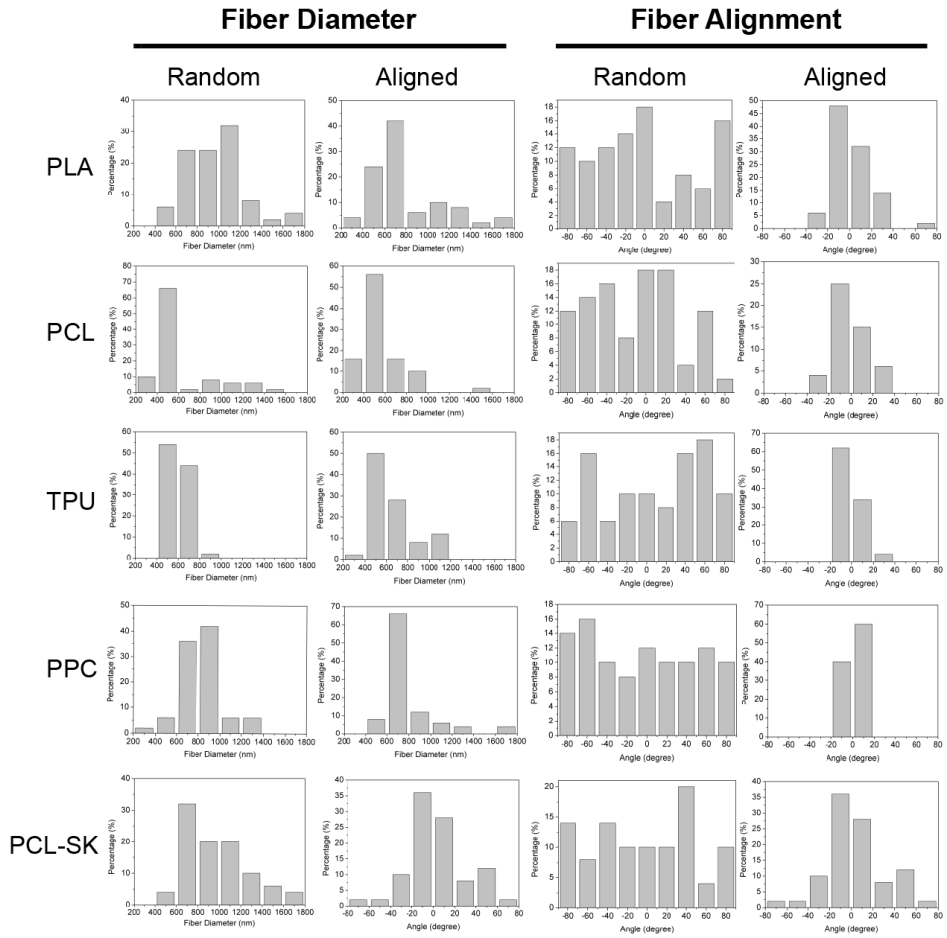


**Figure 3-2. Distribution of nanofiber diameter and alignment.** Histograms of fiber diameter and fiber alignment for each nanofibrous substrate constructed. Measurements were gathered by ImageJ analysis of SEM images. A fiber alignment of zero degrees would indicate perfect alignment.

Each substrate in the library was characterized for its surface area, surface hydrophobicity, elastic modulus, flexibility and porosity. A nitrogen adsorption isotherm on a large electrospun sample was utilized for surface area calculations. Areas per substrate reached three orders of magnitude higher than tissue culture polystyrene (TCPS, Table 3-3). The surface hydrophobicity of the substrates were characterized via water contact angles (WCAs) and were higher than 90°, indicating that all the prepared substrates were hydrophobic (Table 3-3). TCPS had the smallest WCA, which is consistent with prior reports[35]. The mechanical properties of substrates were

significantly softer than TCPS but stiffer than native ECM[36], with a Young's Modulus range between 7 to 40 MPa (Table 3-3). Flexibility of substrates was assessed by elongation at break. Nanofibrous substrates were more flexible than TCPS (Table 3-3).

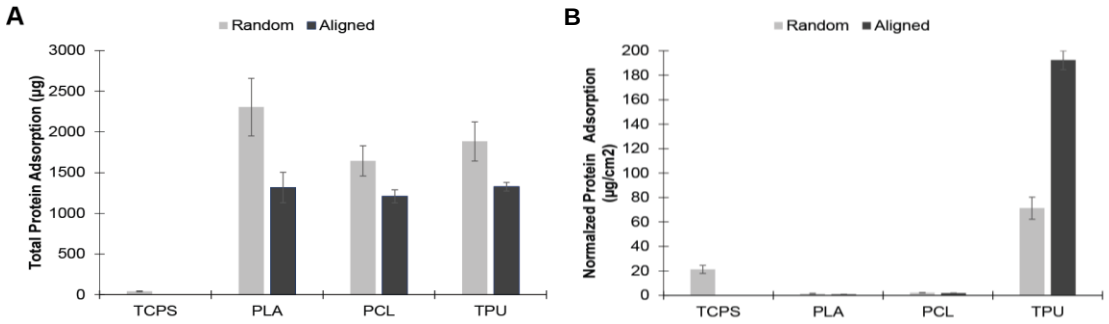


**Figure 3-3. Protein adsorption to nanofibrous substrates. A)** Total protein adsorption to each substrate. **B)** Protein adsorption normalized by substrate surface area. Protein was allowed to adsorb to substrates overnight in standard cell culture conditions and measured by a BCA protein assay on the following day.

Prior to cell seeding, nanofibrous substrates were pre-coated with a thin adsorbed layer of Matrigel, because pre-coating synthetic polymeric substrates with proteins can be important for cell-surface interaction with human pluripotent stem cells[35]. Matrigel adsorbed well to nanofibrous substrates as measured through a bicinchoninic acid assay (Figure 9-3 and Table 9-3). Shortly after seeding, fibroblasts on randomly oriented fibers exhibited morphology similar to fibroblasts grown on TCPS (Figure 3-1). On all of the aligned substrates, fibroblasts were more elongated in comparison to cells on random substrates and TCPS (Figure 3-1, white arrows indicate fiber orientation). Despite these differences in cell morphology, fibroblasts on all substrates were able to attach and proliferate at similar levels (Figure 3-4).

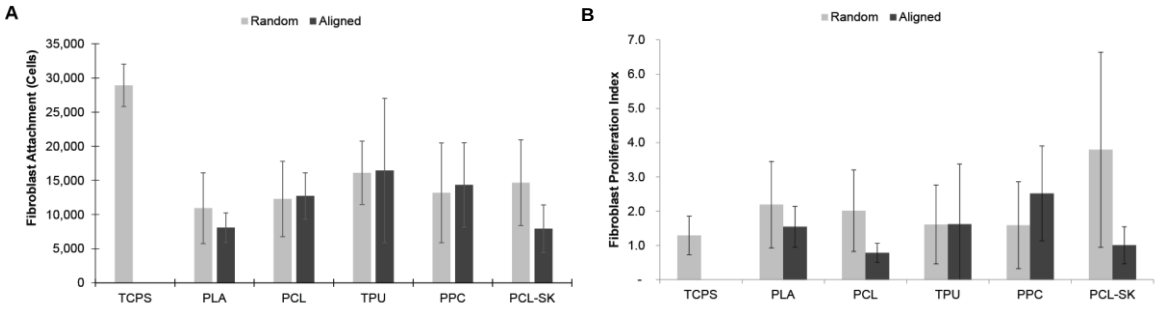


**Figure 3-4. Attachment and proliferation of fibroblasts on nanofibrous substrates.** **A)** Attachment of WA01-H2B-mCherry fibroblasts at 24 hours. Cells were counted by flow cytometry after dissociation from substrates. **B)** Proliferation of fibroblasts over 72 hours. Proliferation Index is the ratio of cell counts after 24 to cell counts after 72 hours.

Human pluripotent stem cells were also able to attach and proliferate at similar levels on all substrates (Figure 3-5). These results demonstrate that all of our matrigel-coated nanofibrous substrates can support the attachment and proliferation of both the starting and ending cell types – fibroblasts and pluripotent stem cells, respectively - of reprogramming experiments.

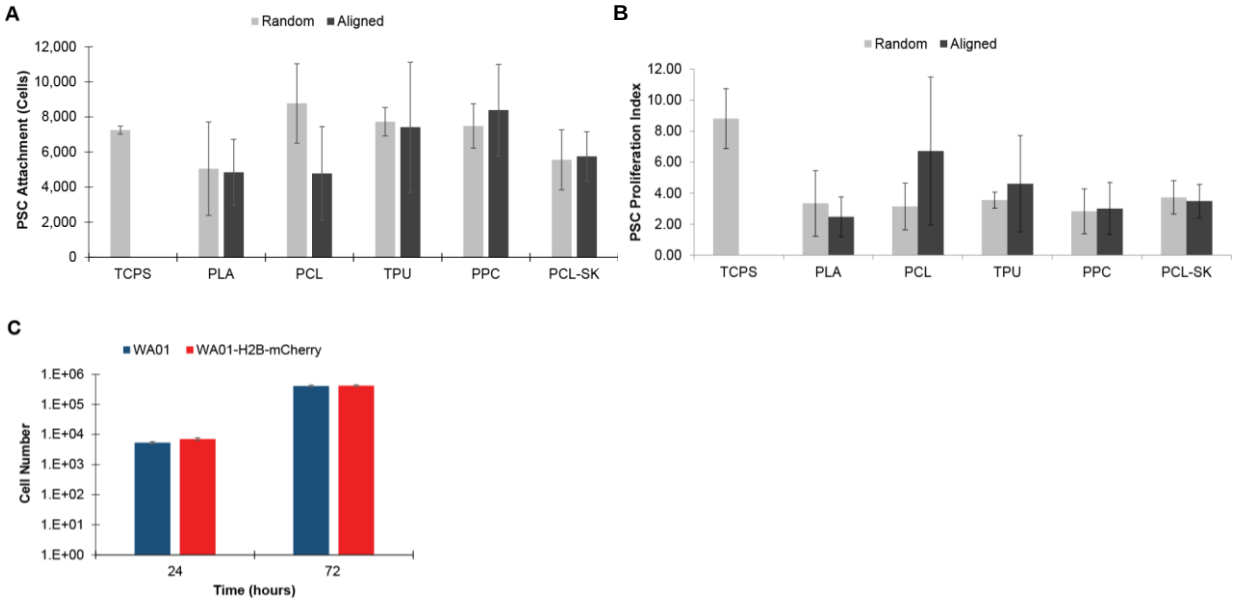


**Figure 3-5. Attachment and proliferation of pluripotent stem cells on nanofibrous substrates.** **A)** Attachment of WA09 hESCs at 24 hours. Cells were counted by flow cytometry after dissociation from substrates. **B)** Proliferation of fibroblasts over 72 hours. Proliferation Index is the ratio of cell counts after 24 to cell counts after 72 hours. **C)** Growth rate comparison of parental WA01 and daughter WA01-H2B-mCherry cell lines.

*3.3.2 Reprogramming on Nanofibrous Substrates*

Fibroblasts were next seeded on the material library and induced to express Oct3/4, Sox2, Klf4 and c-Myc reprogramming factors. We utilized a "secondary" reprogramming fibroblast system[28] that harbored doxycycline (DXC)-inducible transgenes for the reprogramming factors to achieve transgene expression during reprogramming without viral infection. For subsequent reprogramming experiments that required culture over three to four weeks, we focused on TPU, PLA and PCL substrates due to their ease of synthesis and handling. A large fraction of PPC substrates tore or broke during routine handling in the initial cell attachment and proliferation studies. These substrates were deemed to be too fragile to be immersed in media and transported to and from standard incubators for multiple weeks.

Fibroblasts express a cell-surface marker, CD44, and gradually lose expression of CD44 as cells progress in reprogramming to intermediate states[37] (Figure 3-6A). In contrast, fully reprogrammed cells express the pluripotency marker, TRA-1-60, and are negative for CD44 (Figure 3-6A). At 7, 12, 17 and 22 days after factor induction, cells were isolated from each substrate, co-stained for CD44 and TRA-1-60 via immunocytochemistry and analyzed for levels of these markers by flow cytometry. By following the percent of cells in each gate (Figure 3-6A-B), we were able to follow the progression and kinetics of cellular reprogramming on the materials library.

On all nanofibrous substrates, cells initially were CD44+ and then ~40-60% of these cells lost CD44, thereby losing fibroblast identity and gaining an intermediate phenotype (Figure 3-6B and Figure 3-7). Over the subsequent 15 days, a small percentage of intermediate cells gain hallmarks of pluripotent cells, leading to 1-7% of

the overall population being TRA-1-60+/CD44- by day 22 (Figure 3-6B and Figure 3-7). After reprogramming culture on nanofibrous substrates, DXC was removed from the media to shutdown reprogramming factor expression, and cells were grown and passaged for several weeks to see whether the observed TRA-1-60+/CD44- cells would retain their pluripotent markers. For all substrates, reprogrammed colonies could be identified that stained positive simultaneously for pluripotency markers: Nanog, Oct4, Sox2, SSEA-4 and TRA-1-60 (Figure 3-6C). These reprogrammed cells were factor independent and acquired all marks of pluripotency, indicating robust reprogramming of fibroblast state[9]. The nanofibrous substrates had similar kinetics of reprogramming overall (Figure 3-7), but important differences in the progression to intermediate states could be identified (Figure 3-6D). The average time that it took cells to transit out of the fibroblast CD44+ state correlated strongly with the number of TRA-1-60+/CD44- pluripotent cells seen on day 22 (Figure 3-6D). Top performing substrates were TPU-R, TCPS, TPU-A and PCL-R.

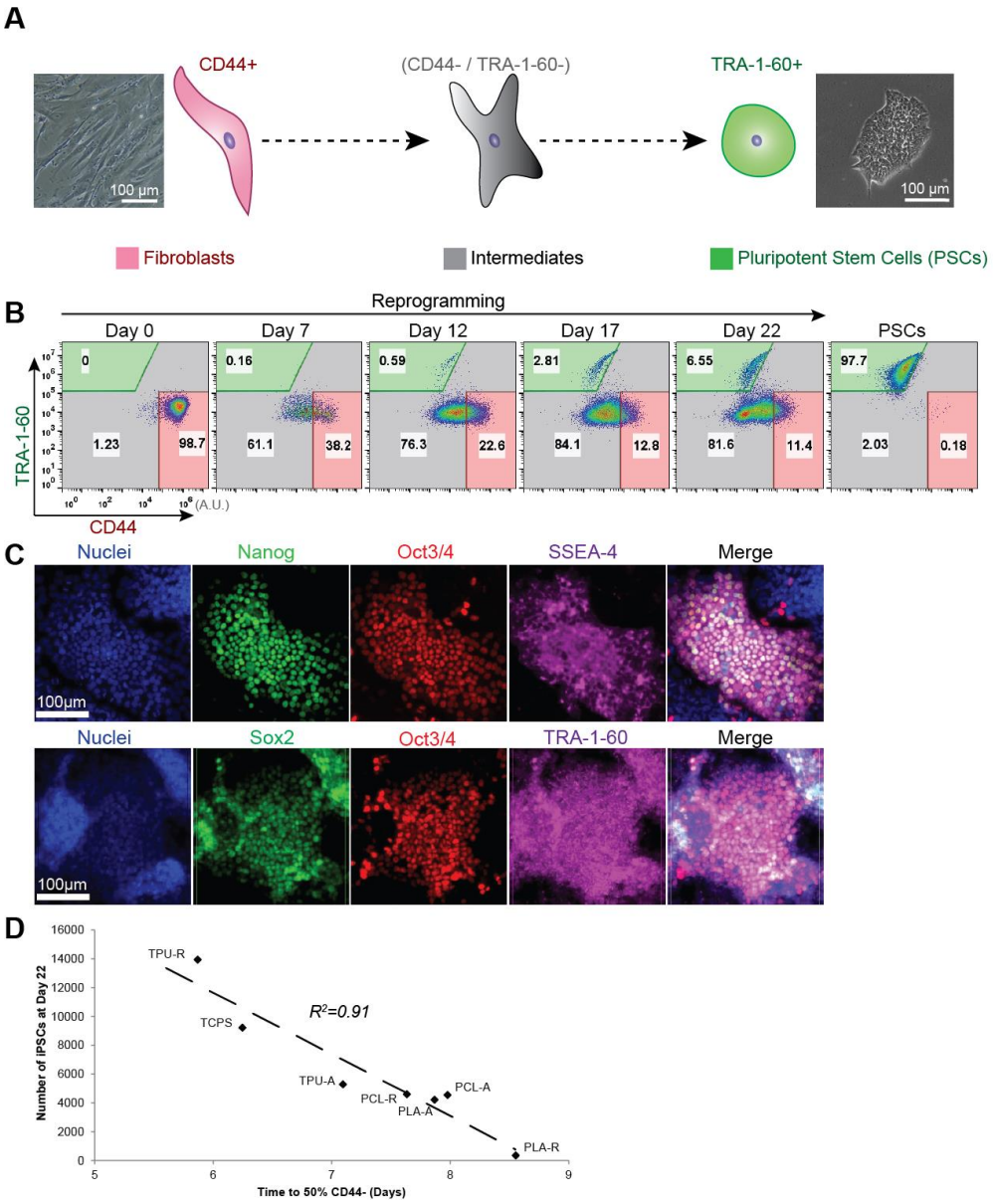


**Figure 3-6. Nanofibrous substrates support the reprogramming of human fibroblasts. A)** Schematic of reprogramming. Mature fibroblast cells are CD44 positive (red) and, upon factor expression, progress stochastically to an intermediate state between fibroblasts and pluripotent stem cells (PSCs), which are positive for TRA-1-60 (green). Phase-contrast images of fibroblasts and PSCs were taken on TCPS. **B)** Time course of marker levels during reprogramming on TPU-R as measured by flow cytometry. Numbers within plot indicate percent of total cells in each gate (shaded in red, grey or green). A.U., arbitrary fluorescent units. **C)** Pluripotency marker staining of reprogrammed cells after removal of reprogramming factors. Central colonies are positive for all the pluripotency markers, Nanog, Oct3/4, SSEA-4, Sox2 and TRA-1-60. **D)** Quantification of the kinetics of reprogramming on nanofibrous substrates. Amount of time required to lose fibroblast identity (50% of cells are CD44-) correlated with the number of reprogrammed cells at day 22. Dashed line represents linear regression best-fit line. All experiments were conducted in E7 media with hydrocortisone and doxycycline.

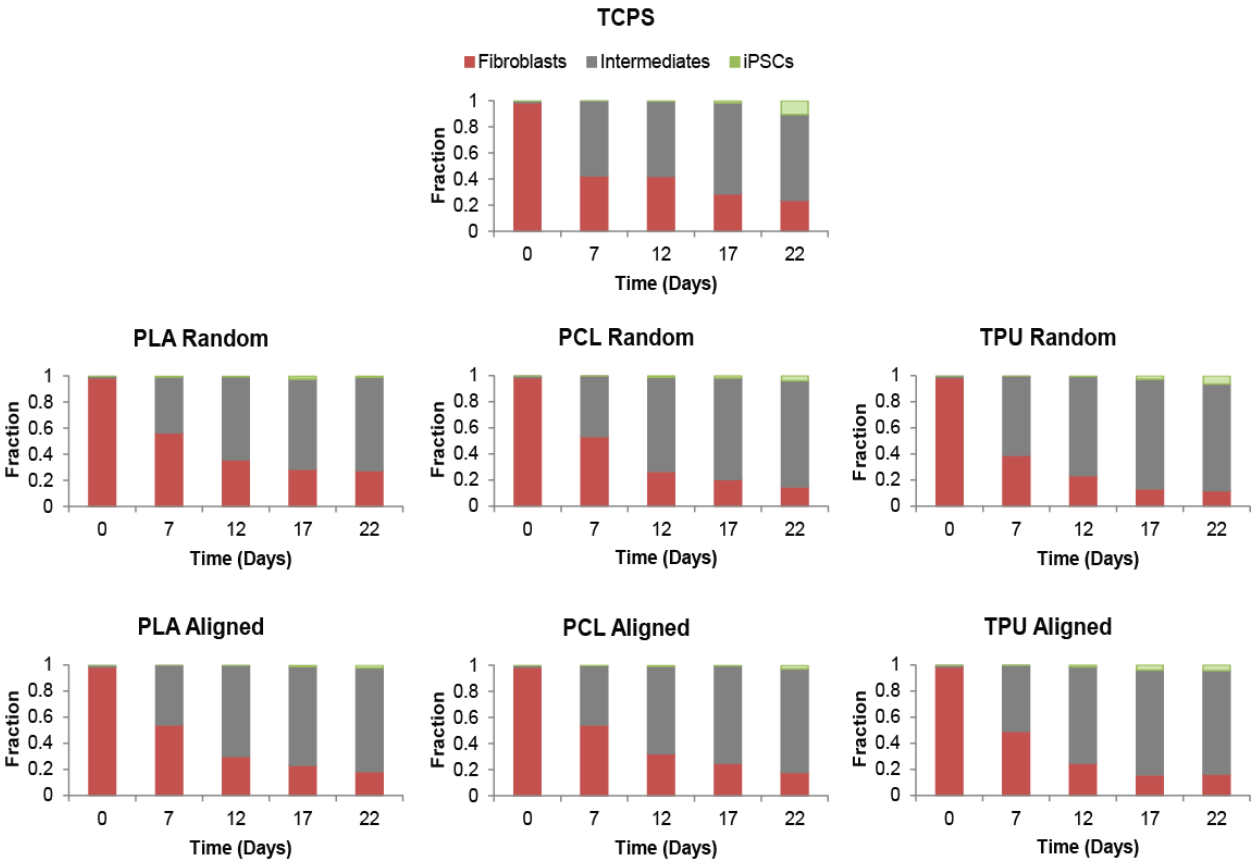


**Figure 3-7. Kinetics of reprogramming on nanofibrous substrates.** Fraction of reprogramming population belonging to each of three cellular identities (see also Figure 3-6A-B) over a 22 day time course of reprogramming on nanofibrous substrates. All experiments were conducted in E7 media with hydrocortisone and doxycycline.

### *3.3.4 Early effects of nanofibrous substrates*

To narrow the time window over which nanofibrous substrates affect reprogramming, we switched substrates in the middle of reprogramming, dividing the process into an “early” (day 0-17) and “late” phase (day 18-24). For the “early” conditions, reprogramming factor-expressing fibroblasts were grown on a nanofibrous substrate for the first 17 days and passaged to TCPS for the last seven days (Figure 3-8). For the “late” conditions, reprogramming factor-expressing fibroblasts were cultured on TCPS for the first 17 days and passaged to a nanofibrous substrate for the last seven days (Figure 3-8). Flow cytometric analysis of cells at the end of these

experiments indicated that early culture on nanofibrous substrates could boost reprogramming, with up to 30% of cells being reprogrammed, while late culture did not boost reprogramming over TCPS levels (Figure 3-8). The top performing nanofibrous substrates that had faster kinetics - TPU-Random (TPU-R), TPU-Aligned (TPU-A) and PCL-Random (PCL-R) (Fig. 2D) – performed well in the early conditions only (Figure 3-8).

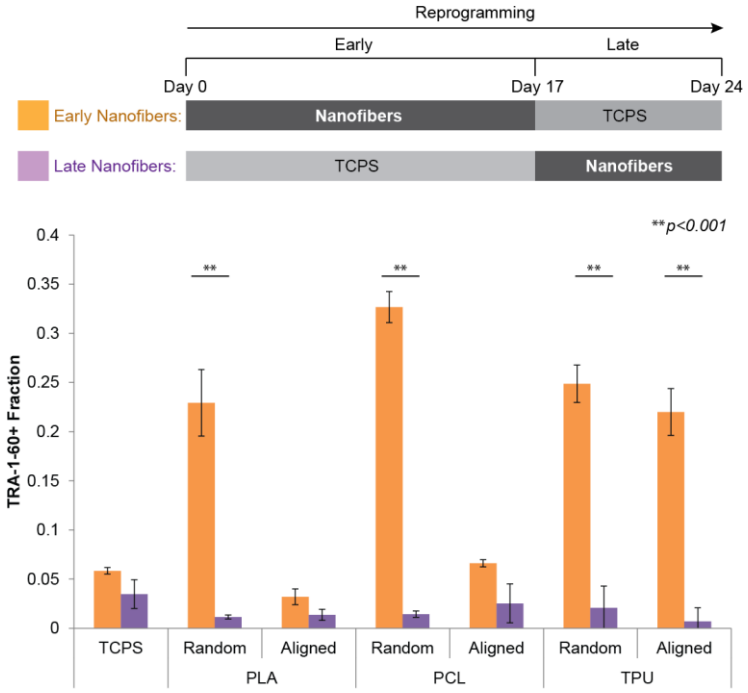


**Figure 3-8. Nanofibrous substrates enhance early events during reprogramming.** *Top:* Schematic of experimental design. Reprogramming was carried out for 24 days under two conditions: early versus late culture on nanofibrous scaffolds. "Early Nanofibers" labels culture on indicated nanofibrous substrate during days 0-17 of factor expression, while "Late Nanofibers" labels culture on indicated nanofibrous substrate during days 18-24 of factor expression. Cells were cultured on TCPS during the other periods of reprogramming. *Bottom:* Percent of TRA-1-60$^{+}$ cells after 24 days of reprogramming in both conditions. Error bars denote 95% confidence intervals. Asterisks indicate *p*-values <0.001 from an unpaired student's t-test.

### *3.3.5 Reprogramming factors quickly induce circular nuclei*

We reasoned that early effects of nanofibrous substrates could be mediated by early perturbations of nuclear shape, area and structure. Immunocytochemical analysis of cells on scaffolds permits the tracking of nuclear size and nuclear shape index (NSI),

which ranges from 1 for circular nuclei to near zero for a more elongated shape (Figure 3-9A). Fibroblasts grown in basal media conditions adopted a more elongated nuclear morphology on aligned substrates compared to TCPS and random substrates, consistent with results seen in fibroblast attachment and proliferation experiments (Figure 3-9B and Figure 3-1). Reprogramming factor expression abolished nuclear shape differences (Figure 3-9B), indicating all nuclei on average have the same shape on all of the substrates.

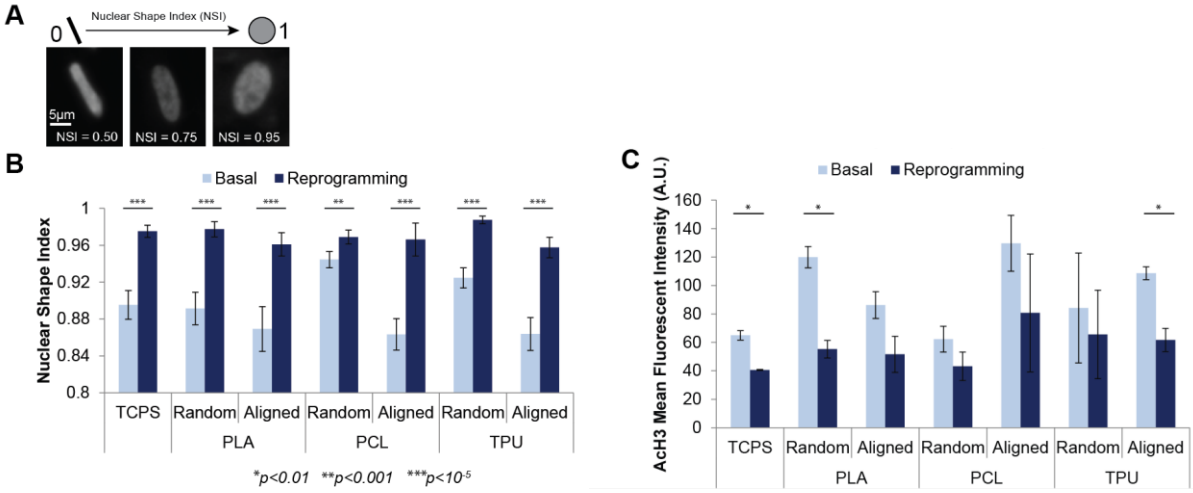


**Figure 3-9. Reprogramming factors induce circular nuclear shape for all conditions. A**) Diagram of the nuclear shape index (NSI) metric. Grey-scale image for nuclei stained with Hoechst. The NSI of a perfect circle is equal to one, while the NSI of a line approaches zero. **B**) Effects of nanofibrous substrates on NSI of C1.2 fibroblast cells during normal growth (Basal, E7 media, light blue) and during reprogramming (E7 media with hydrocortisone and doxycycline, dark blue). After seven days of treatment, cells were fixed and stained nuclei were analyzed. Error bars denote 95% confidence intervals. Asterisks indicate *p*-values from an unpaired student's t-test (*p<0.01, **p<0.001, ***p<$10^{-5}$). **C**) Mean histone 3 acetylation (AcH3) levels in cells with and without reprogramming factors for seven days, as measured by flow cytometry.

Similarly, nuclear area was uniform after seven days of factor expression(Figure 3-10), and reduced slightly in reprogramming conditions compared to basal media conditions, as previously reported[38]. We probed the global histone 3 acetylation (AcH3) levels of these nuclei via immunocytochemistry followed by flow cytometry analysis (for

representative data, see Figure 3-10B). For all conditions, global histone acetylation levels decreased modestly within the nuclei of cells after seven days of induction of reprogramming factors (Figure 3-9). Only a weak correlation between AcH3 levels and NSI ($R^2$=0.51) was observed (Figure 3-10). To summarize, aligned nanofibrous substrates altered nuclear shape during routine culture, but expression of reprogramming factors within seven days abolishes these changes, leading to smaller nuclei without any elevation in global AcH3 levels.

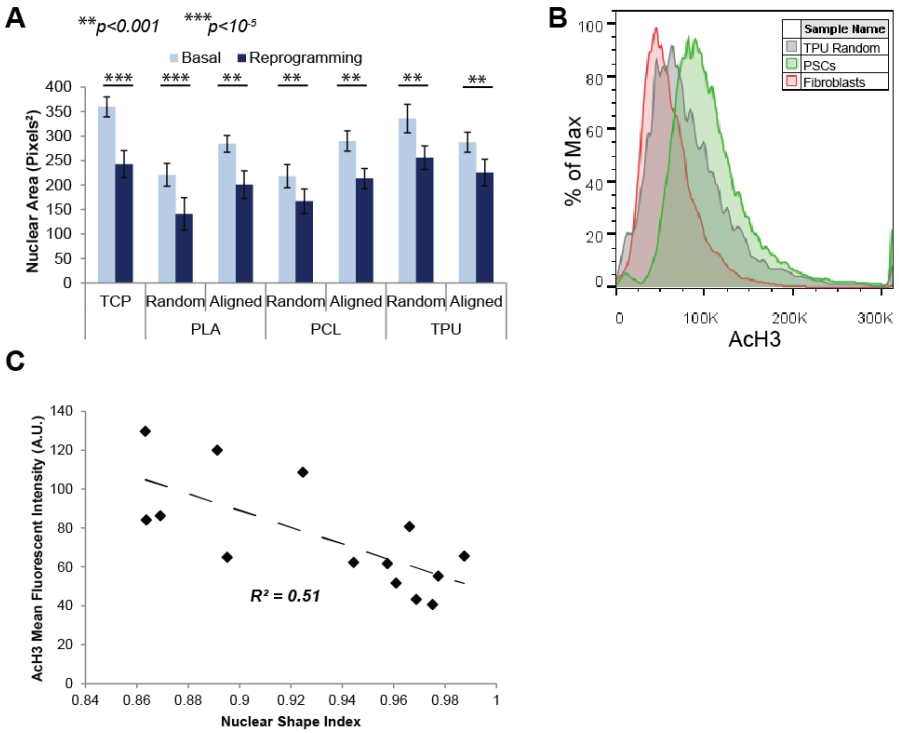


**Figure 3-10. Nuclear morphology and histone acetylation on nanofibrous substrates. A**) Effects of nanofibrous substrates on nuclear size of C1.2 fibroblast cells during normal growth (Basal, E7 media, light blue) and during reprogramming (E7 media with hydrocortisone and doxycycline, dark blue). After seven days of treatment, cells were fixed and stained nuclei were analyzed. Error bars denote 95% confidence intervals. Asterisks indicate *p*-values from an unpaired student's t-test (**p<0.001, ***p<$10^{-5}$). **B**) Representative histogram from flow cytometric analysis of histone acetylation (AcH3). **C**) Mean AcH3 levels at day 7 weakly correlated with nuclear shape index.

### *3.3.6 TGF-β inhibits effects of nanofibrous substrates*

Given that transforming growth factor beta (TGF-β) can perturb early phases of reprogramming by inhibiting the mesenchymal to epithelial transition (MET)[39-41], this growth factor was added to our reprogramming media to see if it would affect reprogramming on nanofibrous substrates. TGF-β slowed reprogramming in all conditions, as measured by the lower percentage of CD44- cells that have lost fibroblast identity throughout the time course (Figure 3-11A). Analysis at the end of reprogramming also indicated that TGF-β decreases the number of intermediate and reprogrammed cells across all conditions (Figure 3-11B-D). Notably, TGF-β abolished the previously observed differences among the different nanofibrous substrates (Fig. 5C), and no nanofibrous substrates in media conditions with TGF-β outperformed TCPS.

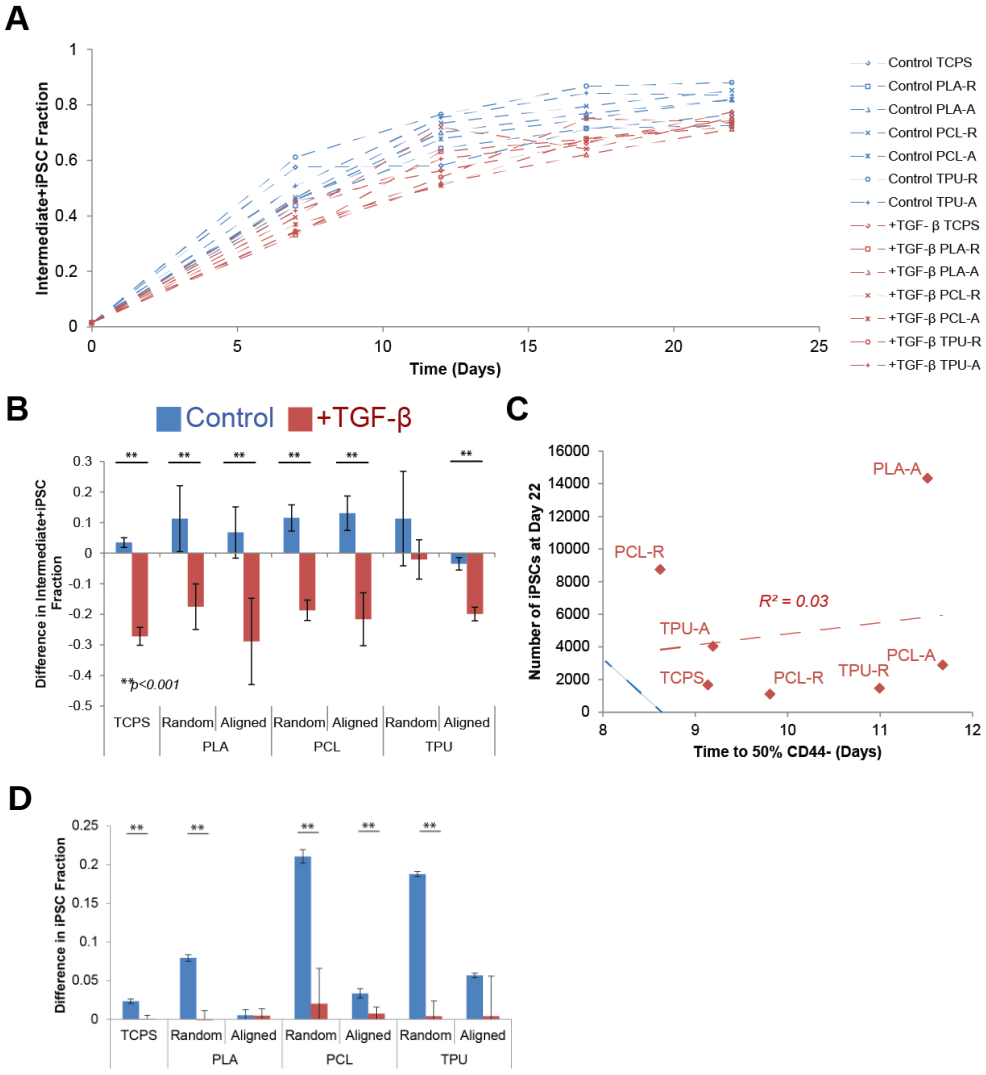


**Figure 3-11. TGF-β inhibits effects of nanofibrous substrates. A**) Kinetics of reprogramming on nanofibrous substrates when media is supplemented with TGF-β. Non-fibroblast population (Intermediate+iPSC fraction) was analyzed by flow cytometry (described in Fig. 2B). **B**) Change in the Intermediate+iPSC fraction on various substrates when media was supplemented with TGF-β. **C**) When TGF-β was added to the media, amount of time required to lose fibroblast identity did not correlate with number of reprogrammed cells at day 22. Red dashed line represents linear regression best-fit line. Blue dashed line represents linear regression best-fit line in control media (as shown in Fig. 2D). Error bars denote 95% confidence intervals. Asterisks indicate *p*-values <0.001 from an unpaired student's t-test. **D)** Change in the iPSC fraction on various substrates when media was supplemented with TGF-β.

*3.3.7 Cues controlling reprogramming*

To gain deeper insight into biophysical and biochemical cues that correlate with observed reprogramming responses, we performed partial least squares regression (PLSR) between cues and responses. A PLSR model was built using datasets with materials properties and media conditions as the multivariate cues and the number and timing of reprogramming as the response inputs. When the experimental values of the numbers and times of reprogramming were plotted against those predicted by the PLSR model (Figure 3-12), a linear relationship with a relatively low root mean square error of prediction (RMSPE) was observed, suggesting a good predictive ability for the cues within the training set (RMSPE ~ 1).

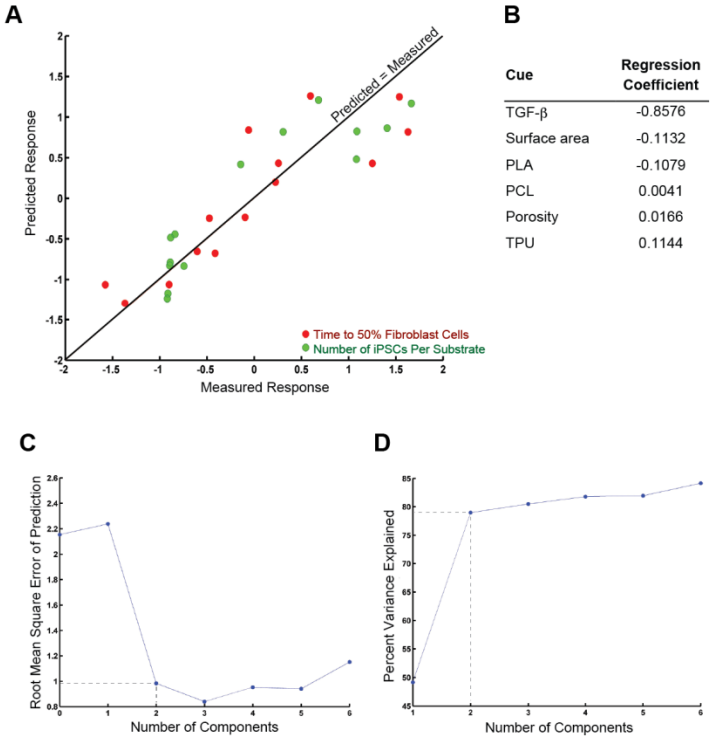


**Figure 3-12. Partial least squares regression of biophysical and biochemical cues and cellular responses. A**) Diagram of the predictability of PLSR model. A perfectly predicted model will follow the line y=x. $R^2$ values are 0.76 and 0.82 for time to 50% fibroblast cells and number or iPSCs per substrate respectively. **B**) Biophysical cues with the largest contribution to principal component transformation of number of iPSCs in a two-component model. Negative regression coefficients indicates inhibition of cellular reprogramming responses, while positive

indicates promotion. **C**) Root mean square error in predictive calculation. Increased number of components leads to greater error in predictions due to overfitting. **D**) Cumulative sum of variance explained by increasing number of components.

Cues with high weights in a two-component model were TGF-β and polymer identity, while fiber diameter, water contact angle, protein adsorption and alignment had low weights (Figure 3-12B and Figure 3-13A). PLSR modeling of all materials properties and cues with all cellular responses yielded a predictive model (Figure 3-13B) with low error (Figure 3-13C) while using five components (Figure 3-13D). In this expanded model, TGF-β again was heavily weighted.

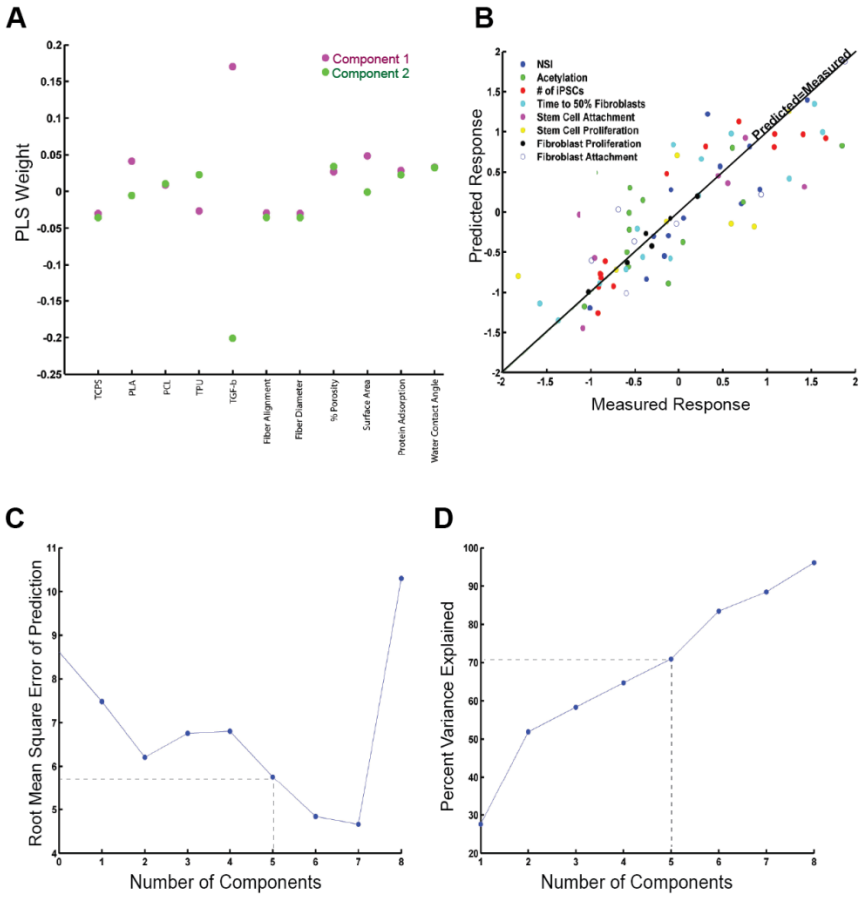


**Figure 3-13. Partial least squares regression of biophysical and biochemical cues and many cellular responses. A**) Contribution of each cue to principal components in the two-component model as described in Fig. 6. **B**) Predictability of the full PLSR model describing 8 responsive variables and 5 principal components. **C**) Root mean square error in predictive calculation. Number of components was picked to reduce probability of overfitting. **D**) Cumulative sum of variance explained by increasing number of components.

## 3.4 Discussion

Our results demonstrate robust reprogramming of human cells on nanofibrous substrates. Reprogrammed cells were similar to those generated on standard polystyrene substrates, were factor-independent, and had all markers of pluripotent cells as reported in prior work[9,42]. Top-performing substrates accelerated early stages of reprogramming that intersect with the timing of MET during reprogramming[39-41]. These substrates may be able to activate pathways involving actin filament organization that have been implicated in mesenchymal-epithelial transitions[43].

Because top-performing substrates varied along many different properties, it is likely that a combination of material characteristics led to enhanced reprogramming. PLSR modeling indicated that polymer identity, following TGF-β, was the next most important cue governing reprogramming response. Surface area and porosity also had a modest effect. Further molecular characterization of the substrates may be necessary to understand the different rates of reprogramming on our library. It is possible that the top performing nanofibrous substrates permit an advantageous conformation of Matrigel[35] that encourages integrin engagement, focal adhesion formation or growth factor stabilization[44] to promote reprogramming. Because the distribution of cytoskeletal stress fibers can be sensitive to geometry of underlying substrates[16], nanofibrous substrates could also change the degree of actin polymerization and actomyosin contractility. Further characterization of these molecular differences involving cell-material interactions among the substrates in our library could provide more insight into why observed differences were seen in the kinetics and efficiencies of reprogramming. Finally, expanding the library to sample materials property space evenly may be able to

provide a more comprehensive picture of how reprogramming occurs on nanofibrous materials. In our library, the total amounts of protein adsorbed to these substrates did not vary more than an order of magnitude. Likewise, mechanical properties and water contact angles did not vary greatly across the library.

A surprising result was that aligned substrates did not retain an elongated nuclear shape during reprogramming. Reprogramming factors within seven days could bypass biophysical constraints imposed by our nanofibrous substrates. The mechanisms by which this rapid change occurred was suppressed by TGF-β and likely intersects with MET pathways[39-41,45].

In a mouse reprogramming system, aligned substrates significantly enhanced reprogramming of mouse fibroblasts[11], but markedly different responses were observed here with human fibroblasts among randomly spun and aligned nanofibrous substrates. In contrast to mouse reprogramming results on aligned nanofibrous substrates, nuclei were not hyperacetylated on histone 3 in our experiments. No correlation of hyperacetylation with enhanced reprogramming was observed, and AcH3 regression coefficients in PLSR models were near zero (Figure 3-13). This disparity may be attributed to known differences in the signaling requirements between mouse and human pluripotent cells[9]. Profiling local acetylation of particular genomic loci, rather than averaging acetylation globally over the whole genome, may be required to understand the differences between the mouse and human results on nanofibrous substrates.

## 3.5 Conclusions

This work represents the first report of reprogramming of human cells on nanofibrous polymeric substrates. All of the polymers tested – PCL, TPU and PCL - supported fibroblast and pluripotent cell attachment and full reprogramming to factor-independent pluripotent stem cells. TPU-R, TPU-A and PCL-R were the best substrates in our library, outperforming standardly used polystyrene substrates. The enhanced reprogramming on nanofibrous substrates occurred during the first 17 days of reprogramming and was inhibited by TGF-β. These results suggest a possible role of nanofibrous substrates to enhance MET of fibroblasts during early stages of reprogramming. Notably, reprogramming factors were able to change nuclear shape of cells on all substrates within seven days regardless of the initial nuclear shape constrained by the substrate. PLSR modeling of several materials properties revealed a complex relationship between polymer identity and reprogramming with less pronounced roles for fiber diameter, fiber alignment, protein adsorption and water contact angle. We believe further work with the identified top-performing substrates will lead to the design of substrates that promote epigenetic reprogramming.

## References

1 Graf, T. & Enver, T. Forcing cells to change lineages. *Nature* **462**, 587-594, doi:10.1038/nature08533 (2009).

2 Takahashi, K. & Yamanaka, S. Induction of pluripotent stem cells from mouse embryonic and adult fibroblast cultures by defined factors. *cell* **126**, 663-676 (2006).

3 Yu, J. *et al.* Induced pluripotent stem cell lines derived from human somatic cells. *Science* **318**, 1917-1920 (2007).

4 Hanna, J. *et al.* Direct cell reprogramming is a stochastic process amenable to acceleration. *Nature* **462**, 595-601 (2009).

5 Armond, J. W. *et al.* A stochastic model dissects cell states in biological transition processes. *Sci. Rep.* **4**, doi:10.1038/srep03692 (2014).

6 Saha, K. & Jaenisch, R. Technical Challenges in Using Human Induced Pluripotent Stem Cells to Model Disease. *Cell Stem Cell* **5**, 584-595, doi:10.1016/j.stem.2009.11.009 (2009).

7 Takahashi, K. & Yamanaka, S. Induced pluripotent stem cells in medicine and biology. *Development* **140**, 2457-2461 (2013).

8 Grskovic, M., Javaherian, A., Strulovici, B. & Daley, G. Q. Induced pluripotent stem cells — opportunities for disease modelling and drug discovery. *Nat Rev Drug Discov* **10**, 915-929, doi:10.1038/nrd3577 (2011).

9 Hanna, J. H., Saha, K. & Jaenisch, R. Pluripotency and cellular reprogramming: facts, hypotheses, unresolved issues. *Cell* **143**, 508-525 (2010).

10 Feng, B., Ng, J.-H., Heng, J.-C. D. & Ng, H.-H. Molecules that promote or enhance reprogramming of somatic cells to induced pluripotent stem cells. *Cell Stem Cell* **4**, 301-312 (2009).

11 Downing, T. L. *et al.* Biophysical regulation of epigenetic state and cell reprogramming. *Nature materials* **12**, 1154-1162 (2013).

12 Shahbazian, M. D. & Grunstein, M. Functions of site-specific histone acetylation and deacetylation. *Annu. Rev. Biochem.* **76**, 75-100, doi:10.1146/annurev.biochem.76.052705.162114 (2007).

13 Shinagawa, T. *et al.* Histone Variants Enriched in Oocytes Enhance Reprogramming to Induced Pluripotent Stem Cells. *Cell Stem Cell* **14**, 217-227, doi:10.1016/j.stem.2013.12.015 (2014).

14 Apostolou, E. & Hochedlinger, K. Chromatin dynamics during cellular reprogramming. *Nature* **502**, 462-471, doi:10.1038/nature12749 (2013).

15 Rais, Y. *et al.* Deterministic direct reprogramming of somatic cells to pluripotency. *Nature* **502**, 65-70, doi:10.1038/nature12587 (2013).

16 Jain, N., Iyer, K. V., Kumar, A. & Shivashankar, G. V. Cell geometric constraints induce modular gene-expression patterns via redistribution of HDAC3 regulated by actomyosin contractility. *Proceedings of the National Academy of Sciences* **110**, 11349-11354, doi:10.1073/pnas.1300801110 (2013).

17 Gaspar-Maia, A., Alajem, A., Meshorer, E. & Ramalho-Santos, M. Open chromatin in pluripotency and reprogramming. *Nature reviews Molecular cell biology* **12**, 36-47 (2011).

18 Kim, I. L., Khetan, S., Baker, B. M., Chen, C. S. & Burdick, J. A. Fibrous hyaluronic acid hydrogels that direct MSC chondrogenesis through mechanical and adhesive cues. *Biomaterials* **34**, 5571-5580, doi:10.1016/j.biomaterials.2013.04.004 (2013).

19 Mi, H.-Y., Jing, X., Jacques, B. R., Turng, L.-S. & Peng, X.-F. Characterization and properties of electrospun thermoplastic polyurethane blend fibers: Effect of solution

rheological properties on fiber formation. *Journal of Materials Research* **28**, 2339-2350 (2013).

20 Rnjak-Kovacina, J. *et al.* Tailoring the porosity and pore size of electrospun synthetic human elastin scaffolds for dermal tissue engineering. *Biomaterials* **32**, 6729-6736 (2011).

21 Beers, J. *et al.* Passaging and colony expansion of human pluripotent stem cells by enzyme-free dissociation in chemically defined culture conditions. *Nature protocols* **7**, 2029-2040 (2012).

22 Mali, P. *et al.* RNA-Guided Human Genome Engineering via Cas9. *Science* **339**, 823-826, doi:10.1126/science.1232033 (2013).

23 McNulty, J. D. *et al.* High-precision robotic microcontact printing (R-μCP) utilizing a vision guided selectively compliant articulated robotic arm. *Lab on a Chip* **14**, 1923-1930 (2014).

24 Watanabe, K. *et al.* A ROCK inhibitor permits survival of dissociated human embryonic stem cells. *Nature biotechnology* **25**, 681-686 (2007).

25 Chen, G. *et al.* Chemically defined conditions for human iPSC derivation and culture. *Nature methods* **8**, 424-429 (2011).

26 Chen, G., Hou, Z., Gulbranson, D. R. & Thomson, J. A. Actin-myosin contractility is responsible for the reduced viability of dissociated human embryonic stem cells. *Cell Stem Cell* **7**, 240-248 (2010).

27 Ohgushi, M. *et al.* Molecular pathway and cell state responsible for dissociation-induced apoptosis in human pluripotent stem cells. *Cell stem cell* **7**, 225-239 (2010).

28 Hockemeyer, D. *et al.* A drug-inducible system for direct reprogramming of human somatic cells to pluripotency. *Cell stem cell* **3**, 346-353 (2008).

29 Schindelin, J. *et al.* Fiji: an open-source platform for biological-image analysis. *Nature methods* **9**, 676-682 (2012).

30 de Jong, S. SIMPLS: an alternative approach to partial least squares regression. *Chemometrics and intelligent laboratory systems* **18**, 251-263 (1993).

31 Eriksson, L. *Multi-and megavariate data analysis*. (MKS Umetrics AB, 2006).

32 Teo, W. & Ramakrishna, S. A review on electrospinning design and nanofibre assemblies. *Nanotechnology* **17**, R89 (2006).

33 Barnes, C. P., Sell, S. A., Boland, E. D., Simpson, D. G. & Bowlin, G. L. Nanofiber technology: Designing the next generation of tissue engineering scaffolds. *Advanced Drug Delivery Reviews* **59**, 1413-1433, doi:10.1016/j.addr.2007.04.022 (2007).

34 Wang, X. *et al.* Poly (ε-caprolactone) Nanofibers with a Self-Induced Nanohybrid Shish-Kebab Structure Mimicking Collagen Fibrils. *Biomacromolecules* **14**, 3557-3569 (2013).

35 Kohen, N. T., Little, L. E. & Healy, K. E. Characterization of Matrigel interfaces during defined human embryonic stem cell culture. *Biointerphases* **4**, 69-79 (2009).

36 Discher, D. E., Mooney, D. J. & Zandstra, P. W. Growth Factors, Matrices, and Forces Combine and Control Stem Cells. *Science* **324**, 1673-1677, doi:10.1126/science.1171643 (2009).

37 Quintanilla, R. H., Jr., Asprer, J. S. T., Vaz, C., Tanavde, V. & Lakshmipathy, U. CD44 Is a Negative Cell Surface Marker for Pluripotent Stem Cell Identification during Human Fibroblast Reprogramming. *PLoS ONE* **9**, doi:10.1371/journal.pone.0085419 (2014).

38 Mattout, A., Biran, A. & Meshorer, E. Global epigenetic changes during somatic cell reprogramming to iPS cells. *Journal of molecular cell biology* **3**, 341-350 (2011).

39 Liu, X. *et al.* Sequential introduction of reprogramming factors reveals a time-sensitive requirement for individual factors and a sequential EMT–MET mechanism for optimal reprogramming. *Nature Cell Biology* (2013).

40 Li, R. *et al.* A mesenchymal-to-epithelial transition initiates and is required for the nuclear reprogramming of mouse fibroblasts. *Cell stem cell* **7**, 51-63 (2010).

41 Samavarchi-Tehrani, P. *et al.* Functional genomics reveals a BMP-driven mesenchymal-to-epithelial transition in the initiation of somatic cell reprogramming. *Cell stem cell* **7**, 64-77 (2010).

42 Saha, K. *et al.* Surface-engineered substrates for improved human pluripotent stem cell culture under fully defined conditions. *Proceedings of the National Academy of Sciences* **108**, 18714-18719 (2011).

43 Haynes, J., Srivastava, J., Madson, N., Wittmann, T. & Barber, D. L. Dynamic actin remodeling during epithelial–mesenchymal transition depends on increased moesin expression. *Molecular Biology of the Cell* **22**, 4750-4764, doi:10.1091/mbc.E11-02-0119 (2011).

44 Jiao, J. *et al.* Promoting reprogramming by FGF2 reveals that the extracellular matrix is a barrier for reprogramming fibroblasts to pluripotency. *Stem Cells* **31**, 729-740 (2012).

45 Craene, B. D. & Berx, G. Regulatory networks defining EMT during cancer initiation and progression. *Nat Rev Cancer* **13**, 97-110, doi:10.1038/nrc3447 (2013).

# Chapter 4. Effects of regulating cytoskeletal and nuclear morphology via micropatterned well plates

Elements of this work have been published as:

**Harkness, T., McNulty, J.D., Prestil, R. et al., High-content imaging with micropatterned multiwell plates reveals influence of cell geometry and cytoskeleton on chromatin dynamics. *Biotechnology Journal.* 2015, *10*, 1555-1567.**

## 4.1 Introduction

Controlling human cell behavior remains an important goal for many in the regenerative medicine, cancer, and stem cell biology fields [1]. Key biophysical cues can be transmitted from the cell exterior to interior in a variety of ways involving integrins, cadherins, focal adhesion kinase, SUN and KASH nucleoskeleton proteins, YAP/TAZ transcription factors and many other proteins[2-10]. In particular, cellular geometry has been shown to influence many cell behaviors, including proliferation[11,12], apoptosis[11,13], differentiation[14-16], and even epigenetic reprogramming[17,18]. Non-invasive tools have been developed to probe the biophysical properties of living cells during these processes[1,19-22]. Together, these studies point to the importance of controlling of cell shape and area with high precision during cell culture. For example, inconsistent differentiation of mesenchymal stem cells has been traced back to variations in cell shape and cytoskeletal tension inherent in standard cell culture methods[23,24].

Microcontact printing offers a versatile and widely used technique for precise control of cell shape and area at the micron scale[25-27], and is compatible with many complementary mechanical assays[28]. Standard microcontact printing techniques employ small glass coverslips that can be difficult to manipulate by hand. Further, these techniques require individual stamps and substrates to be meticulously cleaned and carefully substrate-coated for each replicate created[11,29,30]. As such, it can be difficult to quickly fabricate the replicates necessary to test a wide experimental space, which is an important capability when seeking to understand and engineer the highly multivariate mechanisms underpinning human behavior.

Here we describe the creation of MicroContact-Printed Well Plates (μCP Well Plates) that adapt the spatial control and imaging capabilities of microcontact printed coverslips to the scale and universal compatibility of the standard well plate. Using this platform, we create up to 96 highly-defined, micropatterned arrays in a single step and spatially separate them by the wells of a tissue culture plate. In this format, each stage of a given experiment – including sample preparation, sterilization, cell seeding, cell treatment, and imaging – can be performed in a single, potentially automated step with conventional well plate techniques. This capability not only decreases experimental time and substrate handling, but also lowers the likelihood for inadvertent experimental errors rising from inconsistent stamping techniques or sample mislabeling. A key advantage over prior methods to pattern well plates[31] is the capability of highly consistent patterning at the single-cell level. In addition, the glass bottoms of μCP Well Plates enable flexibility of substrate patterning and functionalization by a wide variety of chemistries[32], as well as confocal and other high-resolution imaging without further

handling or mounting of coverslips. We show that µCP Well Plates are suitable for both high-throughput image analysis of thousands of single-cells and high-resolution subcellular assays on living cells. Analyses at both levels are performed on µCP Well Plates with distinct geometric features of equivalent cell attachment areas to explore how the organization of the cytoskeleton mediates the relationship between cell shape, nuclear shape, and dynamics of the nuclear interior.

## 4.2 Materials and methods

### *4.2.1 Fabrication of Multi-Well Alignment Device*

A multi-well alignment device for µCP Well Plate fabrication was designed with 3D modeling software (Solidworks 2014, Dassault Systemes) and fabricated from 6061 aluminum with a computer numerical control (CNC) vertical machining center (MiniMill 2, Haas) programmed with computer-aided design/manufacturing (CAD/ CAM) software (MasterCAM X7, CNC Software, Inc.). Standard precision leader pins and bushings were acquired from McMaster Carr and used as received to ensure proper alignment. Three cavities were machined into the base at 127.76 mm x 85.48 mm, 116 mm x 77 mm, and 6” diameter dimensions to hold multi-well plates, micropatterned glass, and silicon master molds, respectively.

### *4.2.2 µCP Well Plate Fabrication*

Double-sided adhesive (ARcare 90106) was generously donated by AR Global, Inc. and cut to 116 mm x 77 mm dimensions using a laser cutter (Universal Lasers Systems). Adhesive was placed on well plates using the alignment device and

smoothed to remove air pockets. Well bottoms were then cut out using the laser cutter. 116 mm x 77 mm x 0.2 mm glass sheets were purchased at size from Coresix Precision Glass, Inc. A CHA-600 metal evaporator was used to deposit a 3.5 nm layer of titanium (to increase gold adhesion) followed by an 18 nm layer of gold onto one side of each glass sheet. Custom 6” silicon molds were ordered from FlowJEM, Inc. In 24-well plate designs, each well spot contained twelve 10x10 arrays of single-cell features (Supp. Table 1). Plates were designed to contain four well-replicates for each of five feature geometries. Molds were placed into the 6” cavity of the alignment device for casting. Sylgard 184 elastomer (Dow Corning) was used as the stamp material and cast into molds after degassing. Before setting, a transparency sheet and a flat weight were placed on top of the elastomer, spanning the width of the alignment device cavity. This insured consistent height of the stamps after setting, which was necessary to achieve consistent contact with glass sheets during patterning. Stamps were allowed to set overnight at 37ºC before being carefully removed from the mold and cut by scalpel around the frame of an appropriate multi-well plate with well-bottoms already removed to ensure proper alignment.

As described previously[27], a thin layer of 2mM alkanethiol ethanol solution (Prochimia Surfaces) was spread evenly over the stamp and allowed to air dry. A gold-coated glass sheet was then placed face down into the alignment device frame, and lifted up by vacuum tooling attached to a lift arm. The stamp was placed face up in the well plate sized frame, and the glass was gently lowered onto it for transfer of micropatterned alkanethiol self-assembled monolayers (SAMs).

Chemical growth of PEG brushes was performed as described previously[27], with minor changes to reflect the larger size of glass sheets as compared to coverslips. Reactions were carried out in airtight 300 mL “Snapware” Pyrex containers (Boston Store). Sheets were placed face up in the containers and just enough PEG reaction solution (20 mL) to cover the surface was added. A solution of 164 mg of L-Ascorbic acid in 1.82 mL of deionized water was added to the container to initiate the reaction. Ambient air was flushed from the container with a nitrogen stream and the solution was well mixed before incubating at room temperature for 16 hours. Next, patterned sheets were removed from the solution with a tweezers and rinsed with MilliQ water and ethanol, followed by a two hour incubation in 70% ethanol on a room temperature shaker to remove residual reaction solution. Sheets were then dried and placed onto the multi-well plate frame using the alignment device in the same manner as during stamping. After sealing the glass sheets to the well plate frame by applying pressure by hand, μCP-Well Plates were briefly immersed in a 70% ethanol bath and allowed to air dry in a sterile tissue culture hood.

*4.2.3 Fluorescent modification of PEG Brushes*

Conjugation of fluorophores to PEG brushes was performed as descried previously[27] with volumes scaled just enough to cover glass sheets inside 300 mL Pyrex containers (~20mL).

*4.2.4 Generation and Culture of H2B-LA Cell Line*

The H2B-LA human fibroblast line was derived from the previously reported C1.2 line[18]. Gene-editing and insertion occurred in an induced pluripotent stem cell (iPSC) state to allow for clonal isolation and growth. H2B-mCherry was integrated into the C1.2-iPSC genome via CRISPR/Cas9 gene editing. The H2B-mCherry plasmid was generated by cloning the H2B-mCherry sequence (Addgene # 20972) into the EGFP sequence of the AAV-CAGGS-EGFP plasmid (Addgene #22212). This plasmid was electroporated with Cas9 and gRNA plasmids as described previously [18]. A LifeAct-GFP plasmid (Addgene #51010) was packaged in lentiviral particles by HEK-293T cells via Lipofectamine 2000 (Life Technologies) transfection with third-generation packaging vectors and harvested after 72 hours. Harvested lentiviral solutions were passed through a 0.45 µm filter and exposed to C1.2 iPSCs overnight before rinsing. iPSC lines harboring both labels were purified through puromycin selection and clonal isolation followed by fluorescent imaging and flow cytometry using a C6 Accuri (BD) to confirm expression.

H2B-LA iPSCs were then differentiated into fibroblasts using the embryoid body (EB) method[33]. EBs were created using the Aggrewell (Stem Cell Technologies) system per the manufacturer's protocol. EBs were then cultured in non-adherent cell culture plates (Corning Inc.) suspended in 4 mL per well of "EB Medium" consisting of 80% Iscove's Modified Dulbecco's Medium (IMDM, Life Technologies) with 20% Fetal Bovine Serum (Life Technologies). After 4 days in suspension, aggregates were transferred onto Matrigel-coated 24-well plates and maintained in "Fibroblast Medium" consisting of DMEM-high glucose (Life Technologies) supplemented with 10% Fetal Bovine Serum

(Life Technologies), 1 mM L-glutamine (Life Technologies), and 1% Penicillin/Streptomycin (Life Technologies). After approximately 9 days in culture, cells had proliferated enough to permit expansion. Cells were passaged by washing cells with PBS (Life Technologies) followed by a 5-minute incubation in trypsin (Life Technologies) at 37°C. Cells were then centrifuged, resuspended in fresh Fibroblast Media, and seeded onto tissue culture polystyrene plates (Fisher Scientific) coated with a 0.1% Gelatin A (Sigma) solution. Most cells had taken on a fibroblast-like morphology after three to five passages.

Once derived, fibroblasts were maintained in Fibroblast Medium in 5% $CO_2$ at 37°C on gelatin-coated polystyrene plates. Media was changed once every two days, and cells were passaged approximately every four days (at 90% confluency) with trypsin as described above.

*4.2.5 Immunofluorescence, Proliferation, and Apoptosis Assays*

F-Actin stains (used in Figure 1 only) were performed at room temperature using 10 nM Phalloidin-TRITC and 0.5% Triton-X 100 (Sigma) in PBS for 30 minutes at room temperature after fixing for 15 minutes with 4% Paraformaldahyde in PBS (Sigma). Click-iT EdU and TUNEL assays (Life Technologies) for measuring proliferation and apoptosis, respectively, were performed per manufacturer instructions. Cells were exposed to EdU for a 12 hour period before fixing, beginning 4 hours after cell seeding.

*4.2.6 Automated Imaging*

Automated imaging was performed using a Nikon Eclipse Ti epifluorescence microscope and NIS Elements software. One full-well, multichannel stitched image per well was recorded at 10x magnification using the Nikon Perfect Focus capability to eliminate drift in the z-direction.

*4.2.7 Image Analysis*

To enable accurate measurement of fluorescent intensity across full-well images, all 10x stitched images (Figures 1-3) were corrected for non-uniform illumination across individual frames using CellProfiler software, using a 50 pixel block size and a 200 pixel smoothing filter. Illumination correction leads to increased accuracy in fluorescence intensity measurements by removing uneven illumination across the image, potentially due to imperfect optics. This standard procedure for stitched images removes the artificial “grid” appearance of many stitched images. A custom CellProfiler pipeline was then used to filter and analyze appropriately patterned cells and nuclei. The pipeline is available upon request.

Image analysis of fluorescently-conjugated PEG surfaces was performed using Fiji software[34]. Feature area was calculated by thresholding into binary images and analyzing all features with fluorescent intensities below the threshold.

*4.2.8 Order Parameter*

Maximum-intensity projections of 1.5 µm or 1 µm z-stacks (1 µm for Blebbistatin trials, 1.5 µm for all other trials) obtained using a Nikon A1R confocal microscope were

fed into custom Matlab code[35] to calculate a metric that quantifies the extent of F-actin alignment, what is termed an “order parameter” value for each cell. Briefly, a series of elongated Laplace of Gaussian filters was used to create a maximum response image. The image was then broken down into a grid of small overlapping windows (~30x30 pixels, spaced 5 pixels apart), which were convolved with a Gaussian filter before calculating the two-dimensional fast Fourier transform of each window. A series of line scans then determined the direction of skew in the transform and correlations in alignment were determined by comparing the direction of alignment of a given window to its neighbors via averaging the second Legendre polynomial. This value was then averaged across the entire image.

*4.2.9 Fluorescence Recovery After Photobleaching (FRAP)*

FRAP experiments were performed using a Nikon A1R confocal microscope. ~1 µm diameter spots were photobleached by 1 second exposure to a 405 nm wavelength laser at 100% power and 16 frames per second. Fluorescent images were then collected at 5% laser power every five seconds for the first 4 minutes, and every 15 seconds for an additional four minutes. Stacks were aligned using the StackReg ImageJ plugin[36] and intensity measurements of the photobleached area and whole nucleus were measured at each time point. Mobile fraction was calculated by normalizing the intensity of the photobleached region to the mean intensity of the entire nucleus as well as the intensities of the photobleached region immediately before and after bleaching to obtain a 0-1 scale. Data was then fit to a one-phase association curve of the form

$$Y = P(1 - e^{-kt})$$

by nonlinear least-squares regression where *P* represents the plateau value, *t* represents time, and *k* is a constant.

*4.2.10 Statistics*

All regressions, tests for significance, and confidence intervals were calculated by GraphPad software. Student's *t*-tests were unpaired and two-tailed (*$p$<0.05, **$p$<0.01, ***$p$<0.001, ****$p$<0.0001). *p* values for linear regression best-fit lines were calculated in GraphPad from *F*-tests and indicates the probability that the slope of the regression line is equal to zero.

## 4.3 Results

*4.3.1 Construction and Assembly of µCP Well Plates*

The workflow for creation of µCP Well Plates is described in Figure 1A. To generate the bottom surface of these plates, glass sheets were first cut to the dimensions of the bottom of standard multi-well plates and coated with a thin layer of gold (18 nm) on one side in preparation for alkanethiol-based microcontact printing[37]. Next, patterned polydimethylsiloxane (PDMS) stamps were cast from custom 6" diameter silicon molds designed to create regular arrays of single-cell features, similar to those described in a recent report[30]. Arrays were spaced with dimensions equivalent to standard multi-well tissue culture plates. These stamps are customizable to any well plate format, and we focused on 6-,12-, 24- and 96-well plates (Table 4-1).

**Table 4-1. Description of μCP-Well Plate patterns generated in this study.** Type/scale refers to the number of cells and/or geometry of cell populations that can be contained within a single feature. Characteristic dimension refers to the feature dimension which has the largest effect on cell geometry – usually the smallest dimension.

| | Plate Characteristics | | | Feature Characteristics | | | |
|---|---|---|---|---|---|---|---|
| **Description** | **Wells** | **Features per Well** | **Features per Plate** | **Type/Scale** | **Shape** | **Characteristic Dimension (μm)** | **Area ($\mu m^2$)** |
| 6-well uniform aggregates | 6 | 468 | 2808 | Aggregates | Circular | 600 | 282,743 |
| 12-well multi-size aggregates | 12 | 148 | 1776 | Aggregates | Circular | 300-900 | 70,685-636,173 |
| 96-well uniform aggregates | 96 | 12 | 1152 | Aggregates | Circular | 600 | 282,743 |
| 24-well microchannels | 24 | 25 | 600 | Large constrained populations | Rectangular | 20-100 | 200,000-1,000,000 |
| 24-well single cell geometries | 24 | 1200 | 28800 | Single-cell | Various | 15-125 | 2000 |

PDMS was subsequently allowed to set overnight and cut by scalpel to well plate dimensions. Microcontact printing was performed on the gold-coated glass sheets as described previously[27,38]. Briefly, self-assembled alkanethiol monolayers were transferred to gold-coated glass sheets via a PDMS stamp, after which the sheets were immersed in a polyethylene glycol (PEG) reaction solution overnight to allow for growth of hydrophilic PEG chains surrounding the designed single-cell features (Figure 4-1A).

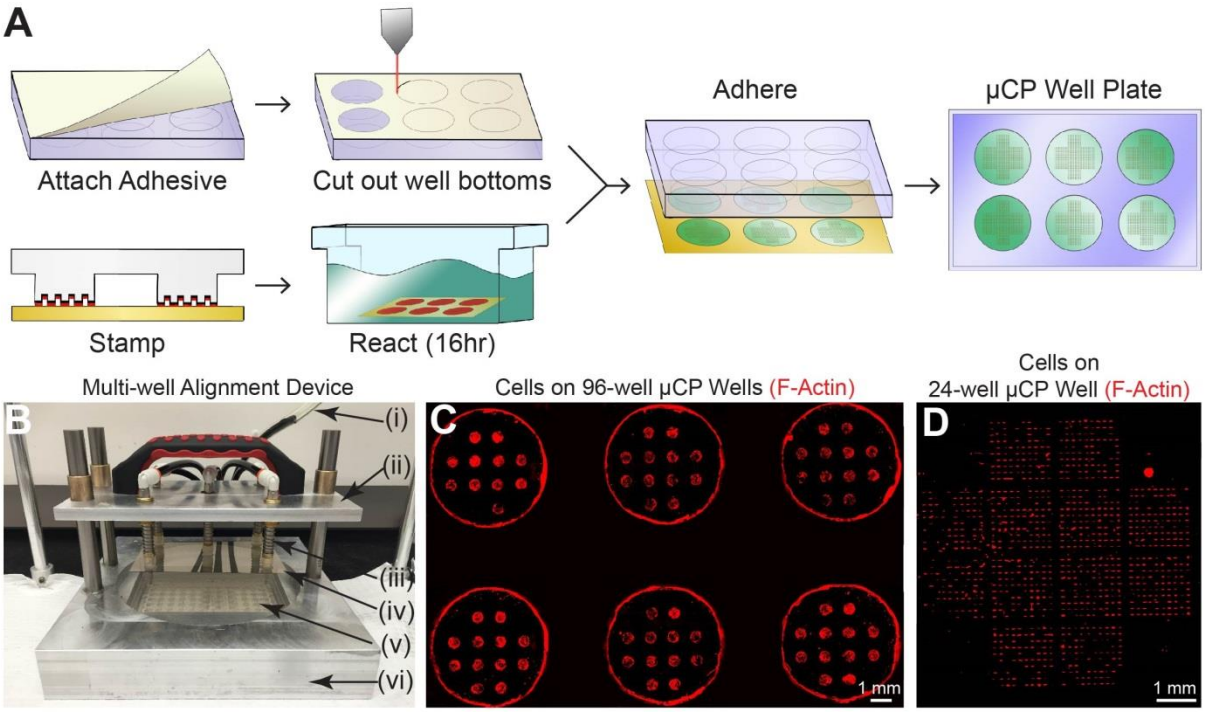


**Figure 4-1. µCP Well Plate. A)** Workflow for creation of µCP Well Plates. **B)** Multi-well alignment device for µCP Well Plate assembly. Pictured: vacuum line (i), lift arm for vacuum tooling (ii), spring-leveled vacuum cup tooling (iii), micropatterned glass sheet (iv), 96-well plate with attached adhesive and cut-out well bottoms (v), and aluminum base with machined cavities designed to fit various µCP Well Plate components (vi). **C)** Cells on a 96-well µCP Well Plate. 6 wells of a fully patterned 96-well plate containing twelve circular features (300 µm radius) per well are shown. Human fibroblasts were seeded 72 hours prior to TRITC-phalloidin staining and imaging. Fluorescent signal at edge of wells is due to auto-fluorescence of tissue culture plastic at well edges, not cells at these locations. Inter-well areas are masked for clarity. **D)** Cells on 24-well µCP Well Plate. One well of a 24-well plate containing twelve 10x10 single-cell feature arrays per well is shown. Human fibroblasts were seeded 16 hours prior to TRITC-phalloidin staining and imaging.

To prepare the well plate, medical grade double-sided adhesive sheets were cut to size and attached to the bottom of standard tissue culture plates. A laser cutter was then used to remove well bottoms by cutting through both tissue culture plastic and adhesive. Finally, patterned glass substrates were attached to the multi-well plates via the double-sided adhesive. To ensure precise control of alignment during this process, a custom multi-well alignment device (Figure 4-1B) was constructed and utilized to align all components of the µCP Well Plate during stamping and assembly. Plates were

sterilized by full immersion in 70% ethanol to remove any potential contaminants prior to cell culture. These techniques were applied to standard multi-well plates from 6- to 96-wells with various substrate patterns (Figure 4-1C). For 24-well µCP plates, 1,200 single-cell features were generated per well (Figure 4-1D), totaling 28,800 features per plate (Table 4-1), or on the order of 32x more features and 24x more conditions available compared to recent reports of similar feature arrays[30,39].

*4.3.2 High Fidelity Patterning of Single-Cell Microarrays on µCP Well Plates*

To investigate cellular responses to cell shape patterning, all features in our µCP Well Plates were designed to cover equivalent surface areas. All features in a given well were of the same shape, but separate wells contained features of one of five distinct geometries – hereafter denoted as circular, square, triangular, compact rectangular (1:2.5 aspect ratio), or elongated rectangular (1:4 aspect ratio) features (Figure 4-2A-E). Patterns were visible by naked eye and under phase microscopy after microcontact printing. However, to increase contrast and allow for more detailed analysis of PEG concentration and distribution, PEG brushes were functionalized with biotin and fluorescently labeled by an avidin-conjugated fluorescent probe[27].

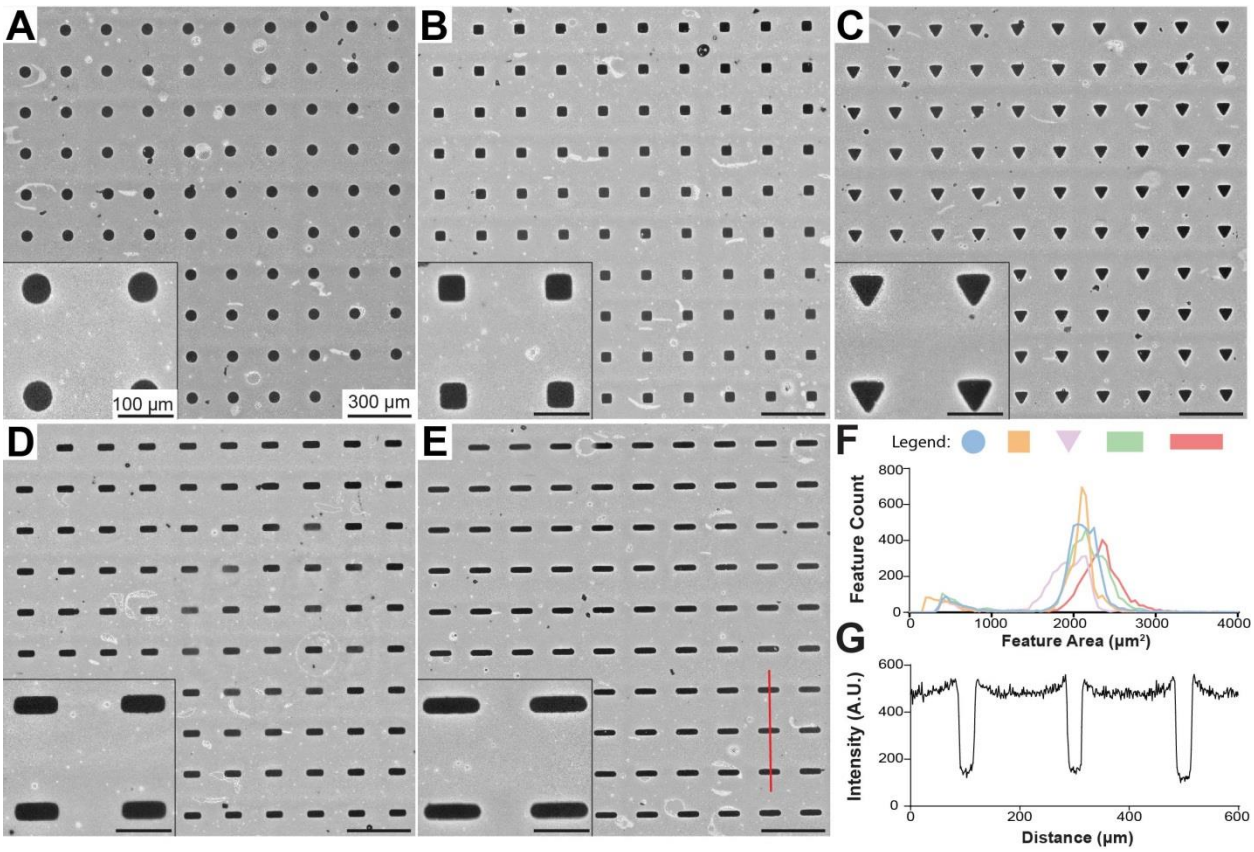


**Figure 4-2. Analysis of micropattern fidelity on µCP Well Plates. A-E)** 10x stitched images of circular (A), square (B), triangular (C), compact rectangular (D), and elongated rectangular (E) single-cell features. Surface-conjugated PEG brushes were biotinylated and fluorescently labeled by an avidin-conjugated fluorescent probe to provide contrast. White areas indicate high fluorescence from conjugated PEG brushes, whereas dark areas indicate no fluorescence of the underlying substrate (gold-coated glass). **F)** Area distribution of single-cell features. Images were thresholded and shape properties were automatically calculated by ImageJ software. **G)** Intensity profile of line scan (red) across three features in (E).

All features were distributed near the intended surface area of 2000 µm$^2$ (Figure 4-2F). Elongated rectangular features covered a slightly larger (~10% on average) surface area than the other geometries, which is a result of the desired minor axes of these geometries (15 µm) reaching the practical resolution of the photomask printer used to create photoresist for silicon master molds. Visible defects comprised <15% of all features after thresholding and were typically much smaller than the designed features (Figure 4-2F, minor peak on left) allowing for straightforward filtering of poorly-

patterned cells by image analysis (see next section). Clear, sharp transitions were obtained at feature borders and regions between features had consistently high levels of PEG attachment (Figure 4-2G).

*4.3.3 µCP Well Plates Enable Precise Single-Cell Patterning and Automated High-Content Imaging*

To enhance cell attachment to the exposed gold portions of the surface, a protein solution was added to each well. Single-cell features are the only portions of assembled µCP wells not occupied by anti-fouling PEG brushes[40], and we adsorbed a Matrigel coating to the gold portions for all subsequent cell culture experiments. Matrigel is a mixture of ECM proteins and associated molecules such as proteoglycans and growth factors produced by mouse sarcoma cells[41]. Although use of this complex substrate could lead to increased variability with regards to cellular organization or behavior, we reasoned that it would also engage a wide range of integrins, resulting in more stable cell attachment. Matrigel can easily be replaced by any protein able to adsorb to gold surfaces for applications requiring completely defined culture conditions. We have successfully used a recombinant vitronectin solution for this purpose (data not shown).

To allow for real-time imaging of actin and nuclear dynamics in live cells, a human fibroblast line harboring stable genomic inserts encoding Histone 2B (H2B)-mCherry fusion protein and LifeAct-GFP[42] (H2B-LA) were derived via CRISPR/Cas9 gene editing and lentiviral transduction. LifeAct is a 17 amino acid peptide derived from the yeast protein Abp 140p that, when linked to a fluorescent protein such as GFP, enables visualization of the actin cytoskeleton. The LifeAct peptide is not covalently

bound to globular actin monomers (G-actin), and LifeAct binding has no discernible effect on actin dynamics[42,43]. Gene-modified cells were added in suspension and allowed to attach to patterns for 14-18 hours before automated fluorescence imaging (Figure 4-3A-E).

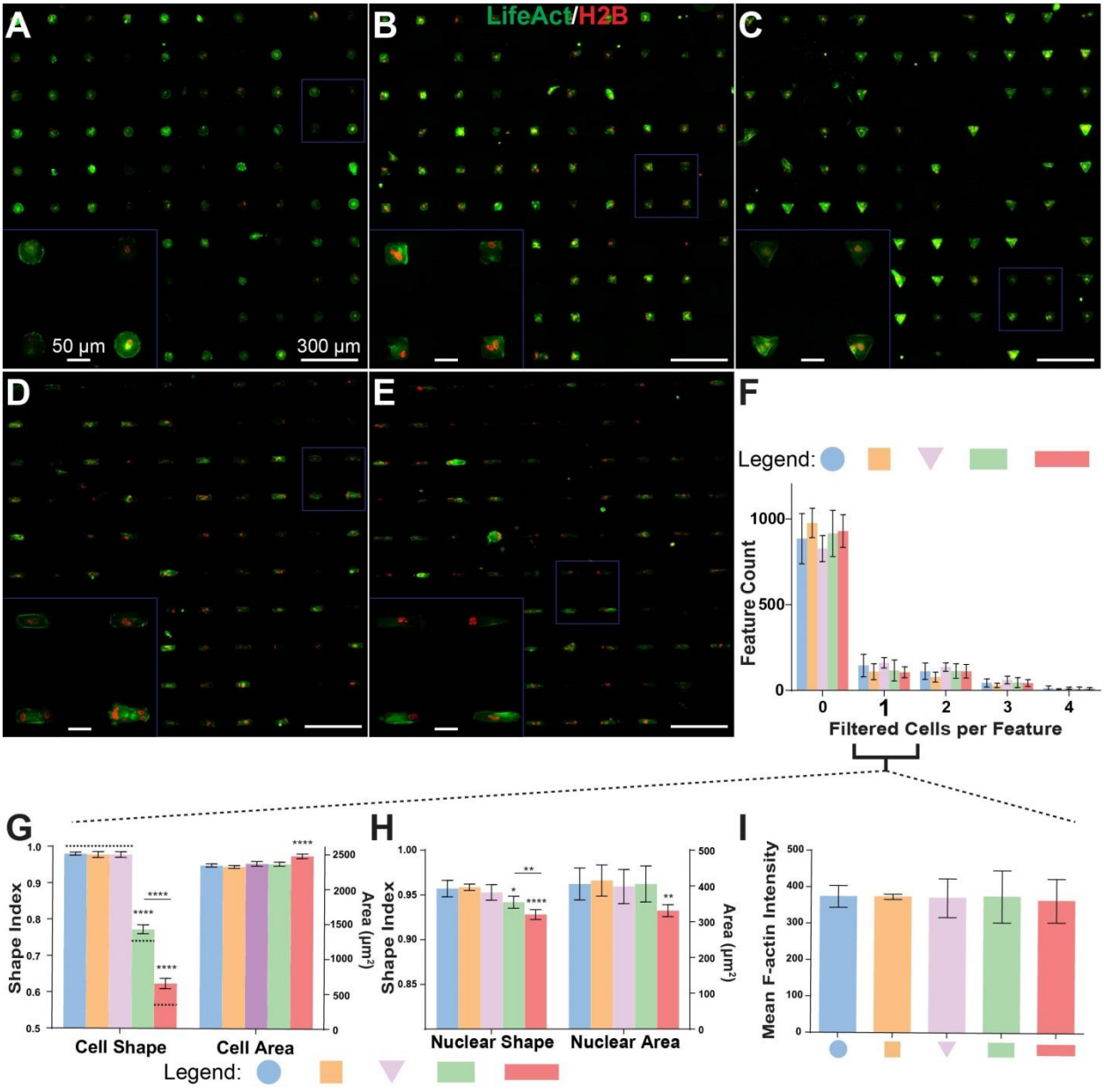


**Figure 4-3. Cell attachment and patterning on µCP Well Plates. A-E)** 20x stitched images of H2B-mCherry- and LifeAct-GFP-labeled human fibroblast lines (H2B-LA) attached to circular (A), square (B), triangular (C), compact rectangular (D), and elongated rectangular (E) single-cell features. Cells were seeded 16 hours prior to imaging and analysis. **F)** Distribution of cells

contained by each feature after automated removal of cells that do not meet user-specified area and shape criteria. “0” filtered cells columns correspond to the sum of both empty features and features containing cells eliminated by filtering. **G-H)** SI (left Y-axis) and area (right Y-axis) measurements for cell bodies (H) and nuclei (I) of features containing a single cell after filtering. Dashed bars in (H) indicate theoretical SI values for each shape. **I)** Mean LifeAct fluorescent intensity (averaged per-pixel across filtered LifeAct features) of patterned single-cells. All error bars denote 95% confidence intervals. Unless otherwise denoted, asterisks indicate *p* values from unpaired Student’s *t*-test compared to data from circular features (**p*<0.05, ***p*<0.01, ****p*<0.001, *****p*<0.0001). Each bar represents data aggregated from 5 to 8 wells of a 24-well plate across two biological replicate experiments.

An automated image analysis workflow was created using CellProfiler software[44] in order to assess attachment and patterning of cells (Figure 4-4A). Briefly, full-well stitched images were fed into CellProfiler, which filtered actin regions (cells or cell clusters) based on their spread area and other shape characteristics and removed poorly patterned or incompletely spread cells from the data set (Figure 4-4B). At this point, nuclei within remaining LifeAct regions were identified and analyzed for area, shape, and intensity characteristics. The number of nuclei contained within a filtered region of high LifeAct intensity was then used to determine the number of cells occupying a given feature (Figure 4-4C).

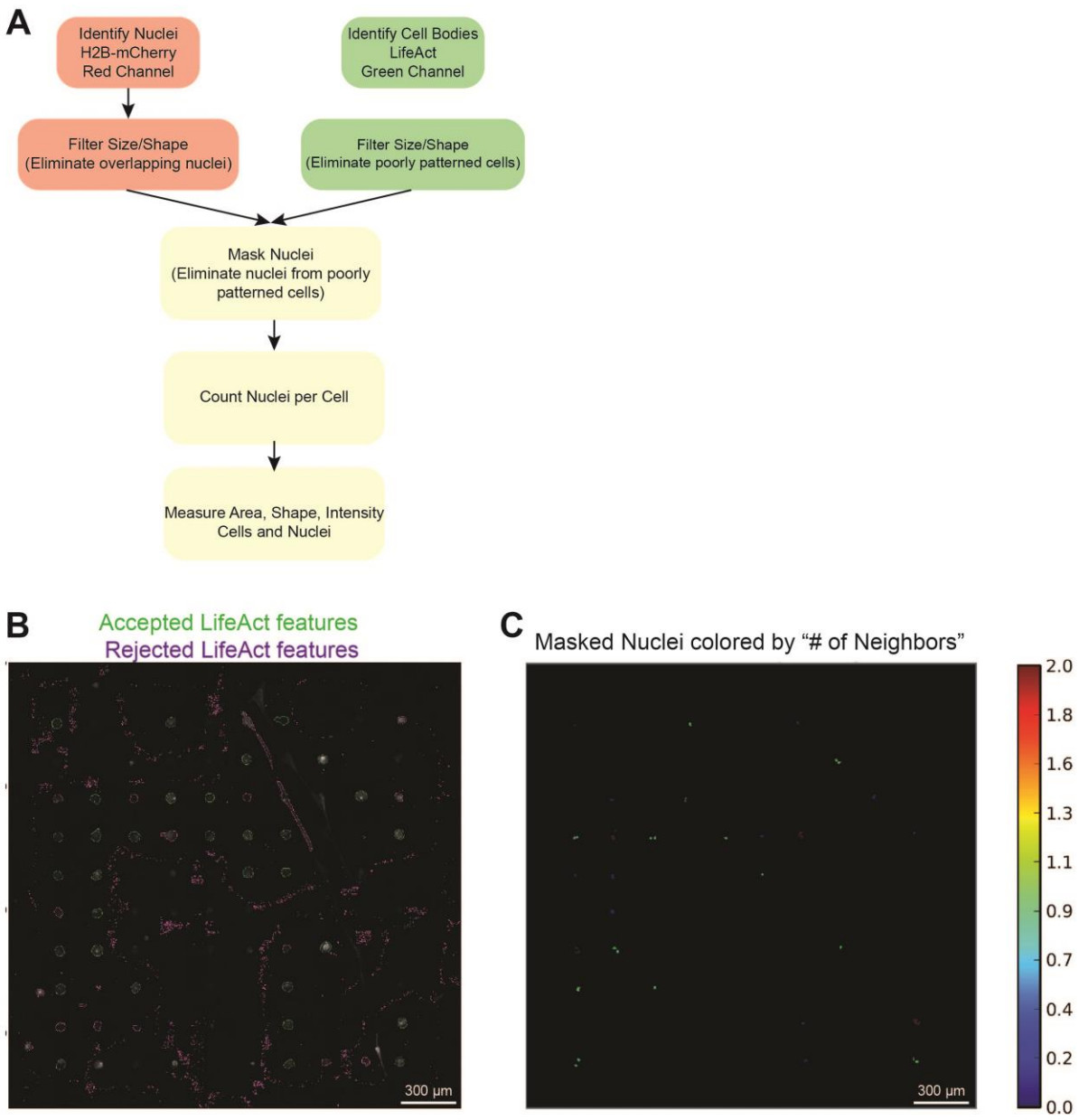


**Figure 4-4. Automated image analysis via CellProfiler software. A)** Workflow of CellProfiler pipeline. **B)** CellProfiler Screenshot depicting filtering step for actin features. **C)** CellProfiler Screenshot depicting nuclei masked by filtered actin features from (B). Nuclei are colored by the number of neighboring nuclei occupying the same actin feature and are ready to proceed to the measurement phase.

At a seeding density of 15,000 cells per well for a 24-well µCP Plate, 100-200 correctly patterned single cells were routinely identified per well (Figure 4-3F), corresponding to approximately 10% of all available patterned features. Image analysis revealed that this strict filtering protocol resulted in high quality cell populations with

highly consistent shape and intensity properties between replicates (Fig. 4-3G-I, Figure 4-5A-E).

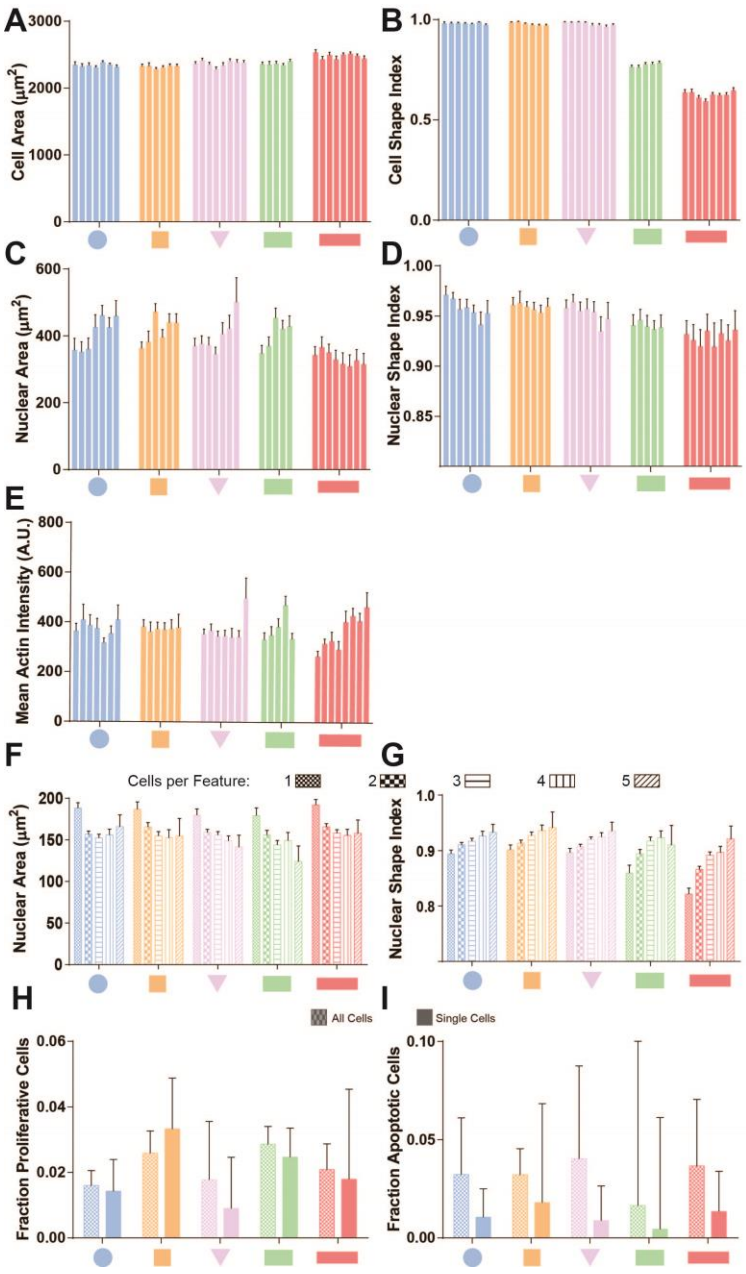


**Figure 4-5. Nuclear and cellular morphology and behavior on μCP Well Plates. A-E)** Technical (single well) replicates for cell area (A), cell shape (B), nuclear area (C), nuclear shape (D), and mean F-actin intensity (E) of filtered, single-cell features across two experiments. Wells containing less than 50 filtered single-cells were removed from the data set. Aggregated data is presented in Figure 3 in the text. **F-G)** Nuclear area (F) and nuclear shape (G) data aggregated by the number of cells identified on each filtered feature. **H-I)** Fraction of proliferative (H) and apoptotic (I) cells on filtered features as assayed by EdU and TUNEL assays, respectively.

Minor differences in nuclear area and shape were detected based on the number of cells contained in each feature (Figure 4-5F-G) in addition to obvious changes in cell shape, so all subsequent analysis was performed exclusively on filtered single cells. We rejected ~90% of features identified via CellProfiler, which reflects mostly autofluorescent or apoptotic cell debris with a minority of cell clusters, poorly patterned cells, and regions of a particular well with artificially high fluorescence intensities (Figure 4-4B, very small purple features). In the 14-18 hour span between cell seeding and imaging, proliferation and apoptosis rates were below 5% for all geometries (Figure 4-5H-I) and therefore were not taken into account during subsequent analyses.

Shape characteristics of cells seeded on geometric arrays were characterized using the shape index (SI) formula[45]

1) $SI = \frac{4\pi A}{P^2}$

where *A* represents spread area of the cell or nucleus and *P* represents the perimeter. Because perimeter measurements of shape borders can be affected greatly by image pixelation or irregular protrusions such as blebs and filopedia, we directly measured major and minor axes of each respective cell body and nucleus and estimated SI from the area and perimeter values of the resulting ellipse (Figure 4-6A). Shape index assessed in this manner is a measure of cell elongation, with a value of one corresponding to a perfect circle and values approaching zero with elongation. SI of cell bodies very nearly matched their theoretical predictions for each respective shape (Figure 4-3G, left, dashed lines). Nuclei were in turn elongated in a similar manner to their respective cell bodies, although to a lesser degree (Figure 4-3H), in agreement with previous results[17,46,47].

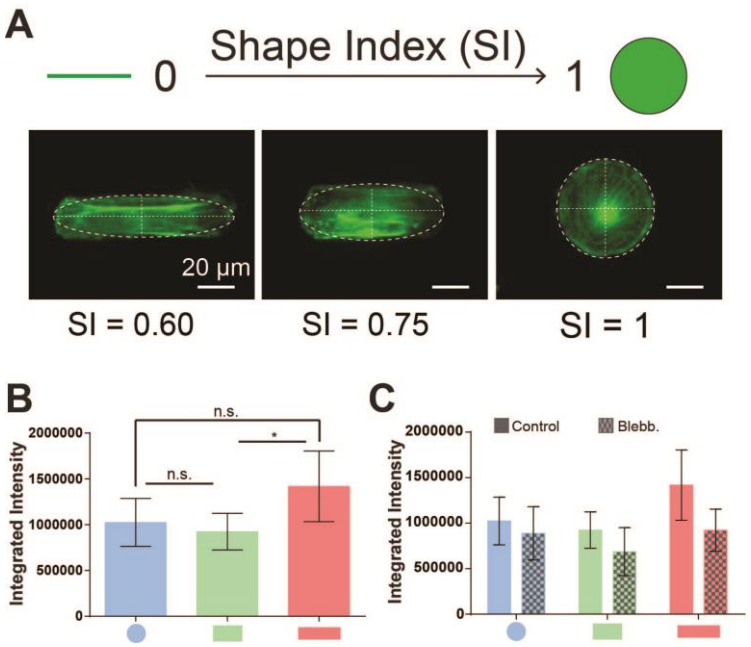


**Figure 4-6. Shape index and LifeAct integrated intensity. A)** Schematic of the shape index (SI) measurement. SI was calculated by fitting ellipses to major and minor axes of cells or nuclei, which were measured directly. **B)** Integrated intensity of H2B-LA cells patterned on circular, compact rectangular, and elongated rectangular geometries. **C)** Integrated intensity of control untreated and blebbistatin treated (50 μM, 60 min. exposure) H2B-LA cells patterned on circular, compact rectangular, and elongated rectangular geometries. Measurements calculated from maximum-intensity projections of 60X confocal z-stacks. All error bars denote 95% confidence intervals. Asterisks indicate *p* values from unpaired Student's *t*-test (**p*<0.05).

Spread area of patterned single-cells was constant with the exception of a <10% increase for elongated rectangular features (Figure 4-3G, right), mirroring results from feature characterization prior to cell attachment. Nuclei within cells patterned on elongated rectangular features did not proportionately increase in area, but had significantly lower projected areas than those of other features (Figure 4-3H, right), a phenomenon which has been previously reported for elongated endothelial cells[47]. Significant changes in integrated actin intensity were observed between compact and elongated geometries when analyzing 60x confocal stacks (Figure 4-6B). A non-significant decrease in LifeAct intensity was detected in all measured shapes after

treatment with blebbistatin, a Myosin II ATPase activity inhibitor that relieves actomyosin tension and can disrupt F-actin networks[48,49] (Figure 4-6C).

*4.3.4 High-Content Imaging of Subcellular Organization*

We hypothesized that actin may be involved in the observed nuclear shape dynamics in our system, as actin fibers have been reported to exert forces on the nucleus in a variety of manners, especially through actin structures directly apical to the nucleus[7,46,47,50-53]. Using stacks of confocal images of single cells at this higher 60x magnification we were able to discern actin fiber alignment, which is known to correlate with cell elongation[13,47,51] (Figure 4-7A-C). We used the previously reported Order Parameter metric[35] to quantify the degree of actin alignment on a scale from 0-1, with 1 being the most aligned. We focused on circular, compact rectangular, and elongated rectangular geometries and found that order parameter increased with elongation of cell shape (Figure 4-7D). These results are consistent with previously reported relationships between cellular elongation and actin fiber alignment[14,46,49]. Furthermore, actin alignment significantly correlated to nuclear shape (Figure 4-7E). The *p* value displayed here is calculated from an *F* test and corresponds to the probability that the slope of the regression line is equal to zero, (i.e., the two variables are unrelated). However, regressions within each measured geometry did not reach statistical significance (Figure 4-8A). Nuclear shape did not significantly correlate to integrated actin intensity (Figure 4-7F, Supp. Figure 4B). We then measured nuclear SI of patterned single-cells after disrupting F-actin networks with blebbistatin (Figure 4-7G-I)[48,49].

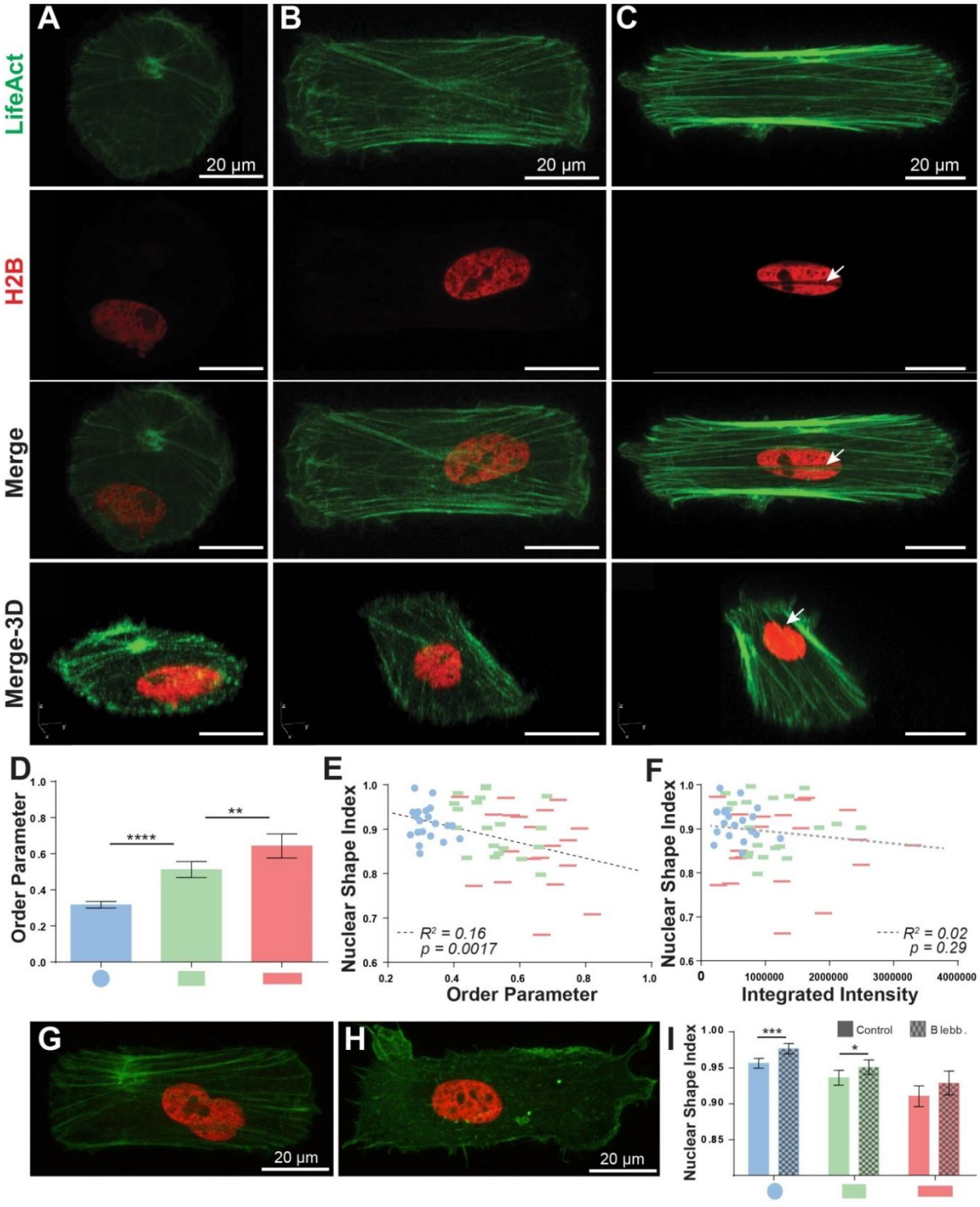


**Figure 4-7. Actin and nuclear organization of patterned single-cells. A-C)** 60x confocal maximum-intensity projection images of H2B-LA single-cells patterned into circular (A), compact rectangular (B), and elongated rectangular (C) geometries. Note that geometries are displayed at slightly different zoom levels. Arrowheads in (C) denote a nuclear indentation site formed by actin stress fibers. **D)** Order parameter of patterned single-cells (n=20). Measurements were taken from maximum-intensity projections of 10-15 1 μm z-stacks (as pictured in A-C). **E-F)**

Single-cell scatter plots of order parameter (E) or LifeAct integrated intensity (F) vs. nuclear shape index. Dashed lines represents linear regression best-fit lines. *p* values for best-fit lines were calculated from *F*-tests and indicate the probability that the slopes of the regression lines are equal to zero. **G-H)** Representative images of untreated control (G) and blebbistatin-treated (H) (50 µM, 60 min exposure) cells in compact rectangular geometries. **I)** Nuclear shape analysis of control or blebbistatin-treated patterned cells (n>100). All error bars denote 95% confidence intervals. Asterisks indicate *p* values from unpaired Student's *t*-test (**p*<0.05, ***p*<0.01, ****p*<0.001, *****p*<0.0001).

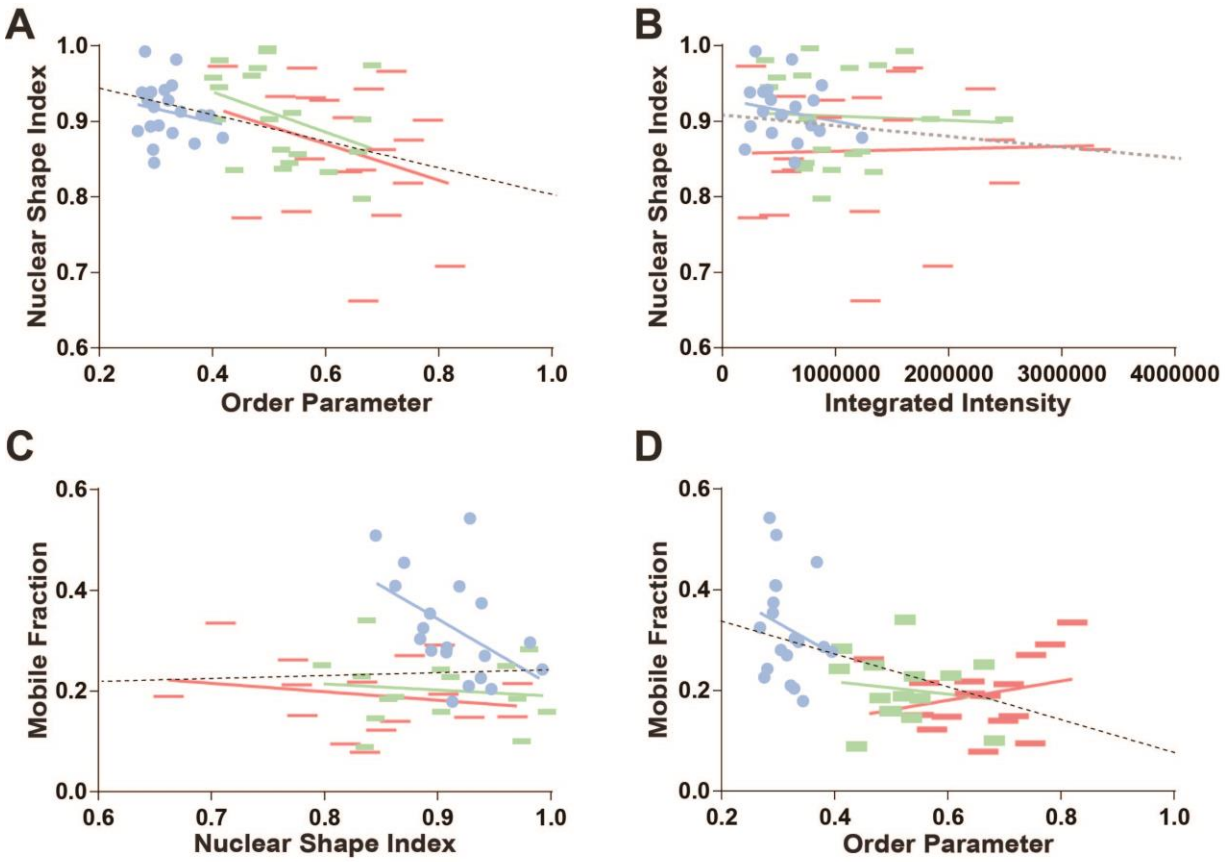


| | | A) Order Parameter vs. Nuclear Shape | | B) Integrated Intensity vs. Nuclear Shape | | C) Nuclear Shape vs. Mobile Fraction | | D) Order Parameter vs. Mobile Fraction | |
|---|---|---|---|---|---|---|---|---|---|
| | *n* | Slope | *p* | Slope | *p* | Slope | *p* | Slope | *p* |
| **Circles** | **19** | -0.17 | 0.42 | -2.90E-08 | 0.38 | -1.3 | 0.036 | -0.64 | 0.36 |
| **Compact Rectangular** | **16** | -0.27 | 0.09 | -5.70E-09 | 0.83 | -0.12 | 0.68 | -0.12 | 0.6 |
| **Elongated Rectangular** | **16** | -0.24 | 0.22 | -3.20E-09 | 0.9 | -0.17 | 0.46 | 0.19 | 0.34 |
| **Combined** | **51** | -0.18 | 0.0017 | -1.40E-08 | 0.29 | 0.058 | 0.78 | -0.33 | 0.0001 |

**Figure 4-8. Single-cell trends within geometries. A-D)** Single-cell scatter plots of order parameter vs. nuclear shape index (A), LifeAct integrated intensity vs. nuclear shape index (B), nuclear shape index vs. mobile fraction (C), or order parameter vs. mobile fraction (D). Dashed lines represent linear regression best-fit lines for all geometries combined, while solid lines represent linear regression best-fit lines of a particular geometry alone (blue=circular, green=compact rectangular, red=elongated rectangular). Slopes and *p* values for each linear regression are listed below charts. *p* values for best-fit lines were calculated from *F*-tests and indicates the probability that the slopes of the regression lines are equal to zero.

We detected a significant increase in nuclear SI for circular and compact geometries upon blebbistatin treatment compared to untreated controls (Figure 4-7I). While a less significant increase occurred in the elongated case ($p$=0.12), these results together suggest a complex connection between the actin cytoskeleton and nuclear shape. Notably, we observed the presence of nuclear indentations along the length of F-actin stress fibers in elongated cells (Figure 4C, arrowheads). These indentations were recently shown to be enriched for LINC complexes[51] that connect the nuclear lamina to the cytoskeleton[50,52,54] and highlight the influence of actin stress fibers on the nucleus.

*4.3.5 Chromatin Dynamics and Cell Geometry*

We next investigated whether the observed changes in cell shape, actin organization, and/or nuclear shape could lead to changes in chromatin dynamics. Histone 2B is a member of the core nucleosome[55], and fluorescently tagged H2B has been well-characterized and remains bound to DNA throughout the cell cycle, although small fractions are continually exchanged[56,57] . Therefore, the mobility of H2B within the nucleus is a measure of (1) the mobility of the core nucleosome itself; (2) the portion of the overall H2B pool bound to DNA (its affinity); or, (3) a combination of both[58]. Changes in either of these properties reflect changes in the epigenome, which can govern gene expression and cell behavior. Fluorescence Recovery After Photobleaching (FRAP) experiments were used to assess the mobility of fluorescently tagged molecules by measuring exchange rates of fluorescent molecules in a given area. As the minutes timescale used for these experiments is far below that needed to

synthesize and localize significant amounts of new fluorescent protein to the photobleached region, any measured recovery is a result of the fluorescent molecule moving into the photobleached region from the surrounding area[59]. The plateau of the fluorescent recovery curve over a given time scale is known as the “Mobile Fraction” of the molecule of interest[60,61].

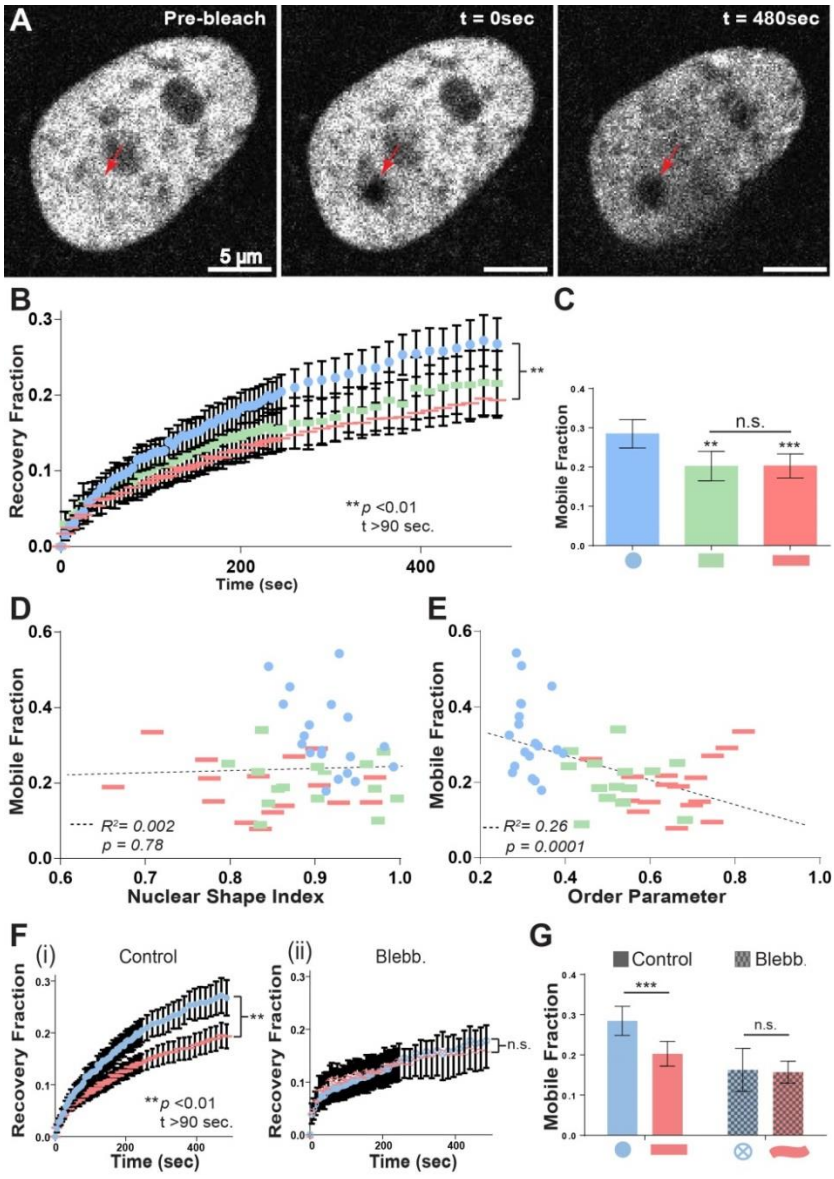


**Figure 4-9. FRAP analysis of patterned single cells. A)** Representative images of H2B-mCherry-labeled nuclei immediately before and after photobleaching, and at the end of the 8-minute recovery period. Arrowheads denote ~1 µm diameter photobleached area. Intensity measurements were collected every five seconds for four minutes following photobleaching, and

every 15 seconds for four more minutes thereafter, and normalized to the intensity of the entire nucleus. **B)** Quantification of fluorescent recovery fraction in nuclei of patterned single-cells. (n=20 for compact rectangles, n=40 for circles and elongated rectangles) **C)** Mobile fraction of patterned single-cells. Mobile fraction was calculated as the plateau of one-phase association curve fit to the recovery fraction time course. **D-E)** Single-cell scatter plots of nuclear shape index (D) or order parameter (E) vs. mobile fraction. Dashed lines represent linear regression best-fit lines. *p* values for best-fit lines were calculated from *F*-tests and indicates the probability that the slopes of the regression lines are equal to zero. **F)** Quantification of fluorescent recovery fraction in nuclei of control (i), (n=40) and blebbistatin-treated (ii), (n=20) patterned single-cells. (50 μM, 60-120 min exposure) **G)** Mobile fraction of control and blebbistatin-treated patterned single-cells. All error bars denote 95% confidence intervals. Asterisks indicate *p* values from unpaired Student's *t*-test (**p*<0.05, ***p*<0.01, ****p*<0.001, *****p*<0.0001).

To investigate chromatin dynamics in our system, ~1 μm diameter regions in the nuclei of patterned single-cells were photobleached by exposure to a high intensity laser beam (100% power) for 1 second followed by normalized intensity measurements over an 8 minute time course (5% power) to track recovery of fluorescence (Figure 4-9A-B). H2B is present in at least two pools in human cells, one that recovers on the minute timescale and one that recovers over a period of hours[56]. The timescale chosen here focuses on the first pool, and is comparable to that used in similar studies measuring H2B mobility [53,56]. H2B recovery curves of circular and elongated rectangular single-cells diverged significantly ($p<0.01$) at time points >90 sec., with the recovery curve for compact rectangular cells lying in between (Figure 4-9B). Mobile fraction was significantly reduced in both compact ($p<0.01$) and elongated rectangular geometries ($p<0.001$) compared to circular geometries (Figure 4-9C).

We next examined whether actin alignment and/or increased nuclear SI might be responsible for the observed decrease in H2B mobility. Accordingly, single-cell H2B mobile fraction measurements were regressed against either order parameter or nuclear SI measurements. When analyzed in this manner, H2B mobile fraction was not correlated to nuclear shape across different geometries (Figure 4-9D), although a significant negative correlation was detected when analyzing circular geometries alone

(Figure 4-8C). In contrast, we detected a highly significant correlation when regressing mobile fraction against order parameter across all geometries (Figure 4-9E). Regressions within each geometry were not significant (Supp. Figure 4-8D). Disruption of the actin cytoskeleton using a blebbistatin treatment eliminated the differences in H2B mobility imposed by cell geometry (Figure 4-9F-G). Surprisingly, blebbistatin treatment resulted in a decrease in H2B mobility (Figure 4-9F-G), rather than the increase that would be expected by H2B mobility trends with respect to actin alignment and cell shape (decreased elongation ~ decreased actin alignment ~ increased H2B mobility). These results are discussed further below.

## 4.4 Discussion

We have presented here the creation of the μCP Well Plate, a novel cell culture system for quantitative imaging and mechanobiological analysis combining the single-cell geometric control, substrate flexibility, and imaging capabilities of microcontact-printed glass coverslips with the multiplexing and compatibility features of standard multi-well plates. μCP Well Plates enable rapid fabrication of many experimental replicates and conditions (>25x more than with comparable coverslip methods) in a single patterning step and high-content analysis of large, uniform single-cell populations. Unused in the current study were the capabilities to independently alter substrate and media components over dozen of conditions in a single plate, which could be of utility in drug screening, functional genomics, and a myriad of similar biotechnology applications.

*4.4.1 µCP Well Plates for High-Content Imaging of Live Human Cells*

We first demonstrated that µCP Well Plates can be patterned consistently with high precision and geometric control (Figure 4-1 and Figure 4-2), and are well tolerated by human cells (Figure 4-3A-E). Merged with high content imaging and analysis software, µCP Well Plates were used to identify high quality single-cell populations suitable for rapid, consistent analysis of shape and intensity characteristics (Figure 4-3G-I). By combining multiple replicate arrays into a single plate, minor differences between populations – such as a reduction in nuclear area in cells on elongated rectangular features (Figure 4-3H) – can be identified in a single experiment with high confidence.

We then performed high-resolution, sub-cellular analyses of live cells using the µCP Well Plate platform to probe how cytoskeletal organization mediates the relationship between cell shape, nuclear shape, and chromatin dynamics at a single-cell level. Actin became more aligned with increasing cell elongation (Figure 4-7D). Nuclei within cells with high actin alignment were elongated (Figure 4-7E), and nuclear elongation was reversed by actomyosin inhibition (Figure 4-7I). Finally, increasing cell elongation gave rise to a graded decrease in Histone H2B mobility inside the nucleus (Figure 4-9B). While the relationship between actin and nucleosome mobility is complex and requires further study, the two most highly correlated cellular properties observed in this study across all geometries were actin alignment and H2B mobile fraction (Figure 4-9E), and differences in H2B mobility based on cell geometry were abolished after actin disruption (Figure 4-9F-G). To our knowledge, this is the first report of the mobility of a core nucleosome component being altered solely by control of cell shape.

*4.4.2 Influence of Actin Cytoskeleton on Chromatin Dynamics*

Reduction in nuclear volume in elongated endothelial cells has been shown to cause chromatin condensation[47], and chromatin hyper-condensation induced by osmotic stress or apoptosis stabilizes binding of nuclear proteins, including H2B, to DNA, resulting in decreased fluorescent recovery rates[58,62]. Thus, aligned actin fibers in elongated cells may impart physical pressure on the nucleus, resulting in reduced nuclear volume, condensed chromatin, and lower mobility of H2B. Importantly, nuclear indentations imposed by F-actin stress fibers in elongated cells can segregate the nucleus and cause chromatin condensation even without gross changes to nuclear shape (Figure 4-7C, Figure 4-10)[51]. This interpretation is supported by recent findings that disrupting F-actin fibers (via small molecules or RNA interference) in randomly oriented cells increases H2B mobility as well as nuclear height[53].

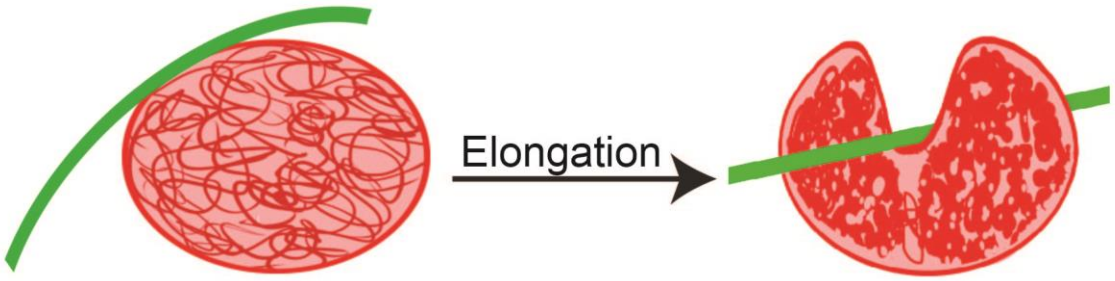


**Figure 4-10. Cytoskeletal Influence on Chromatin Dynamics.** Schematic depicting chromatin condensation (dark red) resulting from nuclear deformations caused by actin fibers (green) in elongated cells.

The reduction of H2B mobile fraction after blebbistatin treatment is a surprising result, as blebbistatin relieves nuclear elongation and increases overall nuclear volume[47] – and would therefore be expected to increase H2B recovery rates. Recovery

of blebbistatin-treated cells is indeed faster than all circular and rectangular control cells over the first ~60 seconds, but at longer time scales recovery is decreased (Figure 5F). Applied external force has been shown to facilitate movement of small particles throughout the nucleus[63], and reduced chromatin mobility upon blebbistatin treatment has been previously reported[39], in contrast to other inhibitors of actin organization[53]. Chemical interactions between actin fibers, the nuclear lamina, and the nucleoskeleton – such as increased LINC complex concentration at nuclear indentation sites[51] – may also be important drivers of H2B mobility, complicating simple physical interpretations.

## 4.5 Conclusions

Overall, more work is needed to mechanistically describe the influence of cell geometry and cytoskeletal organization on chromatin dynamics, as within the same geometry we did not observe significant relationships between actin organization and nuclear shape, nor between actin organization and chromatin dynamics. With future work, the tools described here will enable further characterization of the relationships among actin organization, cell shape, chromatin dynamics and cytoskeletal tension by providing a framework to independently control microenvironmental cues and measure subcellular dynamics in live cells at high resolution. Integration of new and emerging molecular tools, such as CRISPR labeling[64,65], into this platform may permit visualization of these mechanobiological processes at higher resolution.

In summary, μCP Well Plates offer a flexible cell culture platform that enables mechanistic, high-throughput study of subcellular components. This platform expands our ability to precisely and independently control microenvironmental cues such as

substrate composition, cell geometry, and media composition, and the platform is importantly compatible with advances in high-content imaging and single-cell analysis. These capabilities open up new frontiers in screening for molecules that could influence a multitude of human cell behaviors.

## References


1 Iskratsch, T., Wolfenson, H. & Sheetz, M. P. Appreciating force and shape [mdash] the rise of mechanotransduction in cell biology. *Nature Reviews Molecular Cell Biology* (2014).

2 Giancotti, F. G. & Ruoslahti, E. Integrin signaling. *Science* **285**, 1028-1033 (1999).

3 Lee, S. E., Kamm, R. D. & Mofrad, M. R. Force-induced activation of talin and its possible role in focal adhesion mechanotransduction. *Journal of biomechanics* **40**, 2096-2106 (2007).

4 Vogel, V. & Sheetz, M. Local force and geometry sensing regulate cell functions. *Nature reviews molecular cell biology* **7**, 265-275 (2006).

5 Sawada, Y. *et al.* Force sensing by mechanical extension of the Src family kinase substrate p130Cas. *Cell* **127**, 1015-1026 (2006).

6 Mitra, S. K., Hanson, D. A. & Schlaepfer, D. D. Focal adhesion kinase: in command and control of cell motility. *Nature reviews Molecular cell biology* **6**, 56-68 (2005).

7 Maniotis, A. J., Chen, C. S. & Ingber, D. E. Demonstration of mechanical connections between integrins, cytoskeletal filaments, and nucleoplasm that stabilize nuclear structure. *Proceedings of the National Academy of Sciences* **94**, 849-854 (1997).

8 Low, B. C. *et al.* YAP/TAZ as mechanosensors and mechanotransducers in regulating organ size and tumor growth. *FEBS letters* **588**, 2663-2670 (2014).

9 Starr, D. A. & Fridolfsson, H. N. Interactions between nuclei and the cytoskeleton are mediated by SUN-KASH nuclear-envelope bridges. *Annual review of cell and developmental biology* **26**, 421 (2010).

10 Aragona, M. *et al.* A mechanical checkpoint controls multicellular growth through YAP/TAZ regulation by actin-processing factors. *Cell* **154**, 1047-1059 (2013).

11 Chen, C. S., Mrksich, M., Huang, S., Whitesides, G. M. & Ingber, D. E. Geometric control of cell life and death. *Science* **276**, 1425-1428 (1997).

12 Qutub, A. A. & Popel, A. S. Elongation, proliferation & migration differentiate endothelial cell phenotypes and determine capillary sprouting. *BMC systems biology* **3**, 13 (2009).

13 Wang, D. *et al.* Tissue-specific mechanical and geometrical control of cell viability and actin cytoskeleton alignment. *Scientific reports* **4** (2014).

14 Dalby, M. J., Gadegaard, N. & Oreffo, R. O. Harnessing nanotopography and integrin-matrix interactions to influence stem cell fate. *Nature materials* **13**, 558-569 (2014).

15 Bakhru, S. *et al.* Direct and cell signaling-based, geometry-induced neuronal differentiation of neural stem cells. *Integrative Biology* **3**, 1207-1214 (2011).

16 Dike, L. E. *et al.* Geometric control of switching between growth, apoptosis, and differentiation during angiogenesis using micropatterned substrates. *In Vitro Cellular & Developmental Biology-Animal* **35**, 441-448 (1999).

17 Downing, T. L. *et al.* Biophysical regulation of epigenetic state and cell reprogramming. *Nature materials* **12**, 1154-1162 (2013).

18 Cordie, T. *et al.* Nanofibrous electrospun polymers for reprogramming human cells. *Cellular and Molecular Bioengineering* **7**, 379-393 (2014).

19 Afrin, R., Yamada, T. & Ikai, A. Analysis of force curves obtained on the live cell membrane using chemically modified AFM probes. *Ultramicroscopy* **100**, 187-195 (2004).

20 Ghibaudo, M. *et al.* Traction forces and rigidity sensing regulate cell functions. *Soft Matter* **4**, 1836-1843 (2008).

21 Chiou, P. Y., Ohta, A. T. & Wu, M. C. Massively parallel manipulation of single cells and microparticles using optical images. *Nature* **436**, 370-372 (2005).

22 Han, S. J., Bielawski, K. S., Ting, L. H., Rodriguez, M. L. & Sniadecki, N. J. Decoupling substrate stiffness, spread area, and micropost density: a close spatial relationship between traction forces and focal adhesions. *Biophysical journal* **103**, 640-648 (2012).

23 McBeath, R., Pirone, D. M., Nelson, C. M., Bhadriraju, K. & Chen, C. S. Cell shape, cytoskeletal tension, and RhoA regulate stem cell lineage commitment. *Developmental cell* **6**, 483-495 (2004).

24 Kilian, K. A., Bugarija, B., Lahn, B. T. & Mrksich, M. Geometric cues for directing the differentiation of mesenchymal stem cells. *Proceedings of the National Academy of Sciences* **107**, 4872-4877 (2010).

25 Bernard, A., Renault, J. P., Michel, B., Bosshard, H. R. & Delamarche, E. Microcontact printing of proteins. *Advanced Materials* **12**, 1067-1070 (2000).

26 McNulty, J. D. *et al.* High-precision robotic microcontact printing (R-μCP) utilizing a vision guided selectively compliant articulated robotic arm. *Lab on a Chip* **14**, 1923-1930 (2014).

27 Sha, J., Lippmann, E. S., McNulty, J., Ma, Y. & Ashton, R. S. Sequential Nucleophilic Substitutions Permit Orthogonal Click Functionalization of Multicomponent PEG Brushes. *Biomacromolecules* **14**, 3294-3303 (2013).

28 Geisse, N. A., Sheehy, S. P. & Parker, K. K. Control of myocyte remodeling in vitro with engineered substrates. *In Vitro Cellular & Developmental Biology-Animal* **45**, 343-350 (2009).

29 Théry, M. & Piel, M. Adhesive micropatterns for cells: a microcontact printing protocol. *Cold Spring Harbor Protocols* **2009**, pdb. prot5255 (2009).

30 Jain, N., Iyer, K. V., Kumar, A. & Shivashankar, G. Cell geometric constraints induce modular gene-expression patterns via redistribution of HDAC3 regulated by actomyosin contractility. *Proceedings of the National Academy of Sciences* **110**, 11349-11354 (2013).

31 Nazareth, E. J. *et al.* High-throughput fingerprinting of human pluripotent stem cell fate responses and lineage bias. *Nature methods* **10**, 1225-1231 (2013).

32 Knight, G., Sha, J. & Ashton, R. Micropatterned, clickable culture substrates enable in situ spatiotemporal control of human PSC-derived neural tissue morphology. *Chemical Communications* **51**, 5238-5241 (2015).

33 Hockemeyer, D. *et al.* A drug-inducible system for direct reprogramming of human somatic cells to pluripotency. *Cell stem cell* **3**, 346-353 (2008).

34 Schindelin, J. *et al.* Fiji: an open-source platform for biological-image analysis. *Nature methods* **9**, 676-682 (2012).

35 Aratyn-Schaus, Y., Oakes, P. W. & Gardel, M. L. Dynamic and structural signatures of lamellar actomyosin force generation. *Molecular biology of the cell* **22**, 1330-1339 (2011).

36 Thévenaz, P. StackReg: an ImageJ plugin for the recursive alignment of a stack of images. *Biomedical Imaging Group, Swiss Federal Institute of Technology Lausanne* **2012** (1998).

37 Libioulle, L., Bietsch, A., Schmid, H., Michel, B. & Delamarche, E. Contact-inking stamps for microcontact printing of alkanethiols on gold. *Langmuir* **15**, 300-304 (1999).

38 Salick, M. R. *et al.* Micropattern width dependent sarcomere development in human ESC-derived cardiomyocytes. *Biomaterials* **35**, 4454-4464 (2014).

39 Talwar, S., Jain, N. & Shivashankar, G. The regulation of gene expression during onset of differentiation by nuclear mechanical heterogeneity. *Biomaterials* **35**, 2411-2419 (2014).

40 Li, L., Chen, S. & Jiang, S. Protein interactions with oligo (ethylene glycol)(OEG) self-assembled monolayers: OEG stability, surface packing density and protein adsorption. *Journal of Biomaterials Science, Polymer Edition* **18**, 1415-1427 (2007).

41 Hughes, C. S., Postovit, L. M. & Lajoie, G. A. Matrigel: a complex protein mixture required for optimal growth of cell culture. *Proteomics* **10**, 1886-1890 (2010).

42 Riedl, J. *et al.* Lifeact: a versatile marker to visualize F-actin. *Nature methods* **5**, 605-607 (2008).

43 Riedl, J. *et al.* Lifeact mice for studying F-actin dynamics. *Nature methods* **7**, 168-169 (2010).

44 Carpenter, A. E. *et al.* CellProfiler: image analysis software for identifying and quantifying cell phenotypes. *Genome biology* **7**, R100 (2006).

45 Malek, A. M. & Izumo, S. Mechanism of endothelial cell shape change and cytoskeletal remodeling in response to fluid shear stress. *Journal of Cell Science* **109**, 713-726 (1996).

46 Khatau, S. B. *et al.* A perinuclear actin cap regulates nuclear shape. *Proceedings of the National Academy of Sciences* **106**, 19017-19022 (2009).

47 Versaevel, M., Grevesse, T. & Gabriele, S. Spatial coordination between cell and nuclear shape within micropatterned endothelial cells. *Nature communications* **3**, 671 (2012).

48 Goffin, J. M. *et al.* Focal adhesion size controls tension-dependent recruitment of α-smooth muscle actin to stress fibers. *The Journal of cell biology* **172**, 259-268 (2006).

49 Chrzanowska-Wodnicka, M. & Burridge, K. Rho-stimulated contractility drives the formation of stress fibers and focal adhesions. *The Journal of cell biology* **133**, 1403-1415 (1996).

50 Kim, D.-H. *et al.* Actin cap associated focal adhesions and their distinct role in cellular mechanosensing. *Scientific reports* **2** (2012).

51 Versaevel, M. *et al.* Super-resolution microscopy reveals LINC complex recruitment at nuclear indentation sites. *Scientific reports* **4** (2014).

52 Chambliss, A. B. *et al.* The LINC-anchored actin cap connects the extracellular milieu to the nucleus for ultrafast mechanotransduction. *Scientific reports* **3** (2013).

53 Ramdas, N. M. & Shivashankar, G. Cytoskeletal control of nuclear morphology and chromatin organization. *Journal of molecular biology* (2014).

54 Crisp, M. *et al.* Coupling of the nucleus and cytoplasm role of the LINC complex. *The Journal of cell biology* **172**, 41-53 (2006).

55 Luger, K., Mäder, A. W., Richmond, R. K., Sargent, D. F. & Richmond, T. J. Crystal structure of the nucleosome core particle at 2.8 Å resolution. *Nature* **389**, 251-260 (1997).

56 Kimura, H. & Cook, P. R. Kinetics of core histones in living human cells little exchange of H3 and H4 and some rapid exchange of H2B. *The Journal of cell biology* **153**, 1341-1354 (2001).

57 Kuipers, M. A. *et al.* Highly stable loading of Mcm proteins onto chromatin in living cells requires replication to unload. *The Journal of cell biology* **192**, 29-41 (2011).

58 Bhattacharya, D., Mazumder, A., Miriam, S. A. & Shivashankar, G. EGFP-tagged core and linker histones diffuse via distinct mechanisms within living cells. *Biophysical journal* **91**, 2326-2336 (2006).

59 Axelrod, D., Koppel, D., Schlessinger, J., Elson, E. & Webb, W. Mobility measurement by analysis of fluorescence photobleaching recovery kinetics. *Biophysical journal* **16**, 1055 (1976).

60 Ellenberg, J. & Lippincott-Schwartz, J. Dynamics and mobility of nuclear envelope proteins in interphase and mitotic cells revealed by green fluorescent protein chimeras. *Methods* **19**, 362-372 (1999).

61 White, J. & Stelzer, E. Photobleaching GFP reveals protein dynamics inside live cells. *Trends in cell biology* **9**, 61-65 (1999).

62 Martin, R. M. & Cardoso, M. C. Chromatin condensation modulates access and binding of nuclear proteins. *The FASEB Journal* **24**, 1066-1072 (2010).

63 Hameed, F. M., Rao, M. & Shivashankar, G. Dynamics of passive and active particles in the cell nucleus. *PloS one* **7**, e45843 (2012).

64 Chen, B. *et al.* Dynamic imaging of genomic loci in living human cells by an optimized CRISPR/Cas system. *Cell* **155**, 1479-1491 (2013).

65 Ma, H. *et al.* Multicolor CRISPR labeling of chromosomal loci in human cells. *PNAS* **112**, 3002-3007 (2015).

# Chapter 5. Tracking and predicting reprogramming from a biophysical perspective

## 5.1 Introduction

The cellular microenvironment refers to the set of biochemical and biophysical cues presented to a cell by its surroundings. These microenvironmental inputs are increasingly being recognized as an important driver of human cell fate decisions in both healthy and diseased states[1-3]. In particular, the biophysical microenvironment has long been leveraged as a potent method to direct stem cell differentiation[4-7]. In a process termed mechanotransduction, biophysical inputs can be transmitted to the cell nucleus in a variety of ways. Force-sensitive molecules such as Talin[8,9], p130CAS[10], and focal adhesion kinase[11] link the actin cytoskeleton to integrins that span the plasma membrane and physically connect cells to their microenvironments[12]. The cytoskeleton is in turn connected to the nucleoskeleton through linker of nucleoskeleton and cytoskeleton (LINC) complexes that pass through and regulate the nuclear lamina[13-17]. The nuclear lamina represses genes in its physical proximity and is a powerful regulator of chromatin organization and dynamics, and thus plays an active role in gene expression[15,18-21]. As a result of this process, the biophysical state of a cell is not solely determined by gene expression. Rather, a cell's biophysical status – as determined by its microenvironment – is also a powerful regulator of gene expression[22-25].

Another key player in the feedback loop between gene expression and biophysical state are the transcriptional coactivators Yes-associated protein (YAP) and transcriptional coactivator with PDZ-binding motif (TAZ)[26]. YAP and TAZ interact with

Rho GTPase, the actin cytoskeleton, and actin processing factors to detect conditions of mechanical stress, such as those induced by matrix stiffness or shape. Under these conditions, YAP translocates to the nucleus and binds the TEAD family of transcription factors to activate a range of gene targets [26-29]. Many of the genes activated by the YAP/TEAD complex are involved in cell proliferation and epithelial-to-mesenchymal transition (EMT), which allows YAP to act as a potent oncogene[30-32]. Notably, YAP also has an important role as a regulator of pluripotency[33] and the exclusion of YAP from the nucleus through alteration of the biophysical microenvironment leads to stem cell differentiation[26,34,35].

Biophysical regulation has been less studied in the context of somatic cell reprogramming to an induced pluripotent stem cell (iPSC) state, but available data suggest that biophysics is also critical during reprogramming processes. Live imaging of reprogramming cells has identified early-stage reduction of cell size as a critical event for successful reprogramming on standard tissue culture plastic[36], while nuclear geometry is also dramatically altered during reprogramming[37,38]. Additionally, the expression of kinases that activate cytoskeletal remodeling is critical to iPSC generation[39]. These biophysical changes have traditionally been studied in the context of the mesenchymal-to-epithelial transition (MET) which occurs relatively early in the reprogramming process[40-42], concurrent to epigenetic changes indicating loss of somatic identity[42-44]. YAP overexpression has been reported to increase reprogramming efficiency in mouse cells, but has not been investigated temporally throughout a reprogramming time course[33]. As in differentiation, biophysical inputs can also feed back on gene expression during reprogramming. For example, altering the size and

shape of reprogramming cells by culture on 3D hydrogels[45,46] or PDMS microchannels[47] promotes reprogramming by activating the gene set required for MET. The exact mechanisms of this feedback remain unclear, but seem to be mediated through altered patterns of histone modifications and "epigenetic plasticity" in cells cultured on these novel substrates[45,47].

Reprogramming progression has traditionally been studied by tracking transcript or protein expression and chromatin state throughout various intermediate reprogramming stages[48-53]. Here, we test the viability of utilizing the other side of the feedback loop between gene expression and biophysical status, namely biophysical state itself, to track reprogramming progression. We leveraged the Microcontact Printed Well Plate (μCP Well Plate), a recent technological advance enabling multiplexed and independent control of the biophysical and biochemical environment[54], to perform high-content imaging experiments on hundreds of reprogramming aggregates in a single well. Using this approach, we gathered large, high-quality data sets characterizing the biophysical status of reprogramming cells and used this data to generate and investigate novel hypotheses regarding human somatic cell reprogramming.

## 5.2 Materials and Methods

### *5.2.1 Cell culture and derivation of cell lines*

All reprogramming experiments were performed using the previously reported C1.2 human secondary fibroblast line[38], which incorporates the stably integrated transgenes Oct4, Sox2, Klf4 and c-Myc on doxycycline (DXC)-inducible cassettes. All iPSCs were generated through DXC-mediated reprogramming of the C1.2 line. H2B-

mCherry and LifeAct-GFP expressing iPSCs were generated via CRISPR/Cas9 introduction of the H2B-mCherry gene (Addgene #20972) and lentiviral transduction of LifeAct-GFP, (Addgene #22212) followed by clonal isolation of homogeneous cell lines[54]. H2B-mCherry and LifeAct-GFP expressing fibroblasts were then differentiated from this iPSC line via embryoid body differentiation[38,54,55]. During reprogramming studies, the YAP-ΔTA transgene (Addgene #59143) or LifeAct-GFP was introduced via lentivirus into C1.2 fibroblasts three days prior to the onset of reprogramming.

Once derived, all fibroblasts were maintained on gelatin-coated tissue culture plastic in fibroblast media containing DMEM-high glucose (Life Technologies) supplemented with 10% Fetal Bovine Serum (Life Technologies), 1 mM L-glutamine (Life Technologies), 1% non-essential amino acids (Millipore) and 1% Penicillin/Streptomycin (LifeTechnologies) and passaged with 0.05% trypsin (Life Technologies) every 3-5 days. All pluripotent cells were maintained in E8 media made in-house[56,57] on Matrigel-coated tissue culture plastic and passaged with Versene EDTA (Life Technologies) every 3-5 days. NPCs were derived from WA09 ESCs or C1.2 iPSCs using the previously published E6 method[58]. All cells were maintained at 37ºC and 5% $C0_2$.

*5.2.2 µCP Well Plate construction*

µCP Well Plates were constructed as previously described[54]. Briefly, large PDMS stamps were used with traditional microcontact printing techniques[59] to pattern a thin sheet of glass (Coresix Precision Glass, Inc.) that was then fastened to the bottom of a bottomless well plate via medical-grade double sided tape (ARcare 90106). Bottomless

well plates were made in house removing well bottoms of standard tissue culture well plates (Fisher Scientific) using a laser cutter (Universal Lasers Systems) or purchased from Greiner Bio-One.

*5.2.3 Reprogramming and isolation of iPSC lines*

C1.2 secondary fibroblasts were seeded onto patterned or unpatterned surfaces in fibroblast media one day prior to reprogramming initiation. The following day, media was switched to E7 (E8 without TGF-β, but including hydrocortisone)[57] and DXC was added at 2 µg/ml (5 µM) to activate expression of the reprogramming factors. Media was changed every other day. To isolate pure iPSC lines, colonies were picked from micropatterns using a 200 µL micropipette tip and transferred to Matrigel-coated tissue culture plastic in E8 media with DXC. If additional purification was required, one additional manual picking step with a 200 µL micropipette tip was performed. After the first passage, DXC was removed from E8 media and iPSCs were maintained in standard pluripotent culture as described above.

*5.2.4 Antibodies and Staining*

All cells were fixed for 15 minutes with 4% paraformaldehyde in PBS (Sigma) and permeabilized with 0.5% Triton-X (Sigma) for >4 hours before staining. Hoechst (Life Technologies H1399) was used at 5 ug/ml to stain nuclei. Primary antibodies were applied overnight in a blocking buffer of 5% donkey serum (Sigma) at the following concentrations: CD44-PE, BD Biosciences 555479, 1:200; TRA-1-60, Millipore MAB4360, 1:100; Nanog, R&D Systems AF1997, 1:200; Oct4, BD Biosciences 560186,

1:10; Pax6, DSHB AB_528427, 1:200; YAP, Santa Cruz sc-101199, 1:300. Secondary antibodies were obtained from Life Technologies and applied in a blocking buffer of 5% donkey serum for one hour at concentrations of 1:400 – 1:800. Phalloidin-TRITC was used at 10 nM to visualize F-actin. For live-cell stains, antibodies were added to the appropriate cell culture media at equivalent dilutions to those used for fixed cells. Two hour incubations were used for primary antibodies, followed by 30 minute incubations for secondary antibodies.

*5.2.5 High-content analysis*

High-content image analysis was performed similarly to previously published methods[54]. Briefly, a Nikon Eclipse Ti epifluorescence microscope was used to take single 10x images of each micropattern or a Nikon AR1 confocal microscope was used to take 60x stitched images of each micropattern using the z-plane closest to the glass substrate for reprogramming studies. For neural differentiation studies, the z-plane 2 μm above the glass substrate was used to capture rosette formation. Images were fed directly into CellProfiler[60], which analyzed images as described in Supp. Figure 2. Objects <300 pixels in area were filtered out of the data set to exclude apoptotic or other debris from data sets. Neighbors were identified by expanding objects until all pixels on the object boundaries were touching another. Two objects are neighbors if any of their boundary pixels are adjacent after expansion. Measurement of YAP staining intensity across a micropattern was obtained from the *MeanFrac* Radial Distribution function, which measures the fraction of total intensity normalized by the fraction of pixels at a given radius.

*5.2.6 PCA and PLSR*

CellProfiler measurements were averaged across each micropatterned aggregate and fed as mean values into PCA and PLSR analysis via JMP Pro software. PLSR was performed using the NIPALS method and predictions were tested and validated using K-Fold validation with 7 folds. Actual Nanog expression levels were obtained by manually tracing the areas of each micropattern expressing Nanog and dividing by the area of the entire micropattern.

*5.2.7 Statistics*

All error bars are presented as ±95% confidence intervals. *p*-values were calculated using unpaired two-tailed student's *t*-tests.

## 5.3 Results

*5.3.1 Reprogramming on uCP Well Plates*

In order to mechanistically probe cellular behavior during epigenetic transitions such as those present in differentiation and reprogramming, it is necessary to precisely control the microenvironmental cues presented to cells[6,22,25,45,46]. Accordingly, for this study we utilized a recently described cell culture platform – the Microcontact Printed (uCP) Well Plate – that allows for tight, independent control of the biochemical and biophysical microenvironment[54]. Defined media based on the E8 formulation[56,57] supplied soluble biochemical cues, while micropatterned surfaces constrained cell-cell contacts and geometry of cellular aggregates. Matrigel, a complex mixture of extra-cellular matrix proteins and soluble factors[61], was chosen as the cellular substrate on

the basis that it would allow the greatest chance for attachment and proliferation of cells over the multiple-week timespans required for somatic cell reprogramming. uCP Well Plates further offered the advantage of simple multiplexing and high-content imaging capabilities, enabling high-throughput studies with minimal experimental setup.

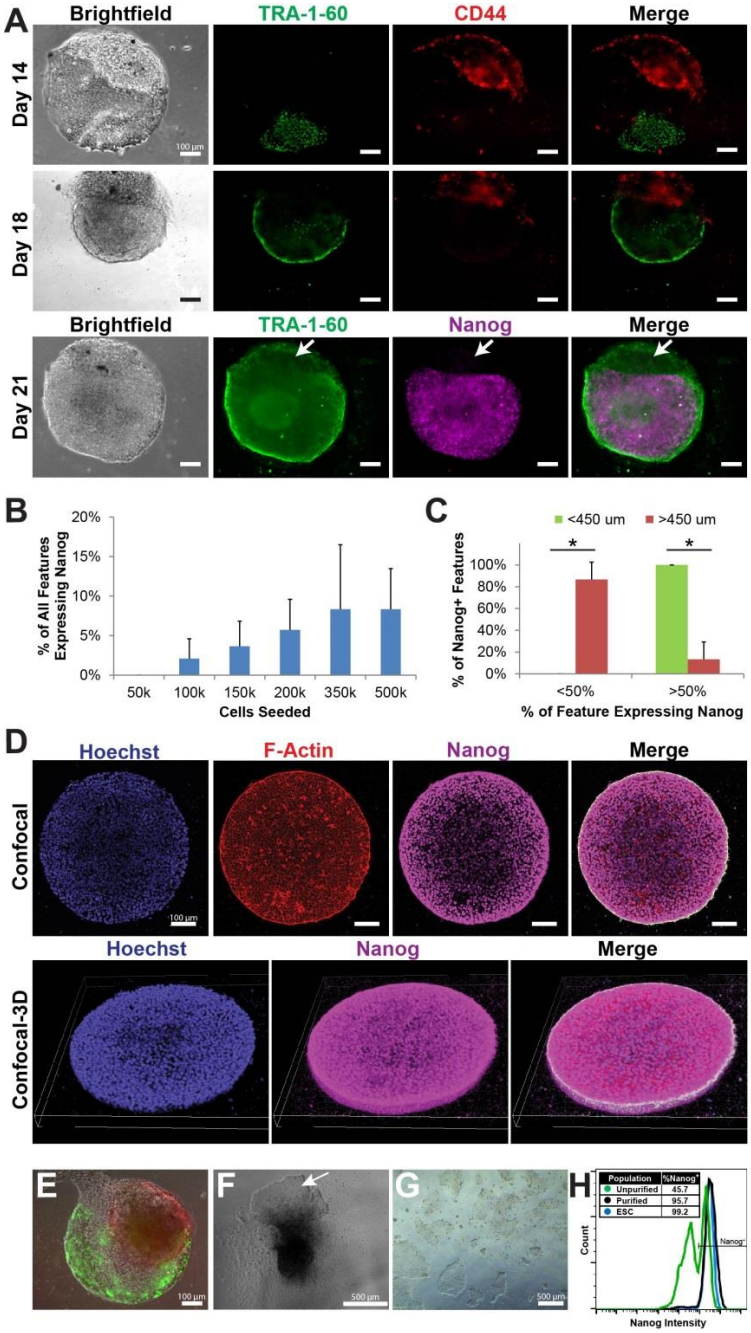


**Figure 5-1. Tracking reprogramming in microscale subpopulations using immunocytochemistry. A)** Representative images of the progression of a cell aggregate on a

μCP Well Plate through a reprogramming time course. Cells were antibody-stained live on Days 14 and 18 and fixed on Day 21 to enable Nanog labeling. **B)** Percentage of all features that express Nanog at any level based on seeding density. **C)** Percentage of Nanog-positive colonies in which ±50% of the micropattern is occupied by Nanog-expressing cells, based on radius of circular micropatterns. **D)** Confocal images of a reprogrammed cell aggregate with nearly 100% Nanog expression. **E-G)** Representative images of the derivation of pure iPSC lines from μCP Well Plates. E) Day 21 aggregate live-stained with CD44 (red) and TRA-1-60 (green) antibodies. F) Aggregate from (B) three days after picking from a μCP Well Plate. White arrow indicates expanding iPSC colony. G) DXC-independent iPSC line after one additional picking step from (G) and several passages in standard pluripotent culture conditions **H)** Flow cytometry histogram indicating the percentage of $Nanog^+$ cells before (F) and after (G) purification. *$p<0.05$*

We first assessed whether μCP Well Plates were a suitable platform for long-term reprogramming studies. The favorable high-content imaging capabilities of uCP Well Plates[54] enabled us to track large numbers of cell aggregates (>100 micropatterned features per well in a 24 well plate) at multiple time points. Reprogramming cells remained viable, attached, and constrained to the desired micropatterns throughout a four-week reprogramming time course (Figure 5-1A, Figure 5-2A). Using a previously established protocol, we labeled live reprogramming aggregates with antibodies targeting cell surface markers identifying fibroblasts (CD44) and pluripotent cells (TRA-1-60) to observe the transition of cell aggregates through intermediate reprogramming states[38,62,63]. Migration constraints provided by the micropatterned surface assured that no cells had migrated into or away from our aggregates between time points.

Cells displaying fibroblast ($CD44^+/TRA\text{-}1\text{-}60^-$), iPSC ($CD44^-/TRA\text{-}1\text{-}60^+$), and intermediate ($CD44^-/TRA\text{-}1\text{-}60^-$) expression profiles were readily detected, even within a single aggregate (Figure 5-1A, top). TRA-1-60 expression was observed as early as 14 days after factor expression. Activation of the pluripotency transcriptional network was observed by Day 21, as indicated by the presence of Nanog protein[52,64-66] (Figure 5-1A, bottom).

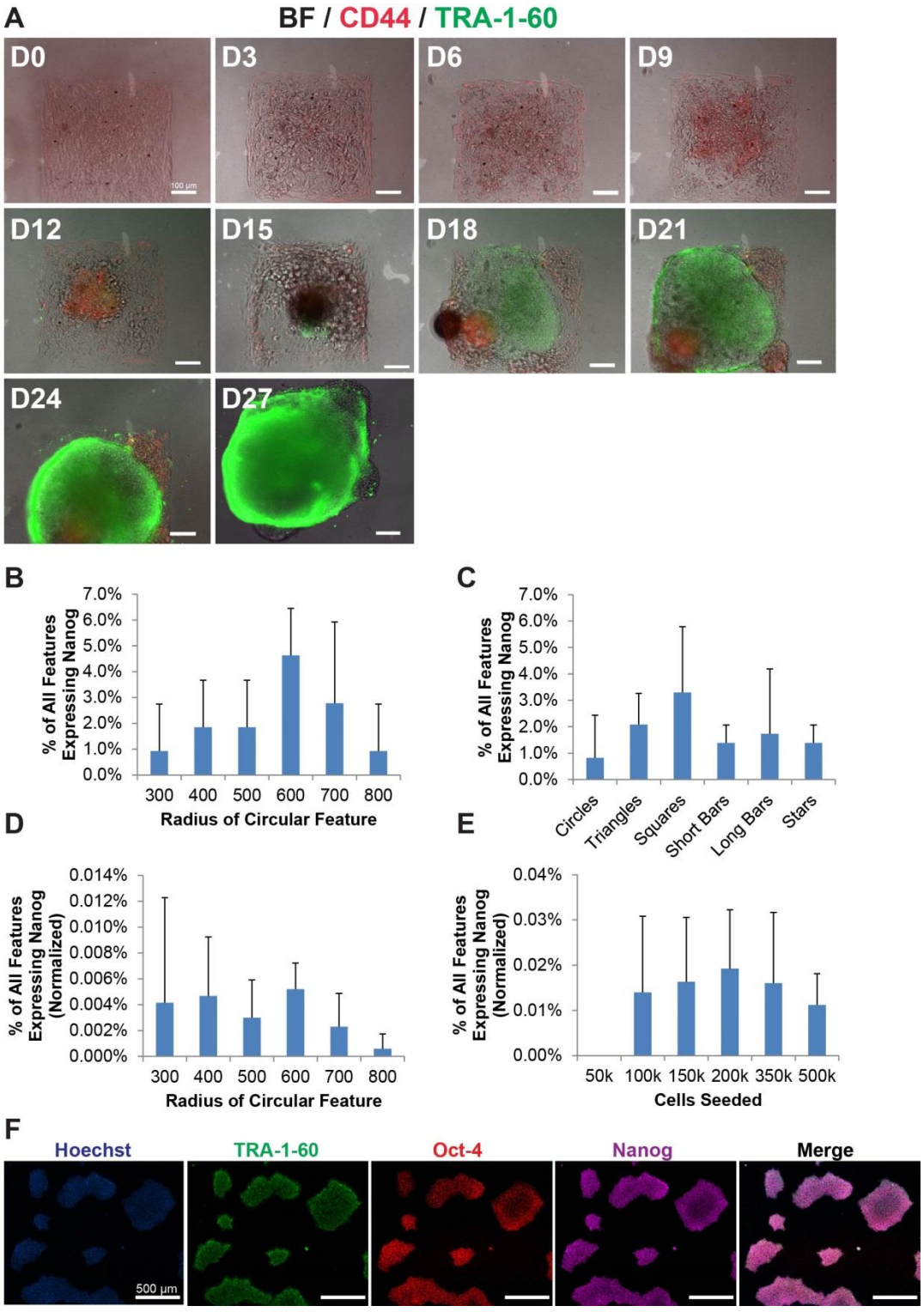


**Figure 5-2. Separation of distinct cell types via nuclear characteristics. A)** Representative nuclear and lineage marker images of human fibroblasts, ESCs, and NPCs seeded on µCP Well Plates. **B)** Score plot of PCA results separating cell types based on nuclear characteristics. **C)** Loading plot of nuclear characteristics and their relative contributions to the first two principal components.

We systematically altered the size and shape of aggregate micropatterns as well as the number of cells seeded on each micropattern in an effort to optimize the reprogramming microenvironment. We found that seeding at high cell densities increased the number of micropatterned features containing reprogrammed cells (Figure 5-1B). Micropattern size did not have a significant effect on the number of aggregates in which Nanog was detected (Figure 5-2B), but micropatterns with a radius of 300-400 μm more frequently produced cell aggregates in which greater than half of the aggregate expressed Nanog than did micropatterns with larger radii (Figure 5-1C). Micropatterns with a radius under 250 μm tended to result in aggregate detachment within the first 14 days of reprogramming (data not shown). Altering aggregate geometry had no significant effect on reprogramming (Figure 5-2C). Importantly, microenvironmental modification did not seem to affect the rate of iPSC generation, as demonstrated by constant Nanog expression rates when data is normalized to cell number per aggregate (Figure 5-2D-E). We chose circular micropatterns with a radius of 300 μm and a seeding density ≥100k per well of a 24-well plate for all further reprogramming experiments.

Nanog$^+$ cells often made up the majority of cells present at the end of a 3-4 week time course and on occasion micropatterned features containing nearly 100% Nanog$^+$ cells were detected (Figure 5-1D). Overall, reprogramming on uCP Well Plates enabled simple derivation of pure iPSC lines with minimal time and effort spent on purification. The physical separation of micropatterns from one another, combined with relatively high fractions of Nanog-expressing cells present within reprogrammed micropatterns, resulted in easy picking and isolation of reprogrammed cells (Figure 5-1E-H). However,

it was observed that picking colonies on the basis of TRA-1-60 expression often overestimated the presence of fully reprogrammed Nanog$^{+}$ cells[63,67] (Figure 5-1A, white arrows). The resulting iPSCs co-expressed all expected markers of pluripotency after several weeks of transgene-independent culture, indicating stable activation of the native pluripotency network[52] (Figure 5-2F).

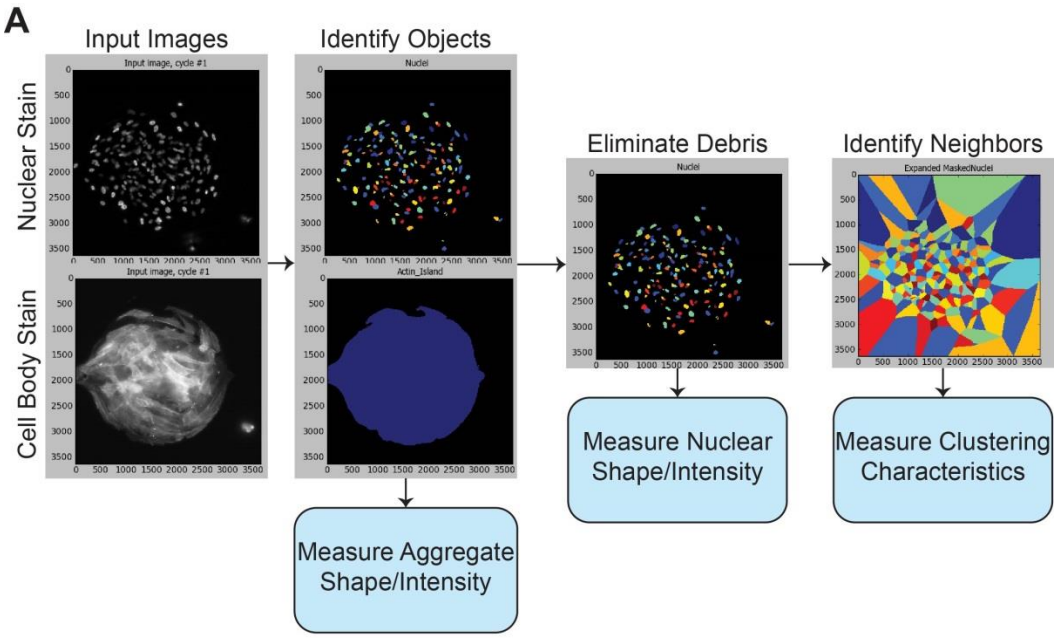


**B**

| Measurement | Description |
|---|---|
| Area | The total number of pixels within an object |
| Perimeter (Perim) | The total number of pixels around the boundary of an object |
| Mean Radius (MeanRad) | The mean distance of any pixel in the object to the closest pixel outside of the object |
| Nuclear Shape Index (NSI) | $NSI = \frac{4\pi A}{p^2}$, where A is the area and P is the perimeter of an ellipse around the object's major and minor axes[54]. NSI=1 for a perfect circle and approaches 0 with elongation. |
| Extent | The proportion of pixels in the bounding box that are also in the object: $\frac{Object\ Area}{Bounding\ Box\ Area}$ |
| Solidity (Solid) | The proportion of pixels in the convex hull that are also in the object: $\frac{Object\ Area}{Convex\ Hull\ Area}$ |
| Distance to closest neighbor (1stNeigh) | The distance to the closest object in pixels |
| Number of neighbors (#Neigh) | The total number of neighbor objects |

**Figure 5-3. CellProfiler analysis. A)** Flowchart depicting image analysis by CellProfiler Software. **B)** Table describing the eight minimal measurements used by the final PCA model.

*5.3.2 Separation of distinct cell types via measurement of nuclear attributes*

Reprogramming of human fibroblasts to an iPSC state necessitates large biophysical changes to both the cell body and nucleus which can be predictive of reprogramming outcomes[36-38]. We hypothesized that these changes could be used as a tool to track progression of reprogramming intermediates. Because high-density cell cultures on our micropatterned features made distinguishing cell borders difficult (Figure 5-3A), we focused our efforts on the nucleus.

To test our hypothesis, we first attempted to separate three distinct cell types – fibroblasts, ESCs, and neural progenitor cells (NPCs) – on the basis of their nuclear attributes alone. Pure cell lines were seeded on circular features of 300um radius and allowed to divide and fill the feature over multiple days before fixing and staining with Hoechst to label nuclei (Figure 5-4A). We utilized a previously published high-content approach to image, process, and analyze large data sets in a rapid, automated fashion[54]. CellProfiler[60] was used to identify individual nuclei within images and output a set of geometrical, intensity, and clustering measurements (Figure 5-3A). Starting with a large dataset of 32 nuclear characteristics measured by CellProfiler, we then fed these measurements into a Principal Components Analysis (PCA) model that attempts to distinguish subpopulations in a dataset by grouping similar variables into linear combinations of Principal Components (PCs), therefore reducing the dimensionality of large datasets and enabling easier visualization[68-70].

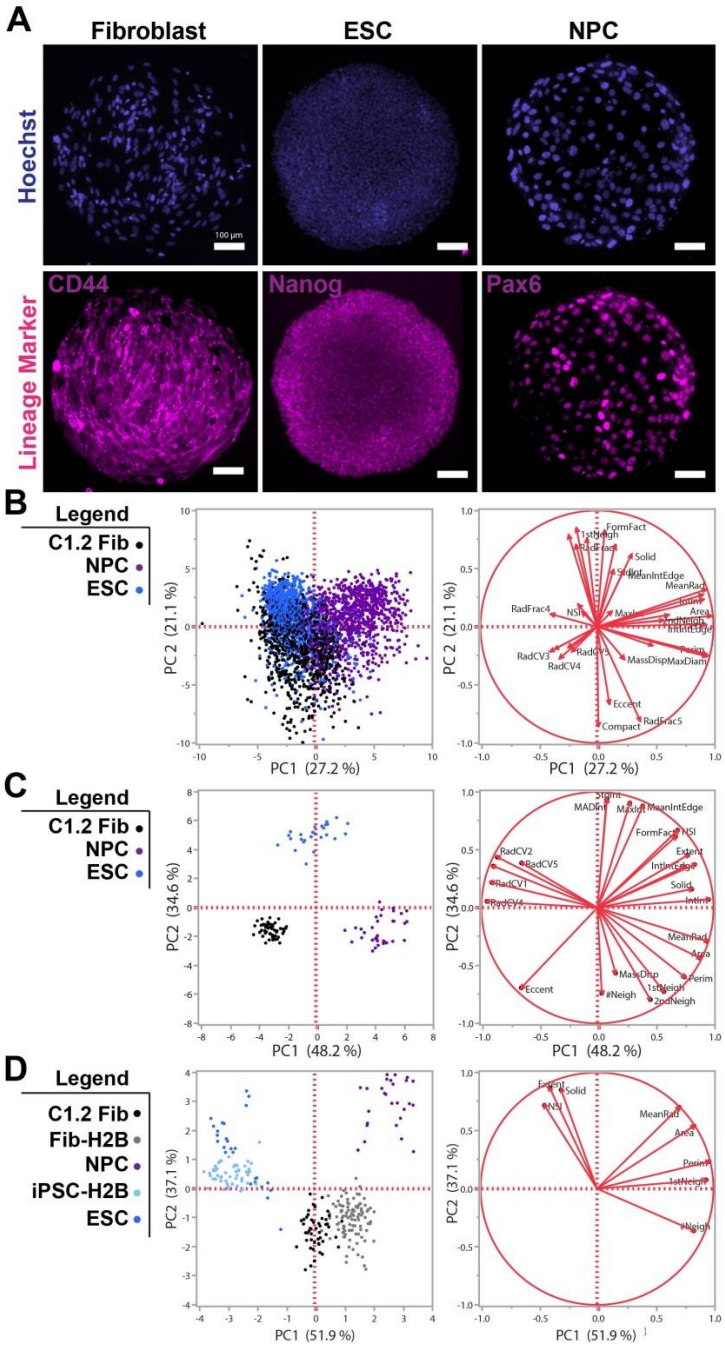


**Figure 5-4. Separation of distinct cell types via nuclear characteristics. A)** Representative confocal images of Hoechst-stained reprogramming intermediates at various time points during reprogramming. Endpoint (D21-24) aggregates were antibody-stained for Nanog expression. Dotted line encircles cells expressing Nanog. **B)** Quantification of PC values throughout the reprogramming time course. **C-D)** Three-dimensional score plots of PCA results separating reprogramming intermediates based on nuclear characteristics**.** Data for individual aggregates (C) and time point averages (D) are depicted. **E)** Loading matrix describing the relative contribution of each biophysical measurement to the first three principle components. **F)** 3D score plot depicting Day 0, Endpoint, and PSC data only. Endpoint data is color-coded to correspond to the fraction of cells within each aggregate expressing Nanog.

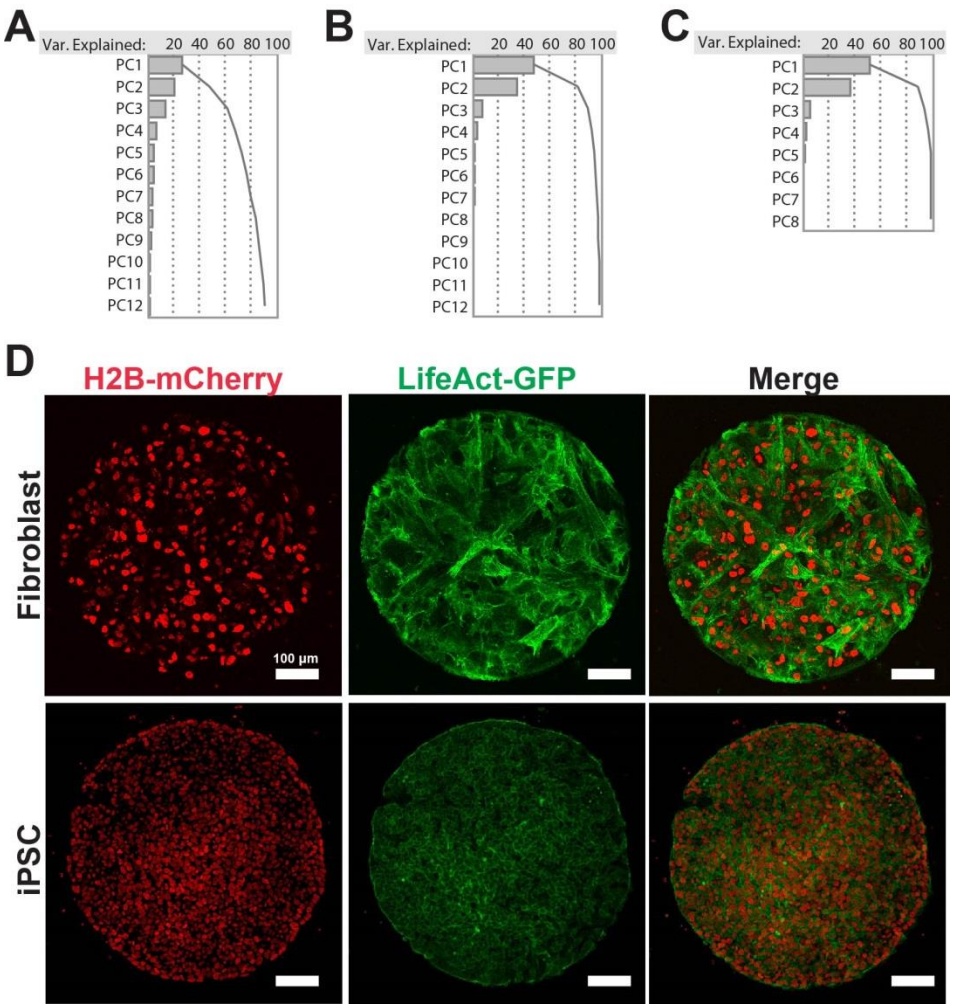


**Figure 5-5. Construction of a minimal PCA model. A-C)** Histograms depicting the variance explained by each principal component in 32-component single cell (A), 32-compenent aggregate-level (B), and eight-component aggregate level (C) PCA models. **D)** Representative confocal images of H2B-mCherry and LifeAct-GFP-expressing fibroblast and iPSC lines used to obtain nuclear measurements in Figure 2B-C.

We first attempted to analyze nuclei on an individual basis (Figure 5-4B). While this analysis was able to distinguish most NPCs from the dataset, separation of fibroblasts from iPSCs was less successful. However, averaging individual nuclear measurements on an aggregate-level basis before feeding into the model resulted in clear separation of all three cell types (Figure 5-4C). We further refined our model by reducing the input data to a set of eight essential variables (Figure 5-3B, Figure 5-4D). The first two PCs of this minimal model captured ~90% of the model variance,

compared to ~80% for the 32-variable aggregate model and only ~50% for our single-cell model (Figure 5-5A-C). Importantly, because all of these essential variables are based on biophysical properties (i.e. nuclear geometry and cell clustering) rather than fluorescent intensity they can be used with any stain or molecular tag that is able to distinguish individual nuclei. We validated the robustness of our model by confirming that different lines of the same cell type clustered together in PC space, even when using distinct nuclear labels (Hoechst stain vs. H2B-mCherry tag) (Figure 5-4D, Supp. Figure 5-5D).

*5.3.3 Tracking reprogramming via biophysical characteristics*

We next utilized our optimized PCA model to track progression of cell aggregates over a full reprogramming time course (Figure 5-6A-C). Because reprogramming latency can be variable from experiment to experiment[71], we fixed and analyzed aggregates from Days 21 and 24 ("endpoint" data) based on morphological appearance. We found that aggregates exhibited biphasic progression from fibroblast to iPSC state in the first two principal components, while PC3 captured a significant amount of model variance and progressed more linearly (Figure 5-6B, Figure 5-7A). Combining the biphasic progression in PC1 and PC2 with the linear progression of PC3 resulted in the formation of a downward 3D spiral tracing progression of cell state from fibroblast to iPSC (Figure 5-6C-D). By analyzing the loading coefficients, we found that PC1 is driven largely by variables describing nuclear shape (extent, perimeter, solidity, NSI), while changes in PC2 correspond largely to differences in nuclear size (area, mean

radius) (Figure 5-6E). In contrast, PC3 is dominated by shifts in nuclear clustering (distance to first neighbor) along with a smaller contribution from NSI.

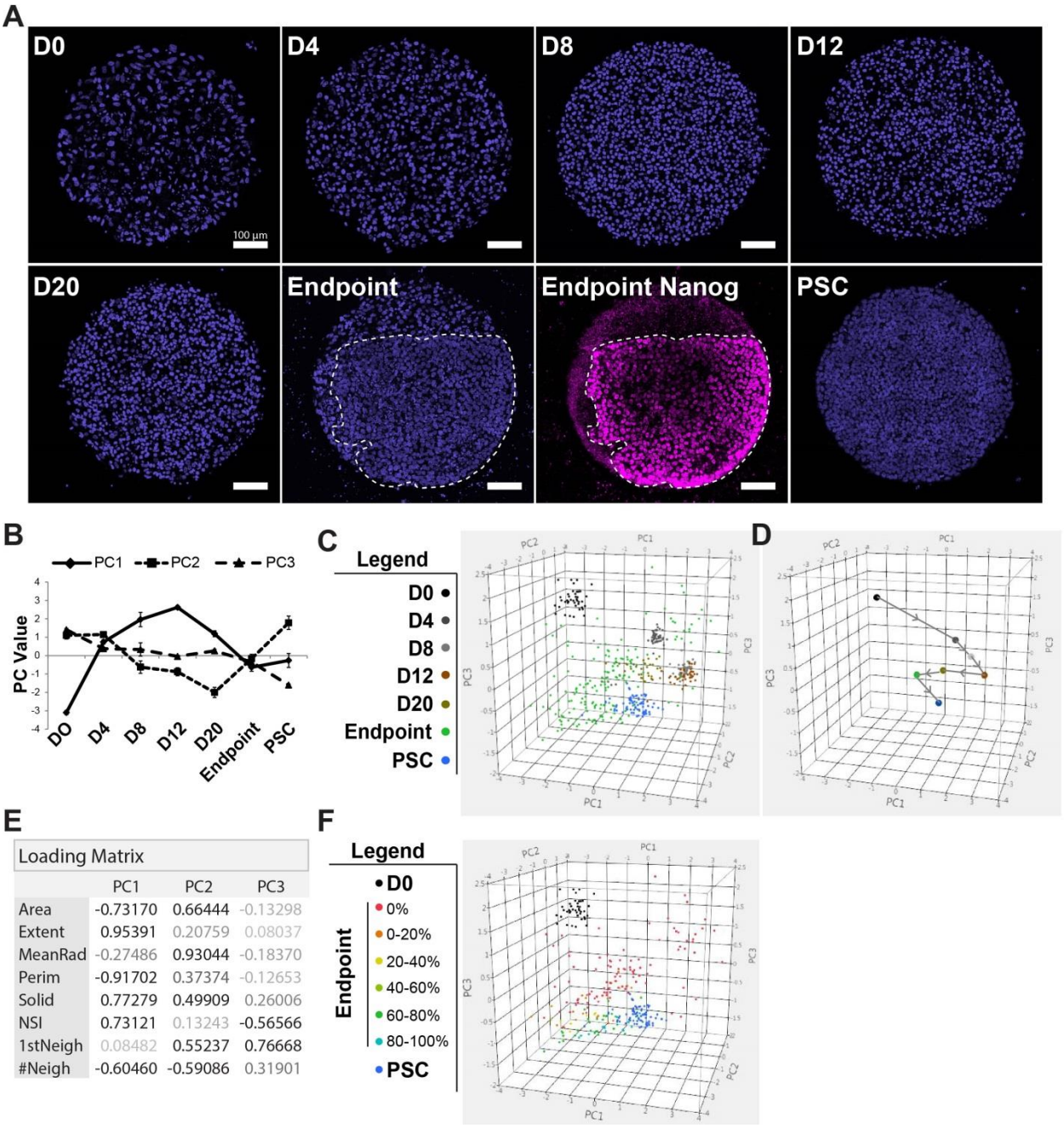


**Figure 5-6. Tracking reprogramming progression via biophysical characteristics. A)** Representative confocal images of Hoechst-stained reprogramming intermediates at various time points during reprogramming. Endpoint (D21-24) aggregates were antibody-stained for Nanog expression. Dotted line encircles cells expressing Nanog. **B)** Quantification of PC values throughout the reprogramming time course. **C-D)** Three-dimensional score plots of PCA results separating reprogramming intermediates based on nuclear characteristics**.** Data for individual

aggregates (C) and time point averages (D) are depicted. **E)** Loading matrix describing the relative contribution of each biophysical measurement to the first three principle components. **F)** 3D score plot depicting Day 0, Endpoint, and PSC data only. Endpoint data is color-coded to correspond to the fraction of cells within each aggregate expressing Nanog.

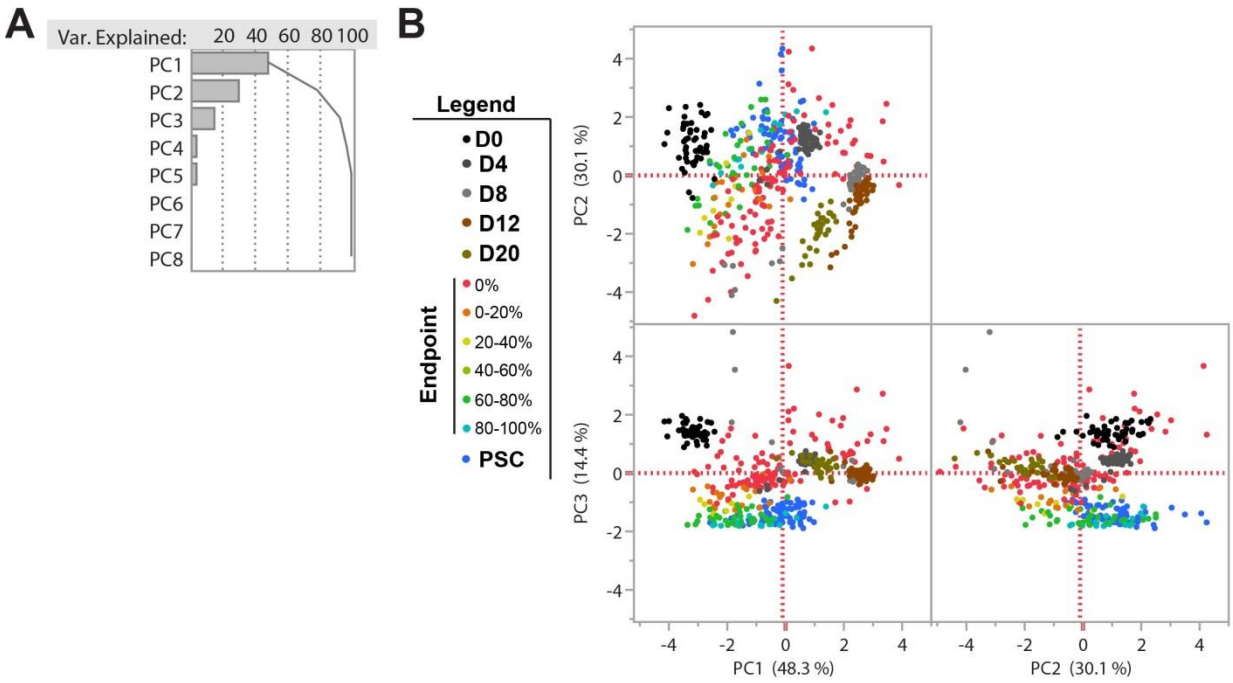


**Figure 5-7. Additional reprogramming PCA data.** Histogram depicting the variance explained by each principal component in the PCA model. **B)** Two-dimensional depictions of the PCA score plots depicted in Figure 3.

The largest shifts in PC space occur in Days 0-8, when aggregates traverse from negative to positive values in PC1. This movement corresponds temporally with the well-studied mesenchymal-to-epithelial transition (MET) that occurs within the first 10 days of reprogramming and involves dramatic shifts in cell morphology[40-42]. A clustering of time points between Days 8 and 20 follows this transition with less movement in PC space, after which non-reprogrammed aggregates ($Nanog^-$, red) are separated from successfully reprogrammed aggregates ($Nanog^+$, orange to blue-green) through shifts in PC2 and PC3 (Figure 5-6F, Figure 5-7B). Aggregates with a majority of $Nanog^+$ cells cluster closely with pure PSC lines (blue), as would be expected for fully reprogrammed iPSCs[72,73].

We also tested the utility of our model for tracking differentiation of pluripotent cells. Using the same eight input variables as in our reprogramming model, we were able to track progression of ESCs into NPCs that spontaneously formed neural rosettes over a nine day time course (Figure 5-8A-F). In comparison to reprogramming, differentiation of ESCs into NPC progressed through PC space in a much more linear fashion Figure 5-8G).

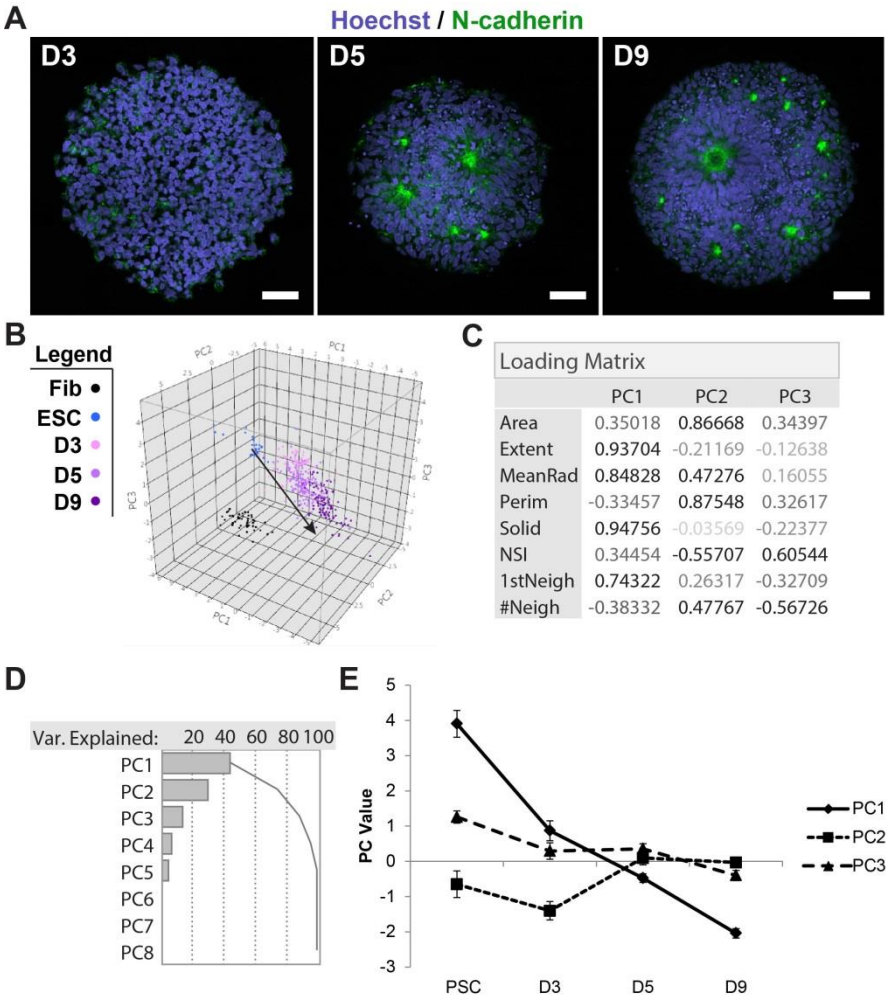


**Figure 5-8. Tracking differentiation of pluripotent cells via biophysical analysis. A)** Representative images of Day 3, 5, and 9 time points of NPC differentiation from ESCs. **B)** 3D score plot of PCA results separating differentiating intermediates based on biophysical characteristics**.** Black arrow depicts linear progression throughout differentiation. **C)** Loading matrix describing the relative contribution of each biophysical characteristic to the first three principle components. **D)** Histogram depicting the variance explained by each principal component in the PCA model. **E)** PC values plotted over the differentiation time course.

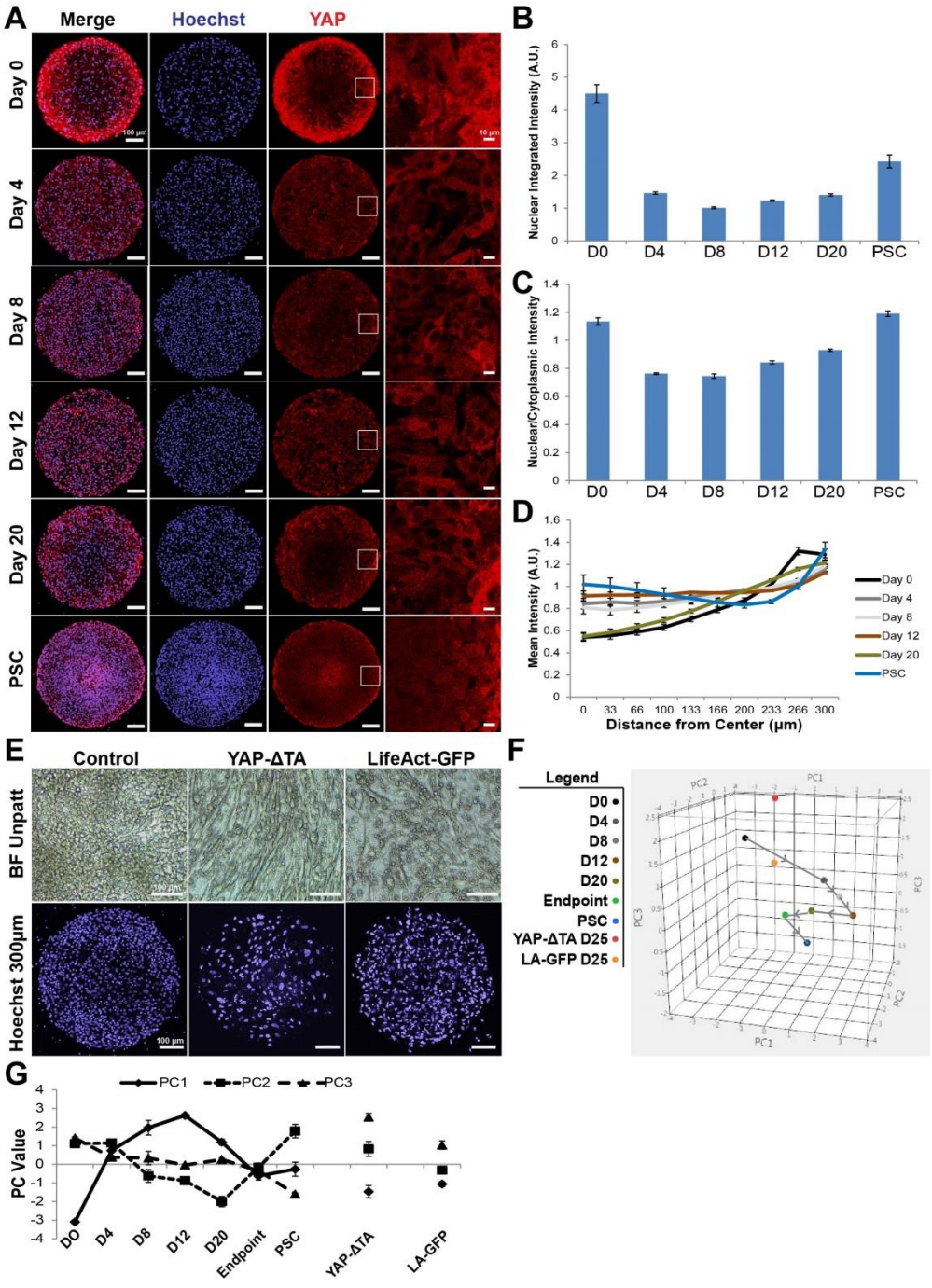


**Figure 5-9. YAP dynamics during reprogramming. A)** Representative confocal images of nuclei and YAP at various time points during reprogramming. Rightmost row depicts magnified view of YAP stains outlined in white boxes. **B)** Quantification of YAP nuclear integrated intensity. **C)** Quantification of the ratio of YAP nuclear to cytoplasmic intensity. **D)** Quantification of YAP intensity as a function of distance from the center of each cell aggregate. **E)** Representative images of control, YAP-ΔTA, and LA-GFP infected C1.2 cells on tissue culture plastic after 19 days of reprogramming factor expression. **F)** 3D time point averaged score plot as in Figure 3D, with Day 25 samples of YAP-ΔTA and LA-GFP aggregates reprogrammed on μCP Well Plates. **G)** Quantification of PC values in (F).

*5.3.4 Role of YAP during reprogramming*

We sought to establish a molecular driver for the biphasic progression observed in PC1 and PC2 during reprogramming progression. YAP/TAZ is an important mechanotransductor[26-29], is crucial for stem cell maintenance[26,33-35], and is also an effector of EMT[30-32]. We found that both YAP expression and nuclear localization displayed biphasic patterns during reprogramming (Figure 5-9A-D). In fibroblasts, YAP protein was expressed at high levels and was evenly spread throughout the nucleus and cytoplasm. After the onset of reprogramming, however, YAP was quickly excluded from the nucleus and expression levels began to drop. From Days 8-20, YAP expression rose and began translocating back into the nucleus, approaching a profile similar to that of iPSCs (Figure 5-9B-C). Additionally, fibroblasts, D20 intermediates, and iPSCs exhibited increased YAP expression near the perimeter of circular micropatterns, which would be expected where mechanical stress is high[27,28]. D4-D12 intermediates, however, had much more evenly distributed YAP levels (Figure 5-9D). When added as an input into our PCA model, the distinct patterns of YAP localization throughout reprogramming resulted in tighter clustering of aggregates within each time point and better separation of time points in the first two principal components (Figure 5-10A-B), demonstrating that simultaneous incorporation of both biophysical and protein expression data can enhance computational models of reprogramming .

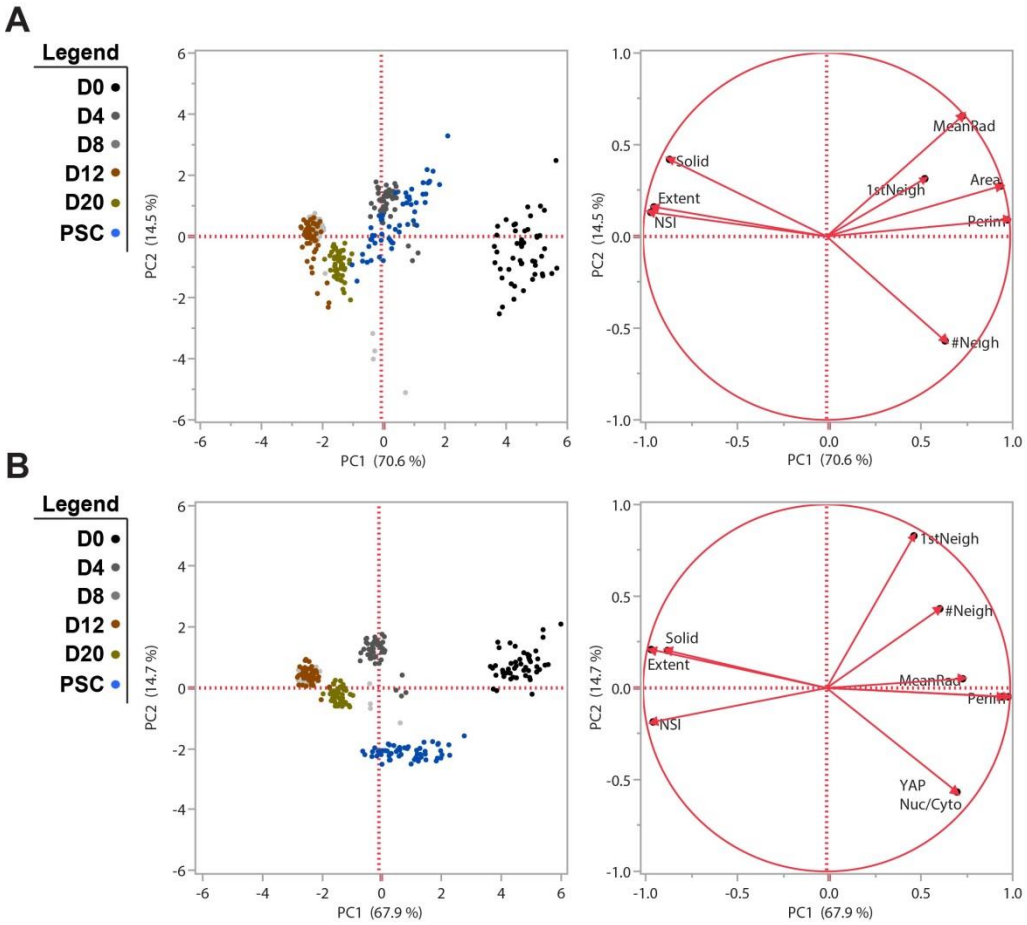


**Figure 5-10. Incorporating expression data into a biophysical PCA model. A-B)** Score and loading plots for PC1 and PC2 over a reprogramming time course. PCA was run excluding (A) and including (B) YAP localization data.

Because YAP is known to induce EMT[30] and the presence of YAP in the nucleus decreases dramatically during early time points in which the reverse process (MET) is expected to occur, we hypothesized that YAP may play an inhibitory role to MET during the early stages of reprogramming. We therefore transduced cell cultures with a hyperactive form of YAP (YAP-ΔTA[74]) prior to reprogramming induction and observed its effects on MET. In the same experiment we included cells transduced with a LifeAct-GFP (LA-GFP) construct[75], which we had previously observed inhibited MET in C1.2 cells (data not shown). Strikingly, even after 25 days of reprogramming factor expression, cells transduced with YAP-ΔTA resembled elongated fibroblasts on tissue

culture plastic, indicating the absence of MET, while LA-GFP transduced cells were more heterogeneous in cell morphology (Figure 5-9E). We reasoned that when reprogrammed on uCP Well Plates and analyzed with our biophysical PCA model, these aggregates should stall near the top end of the reprogramming spiral in PC space, near aggregates that had not yet undergone MET. After performing this analysis we found that YAP-ΔTA aggregates progressed slightly down the reprogramming spiral in the first two principal components while lying above even fibroblasts in PC1. In contrast, LA-GFP aggregates clustered between Day 0 and Day 8 aggregates in all three principal components (Figure 5-9F-G).

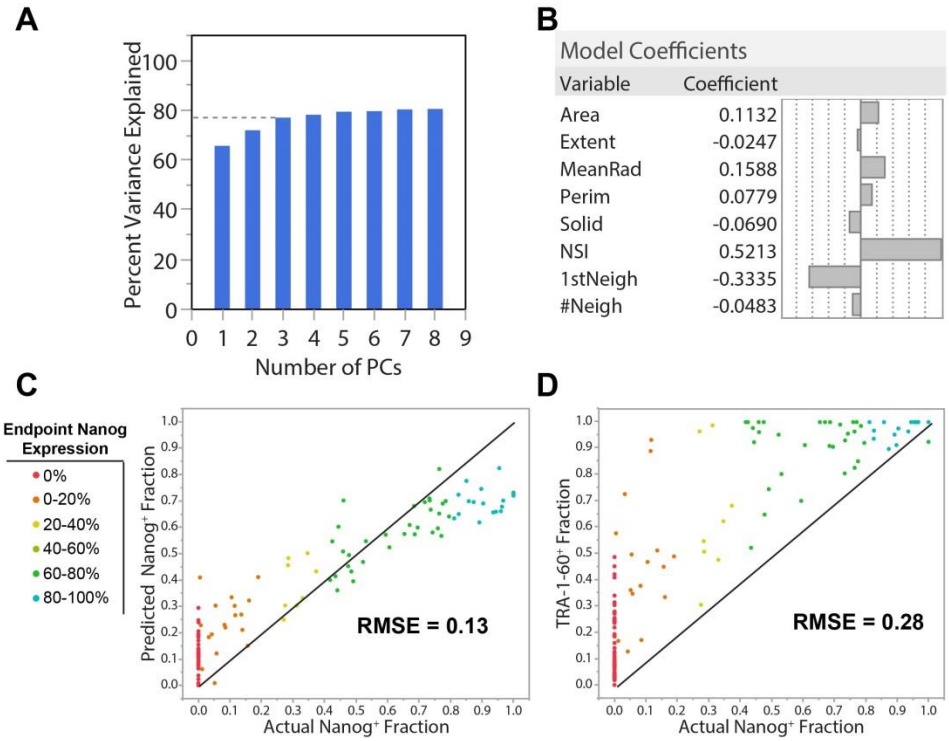


**Figure 5-11. Biophysical characteristics predict reprogramming efficiency. A)** Histogram depicting the variance explained by each principal component. The first three PCs were used to construct our model. **B)** Histogram depicting loading regression coefficients for each nuclear characteristic. **C)** Actual Nanog-positive fraction for each cell aggregate plotted against Nanog-positive fraction predicted by the three-component PLSR model. Black line, predicted=actual. **D)** Actual Nanog-positive fraction for each cell aggregate plotted against Nanog-positive fraction predicted by assuming all cells that express TRA-1-60 also express Nanog. Black line, predicted=actual.

*5.3.5 Predicting reprogramming efficiency via biophysical characteristics*

If analysis of biophysical properties can separate reprogramming intermediates from one another, we then asked whether these measurements could predict which aggregates were successfully reprogrammed at the end of a reprogramming time course. We created a partial least squares regression (PLSR) model using the eight minimal variables from our PCA model as inputs and the fraction of each aggregate expressing Nanog as the output. The resulting model explained ~78% of the variance in endpoint reprogramming cultures using only three PCs and relied heavily on NSI and distance to first neighbor measurements (Figure 5-11A-B). The model was highly predictive of reprogramming efficiency, with a root mean square error of prediction (RMSE) of 0.13, compared to an RMSE of 0.28 when using TRA-1-60 expression as a predictor of Nanog expression (Figure 5-11C-D). It is interesting to note that – with respect to NSI, distance to nearest neighbor, and YAP localization – cells contained in 300 μm micropatterns display characteristics more closely resembling iPSCs at both early and late time points than do cells cultured on unpatterned surfaces (Figure 5-12A-C).

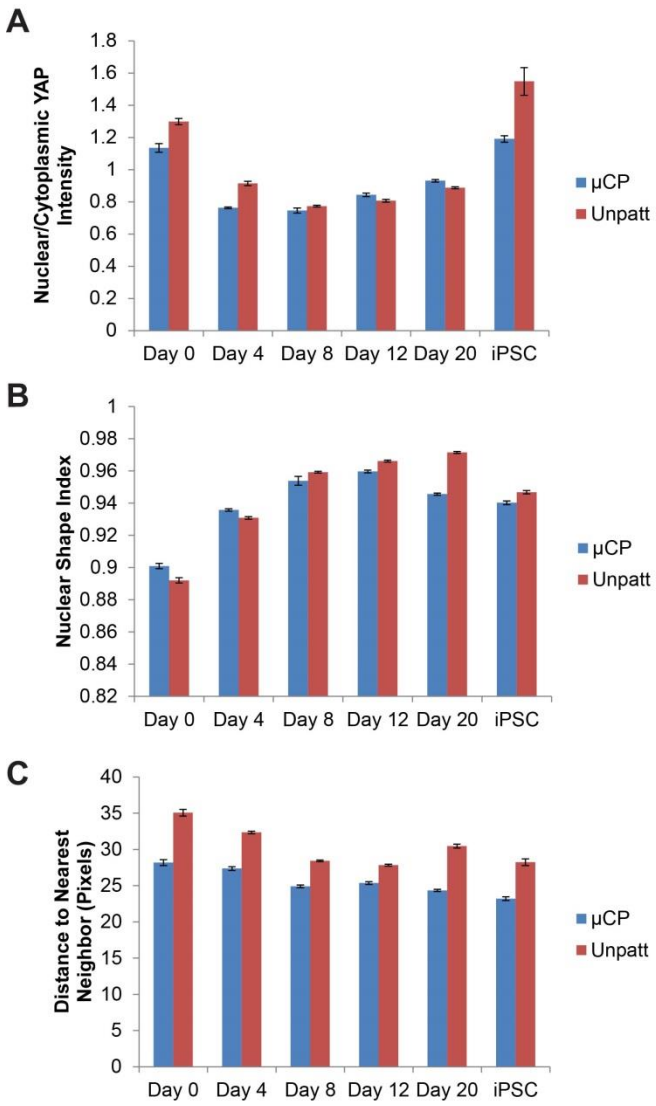


**Figure 5-12. µCP Well Plates encourage iPSC-like characteristics in reprogramming cells. A-C)** Comparison of nuclear to cytoplasmic YAP intensity (A), Nuclear shape index (B), and distance to nearest neighbor (C) over a reprogramming time course between µCP Well Plates and unpatterned glass.

## 5.4 Discussion

As our understanding of the complex interplay between cells and their microenvironment expands, the need to design and execute experiments with tight microenvironmental control in mind also grows. Here, we utilized the µCP Well Plate as a tool to regulate the reprogramming microenvironment, but also took advantage of the

multiplexing and imaging capabilities inherent in the µCP Well Plate platform. After showing that the µCP Well Plate is amenable to tracking reprogramming intermediates *in situ* over a period of up to four weeks, we wondered if we could leverage the µCP Well Plate's capability for high-content analysis into a tool for tracking reprogramming progression in an orthogonal manner to more traditional studies of transcript or protein expression. We found that combining relatively simple computational models with a set of only eight nuclear biophysical characteristics allowed us to clearly distinguish and track cell aggregates throughout a full reprogramming time course, as well as accurately predict the reprogramming efficiency of these aggregates.

In agreement with previous studies of MET during early reprogramming, pronounced biophysical changes took place in reprogramming aggregates within the first eight days of reprogramming factor expression[40-42]. Aggregates from Days 8-20 clustered near each other with relatively little movement, after which a final shift through PC space separated unsuccessfully reprogrammed aggregates from those bearing $Nanog^{+}$ cells. These shifts align closely with those described from transcript and protein expression studies[42-44], suggesting that biophysical analysis can be used as a complementary method to study reprogramming progression.

The biphasic progression of reprogramming aggregates through PC1 and PC2 led us to investigate the mechanotranduction molecule YAP as a potential effector of these biophysical shifts. YAP is essential for maintenance of pluripotency, and YAP overexpression has been previously reported to enhance reprogramming efficiency[33]. The data presented here suggests that YAP's role in reprogramming is more complex and time-dependent. We found that YAP exhibited biphasic expression and localization

patterns during reprogramming. Notably, the presence of YAP in the nucleus decreased dramatically over the first eight days of reprogramming, suggesting that YAP's activity as a transcriptional co-activator in the nucleus may inhibit MET, which aligns with the well-studied role of YAP as an oncogene and activator of EMT[30-32]. Previous studies have reported that both EMT and MET can occur during reprogramming[76]. Although more investigation into the relationship between YAP and MET in the context of reprogramming is needed, our observation of biphasic YAP expression and localization is consistent with this model.

When combined with a linear progression in PC3, the biphasic nature of the first two principal components created a three-dimensional spiral through PC space, which we used as a tool to infer the progress of reprogramming intermediates from a fibroblast phenotype to an ultimate iPSC identity. We found that cells expressing a hyperactive YAP protein or morphologically resembled fibroblasts even after 25 days of reprogramming factor expression, arguing for an inhibitory role for YAP in MET. In fact, YAP-ΔTA aggregates lied above even fibroblasts in PC3, indicating that they became slightly less clustered over time. LifeAct-GFP cells appeared to begin but not complete MET, consistent with their varied morphology on tissue culture plastic. This result would be consistent with an inhibitory role of LifeAct-GFP in cytoskeletal remodeling during MET, although this effect has not been observed in the literature[77]. Thus, our biophysical models provide a new method to identify so-called "roadblocks" that stall reprogramming progression[39,67,78] and to determine in what stage of reprogramming they reside.

Finally, the same eight nuclear attributes utilized to track reprogramming progression were used to create a PLSR model that was more highly predictive of aggregate reprogramming efficiency than expression of the classical reprogramming marker TRA-1-60. TRA-1-60 expression is activated prior to Nanog during reprogramming[63], and many cells that express TRA-1-60 never transition to a fully pluripotent state[67]. While this would be expected to result in overestimation of reprogramming efficiency, it is possible that TRA-1-60 expression would be more predictive of reprogramming outcomes if analyzed at a single-cell level which eliminated confounding variables such as autofluorescence. However, pluripotent cells are notoriously dependent on cell-cell contacts[79] and there may be inherent advantages in analyzing reprogramming outcomes on an aggregate level.

Reprogramming on micropatterns frequently resulted in relatively high-purity iPSC aggregates. Inconsistent stem cell differentiation has previously been traced back to variations in cell shape inherent in standard cell culture methods[6,25], and constraining single cells to uniform micropatterns greatly reduces the intrinsic cell-to-cell variability of mRNA transcript abundance[22]. Combined with the current results indicating that circular micropatterns encourage more iPSC-like profiles of nuclear attributes than unpatterned culture surfaces, these data suggest that constraining reprogramming aggregates into defined geometries may also enhance reprogramming.

## 5.5 Conclusions

Overall, we have utilized a cell culture platform allowing for high-content imaging and highly defined microenvironments to introduce a novel method for the study of human cellular transitions. The models described here can easily be further informed

with gene expression data if desired, but require just one of many available (and inexpensive) nuclear labels to gather eight biophysical measurements of individual nuclei within cell aggregates. These measurements are then fed into models that describe transitions in both reprogramming and differentiation. The resulting biophysical models mirror shifts described by more labor-intensive and costly transcript or protein expression studies, suggesting that biophysical analysis can be an effective orthogonal and complementary approach to more traditional expression-based studies of human cell behavior.

## References


1 Iskratsch, T., Wolfenson, H. & Sheetz, M. P. Appreciating force and shape [mdash] the rise of mechanotransduction in cell biology. *Nature Reviews Molecular Cell Biology* (2014).

2 Bratt-Leal, A. M., Carpenedo, R. L. & McDevitt, T. C. Engineering the embryoid body microenvironment to direct embryonic stem cell differentiation. *Biotechnology progress* **25**, 43-51 (2009).

3 Hendrix, M. J. *et al.* Reprogramming metastatic tumour cells with embryonic microenvironments. *Nat Rev Cancer* **7**, 246-255 (2007).

4 Guilak, F. *et al.* Control of stem cell fate by physical interactions with the extracellular matrix. *Cell stem cell* **5**, 17-26 (2009).

5 Engler, A. J., Sen, S., Sweeney, H. L. & Discher, D. E. Matrix elasticity directs stem cell lineage specification. *Cell* **126**, 677-689 (2006).

6 McBeath, R., Pirone, D. M., Nelson, C. M., Bhadriraju, K. & Chen, C. S. Cell shape, cytoskeletal tension, and RhoA regulate stem cell lineage commitment. *Developmental cell* **6**, 483-495 (2004).

7 Saha, K. *et al.* Substrate modulus directs neural stem cell behavior. *Biophysical journal* **95**, 4426-4438 (2008).

8 Lee, S. E., Kamm, R. D. & Mofrad, M. R. Force-induced activation of talin and its possible role in focal adhesion mechanotransduction. *Journal of biomechanics* **40**, 2096-2106 (2007).

9 Vogel, V. & Sheetz, M. Local force and geometry sensing regulate cell functions. *Nature reviews molecular cell biology* **7**, 265-275 (2006).

10 Sawada, Y. *et al.* Force sensing by mechanical extension of the Src family kinase substrate p130Cas. *Cell* **127**, 1015-1026 (2006).

11 Mitra, S. K., Hanson, D. A. & Schlaepfer, D. D. Focal adhesion kinase: in command and control of cell motility. *Nature reviews Molecular cell biology* **6**, 56-68 (2005).

12 Giancotti, F. G. & Ruoslahti, E. Integrin signaling. *Science* **285**, 1028-1033 (1999).

13 Maniotis, A. J., Chen, C. S. & Ingber, D. E. Demonstration of mechanical connections between integrins, cytoskeletal filaments, and nucleoplasm that stabilize nuclear structure. *Proceedings of the National Academy of Sciences* **94**, 849-854 (1997).

14 Starr, D. A. & Fridolfsson, H. N. Interactions between nuclei and the cytoskeleton are mediated by SUN-KASH nuclear-envelope bridges. *Annual review of cell and developmental biology* **26**, 421 (2010).

15 Toh, K. C., Ramdas, N. M. & Shivashankar, G. Actin cytoskeleton differentially alters the dynamics of lamin A, HP1α and H2B core histone proteins to remodel chromatin condensation state in living cells. *Integrative Biology* **7**, 1309-1317 (2015).

16 Versaevel, M. *et al.* Super-resolution microscopy reveals LINC complex recruitment at nuclear indentation sites. *Scientific reports* **4** (2014).

17 Kim, D.-H. & Wirtz, D. Cytoskeletal tension induces the polarized architecture of the nucleus. *Biomaterials* **48**, 161-172 (2015).

18 Bronshtein, I. *et al.* Loss of lamin A function increases chromatin dynamics in the nuclear interior. *Nature communications* **6** (2015).

19 Guelen, L. *et al.* Domain organization of human chromosomes revealed by mapping of nuclear lamina interactions. *Nature* **453**, 948-951 (2008).

20 Peric-Hupkes, D. *et al.* Molecular maps of the reorganization of genome-nuclear lamina interactions during differentiation. *Molecular cell* **38**, 603-613 (2010).

21 Kind, J. *et al.* Genome-wide maps of nuclear lamina interactions in single human cells. *Cell* **163**, 134-147 (2015).

22 Battich, N., Stoeger, T. & Pelkmans, L. Control of transcript variability in single mammalian cells. *Cell* **163**, 1596-1610 (2015).

23 Snijder, B. & Pelkmans, L. Origins of regulated cell-to-cell variability. *Nature Reviews Molecular Cell Biology* **12**, 119-125 (2011).

24 Snijder, B. *et al.* Population context determines cell-to-cell variability in endocytosis and virus infection. *Nature* **461**, 520-523 (2009).

25 Kilian, K. A., Bugarija, B., Lahn, B. T. & Mrksich, M. Geometric cues for directing the differentiation of mesenchymal stem cells. *Proceedings of the National Academy of Sciences* **107**, 4872-4877 (2010).

26 Dupont, S. *et al.* Role of YAP/TAZ in mechanotransduction. *Nature* **474**, 179-183 (2011).

27 Low, B. C. *et al.* YAP/TAZ as mechanosensors and mechanotransducers in regulating organ size and tumor growth. *FEBS letters* **588**, 2663-2670 (2014).

28 Aragona, M. *et al.* A mechanical checkpoint controls multicellular growth through YAP/TAZ regulation by actin-processing factors. *Cell* **154**, 1047-1059 (2013).

29 Li, Z. *et al.* Structural insights into the YAP and TEAD complex. *Genes & development* **24**, 235-240 (2010).

30 Zhao, B. *et al.* TEAD mediates YAP-dependent gene induction and growth control. *Genes & development* **22**, 1962-1971 (2008).

31 Xie, Q. *et al.* YAP/TEAD–Mediated Transcription Controls Cellular Senescence. *Cancer research* **73**, 3615-3624 (2013).

32 Liu-Chittenden, Y. *et al.* Genetic and pharmacological disruption of the TEAD–YAP complex suppresses the oncogenic activity of YAP. *Genes & development* **26**, 1300-1305 (2012).

33 Lian, I. *et al.* The role of YAP transcription coactivator in regulating stem cell self-renewal and differentiation. *Genes & development* **24**, 1106-1118 (2010).

34 Musah, S. *et al.* Substratum-induced differentiation of human pluripotent stem cells reveals the coactivator YAP is a potent regulator of neuronal specification. *Proceedings of the National Academy of Sciences* **111**, 13805-13810 (2014).

35 Hsiao, C. *et al.* Human pluripotent stem cell culture density modulates YAP signaling. *Biotechnology journal* (2016).

36 Smith, Z. D., Nachman, I., Regev, A. & Meissner, A. Dynamic single-cell imaging of direct reprogramming reveals an early specifying event. *Nature biotechnology* **28**, 521-526 (2010).

37 Mattout, A., Biran, A. & Meshorer, E. Global epigenetic changes during somatic cell reprogramming to iPS cells. *Journal of molecular cell biology* **3**, 341-350 (2011).

38 Cordie, T. *et al.* Nanofibrous electrospun polymers for reprogramming human cells. *Cellular and Molecular Bioengineering* **7**, 379-393 (2014).

39 Sakurai, K. *et al.* Kinome-wide functional analysis highlights the role of cytoskeletal remodeling in somatic cell reprogramming. *Cell stem cell* **14**, 523-534 (2014).

40 Li, R. *et al.* A mesenchymal-to-epithelial transition initiates and is required for the nuclear reprogramming of mouse fibroblasts. *Cell stem cell* **7**, 51-63 (2010).

41 Samavarchi-Tehrani, P. *et al.* Functional genomics reveals a BMP-driven mesenchymal-to-epithelial transition in the initiation of somatic cell reprogramming. *Cell stem cell* **7**, 64-77 (2010).

42 Liao, B. *et al.* MicroRNA cluster 302–367 enhances somatic cell reprogramming by accelerating a mesenchymal-to-epithelial transition. *Journal of Biological Chemistry* **286**, 17359-17364 (2011).

43 Gingold, J. A. *et al.* A genome-wide RNAi screen identifies opposing functions of Snai1 and Snai2 on the Nanog dependency in reprogramming. *Molecular cell* **56**, 140-152 (2014).

44 Koche, R. P. *et al.* Reprogramming factor expression initiates widespread targeted chromatin remodeling. *Cell stem cell* **8**, 96-105 (2011).

45 Caiazzo, M. *et al.* Defined three-dimensional microenvironments boost induction of pluripotency. *Nature materials* (2016).

46 Choi, B. *et al.* Stiffness of Hydrogels Regulates Cellular Reprogramming Efficiency Through Mesenchymal-to-Epithelial Transition and Stemness Markers. *Macromolecular bioscience* (2015).

47 Downing, T. L. *et al.* Biophysical regulation of epigenetic state and cell reprogramming. *Nature materials* **12**, 1154-1162 (2013).

48 Hansson, J. *et al.* Highly coordinated proteome dynamics during reprogramming of somatic cells to pluripotency. *Cell reports* **2**, 1579-1592 (2012).

49 Polo, J. M. *et al.* A molecular roadmap of reprogramming somatic cells into iPS cells. *Cell* **151**, 1617-1632 (2012).

50 Wang, Y. *et al.* A transcriptional roadmap to the induction of pluripotency in somatic cells. *Stem Cell Reviews and Reports* **6**, 282-296 (2010).

51 Mikkelsen, T. S. *et al.* Dissecting direct reprogramming through integrative genomic analysis. *Nature* **454**, 49-55 (2008).

52 Buganim, Y. *et al.* Single-cell expression analyses during cellular reprogramming reveal an early stochastic and a late hierarchic phase. *Cell* **150**, 1209-1222 (2012).

53 Zunder, E. R., Lujan, E., Goltsev, Y., Wernig, M. & Nolan, G. P. A Continuous Molecular Roadmap to iPSC Reprogramming through Progression Analysis of Single-Cell Mass Cytometry. *Cell Stem Cell* **16**, 323-337 (2015).

54 Harkness, T. *et al.* High-content imaging with micropatterned multiwell plates reveals influence of cell geometry and cytoskeleton on chromatin dynamics. *Biotechnology journal* **10**, 1555-1567 (2015).

55 Hockemeyer, D. *et al.* A drug-inducible system for direct reprogramming of human somatic cells to pluripotency. *Cell stem cell* **3**, 346-353 (2008).

56 Chen, G. *et al.* Chemically defined conditions for human iPSC derivation and culture. *Nature methods* **8**, 424-429 (2011).

57 Beers, J. *et al.* Passaging and colony expansion of human pluripotent stem cells by enzyme-free dissociation in chemically defined culture conditions. *Nature protocols* **7**, 2029-2040 (2012).

58 Lippmann, E. S., Estevez-Silva, M. C. & Ashton, R. S. Defined human pluripotent stem cell culture enables highly efficient neuroepithelium derivation without small molecule inhibitors. *Stem Cells* **32**, 1032-1042 (2014).

59 Sha, J., Lippmann, E. S., McNulty, J., Ma, Y. & Ashton, R. S. Sequential Nucleophilic Substitutions Permit Orthogonal Click Functionalization of Multicomponent PEG Brushes. *Biomacromolecules* **14**, 3294-3303 (2013).

60 Carpenter, A. E. *et al.* CellProfiler: image analysis software for identifying and quantifying cell phenotypes. *Genome biology* **7**, R100 (2006).

61 Kleinman, H. K. & Martin, G. R. in *Seminars in cancer biology.* 378-386 (Elsevier).

62 Quintanilla, R. H., Jr., Asprer, J. S. T., Vaz, C., Tanavde, V. & Lakshmipathy, U. CD44 Is a Negative Cell Surface Marker for Pluripotent Stem Cell Identification during Human Fibroblast Reprogramming. *PLoS ONE* **9**, doi:10.1371/journal.pone.0085419 (2014).

63 Chan, E. M. *et al.* Live cell imaging distinguishes bona fide human iPS cells from partially reprogrammed cells. *Nature biotechnology* **27**, 1033-1037 (2009).

64 Pan, G. & Thomson, J. A. Nanog and transcriptional networks in embryonic stem cell pluripotency. *Cell research* **17**, 42-49 (2007).

65 Loh, Y.-H. *et al.* The Oct4 and Nanog transcription network regulates pluripotency in mouse embryonic stem cells. *Nature genetics* **38**, 431-440 (2006).

66 Kim, J., Chu, J., Shen, X., Wang, J. & Orkin, S. H. An extended transcriptional network for pluripotency of embryonic stem cells. *Cell* **132**, 1049-1061 (2008).

67 Tanabe, K., Nakamura, M., Narita, M., Takahashi, K. & Yamanaka, S. Maturation, not initiation, is the major roadblock during reprogramming toward pluripotency from human fibroblasts. *Proceedings of the National Academy of Sciences* **110**, 12172-12179 (2013).

68 Jensen, K. J. & Janes, K. A. Modeling the latent dimensions of multivariate signaling datasets. *Physical biology* **9**, 045004 (2012).

69 Miller-Jensen, K., Janes, K. A., Brugge, J. S. & Lauffenburger, D. A. Common effector processing mediates cell-specific responses to stimuli. *Nature* **448**, 604-608 (2007).

70 Wold, S., Esbensen, K. & Geladi, P. Principal component analysis. *Chemometrics and intelligent laboratory systems* **2**, 37-52 (1987).

71 Hanna, J. *et al.* Direct cell reprogramming is a stochastic process amenable to acceleration. *Nature* **462**, 595-601 (2009).

72 Choi, J. *et al.* A comparison of genetically matched cell lines reveals the equivalence of human iPSCs and ESCs. *Nature biotechnology* (2015).

73 Bock, C. *et al.* Reference Maps of human ES and iPS cell variation enable high-throughput characterization of pluripotent cell lines. *Cell* **144**, 439-452 (2011).

74 Zhang, X., Grusche, F. A. & Harvey, K. F. Control of tissue growth and cell transformation by the Salvador/Warts/Hippo pathway. *PloS one* **7**, e31994 (2012).

75 Riedl, J. *et al.* Lifeact: a versatile marker to visualize F-actin. *Nature methods* **5**, 605-607 (2008).

76 Liu, X. *et al.* Sequential introduction of reprogramming factors reveals a time-sensitive requirement for individual factors and a sequential EMT–MET mechanism for optimal reprogramming. *Nature cell biology* **15**, 829-838 (2013).

77 Riedl, J. *et al.* Lifeact mice for studying F-actin dynamics. *Nature methods* **7**, 168-169 (2010).

78 Chantzoura, E. *et al.* Reprogramming Roadblocks Are System Dependent. *Stem cell reports* **5**, 350-364 (2015).

79 Chen, G., Hou, Z., Gulbranson, D. R. & Thomson, J. A. Actin-myosin contractility is responsible for the reduced viability of dissociated human embryonic stem cells. *Cell Stem Cell* **7**, 240-248 (2010).

# Chapter 6. Conclusions and Future Directions

## 6.1 Introduction

The primary goal of this thesis was to advance towards a mechanistic understanding of human somatic cell reprogramming through rational experimental design and quantitative analysis. While reprogramming is a biological phenomenon traditionally studied by biologists, we combined techniques from the fields of stem cell biology, materials science, biomedical engineering, and computational biology to investigate the phenomenon from multiple angles. Instead of altering gene expression, we focused primarily on the understudied role of the microenvironment during reprogramming. Accordingly, we developed technologies that were capable of tight, independent control of the reprogramming microenvironment as well as relatively simple multiplexing. As often as possible, we used chemically defined components in our cell cultures to minimize experimental variance. These technologies allowed us to gather large, high-quality datasets that could be fed into quantitative computational models for high-confidence analyses that often led to non-intuitive results.

## 6.2 The microenvironment is an important factor in human somatic cell reprogramming

In Chapter 3 we performed an empirical study on the effects of microenvironmental manipulation on human reprogramming efficiency. A combinatorial library of electrospun nanofibrous substrates was combined with the presence or absence of soluble factor TGF-β to provide a wide range of novel microenvironments to probe. It was discovered that multiple microenvironments improved reprogramming

efficiency (by up to 500%) compared to traditional tissue culture plastic. We introduced a new system to track progression of reprogramming intermediates via antibody labeling of cell-surface markers CD44 and TRA-1-60. Further, we discovered a dramatic shift in nuclear geometry during early reprogramming stages and utilized a computational PLSR model to identify important, non-intuitive components of the reprogramming microenvironment with regards to reprogramming outcomes.

This study was among the first to investigate the impact of biophysical microenvironments on human somatic cell reprogramming and established PLSR as a viable method to analyze and understand a complex biological process such as reprogramming without *a priori* knowledge. However, there is much work that could be done to more completely understand the benefits of nanofibrous substrates in reprogramming. Contrary to previous reports, we found that randomly aligned substrates led to more efficient reprogramming than substrates with fibers aligned in parallel. Additionally, the benefits of nanofibrous substrates were restricted to the first 17 days of reprogramming. We hypothesize that constriction and rounding of cells in a pseudo-3D nanofibrous environment may be beneficial in early reprogramming stages such as MET, while late stages may require alternate biophysical inputs. Future work should focus on investigating this relationship, as well as expanding the range of polymers tested.

### 6.3 The μCP Well Plate as a platform to investigate cellular behavior

The cellular response to nanofiber orientation and rapid shifts in nuclear geometry discovered in Chapter 3 left us with a desire to investigate actin and nuclear

dynamics during reprogramming in further detail. Unfortunately, nanofibrous substrates did not offer the spatial control or imaging capabilities to probe these dynamics deeply. Chapter 4 introduced the μCP Well Plate as a solution to this problem. The μCP Well Plate combines the spatial control and imaging capabilities of microcontact printed coverslips with scale and universal compatibility of the standard well plate, enabling independent control of biophysical and biochemical inputs in a highly multiplexed format amenable to both high-throughput and high-resolution imaging.

We utilized μCP Well Plates to create large arrays of human cells patterned into precisely controlled single-cell geometries. Moreover, we established a transgenic H2B-mCherry, LifeAct-GFP fibroblast line to observe actin and nuclear dynamics in live human cells. Automated high-content imaging provided large, high-quality datasets that elucidated relationships between cell geometry, actin organization, nuclear geometry, and chromatin dynamics. We showed for the first time that the mobility of a member of the core nucleosome (H2B) could be controlled solely by altering cell geometry.

The observation that controlling cell geometry can cause epigenetic shifts in the nuclear interior opens many avenues for future investigation. One open question is whether decreased mobility of H2B in elongated cells is a result of increased mobility of nucleosomes themselves, or is a result of a higher affinity of DNA to the H2B protein. If the latter is true, cell geometry may be a useful tool for controlling chromatin condensation, which could be taken advantage of to engineer many cell fate decisions and may help explain observed effects of single-cell geometry on proliferation, apoptosis, and differentiation[1-3]. The flexibility of the μCP Well Plate lends itself to the

study of a wide variety of biological questions and is only limited by the requirement for a phenotype detectable by microscopy.

## 6.4 Reprogramming from a biophysical perspective

Chapter 5 combined the investigation of reprogramming environments in Chapter 3 with the high-content imaging techniques of Chapter 4. Here, we reprogrammed human cell aggregates on µCP Well Plates and used the defined microenvironments and high-content imaging capabilities of µCP Well Plates to track reprogramming progression in a new way. Instead of assaying gene expression, we tracked reprogramming intermediates based on the biophysical characteristics of their nuclei alone. These characteristics, when combined with computational PCA models, were able to distinguish multiple cell types and reprogramming intermediates from each other and track progression of intermediates during both reprogramming and differentiation. PLSR analysis of these nuclear characteristics was able to predict reprogramming efficiency more accurately than the more traditional measure of TRA-1-60 expression. Finally, careful analysis of the progression of reprogramming intermediates through PC space led us to identify the mechanotransductor YAP as a potential inhibitor of early-stage MET during reprogramming, although more work is needed to confirm this relationship.

We believe that biophysical analysis of reprogramming cells offers an orthogonal method to investigating human somatic cell reprogramming that will be complementary to studies of transcript and protein expression. For example, many reprogramming studies have focused on identifying and eliminating “roadblocks” to reprogramming[4-6].

Our biophysical models provide a simple and inexpensive method to identify groups of cells that have stalled during reprogramming and to determine in what stage of reprogramming progression they reside. These models may also help to describe previously unknown alternate cell states during reprogramming and differentiation.

## 6.5 Towards increased clinical utility of reprogramming technologies

The field of reprogramming currently suffers from to a severe lack of standardization, leading to notoriously noisy and variable results[4,7] and slow adaptation of this exciting technology into the clinic. Standardized, defined microenvironments and advanced computational tools that both model and predict reprogramming transitions will lead to more reproducible results and a greater mechanistic understanding of reprogramming progression. Recent developments such as the creation of Good Manufacturing Practice (GMP)-grade iPSCs[8], optimizing and standardizing the workflow of large-scale technician-based iPSC generation[9], and automation of the iPSC reprogramming process through the use of robotics[10] will accelerate progress in this area.

Although many obstacles remain, we believe that these challenges will be best addressed through combining traditional biological techniques with advances in engineering technology, high-content imaging, and computational analysis to advance a mechanistic understanding of reprogramming processes. It is our hope that this thesis contributes in a small way to the adaptation of reprogramming technologies into the clinic and to the ultimate advance of human health.

## References


1 Chen, C. S., Mrksich, M., Huang, S., Whitesides, G. M. & Ingber, D. E. Geometric control of cell life and death. *Science* **276**, 1425-1428 (1997).

2 Kilian, K. A., Bugarija, B., Lahn, B. T. & Mrksich, M. Geometric cues for directing the differentiation of mesenchymal stem cells. *Proceedings of the National Academy of Sciences* **107**, 4872-4877 (2010).

3 McBeath, R., Pirone, D. M., Nelson, C. M., Bhadriraju, K. & Chen, C. S. Cell shape, cytoskeletal tension, and RhoA regulate stem cell lineage commitment. *Developmental cell* **6**, 483-495 (2004).

4 Chantzoura, E. *et al.* Reprogramming Roadblocks Are System Dependent. *Stem cell reports* **5**, 350-364 (2015).

5 Tanabe, K., Nakamura, M., Narita, M., Takahashi, K. & Yamanaka, S. Maturation, not initiation, is the major roadblock during reprogramming toward pluripotency from human fibroblasts. *Proceedings of the National Academy of Sciences* **110**, 12172-12179 (2013).

6 Sakurai, K. *et al.* Kinome-wide functional analysis highlights the role of cytoskeletal remodeling in somatic cell reprogramming. *Cell stem cell* **14**, 523-534 (2014).

7 Robinton, D. A. & Daley, G. Q. The promise of induced pluripotent stem cells in research and therapy. *Nature* **481**, 295-305 (2012).

8 Durruthy-Durruthy, J. *et al.* Rapid and efficient conversion of integration-free human induced pluripotent stem cells to GMP-grade culture conditions. *PloS one* **9**, e94231 (2014).

9 Beers, J. *et al.* A cost-effective and efficient reprogramming platform for large-scale production of integration-free human induced pluripotent stem cells in chemically defined culture. *Scientific reports* **5** (2015).

10 Paull, D. *et al.* Automated, high-throughput derivation, characterization and differentiation of induced pluripotent stem cells. *Nature methods* **12**, 885-892 (2015).

# Appendix

# A1. Direct conversion of human secondary fibroblasts to neural progenitors under serum-free conditions.

## A1.1 Introduction

Sustained expression of the Yamanaka (OSKM) factors leads to a pluripotent iPSC state, but shorter-term OSKM expression followed by exposure to an appropriate microenvironment can give rise to distinct cell types such as cardiomyocytes and neural progenitor cells (NPCs)[1-3]. Reported literature in this area has typically used either viral transduction or murine secondary fibroblasts to explore the limits of this technology[4,5]. In an effort to expand the utility and scope of our secondary reprogramming system, we sought to convert human fibroblasts to neural progenitors with a modified protocol based on a combination of the Thomson protocol for chemically defined iPSC derivation[6] and the Kaspar protocol for direct conversion of human fibroblasts to NPCs[7].

## A1.2 Materials and Methods

### *A1.2.1 Cell culture and media conditions*

The secondary human fibroblast C1.2 cell line was used for all experiments. C1.2 cells harbor Oct4, Sox2, Klf4, and cMyc under the expression of a doxycycline-inducible promoter. Cells were maintained in gelatin-coated tissue culture plastic in fibroblast media containing DMEM, 10% FBS, 1% L-glutamine, 1% non-essential amino acids, and 1% penicillin/streptomycin. Erasure media was composed as E7 media (E8 media

without TGF-β but including hydrocortisone)[6]. Establishment media was equivalent to media from the Kaspar protocol[7] containing DMEM/F12, 1x N2, 1x B27, 20ng/ml FGF2, 20 ng/ml EGF, and 5ug/ml heparin. C1.2 cells were seeded in Matrigel-coated well plates in fibroblast media the day before initiating reprogramming. Doxycycline (DXC) was added at a final concentration of 2ug/ml (5uM) to initiate OSKM expression.

## A1.3Results

*A1.3.1 Optimization of "erasure" and "establishment" phases*

In our attempt to rapidly convert human fibroblasts to NPCs, we divided the reprogramming process into two phases, termed the "initiation phase" and the "establishment phase". During the initiation phase, we expected fibroblasts to lose their somatic identity and transform into a more plastic multi- or pluripotent state. The media during this phase is a traditional chemically defined iPSC reprogramming media (E7). At the start of the establishment phase, we took advantage of this induced plasticity to drive cells towards a neural fate by switching to a neural induction media containing EGF and heparin. First, we designed an experiment to determine the optimal length of each of these two reprogramming phases by varying the point at which media is switched between erasure and establishment media and following colony formation over a 28 day time course. We chose media switching points on Days 7, 9, 11, and 13 and fixed cells at various time points from Days 7-28. We then stained for TRA-1-60 to assess colony formation (Figure A1-1).

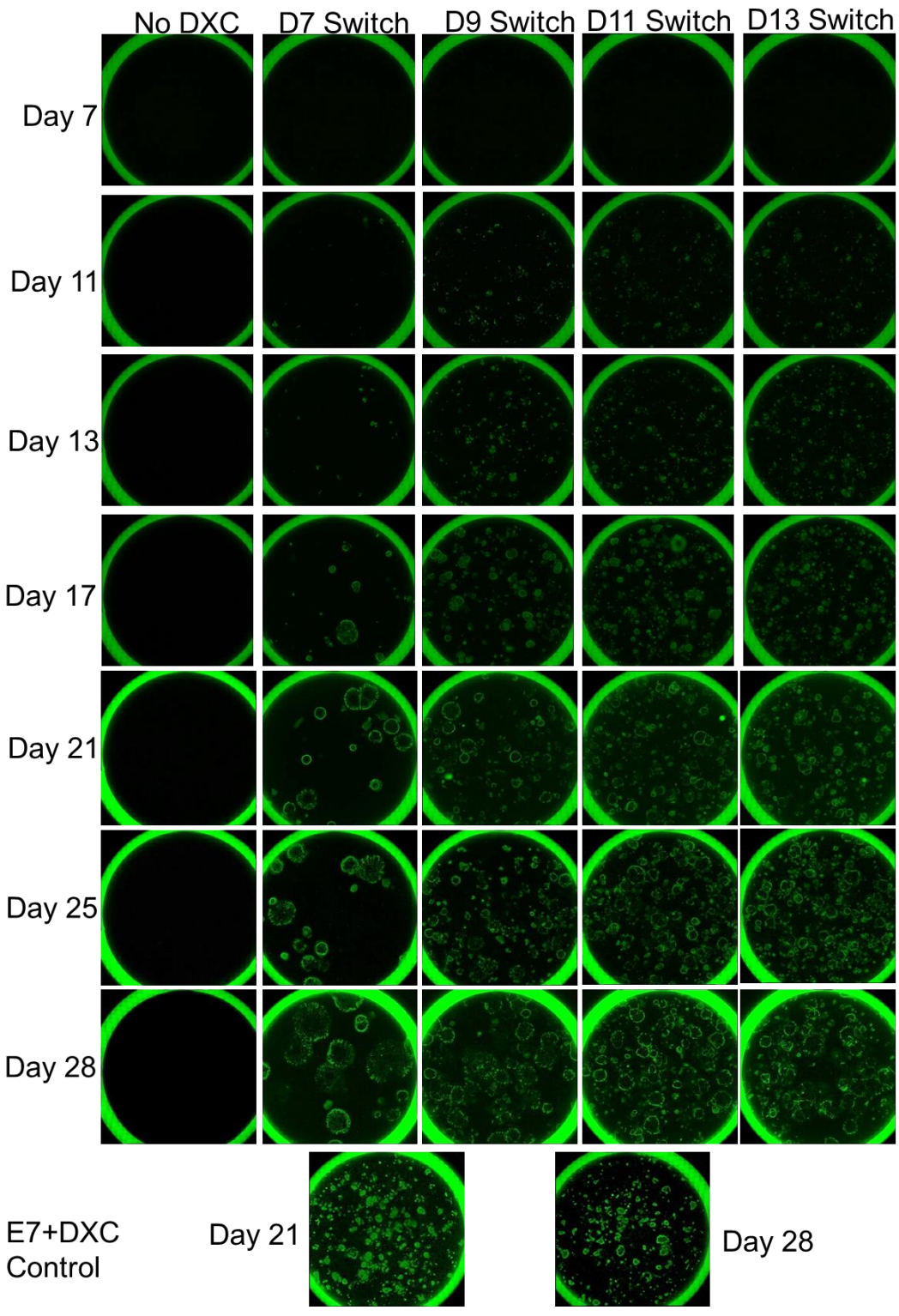


**Figure A1-1. Colony formation during direct conversion of fibroblasts to iNPCs.** Representative full-well images of reprogramming C1.2 cells stained with and anti-TRA-1-60 antibody. Columns represent different time points of media switching and rows represent the time point at which cells were fixed.

Inspection of full-well stitched images revealed that TRA-1-60 positive colonies arose as early as Day 11, after as little as 7 days of DXC exposure. Colonies were subsequently stained for Pax6 and manual counting and measurement on Nikon NIS software revealed that new colony formation ceased roughly two days after DXC withdrawal, while colonies continued to increase in size throughout the time course (Figure A1-2).

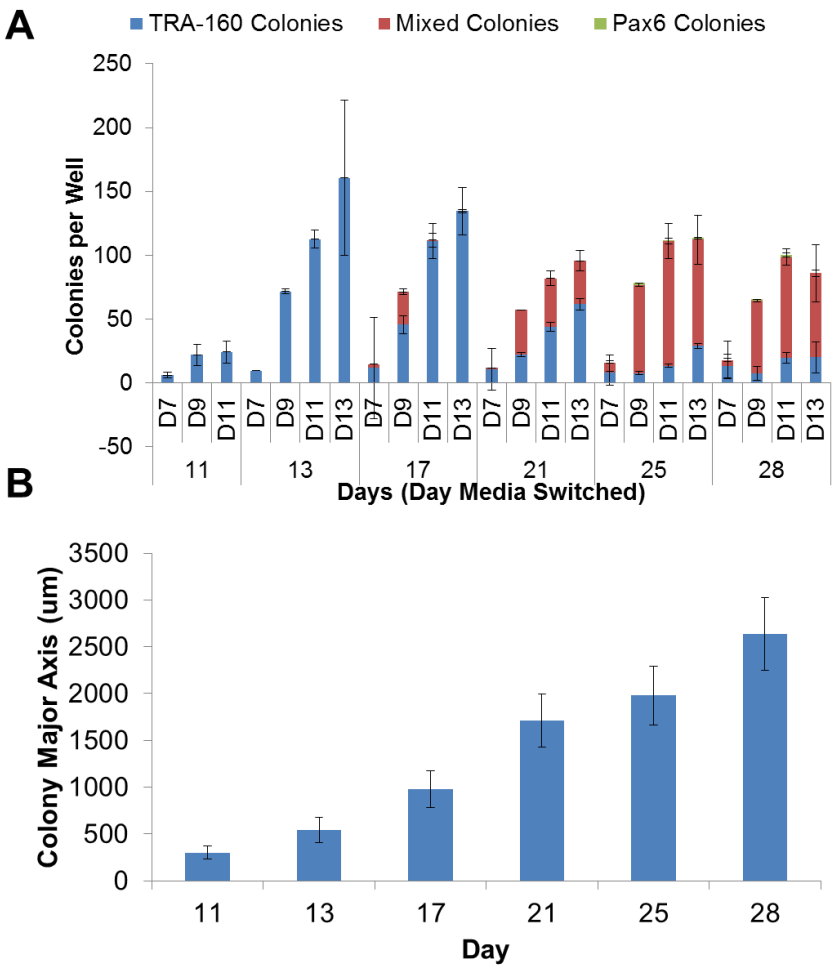


**Figure A1-2. Quantification of colony formation and growth. A)** Quantification of colony formation. Mixed colonies were defined as colonies containing at least one TRA-1-60$^{+}$ cell and one Pax6$^{+}$ cell. TRA-1-60 colonies contained no cells expressing Pax6 and Pax6 colonies contained no cells expressing TRA-1-60. **B)** Quantification of colony size. Data here corresponds to conditions in which media was switched from erasure to establishment media at Day 7.

Pax6 positive cells arose as early as Day 17, but required at least 8 days of exposure to establishment media. A 9 day erasure phase was chosen as the optimal condition based on the proportion of colonies expressing Pax6 after a 16-19 day establishment phase. Figure A1-3 depicts images of representative colony formation and progression using this optimal reprogramming protocol. In addition to TRA-1-60 and Pax6 stains, cells were stained with an anti-CD44 antibody (a fibroblast-specific cell surface marker) to assess erasure of somatic fibroblast identity. CD44 staining was ceased after Day 17, as CD44 expression at that time point was minimal (Figure A1-3). TRA-1-60 expression was very rare at Day 7, at which point clear colonies had not yet formed. By Days 11 and 13 tightly packed TRA-1-60$^{+}$ colonies began forming. These colonies were negative for CD44 expression. At Day 17 colonies were observed containing individual cells that expressed both TRA-1-60 and Pax6. By Day 21 expression of these markers was exclusive on a per-cell basis, with Pax6$^{+}$ cells typically residing in the interior of colonies and TRA-1-60$^{+}$ cells lining the exterior of the colonies. The Pax6$^{+}$ cell number increased through Day 28 with TRA-1-60$^{+}$ cells becoming rarer. In a small subset of colonies at Days 25 and 28, only Pax6$^{+}$ cells remained. We termed these Pax6$^{+}$ cells iNPCs.

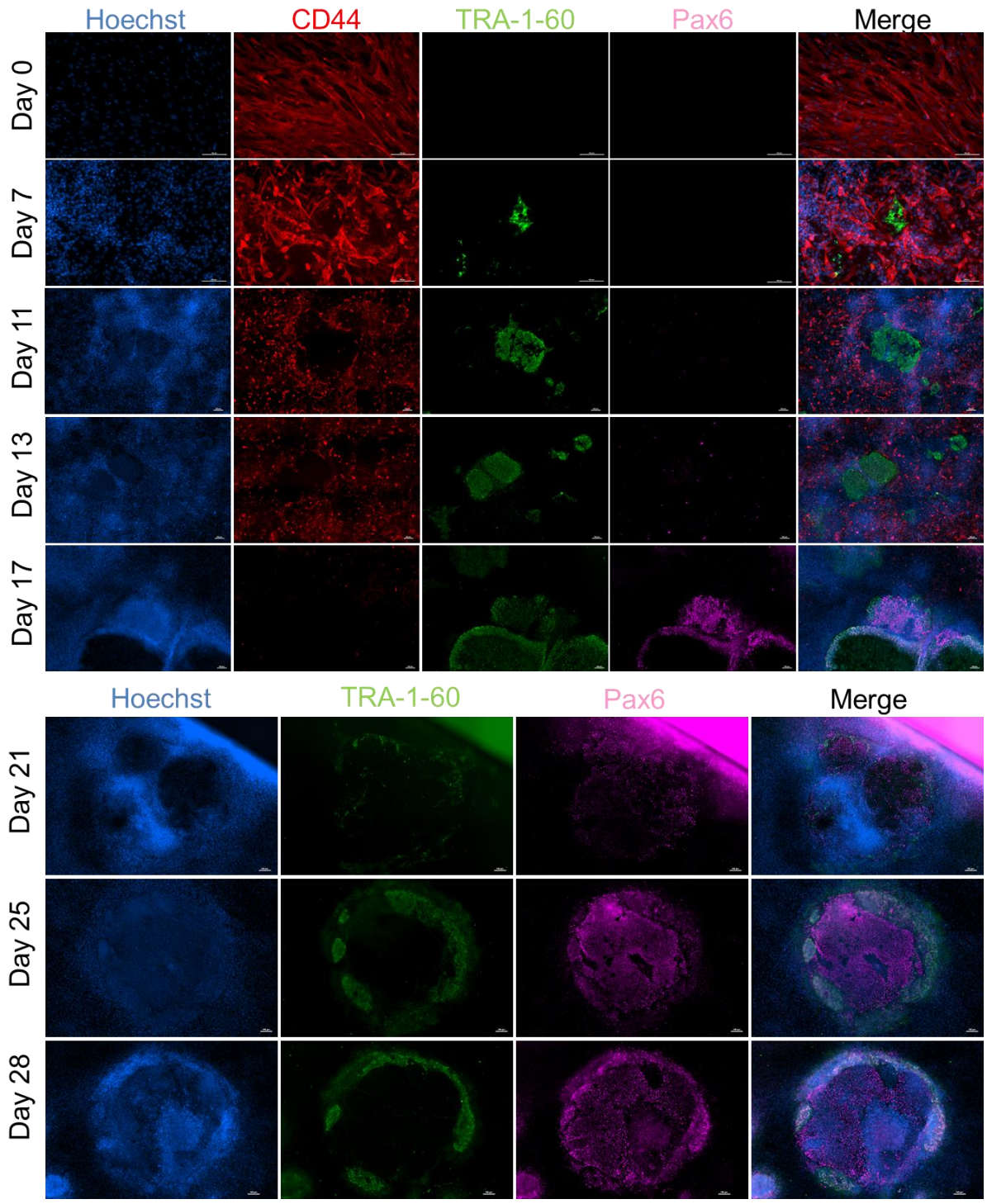


**Figure A1-3. Representative images of fibroblast-to-iNPC direct conversion.**

Rarely, polarization events were observed, in which Pax6$^{+}$ cells formed structures reminiscent of neural rosettes that commonly arise during neural differentiation[8] (Figure A1-4).

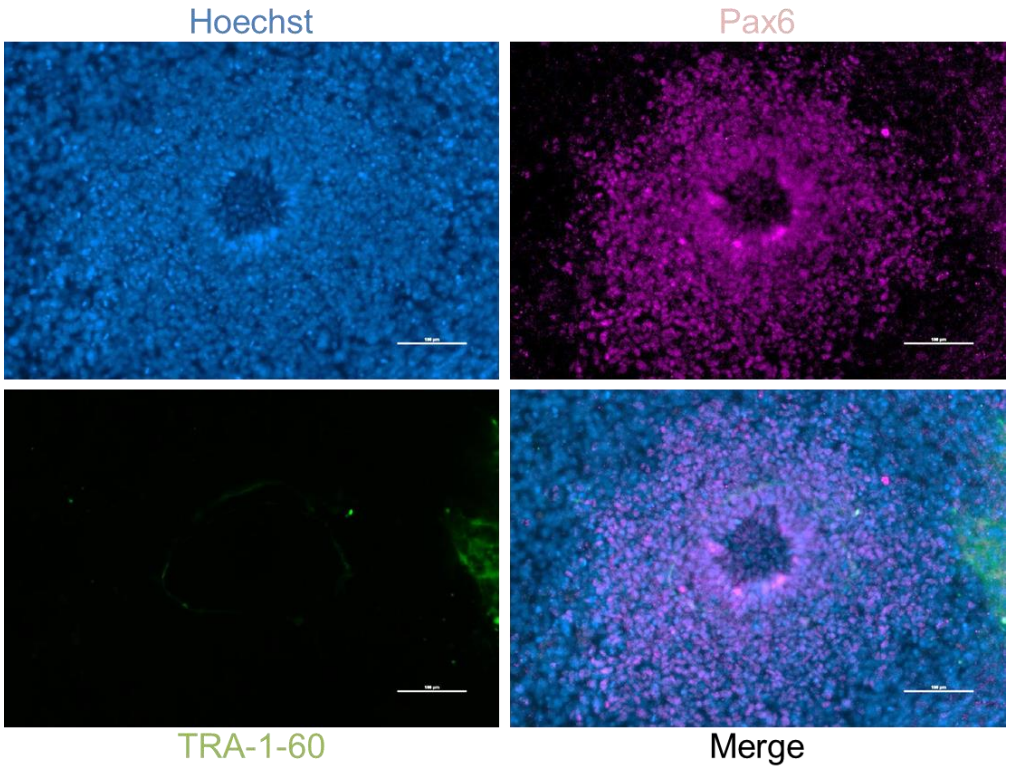


**Figure A1-4. Polarization of iNPCs at Day 25.** Polarization events were extremely rare.

*A1.3.2 Optimization of cell density*

We next wondered if cell seeding density affected iNPC derivation. To investigate, we used our optimized iNPC reprogramming protocol to reprogram cells seeded at densities of 50,000 to 225,000 cells per well of a 12-well plate (Figure A1-5). We found that colony formation peaked at a density of 75,000 cells (Figure A1-5B). Additionally, the percentage of colonies which expressed Pax6 was highest at this cell density (Figure A1-5C-D).

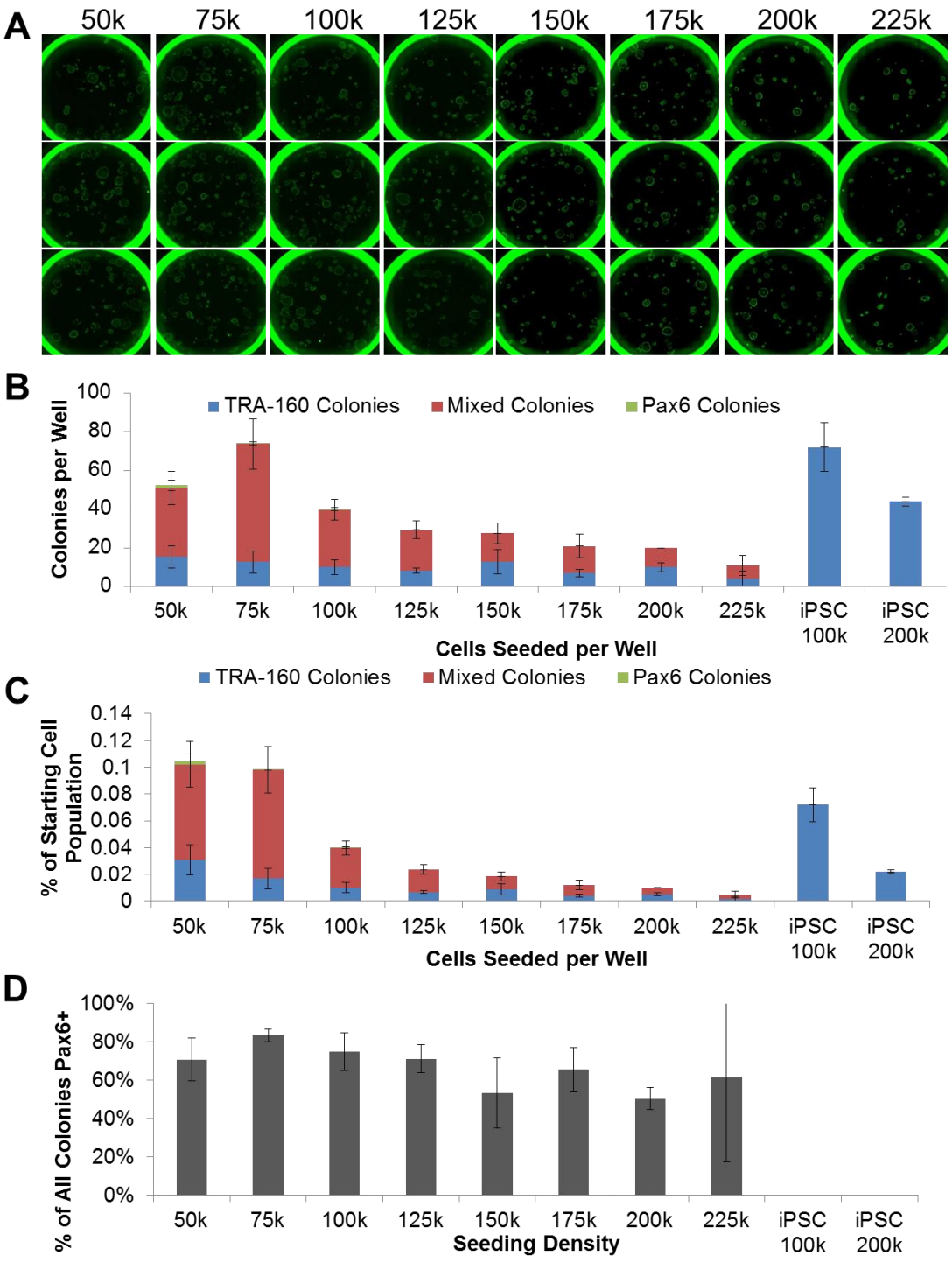


**Figure A1-5. Optimization of seeding density for iNPC direct conversion. A)** Representative images of TRA-1-60 staining showing colony formation at Day 21 for varying seeding densities. **B)** Quantification of colonies per well of a 12 well plate at varying seeding densities. **C)** Quantification of the percentage of the starting cell population that formed colonies, assuming colonies originated with one reprogrammed cell. **D)** Quantification of the fraction of observed colonies containing at least one Pax6$^{+}$ cell.

*A1.3.3 Isolation of iNPCs and confirmation of neural progenitor identity*

Finally, we sought to confirm the neural progenitor identity of our derived iNPCs. Up to Day 28, we were unable to detect Sox2 or neural cell adhesion molecule (NCAM) expression in reprogramming iNPC cultures (data not shown). However, after picking putative iNPC colonies with a micropipette and allowing another 1-2 weeks culture, groups of cells that co-expressed Pax6, Sox2, and NCAM were identified, confirming neural progenitor identity[1] (Figure A1-6).

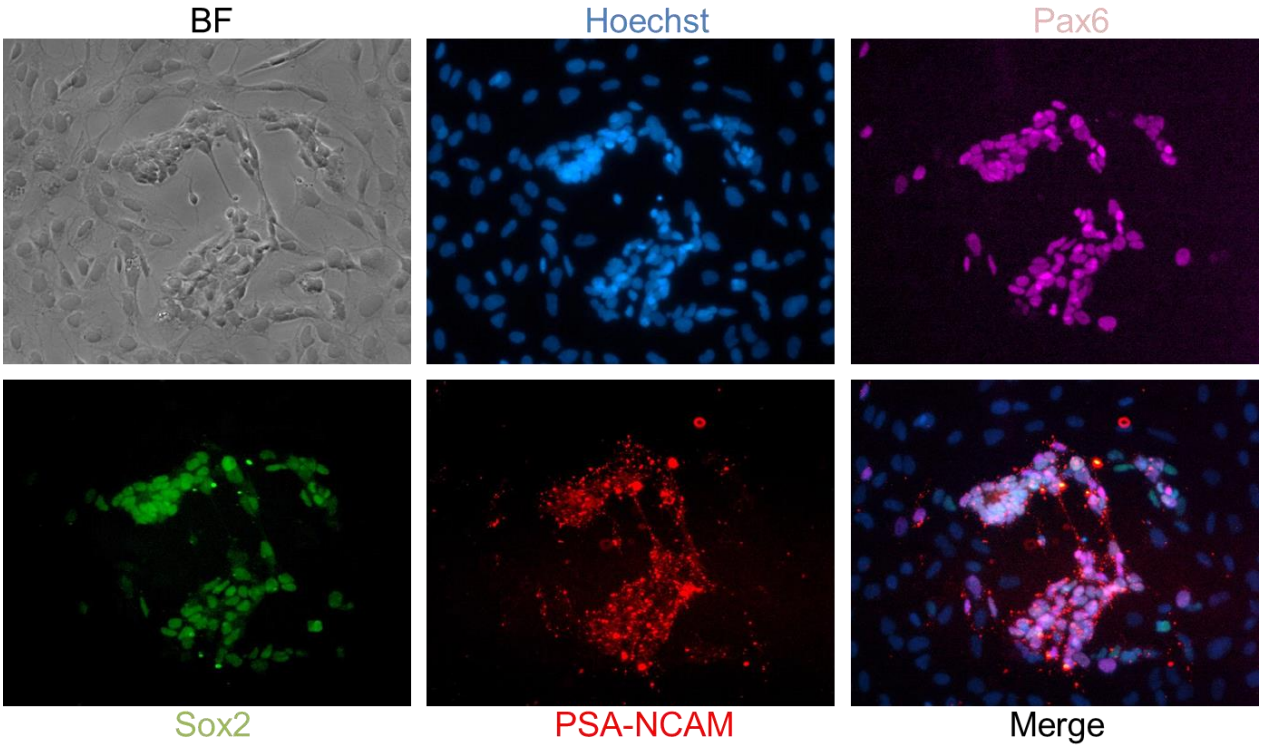


**Figure A1-6. Confirmation of NPC identity via marker expression.**

## A1.4 Discussion and Conclusions

We have described here a serum-free method for deriving neural progenitors (iNPCs) from secondary human fibroblasts. This method could presumably be adapted into a chemically defined xeno-free system fairly simply by replacing the bovine serum albumin contained in the B27 supplement with human recombinant albumin and the

Matrigel substrate with a recombinant ECM such as laminin. Isolation and expansion of iNPCs remains difficult, as it is challenging to distinguish iNPC colonies from colonies expressing only TRA-1-60 on a morphological basis. We were not able to isolate iNPCs at a purity greater than ~20% by picking and expanding colonies alone, although fluorescent sorting such as FACS based in TRA-1-60 and NCAM expression would presumably yield pure cell populations. Further work remains to determine whether these iNPCs can be successfully differentiated into all three neural subtypes, and whether transient OSKM expression can induce alternate cell identities using the basic structure described here, but with alternate “establishment media”.

## References


1 Kim, J. *et al.* Direct reprogramming of mouse fibroblasts to neural progenitors. *Proceedings of the National Academy of Sciences* **108**, 7838-7843 (2011).

2 Efe, J. A. *et al.* Conversion of mouse fibroblasts into cardiomyocytes using a direct reprogramming strategy. *Nature cell biology* **13**, 215-222 (2011).

3 Thier, M. *et al.* Direct conversion of fibroblasts into stably expandable neural stem cells. *Cell stem cell* **10**, 473-479 (2012).

4 Maza, I. *et al.* Transient acquisition of pluripotency during somatic cell transdifferentiation with iPSC reprogramming factors. *Nature biotechnology* **33**, 769-774 (2015).

5 Bar-Nur, O. *et al.* Lineage conversion induced by pluripotency factors involves transient passage through an iPSC stage. *Nature biotechnology* **33**, 761-768 (2015).

6 Beers, J. *et al.* Passaging and colony expansion of human pluripotent stem cells by enzyme-free dissociation in chemically defined culture conditions. *Nature protocols* **7**, 2029-2040 (2012).

7 Meyer, K. *et al.* Direct conversion of patient fibroblasts demonstrates non-cell autonomous toxicity of astrocytes to motor neurons in familial and sporadic ALS. *Proceedings of the National Academy of Sciences* **111**, 829-832 (2014).

8 Lippmann, E. S., Estevez-Silva, M. C. & Ashton, R. S. Defined human pluripotent stem cell culture enables highly efficient neuroepithelium derivation without small molecule inhibitors. *Stem Cells* **32**, 1032-1042 (2014).

# A2. A review of cell fusion in tumor development

Elements of this work have been published as:

**Harkness, T., Weaver, B.A., Alexander, C.M., Ogle, B.M. Cell fusion in tumor development: Accelerated genetic evolution. *Critical Reviews in Oncogenesis.* 2013, *18*, 19–42.**

## A2.1 Introduction

Cell fusion is an incompletely understood process that occurs spontaneously during normal development as well as in response to viral infection, including infections known to promote transformation, such as HPV.[1] By increasing DNA content as well as centrosome number, cell fusion rapidly alters cellular genotypes and phenotypes and catalyzes genetic diversity. Through stimulating genetic diversity, cell fusion may contribute to the formation, propagation and metastasis of tumor cells. For instance, fusion of a healthy epithelial cell with an activated fibroblast of the local stroma can allow it to acquire the ability to proliferate inappropriately. Fusion of a tumor cell with a mesenchymal stem cell can allow it to degrade extracellular matrix proteins and migrate beyond the basement membrane. Fusion of an epithelial tumor cell with a macrophage could lead to the temporary acquisition of macrophage-associated properties of transit through the vasculature and invasion of distant tissue sites.

The current view of cancer is evolving beyond the accumulation of genomic and epigenetic aberrations in epithelial cells to one that appreciates the impact of the “soil”[2]

or microenvironment on the formation, propagation and metastasis of tumor cells. Focus of this effort centers on the impact of close contact with cellular members of the stroma and immune system, which generate insoluble extracellular matrix proteins and/or soluble paracrine and autocrine factors. Activated stromal fibroblasts secrete a myriad of soluble factors including SDF-1,[3] MMPs,[4] VEGF-A,[5] HGF,[6] Sdc1[7] and TGF-β[8] that have been shown to enhance tumor growth and angiogenesis. As one example, cells of the human breast cell line MCF-7 are weakly tumorigenic in SCID mice, but are strongly tumorigenic when inoculated with stromal fibroblasts.[9,10] In addition to secreted factors, the impact of cell-cell communication is also coming to the fore as a means by which the microenvironment facilitates oncogenesis. Recent work by Apostolopoulou et al shows that MCF-7 breast cancer epithelial cells form cadherin-23-dependent, heterotypic adhesions with normal breast fibroblasts when grown in co-culture, and suggests that cadherin-23 upregulation may play a role in the early stages of metastasis.[11] A logical extension of cell adhesion or close cell contact is the possibility that tumor cells or their precursors fuse with cells of the local microenvironment. Known examples of cell fusion, along with their demonstrated and potential roles in oncogenesis and metastasis are reviewed here.

## A2.2 Context and Outcomes of Cell Fusion

### *A2.2.1 Spontaneous Heterotypic Fusion Occurs in Nature*

Fusion occurs spontaneously between cells of the same type (homotypic) and cells of different types (heterotypic). Homotypic cell fusion was first observed more than eighty years ago in the formation of foreign body giant cells[12] and was soon followed by

reports of fusion between trophoblasts of the placenta, myoblasts of muscle fibers and osteoclasts of bone.[13] However, it was not appreciated until recently that fusion products may form between heterogeneous cell types *in vivo* and that nuclei themselves often fuse to give rise to synkaryons.[14] Spontaneous heterotypic cell fusion *in vivo* was first observed in transplantation studies in animal models and later in humans, both in healthy and diseased states.[15-18] Mesenchymal stem cells and other bone marrow-derived cells (BMDCs) have often been implicated in these studies, especially in synkaryon formation.[19,20]

*A2.2.2 Cell Fusion Generates Diversity*

The immediate consequence of both homotypic and heterotypic cell fusion is tetraploidy, a doubling of the genetic material available to the cell and the first opportunity to augment clonal diversity. Given the correlation between copy number and gene expression, tetraploidy alone has the potential to radically alter cell state.[21,22] Tetraploidy has also been reported to increase the sensitivity of both yeast and human cells to DNA-damaging agents.[23,24] Fusion between cells in different stages of the cell cycle can also result in DNA damage – particularly double-strand breaks mediated by premature chromosome condensation.[25,26] In addition, tetraploidy has been suggested to “overwhelm” the mitotic machinery, making chromosome missegregation more likely[25]. A second immediate consequence of cell fusion is an increase in centrosome number. Supernumerary centrosomes can result in multipolar spindles or the missegregation of individual chromosomes after multipolar spindles are focused into

bipolar ones.[27,28] In any scenario, fusion would be expected to increase genetic diversity of the fusion product compared to individual fusion partners.

Of course genetic diversity is likely to result in phenotypic diversity, dependent on the degree of change and the localization of change. Perhaps the most familiar example of how a fusion product attains diversity of phenotype is the hybridoma cell, a Sendai virus-induced fusion of a murine myeloma cell with a B cell from an immunized mouse.[29] The entire hybridoma system is based on the assumption that the fusion product has a competitive advantage over the parental cells, as neither parental cell line can survive in selective media. The fusion products of these experiments were known to have highly variable phenotypes. In practice, this made the process of hybridoma selection frustrating, since only a percentage of fusions resulted in nuclear hybrids, a fraction of those produced antibodies, and a small percentage of antibody-producing hybrids were able to be expanded into functional hybridomas.[30] The ability of hybridomas to "evolve" upon continuous culture was even used to map genes to specific chromosomes.[31] In a study that mapped an "IL-6 dependency gene" to human chromosome 21 it was found that newly fused hybridomas displayed IL-6 dependence, however this dependency was lost at frequencies up to 50% upon continuous culture, suggesting that genetic material was lost after fusion.[31] Karyotyping of stable clones showed a great variety of seemingly randomized chromosome content. Thus, early hybridomas show a high degree of chromosomal instability (CIN), defined here as an increased and continuous rate of large chromosomal aberrations, including deletions, duplications, or translocations as well as loss or gain of whole chromosomes. Despite the great degree of genetic rearrangement after fusion, hybridoma genotypes eventually

stabilize in culture, as evidenced by the extent of their use in industry to provide an extremely pure monoclonal antibody product in a highly reproducible fashion.[32,33]

Although the progression from tetraploidy to aneuploidy or diploidy in hybridomas may be dismissed as a product of extreme culture conditions, there is considerable evidence that this process also occurs in normal culture conditions and even *in vivo*. Observations that tetraploid yeast cells could progress to aneuploidy,[34] and that cells with more than four centrioles could be found in mouse models,[35] along with the fact that multipolar mitoses are often seen in human cancers[36] led to the hypothesis that supernumerary centrosomes lead to multipolar cell division in tetraploid cells and diverse aneuploid progeny.[36,37] However, multipolar spindles are frequently focused into bipolar spindles before anaphase onset and chromosome segregation.[28] Ganem et al. recently showed that, even when cells ultimately proceed through a bipolar division, extra centrosomes promote missegregation of individual chromosomes in a variety of human cell lines by merotelic attachment, in which a single kinetochore attaches to microtubules originating from multiple centrosomes.[27] If these centrosomes are focused into different spindle poles, this phenomenon can lead to chromosome lagging during anaphase and the production of diverse aneuploid progeny even in the absence of multipolar division.

Diversification of the genome and the phenome could be advantageous in many scenarios beyond the generation of hybridomas. As one example, Grompe and colleagues have reported detailed studies of the consequences of hepatocyte fusion with BMDCs in a regenerative context *in vivo*. It was first shown that hepatocyte-BMDC fusion products had a competitive advantage in the diseased liver microenvironment

and were able to completely repopulate the host liver.[38,39] After diploid fusion products (as determined by a Cre-Lox reporter system) were observed[19] genetic studies were performed to elucidate the mechanism of chromosome loss after cell fusion. Using a three-marker system in which fusion-derived hepatocytes alone expressed β-gal, FAH, and bore a Y-chromosome, ploidy reduction was demonstrated, frequently resulting in aneuploid progeny of diverse karyotypes.[40] Subsequent single-cell PCR genotyping revealed that parent-specific markers segregated independently via ploidy reduction after cell fusion, with the incidence of loss ranging from 33-70% of cells analyzed. Only 13% of fusion products tested retained all parental markers, suggesting that ploidy reduction is a very common phenomenon after cell fusion *in vivo*. It is also interesting that the incidence of single marker loss did not cluster around 50%, as would be expected for random chromosome loss, again suggesting that environmental pressure may enrich for cells with favorable phenotypes. Later studies also implicated merotely and chromosome lagging in aneuploidy generation in this process.[41] In addition, it was shown that hepatocytes can regularly increase and reduce their ploidy while maintaining viability and producing high levels of genetic heterogeneity – a process termed the "ploidy conveyor".[41] It is interesting to note that regrowth of the liver after hepatectomy is associated with an increase in polyploid cells.[42] Populations of tetraploid fibroblasts have also been observed in a variety of wound healing contexts in humans and mice and the frequency of tetraploidy has been shown to increase during the proliferative phase of wound healing.[43] Importantly, these tetraploid cells often appeared in clusters suggesting a clonal evolution, possibly from an initial cell-cell fusion event. It is easy to envision an invading inflammatory BMDC being involved in this context as well. These

examples suggest that polyploidy may in fact be an adaptive response to the need to repopulate a damaged tissue.[44]

While genetic recombination is certainly an important event in heterotypic fusion, the mixing of epigenetic factors from diverse cell types may be just as crucial. In a process termed “nuclear reprogramming”,[45,46] cell fusion can result in activation or silencing of genes of one parent via outside epigenetic factors. The most well-known example of nuclear reprogramming by the cytoplasm is probably somatic cell nuclear transfer, which has been utilized to reset a mature nucleus to a pluripotent or totipotent state and resulted in the cloning of Dolly the sheep.[47] Decades ago, it was shown that trans-acting epigenetic factors from one nucleus of a heterokaryon can silence or activate genes in a partner nucleus.[48,49] Through work in stem cell biology, it has been shown that fusion of pluripotent murine germ cells with thymocytes from adult mice alters the methylation status of previously imprinted somatic genes.[50] However, when embryonic stem cells were used as fusion partners instead of germ cells, imprinted genes were not demethylated but hyperacetylation of histones H3 and H4 led to a pluripotent state.[51,52] The result of these epigenetic changes can be expression of genes already active in one (or both) fusion partners[48] or expression of genes not expressed in either parent, an outcome seen more recently in the context of cancer.[53]

An altered phenotype may also be produced solely by the physical changes of a fusion product, specifically an increase in cytoplasmic and/or nuclear volume. Effects of increased volume could include less efficient transfer or decreased concentration of transcription factors and other proteins, less efficient interactions between organelles,

and lowered efficiency of membrane-dependent activities due to an increased ratio of cell volume to organelle surface area.[44]

The process of combining genetic or phenotypic information to create diversity and selective competitive advantages is also an important concept in evolutionary biology. There is considerable evidence of polyploidization in the evolutionary history of many organisms including mammals,[54] which although not well understood is thought to increase evolutionary innovation through genome recombination.[55] Furthermore, a recent study on a newly formed (~80 yr) naturally polyploid plant species revealed massive chromosomal instability, with 69% of individuals studied displaying aneuploidy for one or more chromosomes and 76% showing intergenomic translocations.[56] The high degree of genomic diversity still being generated after ~40 generations of this biennial species suggests that prolonged periods of chromosomal instability may commonly precede genomic stabilization in naturally forming polyploid species. The evolutionary theory of symbiogenesis takes this idea a step further.[57] It holds that mergers of species, rather than Darwinian evolution via accumulation of mutations, are the drivers of diversity and speciation. The most convincing evidence to support the symbiogenic theory is the finding that mitochondria and chloroplasts are of bacterial origin.[58] What fraction of evolutionary adaptations can be ascribed to symbiogenesis is unknown, but it is not difficult to imagine a corollary to symbiogenesis, which states that one means by which species or structures of species are merged is via fusion.

## A2.3 Mechanisms of Cell Fusion

### *A2.3.1 Spontaneous Cell Fusion*

Cell membranes allow the cell to function independently and preserve self-regulation from outside influence. In normal development, this compartmentalization is overcome by cell-cell fusion only in a tightly regulated manner. The process of fusion is thermodynamically unfavorable owing to the need to expunge water between the cells, the negative and opposing charges of the outer phospholipid bilayer, and the need to disrupt the membrane. One way that the formation of a syncytium is enabled is via specific integral membrane proteins, termed fusogens, which minimize the incredible energy cost required to overcome the merger of the two hydrophobic membranes.[59] Establishing true fusogens has proven difficult since removal of facilitating proteins from the system reduces overall fusion rates. As technologies advance, many “fusogens” have been contested and shown to be merely adhesion proteins that bring cell membranes in close apposition but do not actually facilitate fusion. Although the mechanisms of spontaneous cell fusion are still not well understood, studies of fusion in normal development have given us some clues.

### *A2.3.2 Homotypic Fusion: Macrophages*

While some cells, such as myoblasts and placental trophoblasts, are required to fuse for normal development, macrophages are normally present as mononuclear cells in the body, and undergo rare (and inducible) fusion events to form multinucleated osteoclasts and giant cells.[60] As such, macrophages may prove to be the most useful model to study inducible fusion. When the recent evidence of BMDC fusion with

somatic and cancer cells is taken into account, the mechanisms of macrophage fusion become even more interesting.

Osteoclast and giant cell development is thought to progress similarly and include a series of functional steps including induction of a fusion-competent status, chemotaxis, cell-cell attachment, cytoskeletal rearrangements, and fusion.[61,62] IL-4 and IL-13 are secreted by a number of immune cells and can induce giant cell formation *in vitro* and *in vivo*,[61] while RANKL and M-CSF can induce osteoclast formation *in vitro*.[63] These soluble factors are thought to lead to a fusion competent status by upregulating fusion mediator expression on macrophage cell membranes. For example, IL-4 stimulates DC-STAMP and E-cadherin expression, both of which are implicated in macrophage fusion.[64-66] Internal signaling via DAP12 also seems to be important in this process by mediating transcription of other fusion mediators.[67] Little is known about chemotactic and adhesive factors in macrophage fusion. CCL2 (MCP1) is thought to be important in chemotaxis, as deficiency in mice has been shown to impair giant cell formation while leaving macrophage recruitment unaffected,[68] and E-cadherin has been implicated in macrophage adhesion.[61] Final temporal regulation of macrophage fusion may be determined by the macrophage fusion receptor (MFR) and its ligand CD47. CD47 is expressed ubiquitously, while MFR is expressed only in myeloid cells and neurons. Additionally, MFR is strongly and transiently expressed in macrophages at the onset of fusion.[69] Notably, CD47[70,71] and CCL2[72,73] are both expressed in diverse cancers[74] and IL-4 and IL-13 are secreted by $CD4^+$ T cells in the breast tumor microenvironment.[75]

It has recently been shown that a podosome-like structure is created around actin foci in fusion-competent myoblasts. These podosomes invade adjacent founder myoblasts and mediate fusion pore formation.[76] Interestingly, lamellipodia form in IL-4 stimulated macrophages before giant cell formation, and these structures have been suggested to be critical in the fusion process.[77]

*A2.3.3 Heterotypic Fusion: Gametes*

Despite its essential role in the generation of life, the most well known example of developmental heterotypic cell fusion is similarly shrouded in mystery. Mammalian reproduction occurs through heterotypic gamete fusion. As a fusion product, the fertilized embryo can proliferate and differentiate into all the tissues of the adult body as well as the extra-embryonic tissues. CD9 is an egg-associated putative fusogen. Knockout mice for CD9 have show severely hampered fertilization[78] which is restored with polyadenylated CD9 mRNA.[79] Additionally, CD9 has been shown to generate the strongest observed interactions with the sperm.[80] In contrast, Izumo is a putative fusogen found only on the sperm membrane following acrosomal reaction.[81] Supporting the role of Izumo as a fusogen is the finding that Izumo-deficient mice have normal sperm migration into the oviduct, motility, zona pellucida penetration, and acrosomal reaction, but are completely insterile.[82] Furthermore, successful fertilization occurs after artificial injection of Izumo-deficient sperm into oocytes, indicating that Izumo-null mice lacked other developmental defects. Although the expression of each protein is essential for fusion and fertilization, the molecular mechanism of Izumo/CD9 induced fusion is not well understood. For example, it is not known whether other facilitating proteins are required.[59,82]

*A2.3.4 Viral-Mediated Fusion*

In contrast to spontaneous cell-cell fusion, mechanisms of many virus-cell fusion events have been well characterized.[83] The first step of viral fusion is attachment; capsid proteins bind to specific receptor proteins on the cell membrane. Next, depending upon the type of virus, one of two pathways occurs: plasma membrane fusion or endocytosis followed by endosomal membrane fusion. Typically, a hidden fusogenic protein in the envelope is activated either by the induction of a conformational change upon receptor binding, or exposure to low pH within the endosome. Class I fusion proteins, such as the human immunodeficiency virus type-1 (HIV-1) envelope protein (Env) use a hydrophobic fusion peptide that is only exposed after specific receptor binding or under low pH conditions. The fusion protein then undergoes a conformational change that brings the viral and cell membranes into close apposition to mediate fusion.[84]

After viral infection, cells may express fusogenic proteins such as Env on their cell membranes, facilitating fusion with adjacent healthy cells. This characteristic has been used to induce cell fusion *in vitro* for years[85] and viruses that are able to fuse cells are nearly ubiquitous in humans.[26] This property is especially interesting in the context of oncogenesis in light of recent findings that certain viruses such as HPV are indeed causative of cancer and capable of inducing cell fusion.[1,86] It is also worth noting that tumors often create an acidic microenvironment that could activate pH-sensitive viral fusogens.[87]

## A2.4 Cell Fusion and Oncogenesis

CIN and aneuploidy are classic hallmarks of cancer[88,89] and are documented consequences of cell fusion.[25] However, it is unclear exactly how CIN is initiated in cancer progression. Supernumerary centrosomes, with or without tetraploidy, can lead to CIN due to the formation of merotelic attachments.[27,36] It has also been suggested that CIN could arise as a direct result of extra chromosomes through an increased rate of DNA damage [34,90] or that increased chromosome content could "overwhelm" the mitotic machinery resulting in missegregation of chromosomes.[25,37] As was discussed earlier, cell fusion-induced tetraploidy can lead to aneuploid progeny through a transient period of CIN. Fittingly, the first clue that fusion may be involved in oncogenesis is that tetraploidy is common in premalignant lesions and often gives way to aneuploidy in later stages.[25,91,92] The best studied example of this phenomenon is probably Barret's esophagus, a premalignant condition in which tetraploid cells are predictive of progression into both aneuploidy and cancer.[93,94] Tetraploidy has also been detected in premalignant lesions in cervical cancer,[95] head and neck squamous cell carcinoma,[96] and Kaposi sarcoma,[97] however it is unknown whether tetraploid cells in these lesions progress to malignancy. Direct evidence for carcinogenesis as a result of tetraploidy comes from a 2005 study in which $p53^{-/-}$ tetraploid cells were derived through chemically inhibiting cytokinesis. [98] These $p53^{-/-}$ tetraploid cells formed tumors when implanted subcutaneously in nude mice while isogenic $p53^{-/-}$ diploid cells did not. Karyotyping of resultant tumors showed they were near-tetraploid with numerous structural rearrangements. The observations that a majority of cancer cell lines in the NCI-60 drug screening panel[99] and elsewhere[100-102] are hyperdiploid and that karyotypes are

generally preserved between cell lines and the primary tumors they were derived from[100,103] suggest that the progression from tetraploidy to aneuploidy may be common in many cancers *in vivo*.

It has been reported that there exists a p53-dependent "tetraploidy checkpoint" that must be overcome for proliferation of these cells.[104,105] However, subsequent experiments using the same cell type have failed to replicate this finding.[24,106] Even though cell cycle arrest is not directly related to DNA content, suppression of proliferation is common in fusion products, as evidenced by the low survival of hybridomas[30] and lack of proliferation of developmental fusion products such as osteoclasts and muscle fibers.[13] Additional proof was provided by Duelli et al. in the context of viral-induced cell fusion. It was observed that cell fusion induced by viral infection of normal human fibroblasts, but not the viral infection itself, caused cell cycle arrest.[107] However, if one parental cell expressed the adenoviral oncogene E1A or a mutated form of the tumor suppressor p53 the fusion products proliferated, producing diverse aneuploid progeny, some of which were capable of producing tumors in nude mice.[108] Furthermore, Duelli et al. have suggested that fusion-specific mechanisms of combining DNA content from cells in different epigenetic states, possibly including premature chromosome condensation, may result in instability, double strand breaks, and consequent translocations often seen in aneuploid progeny.[26]

An alternative explanation of the appearance of diverse aneuploid progeny after a period of CIN in cancer progression is progression through "telomere crisis". This theory holds that while a great majority of cells will trigger senescence or apoptosis pathways upon sufficient erosion of telomeres (i.e. reaching the Hayflick limit),

oncogene expression may allow continued proliferation to the point of crisis. Telomere crisis is characterized by genetic aberrations including chromosomal end-to-end fusions, translocations, losses, and duplications. Out of this period of genetic instability, rare cells emerge that are able to maintain telomere length by reactivating telomerase. These dysregulated aneuploid cells may then go on to form malignant tumors.[109,110]

In a landmark study of *in situ* genome instability in breast cancer, Chin et al. demonstrated a transient period of genomic instability coinciding with telomerase activation and with transition from ductal hyperplasia to ductal carcinoma *in situ*.[110] This period of instability was attributed to telomere crisis, although telomere length was also shown to decrease at a steady rate throughout disease progression. However, two observations made by Chin and colleagues are reminiscent of CIN following cell fusion. First, it was noted that the increase in genome instability was contemporaneous to an increase in DNA content. Second, the frequency of anaphase bridges were low in hyperplasia, highest during the period of instability, and reduced thereafter. The occurrence of anaphase bridges is often used as an indicator of telomere crisis,[111,112] but can also occur as a consequence of chromosome lagging due to supernumerary centrosomes and merotely as discussed earlier.[27,113] Thus, the same temporal pattern of anaphase bridge frequency peaking alongside increased DNA content and genomic instability would be expected to occur after cell fusion.

Further confusing the debate around CIN and aneuploidy in the context of cancer is that aneuploidy can act as a tumor promoter or suppressor depending on the cellular context.[114] Aneuploidy caused by depletion of the mitotic checkpoint component BubR1 promotes tumor formation in the colon of $APC^{Min/+}$ mice, which are predisposed to

intestinal tumors due to heterozygous expression of a truncation mutant of the Adenomatous Polyposis Coli tumor suppressor, but inhibits tumor formation in the small intestine.[115] Similarly, monosomy of 33 genes on mouse chromosome 16 enhances intestinal tumor formation in $APC^{Min/+}$ mice, but trisomy of these same 33 genes suppresses tumor formation.[116] Aneuploidy caused by partial reduction of the mitotic checkpoint component Bub1 drives liver tumor formation, but further reducing the level of Bub1 causes an increased rate of chromosome missegregation and suppresses liver tumors.[117] Both loss and overexpression of securin, a protein that prevents premature sister chromatid separation, result in aneuploidy.[118,119] However, loss of securin reduces pituitary tumor formation in $Rb^{+/-}$ animals,[120] while overexpression of securin facilitates pituitary tumor development.[121] Finally, epidemiological studies have shown that Down's syndrome/trisomy 21 patients have much higher rates of hematopoietic malignancies, but lower incidence of solid tumors.[122-124]

In another study, Weaver et al. utilized a low-expression Centromere-associated Protein-E (CENP-$E^{+/-}$) model to induce aneuploidy and CIN due to whole chromosome gain and loss *in vitro* and *in vivo*.[114] When CENP-$E^{+/-}$ transgenic mice were inspected for spontaneous tumor formation, it was found that transgenic animals developed higher rates of lymphomas and lung tumors than their littermates, but significantly decreased rates of tumorigenesis in tissues normally prone to tumor formation, such as the liver. Additionally, CENP-$E^{+/-}$ animals exhibited decreased tumorigenesis compared to wild type animals when exposed to the well characterized carcinogen DMBA and a highly significant increase in tumor-free survival in the absence of the ARF tumor suppressor when compared to $ARF^{-/-}$, CENP-$E^{+/+}$ littermates. Another important observation of the

study was that aneuploidy in nontransformed cells *in vivo* was characterized by a disproportionate tendency toward whole-chromosomal loss relative to gain.

Taken together, these results argue that aneuploidy promotes tumorigenesis in otherwise genetically stable tissues and cells but inhibits tumor formation in tissues with a preexisting rate of CIN. This mechanism may explain why cell fusion is tumor suppressive in certain contexts, [74,125,126] which led to the early belief that tumor cell fusion always suppressed malignancy and even aided in the discovery of tumor suppressor genes.[127]

If high or sustained levels of CIN could result in the extinction of a neoplasia, Storchova et al. raise the possibility that cell fusion via the introduction of additional genetic material gives a sort of “cushion” to the deleterious effects of CIN, as redundant genes could compensate for the loss of single alleles or whole chromosomes.[88] It is also possible that a polyploid genotype after fusion has a larger selection of dormant genes that can be activated in response to environmental challenge and thus display the remarkable adaptive ability found in tumor cells.[48,51] In any case, in order for a clinically significant tumor to arise, at least one stable genome capable of continuous proliferation must be generated from the period of CIN (Figure 1A). This seems to be the case in many cancers by the time of clinical appearance,[44,60,128] and is further supported by the observation that karyotypes from relapsed tumors many years after treatment can be identical to the original tumor.[129,130]

## A2.5 Cell Fusion and Metastasis

Although much progress has been made in recent years in understanding the pathways of metastasis and the role of the microenvironment in this process,[131] very little is known about the generation of metastatic cells within a previously non-metastatic primary tumor. The question of why only a tiny fraction of transformed cells are able to free themselves from the cell and ECM adhesions of the tumor site, migrate through the surrounding tissues and basement membranes, intravasate into the bloodstream or lymphatic system, and extravasate, invade, and proliferate at a distant site is a critical one for the development of effective therapeutics. The importance of understanding this process is underscored by the fact that a majority of cancer deaths are attributed not to primary tumors, but to complications arising from distal metastases. A recent publication[132] further emphasizes the importance of understanding metastasis by pointing out that of the six famed "hallmarks of cancer",[133] only one – tissue invasion and metastasis – can be used to distinguish a life-threatening malignant tumor from an essentially harmless benign tumor.

The dogmatic view of metastasis is that it evolves gradually during tumor evolution, as part of the selective adaptation of the tumor genome.[134] In this linear progression model, primary tumor cells accumulate genetic changes randomly, those mutations that support survival and proliferation in the tumor microenvironment are selected for, and clonal expansion occurs within the tumor. Eventually, a cell arises with a combination of chance genetic alterations that enable it to depart the primary tumor and take up residence elsewhere in the body. This model has become popular for good reason. First, it follows logically from the discovery of oncogenes in malignant

transformation and second, it does an excellent job of explaining the positive clinical correlation between tumor size and frequency of metastasis.[134,135] A large tumor has presumably been in existence longer than a smaller tumor, giving it both more time for accumulation of mutations and a larger cell population in which to select for cells capable of metastasis. However, several lines of evidence argue against the linear progression model of metastasis.

First, advances in parallel-sequencing technology now allow for whole-genome analysis of primary and metastatic tumor cells. One recent study compared the whole genome of a brain metastasis to that of the primary breast tumor and found only two *de novo* mutations in the metastatic tumor.[136] One was a silent mutation while the other was determined to be non-essential to metastasis, suggesting that a mechanism other than genetic mutation initiated the metastatic process. It is important to note that this methodology would not detect polyploidy of the tumor cells.

Another argument involves the growth kinetics of primary and metastatic tumors. The linear progression hypothesis predicts that significant time and cell divisions will be required for a tumor cell to gain and “fix” the chance mutations needed for metastasis. Therefore, according to this hypothesis primary tumors should be of sufficient size to sustain the establishment of clonogens that form with low frequency. In fact, metastases are often seen in early disease stages, and 5-10% of patients diagnosed with cancer in Europe and the United States present with unknown primary tumors.[137,138] For the linear progression hypothesis to hold in these cases, growth rates of metastases would need to be far greater than those of the primary tumor. Primary and metastatic breast cancer growth rates have been well studied[139,140] and argue

against this possibility. Several methods of investigation have shown that growth rates of primary and metastatic tumors are comparable at the time of diagnosis, typically within a factor of two.[134]

A third, primarily hypothetical argument against linear progression has been put forward by George Parris[141] and expands on the discussion of CIN and consequent genomic stabilization above. If a tumor is conceptualized as a new, "parasitic" species within the host,[142] it will be subject to the ecological pressures of any other species. By the widely known ecological concept of Muller's Ratchet,[143] an asexual population with only genetic mutations available to generate diversity may gain a momentary genetic advantage via a desirable mutation. However, when a deleterious mutation occurs in this asexual population it must (with the exception of back mutations) be passed on to all progeny. As a given mutation is more likely to be deleterious than advantageous, undesirable mutations build up in an asexual population until it finally becomes extinct. In the context of cancer progression, this theory would allow for the formation of neoplasia due to somatic mutations, but tumors would be expected to become extinct before clinical relevance or metastasis. We and others[13,74,141] argue that a "sexual" method of reproduction – such as cell fusion – that allows for genetic recombination offers a more likely explanation for tumor progression into metastasis than the linear progression model (Figure 1B). This hypothesis is initially supported by the correlation between the most immediate consequence of genetic recombination – aneuploidy – and poor prognosis in a variety of cancers[92,144-147] as well as the finding that polyploidy is strongly correlated with growth rate in many species[148]. In more concentrated studies, it was found that polyploidy in the liver was increased in faster growing mouse pups[149]

and in rat hepatocytes after growth hormone stimulation.[150] Thus, fusion-induced polyploidy may be an adaptive response to the increased rate of proliferation throughout disease progression.

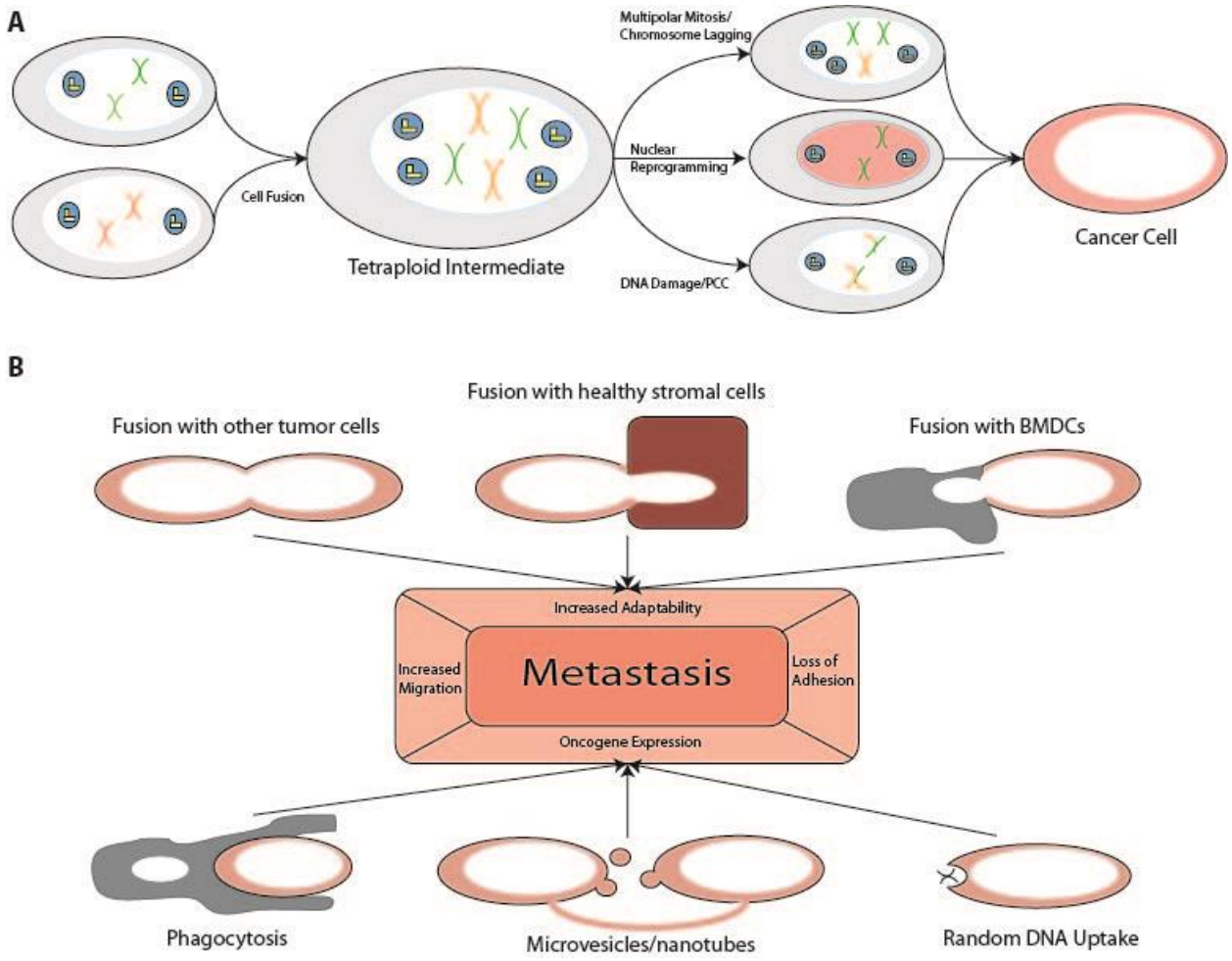


**Figure A2-1. Schematic of cancer progression via cell fusion.** **A)** Fusion can lead to oncogenesis. An initial fusion event leads to an intermediate tetraploid fusion product with doubled centrosome content. This intermediate is unstable and is capable of progression into malignancy through several mechanisms. **B)** Fusion can lead to metastasis. Cell fusion or alternative methods of genetic transfer impart new phenotypic capabilities to the tumor cell which enable the cell to metastasize.

*A2.5.1 Tumor cell fusion with other tumor cells*

If fusion is a viable means by which metastasis is initiated, the next question is "which two (or more) cells fuse?" The definitive answer to this question remains elusive, but several studies are suggestive of certain pairings. One pairing is fusion between

tumor cells. If tumor cells fuse with each other, detection of such an event within a single tumor is challenging, as most detection techniques rely on overlapping lineage-specific markers to identify fusion partners. Accordingly, a fusion event between phenotypically identical tumor cells would be undetectable in most experimental systems. However, spontaneous fusion between cancer cells has been observed *in vitro*. As early as 1984, it was observed that multi-nucleated giant cells arose in suspension cultures of B16 melanoma cells.[151] More recently, co-culture of two variants of the MDA-MB-231 breast cancer line, one of which metastasizes almost exclusively to bone and the other primarily to the lung, resulted in fusion hybrids that had gene expression signatures of both parental strains and retained strong metastatic ability to both lung and bone *in vivo*.[152] Interestingly, fusion products were phenotypically and genomically stable at a nearly doubled genome size after passage *in vivo* up to the time of publication (almost 1 year).

*A2.5.2 Tumor cell fusion with local non-malignant cells*

Evidence of fusion between xeno- or allogeneic transplanted malignant cells and host cells *in vivo* was reported repeatedly in the 1970s and early 1980s,[153,154] often resulting in increased metastatic ability. However, it was not until recently that advances in genetic profiling techniques such as fluorescence *in situ* hybridization (FISH) could provide conclusive evidence of synkaryon formation.

In the last decade, fusion of epithelial tumor cells with local endothelial and other stromal cells *in vivo* has been reported. In one study, human breast cancer cells were injected into the tail vein of nude mice. Subsequent analysis of lung sections revealed that 0.5-2.0% of tumor cell nuclei contained both human and murine DNA.[155] A portion

of these hybrid cells also stained positively for the endothelial marker von Willebrand factor, suggesting that at least some of the murine fusion partners were of endothelial origin. FISH analysis of the hybrid cells revealed consistent spatial separation of human and murine DNA into distinct subcompartments of hybrid nuclei, a phenotype that was reproduced *in vitro*. Although the relevance of this spatial separation is unknown, it is interesting to speculate on the epigenetic and mitotic consequences of this arrangement. It is possible that chromosomes of one fusion partner are epigenetically favored over the other, resulting in transcriptional profiles very similar to parent cells. Alternatively, this compartmentalization could allow for lineage-specific DNA content to be easily separated in subsequent asymmetric cell divisions,[37] resulting in progeny with little or no genomic alterations. Because of the great similarities between the progeny of fusion products and unfused cells either of these mechanisms could lead to underestimation of the frequency of cell fusion by common detection techniques.

Further evidence for tumor cell-stromal cell fusion comes from implantation of primary human breast cancer cells from a pleural effusion into the mammary glands of nude mice.[156] Resultant tumor nuclei stained positive for both human and murine DNA. In addition, a cell line was created from the tumor that had a spindle-shaped stromal morphology and stained positive for several stromal markers. After immortalization, FISH analysis indicated that ~64% of interphase nuclei were mouse-human hybrids, while a significant portion of mitotic cells showed mouse/human chromosomal translocations. The DNA content of the analyzed synkaryons was ~4N in early passages, but gradual reduction of chromosomes was observed upon serial passaging. These data suggest that increased chromosomal content was beneficial for tumor cells

adapting to a new environment *in vitro*. Gradual loss of chromosomes with passage number could represent the stabilization of a new karyotype after cell fusion-induced CIN or simply the reduction of genetic load of cultured cells by loss of DNA content unnecessary for survival. Similar behavior is often observed in antibiotic resistant bacterial and mammalian cell lines upon removal of the selective pressure of antibiotics in the culture media.[157]

A more recent study investigated long-term gene expression of hybrid cells formed after transplantation of a primary human glioblastoma into a hamster cheek pouch.[158] After a year of passage *in vivo*, metastases were found to contain primarily hamster DNA, but still retained genes from at least six different human chromosomes as detected by PCR. Additionally, histochemical examination showed protein expression of at least three human genes after one year of passage. All three of the human proteins detected (CD74, CXCR4, and PLAGL2) have been implicated in cancer progression,[158] again suggesting selective retention and/or expression of genes beneficial for tumor cell survival and proliferation after cell fusion.

*A2.5.3 Tumor cell fusion with BMDCs*

Perhaps the longest[159] and most extensively investigated tumor cell fusion partners have been bone-marrow derived cells, especially immune cells such as macrophages. This is in part because the consequences of tumor cell fusion with immune cells agree well with numerous observations of cancer progression.

Tumors have been described as “wounds that do not heal”[160] and as such, recruit immune cells through the activation of the body’s natural inflammation response. A plethora of BMDCs are known to be present in the tumor microenvironment (reviewed

in[161]) and many, including $CD4^+$ T cells[162], mast cells[163], B cells[164], and macrophages[165] have been implicated in cancer progression or poor prognosis. Interestingly, chronic inflammation or other tissue injury has been shown to induce BMDC fusion in a wide variety of tissues, both in a cancer context[53,166] and in normal regenerative processes[38,39,167,168]. Especially interesting is the observation that BMDC fusion with diseased hepatocytes results in fusion products that repopulate the liver due to a selective advantage in the microenvironment[19]– a model that could be recapitulated in the tumor microenvironment.

Given these observations, it is not surprising that all three clinical case studies implicating cancer cell fusion have suggested BMDCs as the fusion partner. In two studies reported by Pawelek and colleagues, patients with a prior bone marrow transplant developed renal cell carcinomas.[20,169] In both cases, marrow-donor DNA was detected in mononuclear tumor cells. In the most striking example, the donor Y-chromosome was identified via FISH analysis in mononuclear tumor nuclei also containing three copies of the female host's $17^{th}$ chromosome, a signature of the tumor. Importantly, the Y chromosome was detected in a small area at the border of the tumor accounting for ~10% of the tumor area. This observation suggests a possible clonal expansion from the initial fusion event. In a third case, FISH analysis indicated that up to 48% of nuclei in multinucleated osteoclasts of a multiple myeloma patient were of myeloma origin, with all nuclei maintaining activation of transcription.[170]

It has also been suggested that carcinoma cells can undergo an epithelial-to-mesenchymal conversion during the transition from benign to malignant tumors. During this transition, cells lose tight cell-cell contacts and E-cadherin expression, and gain

migratory and invasive capacities of mesenchymal cells (reviewed in [171]). This change in phenotype can be easily imagined as a result of fusion of a tumor cell with an immune cell that depends on efficient migration to function effectively. Indeed, melanoma cell/macrophage fusion products have shown increased migratory capacity *in vitro*[172] and greater metastatic potential *in vivo*[173] compared to the parent melanoma line.

Macrophages are an especially promising fusion partner candidate, as they routinely fuse *in vivo* to form osteoclasts and giant cells.[69] It is worth noting that macrophages also share many characteristic properties of tumors, such as angiogenesis, protease secretion, and growth factor and other cytokine production.[174] Pollard and colleagues have pioneered the study of tumor-associated macrophages (TAMs) in mice models and have suggested that TAMs are essential for metastasis.[175] In human patients, macrophage density around the primary tumor has been correlated to poor prognosis in several studies.[165,176,177]

The characteristics of macrophage/melanoma fusion products *in vitro* have been studied extensively by Pawelek and colleagues and have been shown to exhibit multiple metastatic characteristics absent in the parent melanoma line, including increased motility,[172] increased proto-oncogene expression,[178] and macrophage-associated expression of β1,6 oligosaccharides.[179] Notably, many of these characteristics were reproduced after culturing cells from spontaneous metastases developed *in vivo*.[173] In this important study, a nude mouse with a homozygous tyrosinase mutation (c/c) developed a tumor after subcutaneous implantation of wild type (C/C) melanoma cells. Genetic analysis of metastases revealed a C/c genotype and a 30-40% increase in DNA content, suggesting the tumor cells had fused with host cells, possibly with metastasis

as a direct consequence. Subsequent *in vitro* culture of cells isolated from the metastases revealed characteristics similar to artificially derived melanoma-macrophage hybrids, such as increased motility and β1,6 oligosaccharide expression.

Additional evidence of *in vivo* tumor cell fusion with macrophages has been supplied recently in a study by Powell et al., in which green fluorescent protein (GFP)-labeled macrophages were introduced via parabiosis into a host harboring β-galactosidase-expressing intestinal tumors.[53] Double-labeled cells were observed in up to 20% of the tumor epithelia after parabiosis, however, as the intestinal epithelium completely renews every 3-5 days[180] it is unclear whether labeled macrophages fused with tumor epithelia or rather with a progenitor cell that later differentiated into epithelium, as has been shown previously.[166] In any case, transcriptome analysis of fusion products revealed transcription profiles with similarities to both native epithelial and macrophage transcriptomes. Significantly, over 3% of differentially regulated transcripts in the fusion products were unique in the fusion product compared to either parental cell line, providing evidence that nuclear reprogramming following cell fusion can result in gene expression completely distinct from either parent cell.

## A2.6 Alternative Mechanisms of Gene Transfer

Although cell fusion offers a promising route for genetic recombination and diversity generation within tumors, it is not the only possible mechanism. Macrophages also routinely perform phagocytosis and digestion of apoptotic cells, a process that has been shown to result in horizontal transfer of oncogenes into the phagocytic host.[181,182] Macrophages are known to associate extensively with necrotic areas in advanced

tumors[177] and it is reasonable to speculate that clearance of necrotic debris by macrophages may also result in genetic transfer of tumor cell DNA into the macrophage genome.

Tumor cell secretion of microvesicles via membrane blebbing and other mechanisms has been a recent focus of study.[183] These microvesicles have not been shown to contain DNA, but commonly harbor RNA and proteins, including activated oncogenic proteins.[184] Microvesicles could therefore transfer information between tumor cells or from tumor cells to the stroma through RNA or protein, bypassing the need for genetic recombination. Similarly, membrane nanotubes allow for transfer of vesicles and signaling molecules between cells, although evidence of these structures *in vivo* is lacking.[185]

It is also possible that information flows in the opposite direction, from the stroma to the tumor. A recent model of tumor progression returns to the idea of the tumor as a parasite. The model posits that tumor cells induce autophagy in the stromal microenvironment through oxidative stress, resulting in a release of nutrients that are used by the tumor for continued growth.[186] Although autophagy is normally thought to preserve genomic DNA content, mitochondrial DNA could be transferred to the tumor in this manner. Alternatively, information could again be transferred via RNA or proteins.

Finally, naked DNA is known to be taken up and expressed by a variety of cell types *in vivo*.[187] It is possible that DNA is released into the tumor microenvironment through apoptosis or necrosis and is simply randomly incorporated into the genome of tumor or stromal cells.

## A2.7 Detection of Cell Fusion

Given the potential impact, it is surprising that fundamental aspects of tumor cell fusion are unknown, including the soluble or insoluble signals that trigger fusion, the cell surface proteins responsible for mediating fusion, the kinetics of fusion within the metastatic cascade, or the mechanism of reprogramming and the functional capacity of hybrid cells after fusion. Hindering discovery in this area is lack of appropriate technology to 1) identify fusion partners poised to fuse and to 2) track fusion products over time. To address this problem we have recently developed imaging and characterization technologies to accurately identify fusion products immediately after cell fusion and to track fusion products over time both in vitro and in vivo.

### *A2.7.1 Historical Methods*

The origin of a cell as the product of a fusion event can be difficult to deduce since in many cases hybrid cells are morphologically identical to unfused cells (Figure 2B). Three methods have been used traditionally to overcome this difficulty. First, cell fusion can be detected using fluorescent cytoplasmic dyes which diffuse freely through the membranes of live cells. Once inside the cell, these mildly thiol-reactive probes react with intracellular components to produce cells that are fluorescent for at least 24 hours after labeling. Different dyes are used to label each fusion partner and fusion products are discerned by detecting overlapping fluorescence emission via flow cytometry or fluorescence microscopy. This method is ideal for short term *in vitro* studies; however *in vivo* studies are not possible and the fluorescence signal is undetectable at 72 hours in proliferating cells. In addition, dead cells can be endocytosed and the cell dye transferred as a consequence leading to false positives.

Second, cell fusion can be detected by the complementary action of genes; most commonly, the Cre-Lox system.[18] This method is robust, detecting only true fusion events and can be used *in vivo*. However, available reporter systems (i.e., beta-galactosidase, fluorescent proteins) limit *in vivo* analysis to excised tissues precluding the tracking of fusion events in the same organism over time. Third, fusion events can be detected by probing the DNA of different species or genders (X, Y chromosomes). When a cell of one species/gender fuses with a cell of another species/gender, *in situ* hybridization probes can be generated to species/gender-specific sites in the genome. More recently, genetic techniques such as single nucleotide polymorphism (SNP) and short-tandem repeat (STR) analysis have been utilized to identify DNA from multiple parents in fusion products.[188] However, these methods of detection of fusion events are also limited to excised tissue. Thus, there is a distinct lack of means to detect and track fusion products long term *in vitro* and *in vivo*.

*A2.7.2 New Approaches*

We have developed two new approaches for the detection of fusion products. The first utilizes bimolecular fluorescence complementation (BiFC). BiFC is a method of viewing the association of proteins inside living cells. Intact GFP (and its variants YFP, BFP, RFP, etc.) is fluorescent, and this property can be reconstituted when these proteins are broken into two halves by making each into an interactive fusion protein (Figure 2A).[189-191] Fluorescence is detected and recorded via traditional, time lapse, fluorescence microscopy. We believe this technique to be a powerful tool for detecting fusion *in vitro* and will be especially useful to determine the mechanism by which the fate of tumor cell hybrids is accomplished (i.e., nuclear fusion, rearrangement of genetic

material or other). Due to the inducible nature of the signal (i.e., fluorescent signal is detected only after a fusion event, instead of detection of overlapping fluorescent signals), the incidence of false-positives is essentially zero. In addition, the hybrids synthesize accumulating amounts of BiFC genes over time and so signal intensity increases over time (Figure 2B), instead of degrading over time as is the case for cytoplasmic dyes. However, this approach is limited in that it cannot easily be adapted to *in vivo* systems.

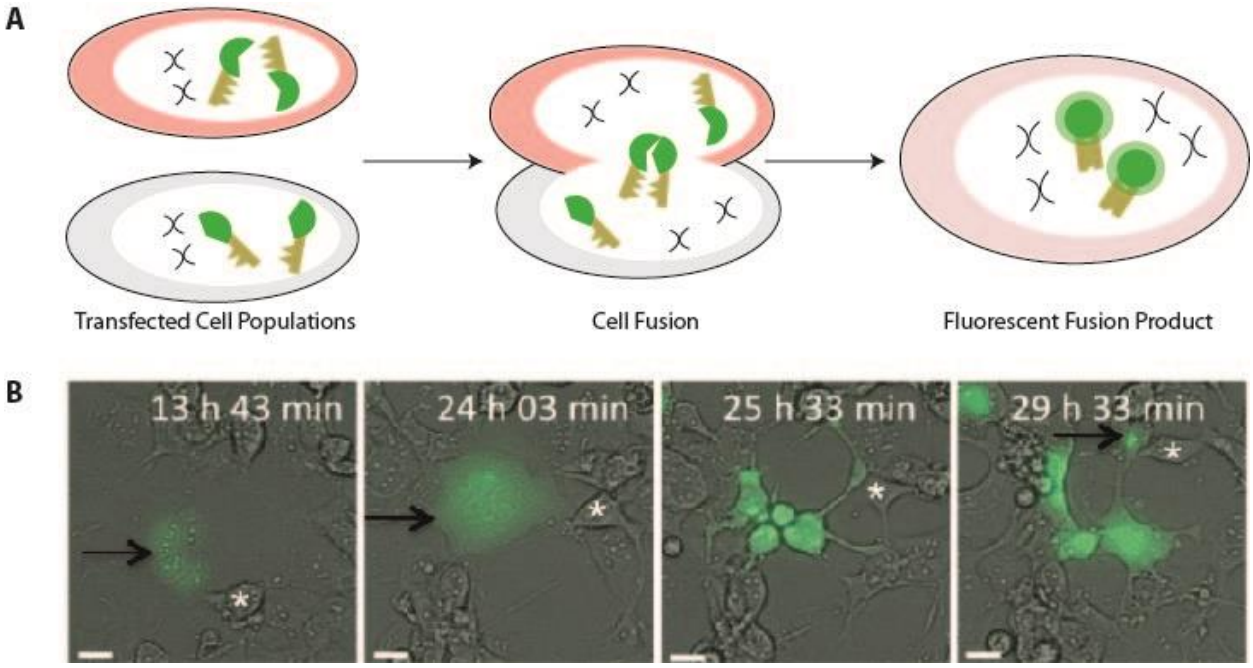


**Figure A2-2. Detection of cell fusion in vitro via BiFC. A)** Schematic of BiFC mechanism. Each BiFC construct contains half a YFP gene fused to genes encoding histone H3.1, which naturally dimerizes in the cell. The two BiFC constructs are transduced into separate cells. When the cells fuse, the YFP protein is reconstituted and a fluorescent signal is generated. **B)** Morphologic comparison of fusion products with unfused cells.[191] Plasmids corresponding to complementary BiFC constructs (YN-CBX5 and YC-CBX5) were transfected into separate populations of COS-1 cells. After transfection, populations were mixed and fusion was induced with poly(ethylene glycol). Fusion signals (green) were detected using fluorescence microscopy. The morphology of fused cells was monitored via time-lapse imaging for 30 hours. The initial fusion product is a clearly larger cell (black arrow, first two frames). When this cell divides, the four daughters remain green (and would be difficult to distinguish from other non-fused cells (white asterisk) were it not for the BiFC label).

To detect fusion products *in vivo* we have developed an approach to trigger bioluminescence upon fusion. We have developed a construct encoding the firefly (*Photinus pyralis*) luciferase gene placed downstream of a stop codon flanked by LoxP sequences (Figure 3A). When cells expressing this gene fuse with cells expressing the Cre protein, the LoxP sites are recombined resulting in excision of the stop signal and expression of luciferase (Figure 3B).[192] Akin to the BiFC method, this is an inducible method thereby limiting the incidence of false-positive signals. Unlike existing methods which utilize the Cre/Lox system, we have incorporated a "living" detection signal and thereby afford for the first time the opportunity to track the kinetics of cell fusion *in vivo*.

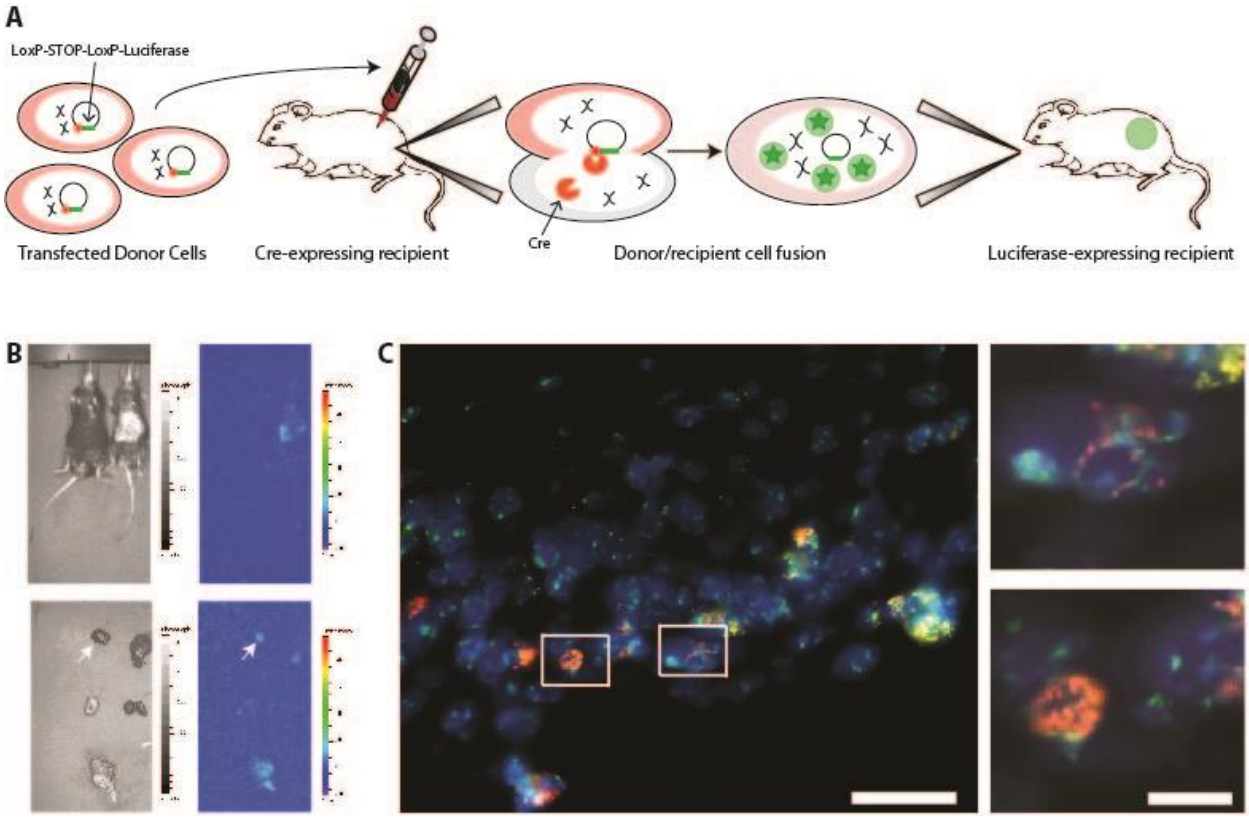


**Figure A2-3. Detection of cell fusion in vivo via Cre-LoxP bioluminescence. A)** Schematic of Cre-LoxP bioluminescence mechanism. Upon donor/recipient cell fusion, the Cre protein excises the floxed stop codon and luciferase is expressed in the fusion product. **B)** Detection of cell fusion *in vivo* via bioluminescent imaging. Human MSCs were transfected with two plasmids, one containing luciferace downstream of a floxed stop codon and the other containing the viral fusogen VSVG. Transfected MSCs were then transplanted into Cre-expressing mice.

Luminescent signal was present in experimental mice (top, right mouse) but not in sham controls (top, left mouse). Excision of organs (bottom) revealed luminescent signal, indicative of fusion, in multiple tissues including the heart (arrow). **C)** FISH analysis of bioluminescent heart tissue.[193] Insets display fusion products with nuclei staining positive for both human centromeres (red) and mouse centromeres (green). One fusion product (bottom right) is undergoing mitosis. Scale bar = 25μm.

## A2.8 Cancer Relevance

Despite mounting evidence that cell fusion or transfer of genetic material by various mechanisms could contribute to carcinogenesis and metastasis, critics contend that spontaneous fusion occurs too rarely to contribute in a relevant way to the initiation and propagation of diseases like cancer. In response, we offer a few points for consideration. First, we point to the lack of technology sensitive enough to determine the relative frequency of spontaneous fusion between tumor cells or their precursors with surrounding cell types. As noted above, the task is complicated by the uncertainty of rearrangement of cytoplasmic and nuclear components and the relative speed with which rearrangement takes place.

The choice of model system will be important to the assessment of the role of fusion in the future. Since it is unlikely that fusion assays will ever be done in humans, rodent models are an obvious choice. However, many mouse models are not spontaneously metastatic. The human tumor cell lines or human grafts that are in common use have already progressed past the point of genetic evolution likely to be catalyzed by cell fusion, and results from these may not reveal the full potential of this mechanism. Even if early stage lesions were transplanted, the mouse hosts will be immune-compromised, and this microenvironment may therefore be deficient in key cell fusion partners. It will be important to choose the correct assay to test this hypothesis.

How frequently does cell fusion have to occur to make it a credible mechanism? Given that fusion occurs frequently enough to be detected despite the limitations of current technology, using clinically relevant samples of tumors we propose that the answer may be “less frequently than is currently detected”. Now that novel tools exist for examining the role of fusion, we expect this hypothesis will be tested over the next few years. If cell fusion is indeed implicated in one (or all) facets of oncogenesis, this will represent an altogether novel and untested target for cancer therapeutics.

## A2.9 Conclusions

We have discussed the processes that regulate cell fusion, as it occurs naturally and spontaneously to govern normal tissue development and functionality, and the evidence for novel cell fusion events (and/or genetic transfer) that occur during pathogenic processes. These include viral infections, which include fusion events at various points of their life cycles, and the immune reactions that characterize inflammation. The details of these processes are known, including their molecular mediators. Given the emerging importance of inflammatory mediators during metastasis, it seems a logical extension to propose that cell fusion will be associated with this process, and that it could indeed be a functional effector of neoplastic changes. Cell fusion offers an opportunity for rapid genomic evolution. It may offer practical solutions to explain the (arguably) paradoxical timelines for tumors, and to generate mechanisms for the evolution of the massively rearranged genomes that are so characteristic of these tumors. Cell fusion can account for re-assortment of combinations of mutant and normal genomes in various copy numbers. It also offers

the potential to acquire cytoplasmic determinants of function (including mitochondria, trafficking components and cell signaling-related functions) that have been shown historically to be powerful mediators of the cancer cell phenotype. These functionalities may be acquired only transiently, to enable for example the enhanced motility or altered metabolism required for metastasis, and may largely revert after the fusion products resolve to stable daughter cells in metastatic outgrowths. The potential of this novel hypothesis stands on the brink of a full evaluation, with the development of new tools and methods. If these studies generate evidence in support of this hypothesis, this avenue opens the way to a whole new class of therapeutics that are likely to be highly selective for pathogenic processes.

## References


1 Gao, P. & Zheng, J. High-risk HPV E5-induced cell fusion: a critical initiating event in the early stage of HPV-associated cervical cancer. *J Virol* **7**, 238 (2010).

2 Paget, S. The distribution of secondary growth in cancer of breast. *Lancet* **1**, 571-573 (1889).

3 Huang, M., Li, Y., Zhang, H. & Nan, F. Research Breast cancer stromal fibroblasts promote the generation of CD44+CD24-cells through SDF-1/CXCR4 interaction. (2010).

4 Kessenbrock, K., Plaks, V. & Werb, Z. Matrix metalloproteinases: regulators of the tumor microenvironment. *Cell* **141**, 52-67 (2010).

5 Pinto, M. P. *et al.* Vascular Endothelial Growth Factor Secreted by Activated Stroma Enhances Angiogenesis and Hormone-Independent Growth of Estrogen Receptor–Positive Breast Cancer. *Cancer research* **70**, 2655 (2010).

6 Tyan, S. W. *et al.* Breast cancer cells induce cancer-associated fibroblasts to secrete hepatocyte growth factor to enhance breast tumorigenesis. *PloS one* **6**, e15313 (2011).

7 Su, G., Blaine, S. A., Qiao, D. & Friedl, A. Shedding of syndecan-1 by stromal fibroblasts stimulates human breast cancer cell proliferation via FGF2 activation. *Journal of Biological Chemistry* **282**, 14906-14915 (2007).

8 Wu, M. *et al.* Dissecting genetic requirements of human breast tumorigenesis in a tissue transgenic model of human breast cancer in mice. *Proceedings of the National Academy of Sciences* **106**, 7022 (2009).

9 Trimis, G., Chatzistamou, I., Politi, K., Kiaris, H. & Papavassiliou, A. G. Expression of p21waf1/Cip1 in stromal fibroblasts of primary breast tumors. *Human molecular genetics* **17**, 3596-3600 (2008).

10 Kiaris, H. *et al.* Evidence for nonautonomous effect of p53 tumor suppressor in carcinogenesis. *Cancer research* **65**, 1627 (2005).

11 Apostolopoulou, M. & Ligon, L. Cadherin-23 Mediates Heterotypic Cell-Cell Adhesion between Breast Cancer Epithelial Cells and Fibroblasts. *PloS one* **7**, e33289 (2012).

12 Forkner, C. E. THE ORIGIN AND FATE OF TWO TYPES OF MULTI-NUCLEATED GIANT CELLS IN THE CIRCULATING BLOOD. *J Exp Med* **52**, 279 (1930).

13 Duelli, D. & Lazebnik, Y. Cell fusion: a hidden enemy? *Cancer cell* **3**, 445-448 (2003).

14 Ogle, B. M., Cascalho, M. & Platt, J. L. Biological implications of cell fusion. *Nature reviews. Molecular cell biology* **6**, 567-575, doi:10.1038/nrm1678 (2005).

15 Gussoni, E. *et al.* Long-term persistence of donor nuclei in a Duchenne muscular dystrophy patient receiving bone marrow transplantation. *Journal of Clinical Investigation* **110**, 807-814 (2002).

16 Gibson, A. J. *et al.* Dermal fibroblasts convert to a myogenic lineage in mdx mouse muscle. *J Cell Sci* **108 ( Pt 1)**, 207-214 (1995).

17 Weimann, J. M., Johansson, C. B., Trejo, A. & Blau, H. M. Stable reprogrammed heterokaryons form spontaneously in Purkinje neurons after bone marrow transplant. *Nat Cell Biol* **5**, 959-966, doi:10.1038/ncb1053 (2003).

18 Alvarez-Dolado, M. *et al.* Fusion of bone-marrow-derived cells with Purkinje neurons, cardiomyocytes and hepatocytes. *Nature* **425**, 968-973, doi:10.1038/nature02069 (2003).

19 Wang, X. *et al.* Cell fusion is the principal source of bone-marrow-derived hepatocytes. *Nature* **422**, 897-901, doi:10.1038/nature01531 (2003).

20 Yilmaz, Y., Lazova, R., Qumsiyeh, M., Cooper, D. & Pawelek, J. Donor Y chromosome in renal carcinoma cells of a female BMT recipient: visualization of putative BMT-tumor hybrids by FISH. *Bone marrow transplantation* **35**, 1021-1024, doi:10.1038/sj.bmt.1704939 (2005).

21 Hyman, E. *et al.* Impact of DNA amplification on gene expression patterns in breast cancer. *Cancer research* **62**, 6240 (2002).

22 Pollack, J. R. *et al.* Microarray analysis reveals a major direct role of DNA copy number alteration in the transcriptional program of human breast tumors. *Proceedings of the National Academy of Sciences* **99**, 12963 (2002).

23 Hau, P. M., Siu, W. Y., Wong, N., Lai, P. B. & Poon, R. Y. Polyploidization increases the sensitivity to DNA-damaging agents in mammalian cells. *FEBS Lett* **580**, 4727-4736, doi:10.1016/j.febslet.2006.07.059 (2006).

24 Wong, C. & Stearns, T. Mammalian cells lack checkpoints for tetraploidy, aberrant centrosome number, and cytokinesis failure. *BMC cell biology* **6**, 6 (2005).

25 Gao, P. & Zheng, J. Oncogenic virus-mediated cell fusion: new insights into initiation and progression of oncogenic viruses--related cancers. *Cancer letters* **303**, 1-8, doi:10.1016/j.canlet.2010.12.021 (2011).

26 Duelli, D. & Lazebnik, Y. Cell-to-cell fusion as a link between viruses and cancer. *Nat Rev Cancer* **7**, 968-976, doi:10.1038/nrc2272 (2007).

27 Ganem, N. J., Godinho, S. A. & Pellman, D. A mechanism linking extra centrosomes to chromosomal instability. *Nature* **460**, 278-282 (2009).

28 Yang, Z., Lončarek, J., Khodjakov, A. & Rieder, C. L. Extra centrosomes and/or chromosomes prolong mitosis in human cells. *Nat Cell Biol* **10**, 748-751 (2008).

29 Köhler, G. & Milstein, C. Continuous cultures of fused cells secreting antibody of predefined specificity. *Nature* **256**, 495-497 (1975).

30 Olsson, L. *et al.* Antibody producing human-human hybridomas. I. Technical aspects. *Journal of Immunological methods* **61**, 17-32 (1983).

31 Ebeling, S. B. *et al.* Human chromosome 21 determines growth factor dependence in human/mouse B-cell hybridomas. *Cancer research* **58**, 2863-2868 (1998).

32 Dalm, M. C. F. *et al.* Stable hybridoma cultivation in a pilot-scale acoustic perfusion system: Long-term process performance and effect of recirculation rate. *Biotechnology and bioengineering* **91**, 894-900 (2005).

33 Dewar, V., Voet, P., Denamur, F. & Smal, J. Industrial implementation of in vitro production of monoclonal antibodies. *ILAR JOURNAL* **46**, 307 (2005).

34 Mable, B. K. & Otto, S. P. Masking and purging mutations following EMS treatment in haploid, diploid and tetraploid yeast (Saccharomyces cerevisiae). *Genetical research* **77**, 9-26 (2001).

35 Levine, D. S., Sanchez, C. A., Rabinovitch, P. S. & Reid, B. J. Formation of the tetraploid intermediate is associated with the development of cells with more than four centrioles in the elastase-simian virus 40 tumor antigen transgenic mouse model of pancreatic cancer. *Proceedings of the National Academy of Sciences* **88**, 6427 (1991).

36 Nigg, E. A. Centrosome aberrations: cause or consequence of cancer progression? *Nat Rev Cancer* **2**, 815-825 (2002).

37 Vitale, I. *et al.* Multipolar mitosis of tetraploid cells: inhibition by p53 and dependency on Mos. *The EMBO journal* **29**, 1272-1284 (2010).

38 Grompe, M. The role of bone marrow stem cells in liver regeneration. *Seminars in liver disease* **23**, 363-372, doi:10.1055/s-2004-815560 (2003).

39 Vassilopoulos, G., Wang, P. R. & Russell, D. W. Transplanted bone marrow regenerates liver by cell fusion. *Nature* **422**, 901-904 (2003).

40 Duncan, A. W. *et al.* Ploidy reductions in murine fusion-derived hepatocytes. *PLoS genetics* **5**, e1000385 (2009).

41 Duncan, A. W. *et al.* The ploidy conveyor of mature hepatocytes as a source of genetic variation. *Nature* **467**, 707-710 (2010).

42 Gupta, S. 161-171 (Elsevier).

43 Oberringer, M. *et al.* Centrosome multiplication accompanies a transient clustering of polyploid cells during tissue repair. *Molecular Cell Biology Research Communications* **2**, 190-196 (1999).

44 Storchova, Z. & Pellman, D. From polyploidy to aneuploidy, genome instability and cancer. *Nature Reviews Molecular Cell Biology* **5**, 45-54 (2004).

45 Gurdon, J. & Melton, D. Nuclear reprogramming in cells. *Science* **322**, 1811 (2008).

46 Lin, H. P. & Ogle, B. M. in *Encyclopedia for Stem Cell Research* 369-399 (Sage Publications, 2008).

47 Wilmut, I., Schnieke, A., McWhir, J., Kind, A. & Campbell, K. Viable offspring derived from fetal and adult mammalian cells. *Clones and clones: facts and fantasies about human cloning*, 21 (1999).

48 Blau, H. M., Chiu, C. P. & Webster, C. Cytoplasmic activation of human nuclear genes in stable heterocaryons. *Cell* **32**, 1171-1180 (1983).

49 Davidson, R. L., Ephrussi, B. & Yamamoto, K. Regulation of pigment synthesis in mammalian cells, as studied by somatic hybridization. *Proc Natl Acad Sci U S A* **56**, 1437 (1966).

50 Tada, M., Tada, T., Lefebvre, L., Barton, S. C. & Surani, M. A. Embryonic germ cells induce epigenetic reprogramming of somatic nucleus in hybrid cells. *The EMBO journal* **16**, 6510-6520 (1997).

51 Yamanaka, S. & Blau, H. M. Nuclear reprogramming to a pluripotent state by three approaches. *Nature* **465**, 704-712 (2010).

52 Kimura, H., Tada, M., Nakatsuji, N. & Tada, T. Histone code modifications on pluripotential nuclei of reprogrammed somatic cells. *Molecular and Cellular Biology* **24**, 5710 (2004).

53 Powell, A. E. *et al.* Fusion between intestinal epithelial cells and macrophages in a cancer context results in nuclear reprogramming. *Cancer research* **71**, 1497 (2011).

54 Wolfe, K. H. Yesterday's polyploids and the mystery of diploidization. *Nature Reviews Genetics* **2**, 333-341 (2001).

55 Wendel, J. F. Genome evolution in polyploids. *Plant molecular biology* **42**, 225-249 (2000).

56 Chester, M. *et al.* Extensive chromosomal variation in a recently formed natural allopolyploid species, Tragopogon miscellus (Asteraceae). *Proceedings of the National Academy of Sciences* **109**, 1176-1181 (2012).

57 Eldredge, N. & Gould, S. J. Punctuated equilibria: an alternative to phyletic gradualism. *Models in paleobiology* **82**, 115 (1972).

58 Sagan, L. On the origin of mitosing cells. *Journal of Theoretical Biology* **14**, 225-274, IN221-IN226 (1967).

59 Oren-Suissa, M. & Podbilewicz, B. Cell fusion during development. *Trends Cell Biol* **17**, 537-546 (2007).

60 Chen, E. H., Grote, E., Mohler, W. & Vignery, A. Cell–cell fusion. *FEBS Lett* **581**, 2181-2193, doi:10.1016/j.febslet.2007.03.033 (2007).

61 Helming, L. & Gordon, S. Molecular mediators of macrophage fusion. *Trends Cell Biol* **19**, 514-522, doi:10.1016/j.tcb.2009.07.005 (2009).

62 Shinn-Thomas, J. H. & Mohler, W. A. in *International Review of Cell and Molecular Biology* Vol. Volume 289 (ed W. Jeon Kwang) 149-209 (Academic Press, 2011).

63 Boyle, W. J., Simonet, W. S. & Lacey, D. L. Osteoclast differentiation and activation. *Nature* **423**, 337-342 (2003).

64 Moreno, J. L., Mikhailenko, I., Tondravi, M. M. & Keegan, A. D. IL-4 promotes the formation of multinucleated giant cells from macrophage precursors by a STAT6-dependent, homotypic mechanism: contribution of E-cadherin. *Journal of leukocyte biology* **82**, 1542-1553 (2007).

65 Yagi, M. *et al.* Induction of DC-STAMP by Alternative Activation and Downstream Signaling Mechanisms. *Journal of Bone and Mineral Research* **22**, 992-1001 (2007).

66 Yagi, M. *et al.* DC-STAMP is essential for cell–cell fusion in osteoclasts and foreign body giant cells. *J Exp Med* **202**, 345 (2005).

67 Helming, L. *et al.* Essential role of DAP12 signaling in macrophage programming into a fusion-competent state. *Science signaling* **1**, ra11 (2008).

68 Kyriakides, T. R. *et al.* The CC chemokine ligand, CCL2/MCP1, participates in macrophage fusion and foreign body giant cell formation. *The American journal of pathology* **165**, 2157 (2004).

69 Vignery, A. Macrophage fusion: the making of osteoclasts and giant cells. *J Exp Med* **202**, 337-340, doi:10.1084/jem.20051123 (2005).

70 Majeti, R. *et al.* CD47 is an adverse prognostic factor and therapeutic antibody target on human acute myeloid leukemia stem cells. *Cell* **138**, 286-299 (2009).

71 Liu, A. Y. Differential expression of cell surface molecules in prostate cancer cells. *Cancer research* **60**, 3429 (2000).

72 Baier, P., Eggstein, S., Wolff-Vorbeck, G., Baumgartner, U. & Hopt, U. Chemokines in human colorectal carcinoma. *Anticancer research* **25**, 3581 (2005).

73 Zijlmans, H. J. *et al.* The absence of CCL2 expression in cervical carcinoma is associated with increased survival and loss of heterozygosity at 17q11. 2. *The Journal of pathology* **208**, 507-517 (2006).

74 Pawelek, J. M. & Chakraborty, A. K. The cancer cell-leukocyte fusion theory of metastasis. *Advances in cancer research* **101**, 397-444 (2008).

75 Aspord, C. *et al.* Breast cancer instructs dendritic cells to prime interleukin 13–secreting CD4+ T cells that facilitate tumor development. *J Exp Med* **204**, 1037 (2007).

76 Sens, K. L. *et al.* An invasive podosome-like structure promotes fusion pore formation during myoblast fusion. *The Journal of cell biology* **191**, 1013 (2010).

77 Jay, S. M., Skokos, E., Laiwalla, F., Krady, M. M. & Kyriakides, T. R. Foreign body giant cell formation is preceded by lamellipodia formation and can be attenuated by inhibition of Rac1 activation. *The American journal of pathology* **171**, 632 (2007).

78 Miyado, K. *et al.* Requirement of CD9 on the egg plasma membrane for fertilization. *Science* **287**, 321 (2000).

79 Kaji, K., Oda, S., Miyazaki, S. & Kudo, A. Infertility of CD9-deficient mouse eggs is reversed by mouse CD9, human CD9, or mouse CD81; polyadenylated mRNA injection developed for molecular analysis of sperm-egg fusion. *Developmental biology* **247**, 327-334 (2002).

80 Jégou, A. *et al.* CD9 tetraspanin generates fusion competent sites on the egg membrane for mammalian fertilization. *Proceedings of the National Academy of Sciences* **108**, 10946 (2011).

81 Okabe, M. *et al.* Capacitation-related changes in antigen distribution on mouse sperm heads and its relation to fertilization rate in vitro. *Journal of reproductive immunology* **11**, 91-100 (1987).

82 Inoue, N., Ikawa, M., Isotani, A. & Okabe, M. The immunoglobulin superfamily protein Izumo is required for sperm to fuse with eggs. *Nature* **434**, 234-238 (2005).

83 Larsson, L. I., Bjerregaard, B. & Talts, J. F. Cell fusions in mammals. *Histochemistry and cell biology* **129**, 551-561 (2008).

84 Chen, E. H. & Olson, E. N. Unveiling the mechanisms of cell-cell fusion. *Science* **308**, 369 (2005).

85 Kohler, G. & Milstein, C. Continuous cultures of fused cells secreting antibody of predefined specificity. *Nature* **256**, 495-497 (1975).

86 Hu, L. *et al.* Human papillomavirus 16 E5 induces bi-nucleated cell formation by cell-cell fusion. *Virology* **384**, 125-134 (2009).

87 Iessi, E., Marino, M. L., Lozupone, F., Fais, S. & De Milito, A. Tumor acidity and malignancy: novel aspects in the design of anti-tumor therapy. *Cancer Therapy* **6**, 55-66 (2008).

88 Storchova, Z. & Kuffer, C. The consequences of tetraploidy and aneuploidy. *J Cell Sci* **121**, 3859 (2008).

89 Hansemann, D. Ueber asymmetrische Zelltheilung in Epithelkrebsen und deren biologische Bedeutung. *Virchows Archiv* **119**, 299-326 (1890).

90 Storchová, Z. *et al.* Genome-wide genetic analysis of polyploidy in yeast. *Nature* **443**, 541-547 (2006).

91 Lu, X. & Kang, Y. Cell fusion as a hidden force in tumor progression. *Cancer research* **69**, 8536 (2009).

92 Rajagopalan, H. & Lengauer, C. Aneuploidy and cancer. *Nature* **432**, 338-341 (2004).

93 Barrett, M. T. *et al.* Molecular phenotype of spontaneously arising 4N (G2-tetraploid) intermediates of neoplastic progression in Barrett's esophagus. *Cancer research* **63**, 4211 (2003).

94 Rabinovitch, P. S., Longton, G., Blount, P. L., Levine, D. S. & Reid, B. J. Predictors of progression in Barrett's esophagus III: baseline flow cytometric variables. *The American journal of gastroenterology* **96**, 3071-3083 (2001).

95 Olaharski, A. J. *et al.* Tetraploidy and chromosomal instability are early events during cervical carcinogenesis. *Carcinogenesis* **27**, 337-343 (2006).

96 Abou-Elhamd, K. E. A. & Habib, T. N. The flow cytometric analysis of premalignant and malignant lesions in head and neck squamous cell carcinoma. *Oral oncology* **43**, 366-372 (2007).

97 Dictor, M., Fernö, M. & Baldetorp, B. Flow cytometric DNA content in Kaposi's sarcoma by histologic stage. Comparison with angiosarcoma. *Analytical and quantitative cytology and histology/the International Academy of Cytology [and] American Society of Cytology* **13**, 201 (1991).

98 Fujiwara, T. *et al.* Cytokinesis failure generating tetraploids promotes tumorigenesis in p53-null cells. *Nature* **437**, 1043-1047 (2005).

99 Roschke, A. V. *et al.* Karyotypic complexity of the NCI-60 drug-screening panel. *Cancer research* **63**, 8634 (2003).

100 Abdel-Rahman, W. M. *et al.* Spectral karyotyping suggests additional subsets of colorectal cancers characterized by pattern of chromosome rearrangement. *Proceedings of the National Academy of Sciences* **98**, 2538 (2001).

101 Sirivatanauksorn, V. *et al.* Non-random chromosomal rearrangements in pancreatic cancer cell lines identified by spectral karyotyping. *International Journal of Cancer* **91**, 350-358 (2001).

102 Davidson, J. *et al.* Molecular cytogenetic analysis of breast cancer cell lines. *British journal of cancer* **83**, 1309 (2000).

103 Wistuba, I. I. *et al.* Comparison of features of human lung cancer cell lines and their corresponding tumors. *Clinical cancer research* **5**, 991-1000 (1999).

104 Andreassen, P. R., Lohez, O. D., Lacroix, F. B. & Margolis, R. L. Tetraploid state induces p53-dependent arrest of nontransformed mammalian cells in G1. *Molecular biology of the cell* **12**, 1315-1328 (2001).

105 Margolis, R. L., Lohez, O. D. & Andreassen, P. R. G1 tetraploidy checkpoint and the suppression of tumorigenesis. *Journal of cellular biochemistry* **88**, 673-683 (2003).

106 Uetake, Y. & Sluder, G. Cell cycle progression after cleavage failure. *The Journal of cell biology* **165**, 609 (2004).

107 Duelli, D. M., Hearn, S., Myers, M. P. & Lazebnik, Y. A primate virus generates transformed human cells by fusion. *The Journal of cell biology* **171**, 493-503 (2005).

108 Duelli, D. M. *et al.* A virus causes cancer by inducing massive chromosomal instability through cell fusion. *Current biology : CB* **17**, 431-437, doi:10.1016/j.cub.2007.01.049 (2007).

109 Greenberg, R. Telomeres, crisis and cancer. *Current molecular medicine* **5**, 213-218 (2005).

110 Chin, K. *et al.* In situ analyses of genome instability in breast cancer. *Nat Genet* **36**, 984-988 (2004).

111 Lin, T. T. *et al.* Telomere dysfunction and fusion during the progression of chronic lymphocytic leukemia: evidence for a telomere crisis. *Blood* **116**, 1899-1907 (2010).

112 Stewénius, Y. *et al.* Structural and numerical chromosome changes in colon cancer develop through telomere-mediated anaphase bridges, not through mitotic multipolarity. *Proc Natl Acad Sci U S A* **102**, 5541 (2005).

113 Chan, J. Y. A Clinical Overview of Centrosome Amplification in Human Cancers. *International journal of biological sciences* **7**, 1122 (2011).

114 Weaver, B. A. A., Silk, A. D., Montagna, C., Verdier-Pinard, P. & Cleveland, D. W. Aneuploidy acts both oncogenically and as a tumor suppressor. *Cancer cell* **11**, 25-36 (2007).

115 Rao, C. V. *et al.* Colonic tumorigenesis in BubR1+/–ApcMin/+ compound mutant mice is linked to premature separation of sister chromatids and enhanced genomic instability. *Proc Natl Acad Sci U S A* **102**, 4365 (2005).

116 Sussan, T. E., Annan Yang, F. L., Ostrowski, M. C. & Reeves, R. H. Trisomy represses ApcMin-mediated tumours in mouse models of Down's syndrome. *Nature* **451**, 73-75 (2008).

117 Jeganathan, K., Malureanu, L., Baker, D. J., Abraham, S. C. & Van Deursen, J. M. Bub1 mediates cell death in response to chromosome missegregation and acts to suppress spontaneous tumorigenesis. *The Journal of cell biology* **179**, 255-267 (2007).

118 Wang, Z., Yu, R. & Melmed, S. Mice lacking pituitary tumor transforming gene show testicular and splenic hypoplasia, thymic hyperplasia, thrombocytopenia, aberrant cell cycle progression, and premature centromere division. *Molecular Endocrinology* **15**, 1870-1879 (2001).

119 Yu, R., Lu, W., Chen, J., McCabe, C. J. & Melmed, S. Overexpressed pituitary tumor-transforming gene causes aneuploidy in live human cells. *Endocrinology* **144**, 4991-4998 (2003).

120 Chesnokova, V., Kovacs, K., Castro, A. V., Zonis, S. & Melmed, S. Pituitary hypoplasia in Pttg−/− mice is protective for Rb+/− pituitary tumorigenesis. *Molecular Endocrinology* **19**, 2371-2379 (2005).

121 Donangelo, I. *et al.* Pituitary tumor transforming gene overexpression facilitates pituitary tumor development. *Endocrinology* **147**, 4781-4791 (2006).

122 Yang, Q., Rasmussen, S. A. & Friedman, J. Mortality associated with Down's syndrome in the USA from 1983 to 1997: a population-based study. *The Lancet* **359**, 1019-1025 (2002).

123 Satge, D. *et al.* A tumor profile in Down syndrome. *American journal of medical genetics* **78**, 207-216 (1998).

124 Hasle, H., Clemmensen, I. H. & Mikkelsen, M. Risks of leukaemia and solid tumours in individuals with Down's syndrome. *The Lancet* **355**, 165-169 (2000).

125 Stanbridge, E. J. Suppression of malignancy in human cells. *Nature* **260**, 17 (1976).

126 Harris, H., Miller, O., Klein, G., Worst, P. & Tachibana, T. Suppression of malignancy by cell fusion. *Nature* **223**, 363 (1969).

127 Anderson, M. & Stanbridge, E. Tumor suppressor genes studied by cell hybridization and chromosome transfer. *The FASEB journal* **7**, 826 (1993).

128 Mitelman, F., Johansson, B. & Mertens, F. (2011).

129 Kuukasjärvi, T. *et al.* Genetic heterogeneity and clonal evolution underlying development of asynchronous metastasis in human breast cancer. *Cancer research* **57**, 1597-1604 (1997).

130 Waldman, F. M. *et al.* Chromosomal alterations in ductal carcinomas in situ and their in situ recurrences. *Journal of the National Cancer Institute* **92**, 313-320 (2000).

131 Hunter, K. W., Crawford, N. & Alsarraj, J. Mechanisms of metastasis. *Breast Cancer Res* **10**, S2 (2008).

132 Lazebnik, Y. What are the hallmarks of cancer? *Nat Rev Cancer* **10**, 232-233 (2010).

133 Hanahan, D. & Weinberg, R. A. Hallmarks of cancer: the next generation. *Cell* **144**, 646-674 (2011).

134 Klein, C. A. Parallel progression of primary tumours and metastases. *Nat Rev Cancer* **9**, 302-312 (2009).

135 Katoh, M., Neumaier, M., Nezam, R., Izbicki, J. & Schumacher, U. Correlation of circulating tumor cells with tumor size and metastatic load in a spontaneous lung metastasis model. *Anticancer research* **24**, 1421-1426 (2004).

136 Ding, L. *et al.* Genome remodelling in a basal-like breast cancer metastasis and xenograft. *Nature* **464**, 999-1005 (2010).

137 Abbruzzese, J. L. *et al.* Unknown primary carcinoma: natural history and prognostic factors in 657 consecutive patients. *Journal of clinical oncology* **12**, 1272-1280 (1994).

138 Van de Wouw, A., Janssen-Heijnen, M., Coebergh, J. & Hillen, H. Epidemiology of unknown primary tumours; incidence and population-based survival of 1285 patients in Southeast Netherlands, 1984–1992. *European Journal of Cancer* **38**, 409-413 (2002).

139 Friberg, S. & Mattson, S. On the growth rates of human malignant tumors: implications for medical decision making. *Journal of surgical oncology* **65**, 284-297 (1997).

140 Peer, P. G. M., Van Dijck, J. A. A. M., Verbeek, A. L. M., Hendriks, J. H. C. L. & Holland, R. Age-dependent growth rate of primary breast cancer. *Cancer* **71**, 3547-3551 (1993).

141 Parris, G. E. Clinically significant cancer evolves from transient mutated and/or aneuploid neoplasia by cell fusion to form unstable syncytia that give rise to ecologically viable parasite species. *Medical hypotheses* **65**, 846-850 (2005).

142 Duesberg, P., Fabarius, A. & Hehlmann, R. Aneuploidy, the primary cause of the multilateral genomic instability of neoplastic and preneoplastic cells. *IUBMB life* **56**, 65-81 (2004).

143 Muller, H. The relation of recombination to mutational advance. *Mutation Research/Fundamental and Molecular Mechanisms of Mutagenesis* **1**, 2-9 (1964).

144 Risques, R. A. *et al.* Genetic pathways and genome-wide determinants of clinical outcome in colorectal cancer. *Cancer research* **63**, 7206 (2003).

145 Staibano, S. *et al.* Loss of oestrogen receptor β, high PCNA and p53 expression and aneuploidy as markers of worse prognosis in ovarian granulosa cell tumours. *Histopathology* **43**, 254-262 (2003).

146 Choma, D., Daures, J., Quantin, X. & Pujol, J. Aneuploidy and prognosis of non-small-cell lung cancer: a meta-analysis of published data. *British journal of cancer* **85**, 14 (2001).

147 Southern, J. F., Warshaw, A. L. & Lewandrowski, K. B. DNA ploidy analysis of mucinous cystic tumors of the pancreas: correlation of aneuploidy with malignancy and poor prognosis. *Cancer* **77**, 58-62 (1996).

148 Vinogradov, A., Anatskaya, O. & Kudryavtsev, B. Relationship of hepatocyte ploidy levels with body size and growth rate in mammals. *Genome* **44**, 350-360 (2001).

149 Brodsky, V. Y. & Delone, G. Functional control of hepatocyte proliferation. Comparison with the temporal control of cardiomyocyte proliferation. *Biomedical science* **1**, 467 (1990).

150 Torres, S. *et al.* Thyroid hormone regulation of rat hepatocyte proliferation and polyploidization. *American Journal of Physiology-Gastrointestinal and Liver Physiology* **276**, G155-G163 (1999).

151 Klein, P. A., Xiang, J. & Kimura, A. K. Melanoma cells growing in aggregates on a non-adhesive poly (HEMA) substrate exhibit polykaryocytosis but do not develop an increased metastatic capability. *Clinical and Experimental Metastasis* **2**, 287-295 (1984).

152 Lu, X. & Kang, Y. Efficient acquisition of dual metastasis organotropism to bone and lung through stable spontaneous fusion between MDA-MB-231 variants. *Proceedings of the National Academy of Sciences* **106**, 9385 (2009).

153 Goldenberg, D. M., Pavia, R. A. & Tsao, M. C. In vivo hybridisation of human tumour and normal hamster cells. (1974).

154 Kerbel, R. S., Lagarde, A., Dennis, J. & Donaghue, T. Spontaneous fusion in vivo between normal host and tumor cells: possible contribution to tumor progression and

metastasis studied with a lectin-resistant mutant tumor. *Molecular and Cellular Biology* **3**, 523 (1983).

155 Mortensen, K., Lichtenberg, J., Thomsen, P. & Larsson, L. I. Spontaneous fusion between cancer cells and endothelial cells. *Cellular and molecular life sciences* **61**, 2125-2131 (2004).

156 Jacobsen, B. M. *et al.* Spontaneous fusion with, and transformation of mouse stroma by, malignant human breast cancer epithelium. *Cancer research* **66**, 8274 (2006).

157 Smith, M. A. & Bidochka, M. J. Bacterial fitness and plasmid loss: the importance of culture conditions and plasmid size. *Canadian journal of microbiology* **44**, 351-355 (1998).

158 Goldenberg, D. M. *et al.* Horizontal transmission and retention of malignancy, as well as functional human genes, after spontaneous fusion of human glioblastoma and hamster host cells in vivo. *International Journal of Cancer* (2011).

159 Aichel, O. *Ueber Zellverschmelzung mit qualitativ abnormer Chromosomenverteilung als Ursache der Geschwulstbildung, von Prof. Dr. Med. Et phil. Otto Aichel*. (W. Engelmann, 1911).

160 Dvorak, H. F. Tumors: wounds that do not heal. Similarities between tumor stroma generation and wound healing. *The New England journal of medicine* **315**, 1650 (1986).

161 Pollard, J. W. Trophic macrophages in development and disease. *Nature Reviews Immunology* **9**, 259-270 (2009).

162 DeNardo, D. G. *et al.* CD4+ T cells regulate pulmonary metastasis of mammary carcinomas by enhancing protumor properties of macrophages. *Cancer cell* **16**, 91-102 (2009).

163 Ribatti, D., Crivellato, E., Roccaro, A., Ria, R. & Vacca, A. Mast cell contribution to angiogenesis related to tumour progression. *Clinical & Experimental Allergy* **34**, 1660-1664 (2004).

164 De Visser, K. E., Korets, L. V. & Coussens, L. M. De novo carcinogenesis promoted by chronic inflammation is B lymphocyte dependent. *Cancer cell* **7**, 411-423 (2005).

165 Dave, S. S. *et al.* Prediction of survival in follicular lymphoma based on molecular features of tumor-infiltrating immune cells. *New England Journal of Medicine* **351**, 2159-2169 (2004).

166 Rizvi, A. Z. *et al.* Bone marrow-derived cells fuse with normal and transformed intestinal stem cells. *PNAS* **103**, 6321-6325 (2006).

167 Johansson, C. B. *et al.* Extensive fusion of haematopoietic cells with Purkinje neurons in response to chronic inflammation. *Nat Cell Biol* **10**, 575-583 (2008).

168 Nygren, J. M. *et al.* Myeloid and lymphoid contribution to non-haematopoietic lineages through irradiation-induced heterotypic cell fusion. *Nat Cell Biol* **10**, 584-592 (2008).

169 Chakraborty, A. *et al.* Donor DNA in a renal cell carcinoma metastasis from a bone marrow transplant recipient. *Bone marrow transplantation* **34**, 183-186 (2004).

170 Andersen, T. L. *et al.* Osteoclast nuclei of myeloma patients show chromosome translocations specific for the myeloma cell clone: a new type of cancer–host partnership? *The Journal of pathology* **211**, 10-17 (2007).

171 Thiery, J. P., Acloque, H., Huang, R. Y. J. & Nieto, M. A. Epithelial-mesenchymal transitions in development and disease. *Cell* **139**, 871-890 (2009).

172 Rachkovsky, M. & Pawelek, J. Acquired melanocyte stimulating hormone-inducible chemotaxis following macrophage fusion with Cloudman S91 melanoma cells. *Cell growth & differentiation: the molecular biology journal of the American Association for Cancer Research* **10**, 517 (1999).

173 Sodi, S. *et al.* Melanoma× Macrophage Fusion Hybrids Acquire Increased Melanogenesis and Metastatic Potential: Altered N-Glycosylation as an Underlying Mechanism. *Pigment cell research* **11**, 299-309 (1998).

174 Pollard, J. W. Tumour-educated macrophages promote tumour progression and metastasis. *Nat Rev Cancer* **4**, 71-78 (2004).

175 Condeelis, J. & Pollard, J. W. Macrophages: obligate partners for tumor cell migration, invasion, and metastasis. *Cell* **124**, 263-266 (2006).

176 Bingle, L., Brown, N. & Lewis, C. The role of tumour-associated macrophages in tumour progression: implications for new anticancer therapies. *The Journal of pathology* **196**, 254-265 (2002).

177 Pollard, J. W. Macrophages define the invasive microenvironment in breast cancer. *Journal of leukocyte biology* **84**, 623-630 (2008).

178 Chakraborty, A. K. *et al.* Expression of c-Met Proto-oncogene in Metastatic Macrophage Melanoma Fusion Hybrids: Implication of Its Possible Role in MSH-Induced Motility. *Oncology Research Featuring Preclinical and Clinical Cancer Therapeutics* **14**, 163-174 (2003).

179 Chakraborty, A. K. *et al.* Fusion hybrids with macrophage and melanoma cells up-regulate N-acetylglucosaminyltransferase V, β1-6 branching, and metastasis. *Cell growth and differentiation* **12**, 623-630 (2001).

180 Wright, N. A. Epithelial stem cell repertoire in the gut: clues to the origin of cell lineages, proliferative units and cancer. *Int J Exp Pathol* **81**, 117-143 (2000).

181 Holmgren, L. *et al.* Horizontal transfer of DNA by the uptake of apoptotic bodies. *Blood* **93**, 3956 (1999).

182 Bergsmedh, A. *et al.* Horizontal transfer of oncogenes by uptake of apoptotic bodies. *Proceedings of the National Academy of Sciences* **98**, 6407 (2001).

183 Al-Nedawi, K., Meehan, B. & Rak, J. Messengers and mediators of tumor progression. *Cell Cycle* **8**, 2014-2018 (2009).

184 Al-Nedawi, K. *et al.* Intercellular transfer of the oncogenic receptor EGFRvIII by microvesicles derived from tumour cells. *Nat Cell Biol* **10**, 619-624 (2008).

185 Davis, D. M. & Sowinski, S. Membrane nanotubes: dynamic long-distance connections between animal cells. *Nature Reviews Molecular Cell Biology* **9**, 431-436 (2008).

186 Martinez-Outschoorn, U. E. *et al.* The autophagic tumor stroma model of cancer or "battery-operated tumor growth": A simple solution to the autophagy paradox. *Cell Cycle* **9**, 4297 (2010).

187 Wolff, J. A. & Budker, V. The mechanism of naked DNA uptake and expression. *Advances in genetics* **54**, 1-20 (2005).

188 Christa, N., Cornelia, H., Kurt, Z. & Thomas, D. Co-cultivation of murine BMDCs with 67NR mouse mammary carcinoma cells give rise to highly drug resistant cells. *Cancer Cell International* **11**.

189 Kerppola, T. K. Visualization of molecular interactions by fluorescence complementation. *Nature Reviews Molecular Cell Biology* **7**, 449-456 (2006).

190 Kerppola, T. K. Bimolecular fluorescence complementation: visualization of molecular interactions in living cells. *Methods in cell biology* **85**, 431-470 (2008).

191 Lin, H. P., Vincenz, C., Eliceiri, K. W., Kerppola, T. K. & Ogle, B. M. Bimolecular fluorescence complementation analysis of eukaryotic fusion products. *Biology of the Cell* **102**, 525 (2010).

192 Sprangers, A., Freeman, B., Kouris, N. & Ogle, B. A Cre-Lox P Recombination Approach for the Detection of Cell Fusion In Vivo. *Journal of visualized experiments: JoVE* (2012).

193 Kouris, N. A. *et al.* Directed fusion of mesenchymal stem cells with cardiomyocytes via VSV-G facilitates stem cell programming. *Stem Cells International* (In Press).

# A3. Apoptosis-induced cell fusion as a possible mechanism for metastasis

Elements of this work have been published as:

**Noubissi, F.K., Harkness, T., Alexander, C.M., Ogle, B.M. Apoptosis-induced cancer cell fusion: a mechanism of breast cancer metastasis. *FASEB Journal.* 2015, *9*, 4036–4045.**

## A3.1 Introduction

Fusion of breast cancer cells with cells of the tumor microenvironment has been proposed as a means of generating widespread genetic and epigenetic diversity[1-4]. Diversity created in this way could rapidly enhance the formation, propagation, and metastasis of tumor cells or could quickly alter drug sensitivity. Yet to be reconciled are the precise mechanisms governing hybrid reprogramming after cell fusion and the means by which cancer cells undergo spontaneous fusion in the first place. The latter was the focus of this work.

One way that spontaneous cell fusion is enabled is via specific integral membrane proteins, termed fusogens, which provide cell anchorage and disrupt cell membranes, to minimize the energy necessary to overcome the merger of the two hydrophobic membranes[5]. The structure and function of many viral fusogens are well characterized, but eukaryotic fusogens are more difficult to establish because removal of facilitating proteins from the system reduces overall fusion rates. As technologies advance, many putative fusogens have been contested and shown to be merely

adhesion proteins that bring cell membranes in close apposition but do not actually facilitate fusion. Take, for example, heterotypic gamete fusion. As a fusion product, the fertilized embryo can proliferate and differentiate into all the tissues of the adult body as well as the extra-embryonic tissues. CD9 is an egg-associated putative fusogen. Cluster of differentiation (CD)9-knockout mice have shown severely hampered fertilization[6] that is restored with polyadenylated CD9 mRNA[7]. In addition, CD9 has been shown to generate the strongest observed interactions with the sperm[8]. However, it is not known whether it specifically facilitates the disruption and merging of membranes or whether other facilitating proteins or conditions are necessary[5].

Bona fide fusogens may not be necessary for cell fusion if cell membranes can be disrupted by other means. Cell stress, including nutrient deprivation, electroporation, and hypoxia, can render cell membranes leaky or unstable[9-11]. For example, changes in the ratio of cholesterol to phospholipid and in the double-bond index of the associated fatty acids have been shown to alter plasma membrane structure during hypoxic injury[12]. In addition, alterations in lipid structure with hypoxia can lead to changes in membrane protein structure and function, resulting in dysregulated enzyme activity and transport properties that could also lead to leakiness of the plasma membrane barrier[13]. Unstable cell membranes are biophysically susceptible to membrane fusion[14,15]. It may be for this reason that cell fusion appears to occur more readily in the context of hypoxia than during normoxia[16,17]. In contrast, cell fusion may be enhanced with hypoxia via signaling events triggered by hypoxic stress. For example, human hematopoietic progenitor cells upregulate VCAM-1 with hypoxia, a protein found to enhance adhesion and fusion with cardiomyocytes. Similarly, fusion of skeletal myocytes is increased

during hypoxia, in part because of signaling events associated with apoptotic cells. Apoptotic cells exhibit exposed phosphatidyl serine and choline, which binds associated phosphatidyl serine and choline receptors expressed by skeletal muscle. Binding of these receptors in skeletal muscle can engage the engulfment cell and mobility protein (ELMO)/dedicator of cytokines (Dock)180/ras-related C3 botulinum toxin substrate (Rac)-1 module to enhance myoblast fusion[18].

To accurately test whether apoptotic cells enable cell fusion, we used a unique tool developed in our lab to detect fusion products that was based on bimolecular fluorescence complementation (BiFC). With this approach, a fluorescent signal is induced by hybrid formation and can be detected in living cells. In addition, the signal intensity in hybrids increases over time as BiFC products are continuously synthesized. Using this robust tool, we showed that spontaneous fusion of multipotent stem/stromal cells (MSCs) with breast cancer cells occurs more readily in hypoxia than in normoxia, a significant finding, given that the microenvironment of breast tumors is often hypoxic. In addition, we found that, like skeletal muscle, cell fusion with hypoxia is enhanced as a consequence of the signaling associated with apoptotic cells. These findings are among the first to address how cancer cells spontaneously fuse in the first place and, as a consequence, reveal novel un-tapped therapeutic targets.

## A3.2 Materials and Methods

### *A3.2.1 Cell lines and culture*

MSCs were a generous gift from Dr. Peiman Hematti (University of Wisconsin, Madison, WI, USA). They were derived from human embryonic stem cells in

accordance with guidelines of the University of Wisconsin Institutional Review Board[19] and maintained in a-minimum essential medium (Sigma-Aldrich, St. Louis, MO, USA), supplemented with 10% heat-inactivated fetal bovine serum (Hyclone, Logan, UT, USA). We reconfirmed the identity of the MSCs in our lab by flow cytometry for specific MSC markers. Human mammary epithelial cells (MCF10a), human ductal breast epithelial tumor cells (T47D), human breast adenocarcinoma cells (MDA-MB-231), and human breast cancer cells (MCF7) (MCF indicates the Michigan Cancer Foundation where the MCF10a and MCF7 lines were established) were obtained from American Type Culture Collection (ATCC; Manassas, VA, USA) and maintained in accordance with the recommendations of ATCC; the cells were not passaged for more than 6 months from the time of receipt. MCF10as were tested for: 1) mycoplasma by DNA stain and agar culture, 2) species determination by short tandem repeat (STR) analysis and cytochrome c oxidase I (COI) assay, 3) sterility by BacT/ALERT 3D (bioMerieux, St. Louis, MO, USA), and 4) the human pathogens HIV, hepatitis B and C (HepB, HepC), human papillomavirus (HPV), Epstein Barr virus (EBV), and cytomegalovirus (CMV). T47Ds were tested for: 1) mycoplasma by DNA stain and agar culture, 2) species determination by STR and COI assays, and 3) sterility by BacT/ ALERT 3D. MDA-MB-231swere tested for: 1) mycoplasma by DNA stain and agar culture, 2) species determination by STR and COI assay, 3) sterility by BacT/ALERT 3D, and 4) the human pathogens listed above. MCF7s were tested for: 1) mycoplasma by DNA stain and agar culture, 2) species determination by STR, 3) sterility by BacT/ALERT 3D, and 4) the human pathogens listed above.

*A3.2.2 BiFC approach*

BiFC is a method of viewing living hybrid cells[20] (Supplemental Fig. S1A). Thus, the fluorescence of green fluorescent protein (GFP) is reconstituted when 2 non-fluorescent halves, expressed in fusion partners, are coexpressed and are in proximity in fusion products[21-26]. To encourage proximity, each non-fluorescent half is coupled to histone 3.1 (H3.1; plasmids, a generous gift of Dr. Thomas Kerppola, University of Michigan, Ann Arbor, MI, USA). Fluorescence was detected and recorded via traditional fluorescence microscopy (excitation 485, emission 530; Olympus IX81; Olympus America, Center Valley, PA, USA). Because of the conditional nature of the signal (i.e., fluorescent signal is detected only after a fusion event), the incidence of false positives was significantly reduced. A fluorescence signal was deemed positive if it was localized to the nucleus (as a consequence of the H3.1 fusion protein), fluoresced above the back-ground fluorescence of unaltered cocultures, and did not fluoresce with excitation/emission at alternate wavelengths. Un-der these criteria, transduction of the cells with each BiFC half alone did not yield a detectable false-positive signal (Supple-mental Fig. S1B).

*A3.2.3 Coculture protocol*

The design of coculture experiments is illustrated in Supplemental Fig. S2A. In our study, we transduced MSCs with lentiviral particles expressing the BiFC complex amino terminus GFP, histone H3.1 (VNH3.1), and the breast epithelial cells (MCF10a) or breast cancer cells (T47D, MDA-MB-231, and MCF7), with the corresponding BiFC complex carboxyl terminus GFP, histone H3.1 (YCH3.1) (Supplemental Fig. S2A). The

histone H3.1 tagged to each construct brought the BiFC halves in close association in the nucleus. MSCs were mixed with each epithelial cell type (i.e., MSC with MDA-MB-231, MSC with T47D, MSC with MCF7, and MSC with MCF10a) in 4-well chamber slides, such that the stromal population was mixed with each epithelial cell type. The ratio of cells for cocultures was 80,000 MSCs to 35,000, 112,000, 100,000, and 90,000 MDA-MB-231, T47D, MCF7, and MCF10a cells, respectively. Cell densities were selected so that surface area coverage for each cell type was approximately 50% at 24 h after the cocultures were initiated (Supplemental Fig. S2B). Forty-eight hours after coculturing began, the cells were fixed and stained with DAPI. Fusion products were identified by fluorescence microscopy. A signal (green fluorescence) was considered positive if it was stronger than the background in the FITC channel for unaltered cocultures, was nuclear (overlapped with DAPI), and did not cross over to the rhodamine and cyanine (Cy)5 channels. The frequency of fusion products was reported relative to the total number of nuclei in at least 200 fields of view per experiment, with about 110 cells per field. We performed each experiment at least 3 times.

*A3.2.4 Hypoxic treatment*

Hypoxic treatment was performed 16 h after the initiation of cocultures. The cocultures were removed from standard tissue culture conditions (21% $O_2$, 5% $CO_2$, and 74% $N_2$) and put in conditions of oxygen deprivation (2% $O_2$, 5% $CO_2$, and 93% $N_2$) for 3 h. At the end of coculturing (48 h after initiation) the cells were fixed and stained with DAPI, and the number of fusion products was recorded. We recognize that standard

tissue culture conditions are actually hyperoxic relative to normal tissue, but for the purposes of this study, we considered the condition of 2% $O_2$ to be hypoxic.

*A3.2.5 Apoptotic cell treatment*

Apoptosis was induced by treatment of T47Ds with 1 mM staurosporine (Sigma-Aldrich) for 12 h. Annexin V staining determined that 50–75% of the cells were apoptotic. Floating and attached cells were collected and used in the experiments. To investigate the involvement of apoptotic cells in cancer cell fusion, MSCs and T47Ds were transduced, and cocultures were initiated as described above. Sixteen hours after initiation of the cocultures, apoptotic cells were added at a ratio of 1 apoptotic cell for 2 coculture cells. The cocultures were analyzed under normoxic and hypoxic conditions, as described above.

*A3.2.6 Annexin V apoptosis assay*

Breast epithelial cells exposed to low oxygen for 3 h were stained with the ApoAlertAnnexin V-FITC Apoptosis Kit (Clontech, Mountain View, CA, USA), in accordance with the recommendations of the manufacturer. Apoptotic cells were detected with a fluorescence microscope.

*A3.2.7 Caspase inhibitor treatment*

Caspase activity was inhibited in cocultures of fusion partners by using the small molecule, Z-VAD-FMK (carbobenzoxy-valyl-ala-nyl-aspartyl-[O-methyl]-fluoromethylketone; Promega, Madison, WI, USA) and the ability of cells to fuse under

normoxic and hypoxic conditions was analyzed. Z-VAD-FMK is a cell-permeable pan-caspase inhibitor that irreversibly binds to the catalytic site of caspase proteases and is widely used to inhibit apoptosis. In our study, each cell population (MSCs, T47D, and MCF7) was transduced with the lentiviral particles expressing the BiFC complex VNH3.1 for MSCs, and the corresponding BiFC complex YCH3.1 for T47Ds or MCF7s, as described above. Twelve hours after transduction, each cell population was treated with Z-VAD-FMK (1 mM) for 1 h, and the cocultures were initiated. The coculture medium was supplemented with Z-VAD-FMK during the entire experiment (36 h), and the cocultures were assessed under normoxic and hypoxic (2% $O_2$, 5%$CO_2$, and 93% $N_2$) conditions, with and without the addition of apoptotic cells. The cells were fixed and stained with DAPI, and the fusion products were recorded.

*A3.2.8 Time-lapse microscopy*

Cocultures for time-lapse microscopy were initiated as described in the protocol above. In brief, MSCs were transduced with lentiviral particles from the BiFC component VNH3.1, and T47D or MCF7s were transduced with lentiviral particles from the BiFC component YCH3.1. At 48 h after initiation of the cocultures, the fusion products were identified by fluorescence microscopy (TE200; Nikon, Inc., Melville, NY, USA). The cells were maintained at 5% $CO_2$, 37°C, in a humidified atmosphere. Phase-contrast and fluorescent images of hybrids were taken every 5 min for 3 h with a 320 objective (0.5 NA, plan fluor 320 phase 1). Images of double-transduced parental cells and of control cells were taken. The paths of migrating cells were analyzed by using the manual tracking and chemotaxis and migration tool in NIH Fiji software (ImageJ; National

Institutes of Health, Bethesda, MD, USA)[27]. In brief, the center of a given nucleus was selected for each frame. Based on the resultant path created, the software was used to calculate velocity, total distance, and directionality.

For long-term tracking (72 h), MSCs and T47Ds were transiently transfected with mCherry- and GFP-expressing plasmids, respectively. Sixteen hours after transfection, the cocultures were initiated, and fusion products (expressing both red and green fluorescence) were identified 24 h later with a fluorescence microscope. Phase-contrast and green fluorescent images of hybrids were taken every 10 min for 72 h with a 310 objective in the Citation 3 imaging reader (Bio-Tek,Winooski,VT, USA). The cells were maintained at 5% $CO_2$ and 37°C, and the medium was replaced every 24 h. At 72 h, a static fluorescence image (green and red) of the tracked hybrid was obtained to confirm the hybrid's identity.

*A3.2.9 Statistical analysis*

All data are presented as means ± SD. When 2 groups were compared, a 2-tailed Student's t test was used. When more than 2 groups were compared, ANOVA with Tukey's honest significant difference (HSD) post hoc test was used. P=0.05 denoted statistically significant differences.

## A3.3 Results

*A3.3.1 Breast tumor cells fuse with MSCs spontaneously*

Fusion between tumor cells and host cells has been shown by several studies, many of which implicate bone marrow–derived cells of myeloid lineage as host fusion partners (reviewed in[17,28]). We propose that fusion of tumor cells with cells of the stroma gives rise to hybrid cells capable of dissemination and new tumor growth.

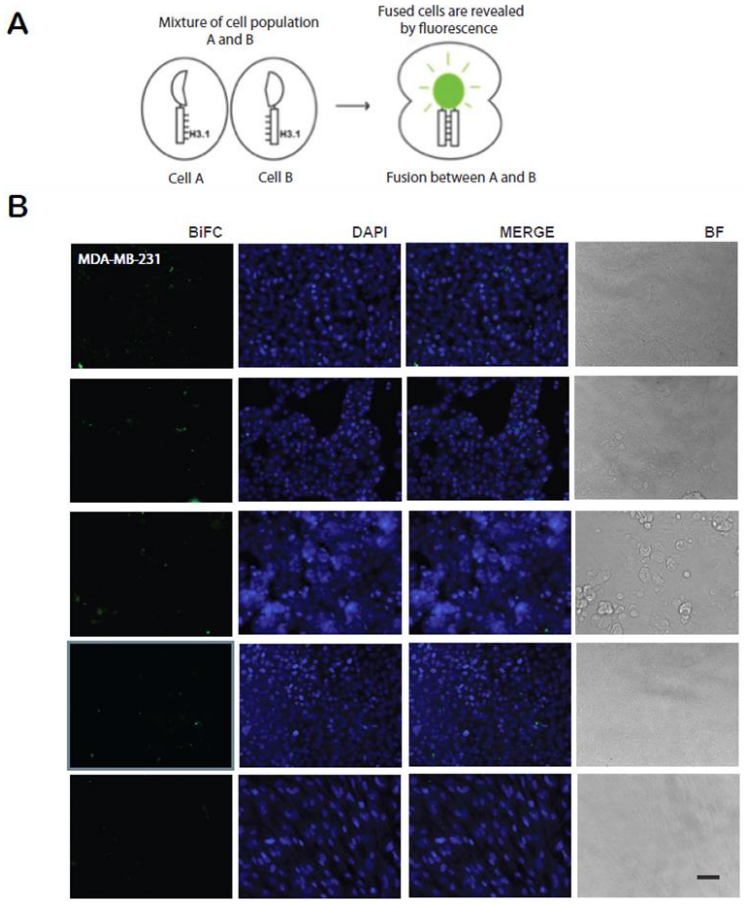


**Figure A3-1. BiFC approach and associated controls. A)** Each BiFC construct containing half of a GFP gene coupled to proteins known to come in close proximity in the cell (in our case Histone 3.1, H3.1 subunits) are transduced into separate cells (open circles). When the cells fuse, the GFP protein is recovered and a fluorescent signal is generated. **B)** Control experiment for the BiFC approach; signle BiFC expression. Cell lines transduced with lentiviral particles expressing the BiFC complex, VNH3.1 (MSC) or YCH3.1 (MDA-MB-231, T47D, MCF7, and MCF10a). Without the complementary BiFC complex, no fluorescence was observed which met the criteria for a positive BiFC signal as described in the Materials and Methods (BiFC approach). Scale bar, 50um.

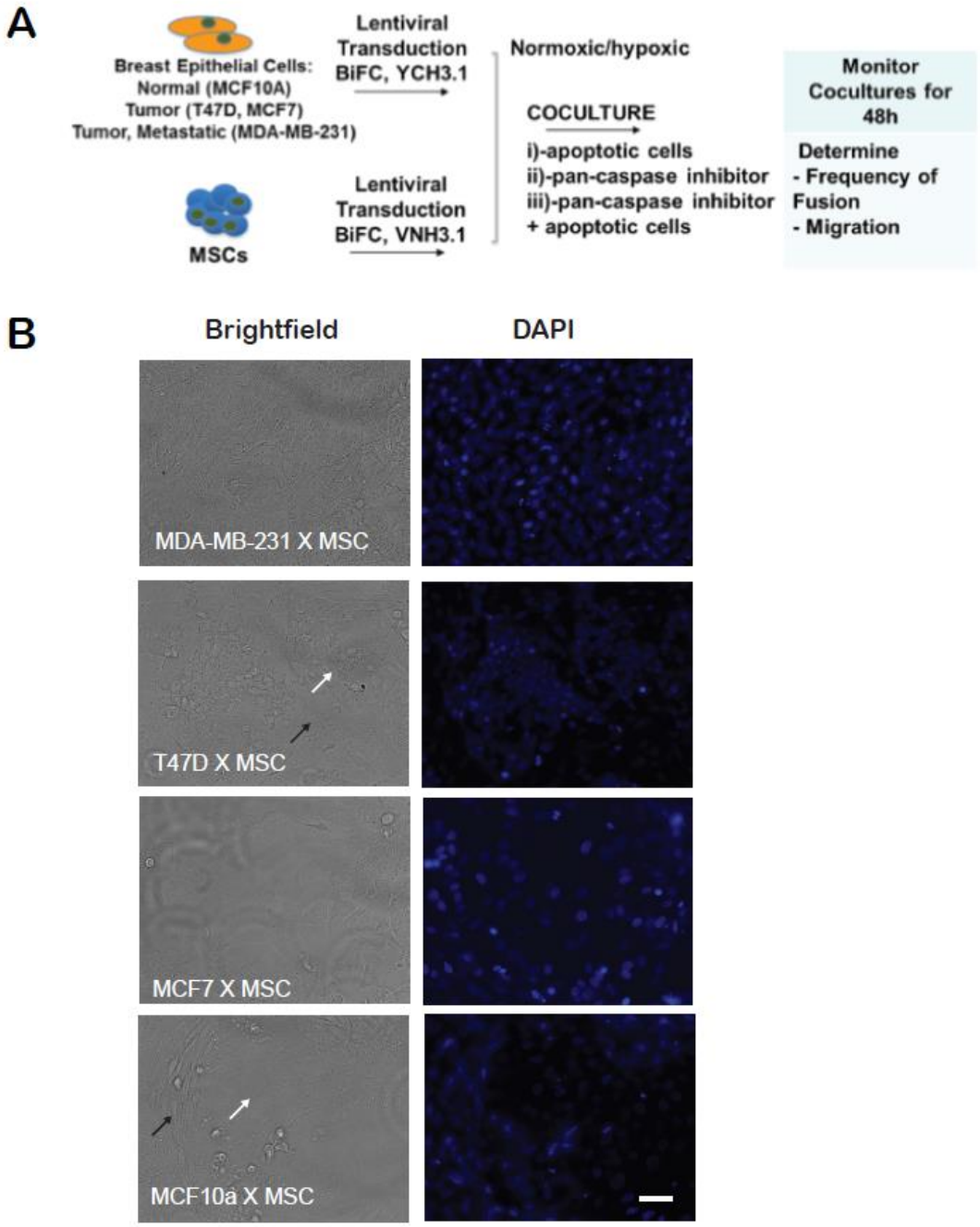


**Figure A3-2. Coculture experimental protocols and visual of morphology and distribution. A)** Schematic depicting coculture experiments. Cocultures were conducted under normoxic and hypoxic conditions and the percentage of cell fusion was assessed. The role of apoptosis in cell fusion was also investigated by treating the cells with pan-caspase inhibitor (z-VAD-FMK) and/or apoptotic cells. **B)** Representative views of the organization of breast epithelial cells in coculture with MSCs. Note in many cases elongated MSCs (black arrow) form circles or boundaries around small populations of breast epithelium (white arrow) Scale bar, 50um.

In the initial step of investigating the role of cell fusion in breast cancer metastasis, we examined the ability of MSCs to fuse spontaneously with breast cancer cells with different degrees of aggressiveness (T47D cells, which are non-metastatic, and MDA-MB-231 cells, which are metastatic) and nontumorigenic MCF10a breast epithelial cells. We have developed a powerful tool for the detection of fusion products in vitro that uses BiFC (see Materials and Methods and Figure A3-1A). Because of the conditional nature of the signal, the incidence of false positives is significantly reduced. Moreover, transduction of the cells with each BiFC half did not yield any detectable false positives (Figure A3-1B). Lentiviral particles expressing each half of the BiFC complex were delivered to the cells, and cocultures were initiated as described in Materials and Methods (Figure A3-2).

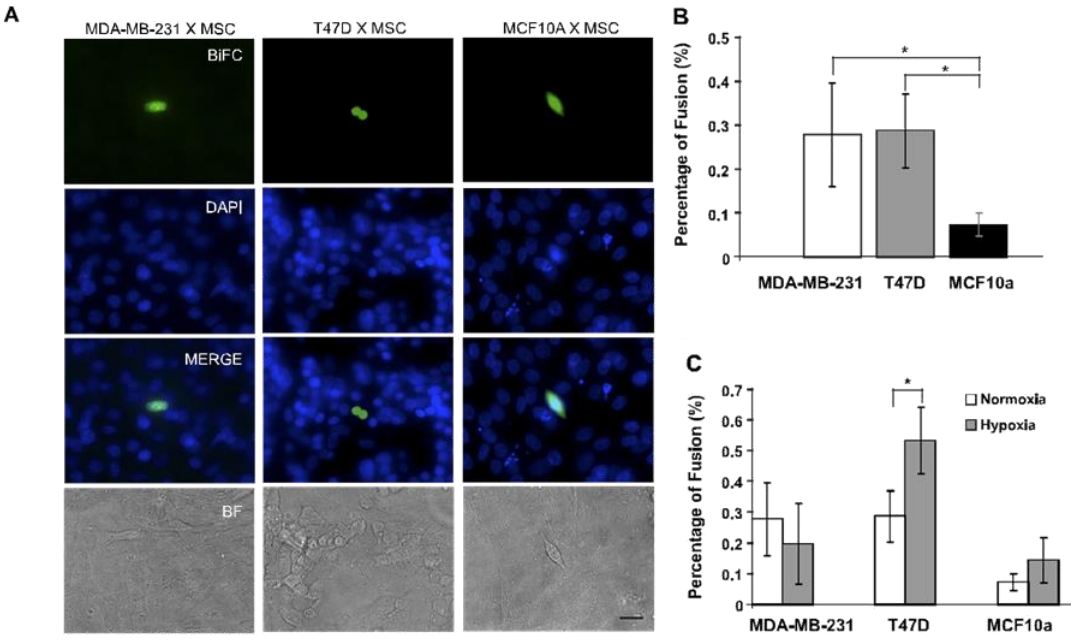


**Figure A3-3. MSCs fuse spontaneously with breast epithelial cells. A)** Representative fusion products from MSC-breast epithelial cell cocultures. Scale bar, 25 mm. **B)** Frequency of fusion of MSCs with breast epithelial cells. **C )** Percentage of cell fusion between MSCs and MDA-BM-231s, T47Ds, or MCF10as under hypoxic and normoxic conditions. Each value (mean 6 SD) represents the average of 3 independent experiments performed in triplicate. ANOVA with Tukey's HSD post hoc test. *P , 0.05.

Fusion products were identified with an epifluorescence microscope. The MSCs fused spontaneously with all breast epithelial cell types (Figures A3-3 and A3-4) at a fusion rate of 1:1000 for cancer cell types and 1:2000 for the nontumorigenic cell line, MCF10a (P , 0.05) (Figures A3-3B and A3-4B).

*A3.3.2 Fusion is enhanced with hypoxia*

To test whether the rate of fusion could be regulated by factors associated with tumor microenvironments, we evaluated the effect of hypoxia[29]. This hypoxic micro-environment puts cancer cells under stress and may promote their fusion with cells of the stroma recruited to the tumor microenvironment, as a means of survival. Cells were transduced with lentiviral particles expressing each half of the BiFC complex, and cocultures were initiated between MSCs and breast epithelial cells. The cocultures were subsequently exposed to low oxygen for 3 h, and fusion products were recorded, as described in Materials and Methods. We found that hypoxia stimulates a significant increase in fusion between MSCs and the T47D nonmetastatic breast cancer cells (P , 0.05; Figure A3-3C). This increase in fusion was not restricted to T47Ds, but was also observed with the nonmetastatic MCF7 cancer cells (P , 0.05; Figure A3-4B).

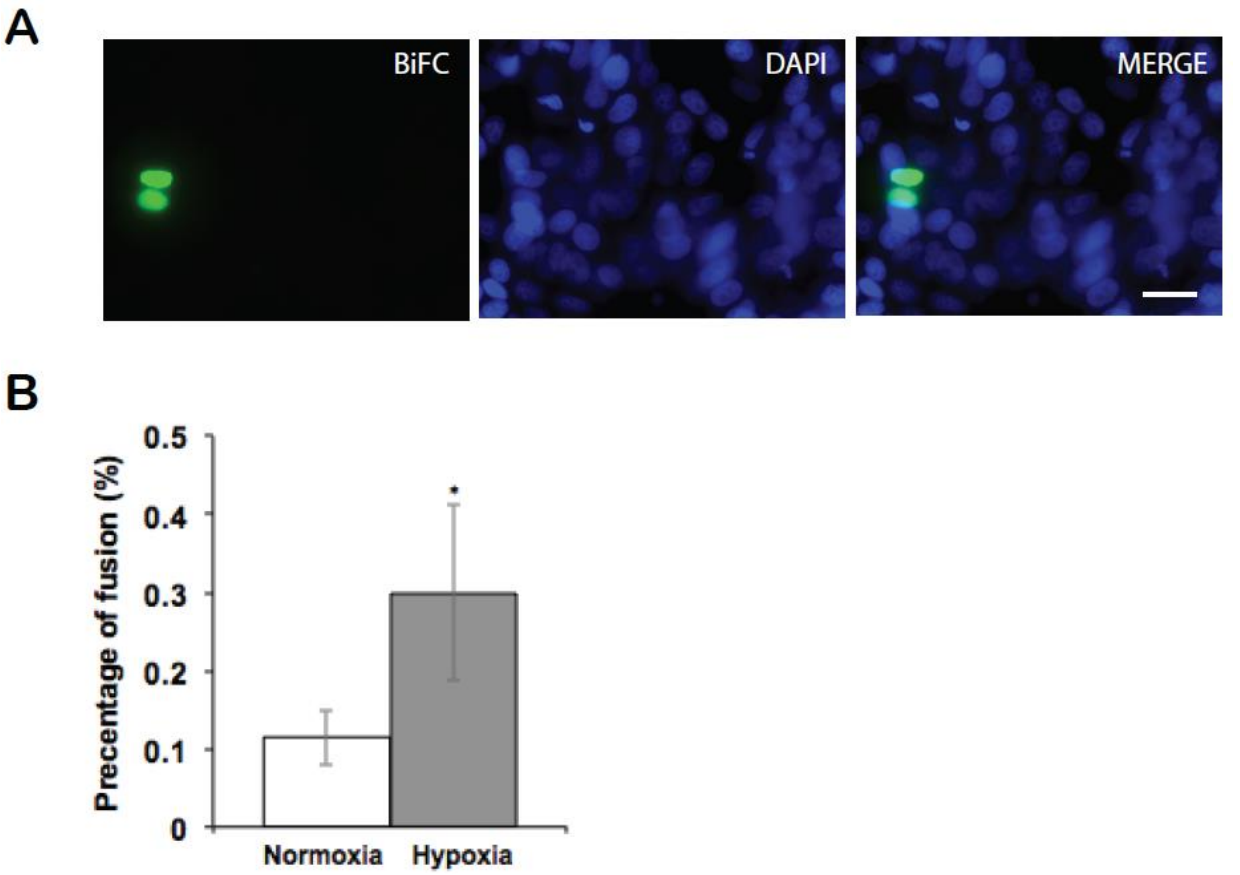


**Figure A3-4. Frequency of fusion in MSC x MCF7 cocultures. A)** Representative fusion product formed in MSC x MCF7 coculture. Scale bar, 25um. **B)** Frequency of fusion of MSCs with MCF7. Each value represents the average of 3 independent experiments done in triplicate. Student's *t* test (*P<0.05, mean ± SD).

*A3.3.3 Fused breast tumor cells show increased migratory capability*

To study the contribution of spontaneous cell fusion to metastasis, we used time-lapse microscopy to analyze the migratory capability of hybrids derived from the fusion between T47Ds and MSCs. Cocultures were initiated be-tween the MSCs and the T47Ds. Forty-eight hours after the initiation of the cocultures, the hybrids were identified and tracked every 5 min for 3 h with an inverted fluorescence microscope. The MSCs were highly motile and showed directed travel patterns. The T47Ds were 3 times less motile and showed little directional travel. The hybrids acquired the enhanced motility of the MSC parent, but were non-directional, similar to their T47D breast cancer cell parent

(Figure A3-5A, B). The same trend in motility and directionality was observed in hybrids between MCF7s and MSCs (Figure A3-5C, D).

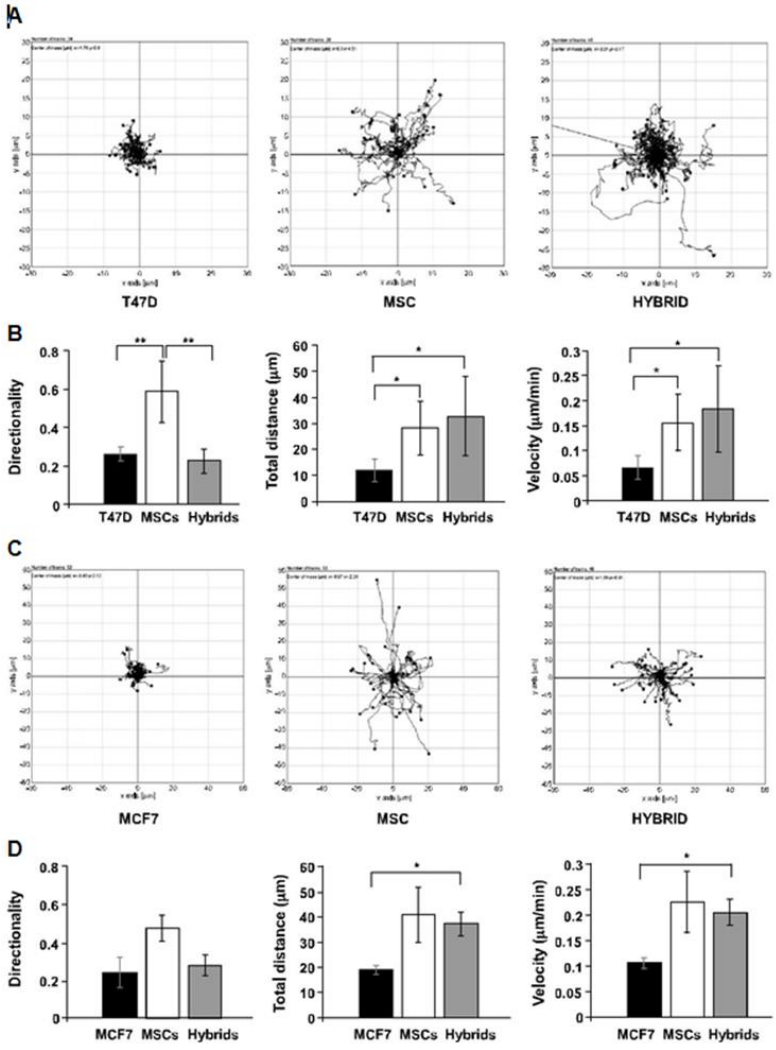


**Figure A3-5. Hybrid cells from MSC-T47D or MSC-MCF7 cocultures show higher migratory capability.** Migration of hybrid cells compared with that of MSCs alone or T47Ds alone (time-lapse microscopy). **A)** Representation of motility pattern of T47Ds, MSCs, and hybrids. **B)** Directionality of motion of cells. Total accumulated distance, and velocity. **C )** Representation of the motility pattern of MCF7s, MSCs, and hybrids. Cells of cocultures of MCF7s and MSCs were identified and tracked by time-lapse microscopy. **D)** Hybrids between MCF7s and MSCs showed increased migratory capability. Migration of hybrid cells compared to that of MSCs alone or MCF7s alone (time-lapse microscopy) including directionality of motion of cells, total accumulated distance, and velocity. Each value (mean 6 SD) represents the average of 3 independent experiments with analysis of at least 40 cells per group and per experiment. ANOVA with Tukey's HSD post hoc test. *P , 0.05, **P , 0.01.

*A3.3.4 The mechanism of fusion of breast cancer cells involves apoptosis*

Given its potential relevance in breast cancer metastasis, it is critical to understand the mechanisms governing cell fusion. In the experiments described above, we noted that hypoxia had little impact on the ability of MDA-MB-231 metastatic cancer cells to fuse spontaneously with MSCs. This observation suggests that hypoxia promotes fusion of nonmetastatic cancer cells with MSCs and therefore enables metastasis, an event that is not necessary or advantageous for the already metastatic MDA-MB-231 cells.

A recent study identified signaling via the phosphatidylserine (PtdSer) receptor brain-specific angiogenesis inhibitor (BAI)-1 as a cue to promote fusion of healthy myoblasts, involving the ELMO/Dock180/Rac1 pathway[18]. Blocking apoptosis potently impaired myoblast fusion, and adding back apoptotic myoblasts restored fusion. The added apoptotic myoblasts exposed PtdSer, but did not attach to the tissue culture plate or fuse on their own. They were necessary to promote myoblast fusion, requiring PtdSer-dependent cell-cell contact between apoptotic and viable myoblasts[18]. Because apoptosis is increased in certain cell types in hypoxic conditions (reviewed in[30]), we tested whether the same would be true of the breast epithelial cells used in this study. In fact, apoptosis was enhanced by hypoxia (2% $O_2$, 3 h) only in the T47D and MCF7 nonmetastatic cancer cells (Figure A3-6).

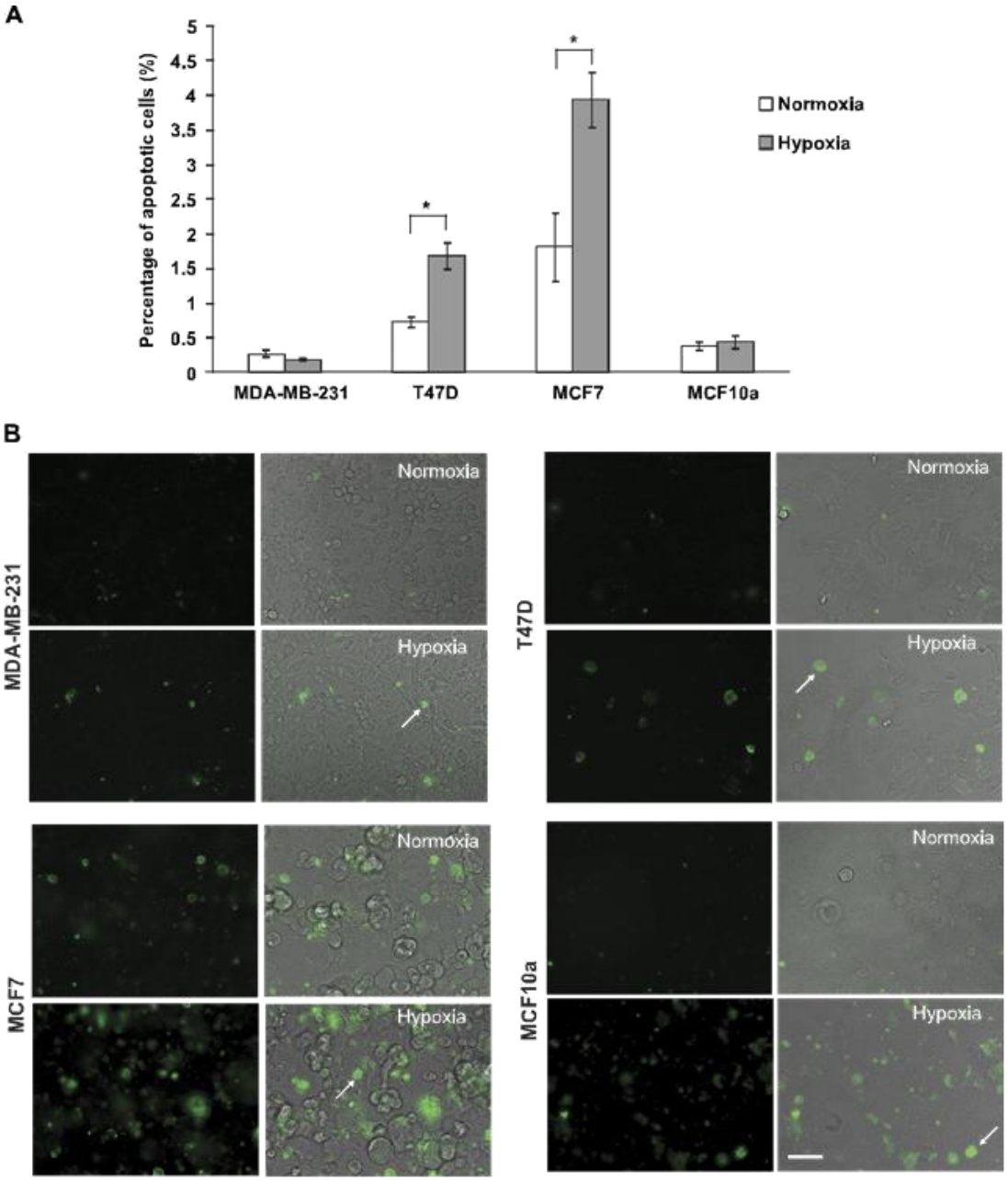


**Figure A3-6. Hypoxia-induced apoptosis of epithelial cells.** Epithelial cells were exposed to low oxygen for 3 h and subsequently stained with annexin V staining. Apoptotic cells were detected by fluorescence microscopy. **A)** Percentage of breast epithelial cells undergoing apoptosis after exposure to normoxic and hypoxic conditions. Student's t test. *P , 0.05. **B)** Representative micrographs of hypoxia-induced apoptotic cells as detected by fluorescence microscopy for MDA-BM-231, T47D, MCF7, and MCF10a cells. Arrows: apoptotic cells. Mean 6 SD. Scale bar, 50 mm.

Because we found that hypoxia considerably increases fusion between MSCs and the T47D and MCF7 breast tumor cells but not between MSCs and MDA-MB-231s or MCF10as (Figure A3-3C and A3-4B), we investigated first whether apoptosis is involved in the fusion of cancer cells. Cocultures between MSCs and T47Ds were initiated as described in Materials and Methods. Sixteen hours after initiation of cocultures, they were supplemented with T47D apoptotic cells, and fusion products were recorded. We found that addition of apoptotic cells to cocultures significantly increased cell fusion between MSCs and T47Ds in normoxic and hypoxic conditions (P , 0.05; Fig. 4A). To continue the investigation of the role of apoptosis in cancer cell fusion, we assessed whether inhibition of apoptosis impairs cell fusion.

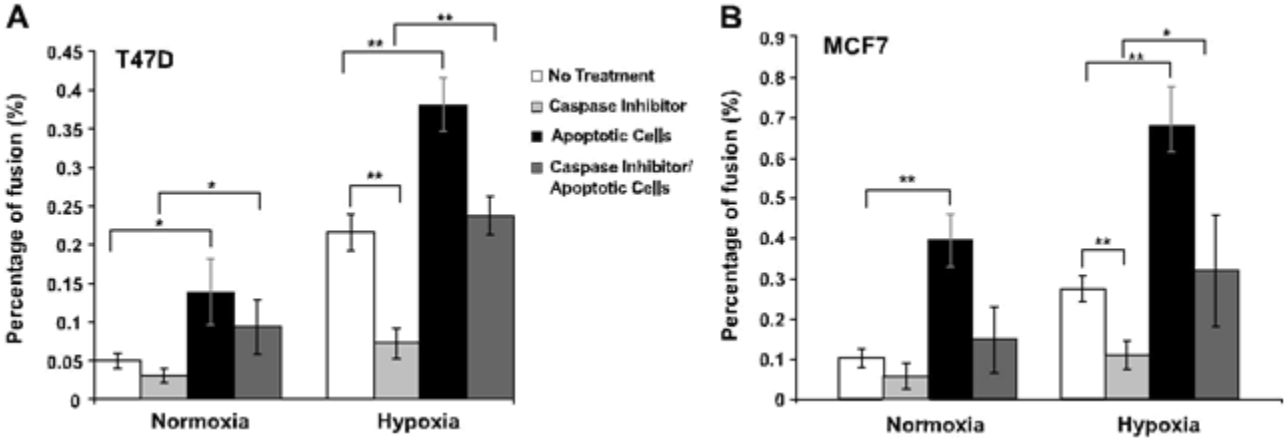


**Figure A3-7. Apoptosis enhances fusion between MSCs and T47Ds or MSCs and MCF7s. A)** Fusion between MSCs and T47Ds was impaired by treatment with the pan-caspase inhibitor Z-VAD-FMK. However, addition of apoptotic cells enhanced fusion between the 2 cell types and even rescued the fusion inhibited by the caspase inhibitor. **B)** Fusion between MSCs and MCF7s was impaired by the pan-caspase inhibitor z-VAD-FMK, as well. However, addition of apoptotic cells enhanced fusion between the 2 cell types and also rescued the fusion inhibited by the caspase inhibitor (mean 6 SD). ANOVA with Tukey's HSD post hoc test. *P , 0.05; **P , 0.01.

Apoptosis was inhibited in the fusion partners before coculture initiation with the pan-caspase inhibitor Z-VAD-FMK (1 mM). The inhibitor remained in the co-culture medium during the entire coculture experiments and did not seem to affect the

morphology or viability of the cells. We analyzed the ability of MSCs and T47D to fuse in normoxic and hypoxic conditions. We found that inhibition of apoptosis reduces cell fusion in normoxic conditions, and this reduction was significant in hypoxic conditions (P , 0.05), whereas addition of apoptotic cells rescued the fusion diminished by the pan-caspase inhibitor (Figure A3-7A). Apoptosis appeared also to regulate the fusion of nonmetastatic MCF7s and MSCs (Figure A3-7B), suggesting that the mechanism by which cancer cells fuse with MSCs involves apoptosis.

## A3.4 Discussion and Conclusions

Our findings describe a novel mechanism by which cancer cells fuse with MSCs, an event that could underlie the development of metastases. The breast cancer cells fused spontaneously with the MSCs. This fusion was significantly enhanced by hypoxia, especially between the non-metastatic breast cancer cells and MSCs, and was considerably increased by apoptosis. In addition, the hybrids formed showed a significantly higher migratory capability, lending support to the prediction that fusion contributes to cancer metastasis.

The possibility that cell fusion gives rise to the metastatic phenotype was first put forward nearly a century ago by Aichel[1] and later by Mekler[31,32] and Goldenberg[33]. In recent years, this hypothesis has gained further support. Spontaneous fusion has been reported between normal breast epithelium and breast cancer cells[34-36], among breast tumor cells themselves[37-39], between breast cancer epithelium and endothelial cells[40], and between breast cancer epithelium and tumor stromal cells[12,13]. In vitro studies of hybrids formed between normal breast epithelium (M13SV1-EGFP-Neo) and breast

cancer cells (HS578T-Hyg) showed increased locomotory activity, compared with the normal parental lines. This fusion-enhanced migration was associated with altered chemokine ligand (CCL)21/chemokine receptor (CCR)-7 signaling, which has been linked to the metastatic spread of breast cancer to lymph nodes[34].

Increased metastatic potential of hybrids was also observed in vivo when breast cancer cell variants (MDA-MB-231) with tropism for either lung or bone injected in nude mice gave rise to hybrids capable of metastases to both organs[41]. Drug susceptibility was also found to be altered in hybrids. Hybrids formed between parental breast cancer cells (MCF-7), with and without resistance to doxorubicin, were heterogeneous, with some exhibiting resistance and others not[39]. Likewise, hybrids derived from breast epithelial cells (M13SV1-EGFP-Neo) and breast cancer cells (MDA-MB-435-Hyg) showed altered sensitivity to the PI3K inhibitor, Ly294002, as a consequence of differential RAF-AKT crosstalk among hybrids[32]. Close probing of the heterogeneity generated by the formation of stromal cell-breast cancer cell hybrids indicated that hybrids can undergo DNA ploidy reduction and morphologic switching from mesenchymal-like to breast carcinoma–like. In addition, analysis of coding single-nucleotide polymorphisms by RNA sequencing showed genetic contributions from both fusion partners in the primary tumor and metastases[42].

Spontaneous fusion was also reported with other cancer cell types. A study showed that mesenchymal stem cells could spontaneously fuse with lung cancer cells in vitro. Fusion was also detected in vivo when freshly mixed lung cancer cells and MSCs were xenografted by subcutaneous injection into non-obese diabetic (NOD)/SCID immunodeficient mice[43]. The hybrids formed acquired in-creased motility and

invasiveness and were found to contribute to highly malignant subpopulations with both epithelial-to-mesenchymal and stem cell–like properties[43]. In addition, cells of a melanoma clone (wild-type for tyrosinase, C/C) implanted into BALB/c nu/nu mice (homozygous mutation for albino tyrosinase, c/c) developed massive pulmonary metastases a few weeks later. Analysis of chromosomes of cells from the metastatic tumors showed that most clones had acquired the c allele (same as that of the BALB/c recipient) while maintaining the C allele. Thus, lung metastases primarily comprised host-tumor hybrids and it is interesting that these hybrids expressed the same traits of enhanced motility and MSH/BMX responsiveness as in vitro–derived melanoma-macrophage hybrids[4].

Clinical studies have confirmed the presence of cell fusion in tumors as well, as found in patients who had undergone hematopoietic stem cell transplantation, with subsequent development of tumors showing evidence of donor genes in their cells[21,44]. In addition, a new report used STR polymorphism and forensic genetic techniques to suggest that a metastatic melanoma lesion in a patient arose from the fusion between a bone marrow–derived cell the patient received as a transplant and a tumor cell[45].

Our findings are in line with those in previous studies supporting the notion that cell fusion contributes to the ability of cancer cells to disseminate and perhaps metastasize. Moreover, a previous study showed that the motility-associated integrin subunits a2, a3, a5, a6, av, b1, and b3, which are involved in the migration of leukocytes and cancer cells, were significantly upregulated in metastatic macrophage-melanoma hybrids compared with parental melanoma cells[46]. A more recent study also indicated that fusion between cancer cells (ovarian and lung) and hematopoietic cells of

the myeloid lineage gave rise to hybrids expressing significantly higher levels of the pro-migratory marker CXC chemokine receptor (CXCR)-4, which was conferred by the parental myeloid cells[47]. Collectively, the increase in motility-associated integrin subunits and CXCR4 levels in hybrids may equip them with superior migratory potential and help their dissemination to various secondary organs, therefore explaining how fusion could provide a means by which adherent cancer cells acquire new qualities necessary to form metastases (i.e., enhanced motility and matrix degradation) under conditions conducive to hematopoietic survival and later resume tumorlike activities (i.e., rapid proliferation) under conditions conducive to epithelial survival. Cancer cell fusion may also provide a non-mutational mechanism that could contribute to aberrant gene expression patterns and give rise to highly malignant subpopulations with properties of cancer stem cells.

In contrast, a study showed that fusion between hematopoietic stem cells and human esophageal cancer cells slowed the growth speed of esophageal cancer cells and decreased the clone formation ability and tumorigenicity in NOD/SCID mice[48]. So far, only the tumorigenicity of some hybrids that were formed in vitro between normal epithelial cells or fibroblasts and tumorigenic cancer cells has been shown to be generally suppressed compared to the parental cancer cells[49-51], probably because of activation of some tumor-suppressor genes, although some exceptions to this observation have been shown[25]. The hybrids obtained in this way may deserve in depth analyses to understand the involvement of fusion in their tumor suppressor phenotype.

MSCs are known to be present in both healthy and cancerous breast tissue[51,52] and have even been observed trafficking directly from bone marrow to sites of primary

breast tumors[53]. These studies have implicated MSCs in encouraging the migration and metastasis of primary tumors, primarily through MSC secretion of chemotactic cytokines such as CCL5. Our results suggest that cell fusion may be an additional mechanism by which MSCs encourage breast cancer metastasis.

Although cell fusion occurs naturally in many fundamental biologic processes (homotypic fusion of myoblasts, placental trophoblasts[24], heterotypic gamete fusion[24], and macrophages[54]) and some pathologic conditions (viral-mediated fusion[55]), the mechanisms by which this phenomenon occurs are poorly understood, especially in the context of cancer. Studies have shown that cancer cell fusion can be induced by viruses[56,57] or cell-cell invasion mechanisms of cellocytosis (cell-cell internalization) or entosis (a non-apoptosis cell death mechanism)[54,58]. A recent work, however, identified apoptotic cells as a new type of cue that induces signaling via the PtdSer receptor BAI1 to promote fusion of healthy myoblasts[18]. The 7-transmembrane protein BAI1 (a member of the adhesion type GPCR family) mediates recognition of PtdSer on apoptotic cells and signals through the ELMO/Dock180/Rac1 pathway to enhance mammalian myoblast fusion. In that study, blocking apoptosis potently impaired myoblast fusion, and adding back apoptotic myoblasts restored it. Our findings are consistent with those in that study, as addition of apoptotic cells significantly increased cell fusion between MSCs and T47D breast cancer cells. We also observed reduction of cell fusion when apoptosis was inhibited, but this reduction was rescued by supplementation of Z-VAD-FMK-treated cocultures with apoptotic cells. It has been shown that myoblasts and macrophages use some of the same molecular components in fusion, including the Dock180 protein[59], suggesting that PtdSer-BAI1 signaling is

used by other cell types for fusion in addition to myoblasts. Moreover, BAI1 is well expressed in other cell types, including breast cancer cells and bone marrow–derived cells. These findings, together with our data, indicate that the mechanism by which cancer cells fuse with MSCs can involve apoptosis and may operate via PtdSer-BAI1 signaling.

We therefore propose that hypoxia-induced apoptosis in primary tumors stimulates cell fusion between MSCs and tumor cells, resulting in hybrids that exhibit both parental properties (mobility and proliferation) that enable their dissemination and new tumor growth at distant sites or metastases. In vivo studies addressing whether metastasis can in fact be initiated by fusion of cancer cells will complement this study. Investigating the involvement of BAI1 in cancer cell fusion will help delineate the molecular mechanisms of fusion of cancer cells and potentially the mechanisms of metastasis development. In the long run, this study may provide new strategies for developing alternate drugs for cancer treatment and preventing metastatic spread.

## References


1 Aichel, O. *Ueber Zellverschmelzung mit qualitativ abnormer Chromosomenverteilung als Ursache der Geschwulstbildung, von Prof. Dr. Med. Et phil. Otto Aichel*. (W. Engelmann, 1911).

2 Duelli, D. M. *et al.* A virus causes cancer by inducing massive chromosomal instability through cell fusion. *Current biology* **17**, 431-437 (2007).

3 Pawelek, J. M. & Chakraborty, A. K. The cancer cell–leukocyte fusion theory of metastasis. *Advances in cancer research* **101**, 397-444 (2008).

4 Chakraborty, A. K. *et al.* A spontaneous murine melanoma lung metastasis comprised of host× tumor hybrids. *Cancer research* **60**, 2512-2519 (2000).

5 Oren-Suissa, M. & Podbilewicz, B. Cell fusion during development. *Trends Cell Biol* **17**, 537-546 (2007).

6 Miyado, K. *et al.* Requirement of CD9 on the egg plasma membrane for fertilization. *Science* **287**, 321 (2000).

7 Kaji, K., Oda, S., Miyazaki, S. & Kudo, A. Infertility of CD9-deficient mouse eggs is reversed by mouse CD9, human CD9, or mouse CD81; polyadenylated mRNA injection developed for molecular analysis of sperm-egg fusion. *Developmental biology* **247**, 327-334 (2002).

8 Jégou, A. *et al.* CD9 tetraspanin generates fusion competent sites on the egg membrane for mammalian fertilization. *Proceedings of the National Academy of Sciences* **108**, 10946 (2011).

9 Hashizume, H. *et al.* Openings between defective endothelial cells explain tumor vessel leakiness. *The American journal of pathology* **156**, 1363-1380 (2000).

10 McDonald, D. M. & Foss, A. J. Endothelial cells of tumor vessels: abnormal but not absent. *Cancer and Metastasis Reviews* **19**, 109-120 (2000).

11 Morikawa, S. *et al.* Abnormalities in pericytes on blood vessels and endothelial sprouts in tumors. *The American journal of pathology* **160**, 985-1000 (2002).

12 Ježová, J. *et al.* Chronic hypoxia alters fatty acid composition of phospholipids in right and left ventricular myocardium. *Molecular and cellular biochemistry* **232**, 49-56 (2002).

13 van Blitterswijk, W. J., Hilkmann, H. & Storme, G. A. Accumulation of an alkyl lysophospholipid in tumor cell membranes affects membrane fluidity and tumor cell invasion. *Lipids* **22**, 820-823 (1987).

14 Mondal Roy, S. & Sarkar, M. Membrane fusion induced by small molecules and ions. *Journal of lipids* **2011** (2011).

15 Hafez, I. M., Ansell, S. & Cullis, P. R. Tunable pH-sensitive liposomes composed of mixtures of cationic and anionic lipids. *Biophysical Journal* **79**, 1438-1446 (2000).

16 Paltsyn, A. A. *et al.* Intermittent hypoxia stimulates formation of binuclear neurons in brain cortex—A role of cell fusion in neuroprotection? *Experimental Biology and Medicine* **239**, 595-600 (2014).

17 Lazova, R., Chakraborty, A. & Pawelek, J. M. in *Cell Fusion in Health and Disease* 151-172 (Springer, 2011).

18 Hochreiter-Hufford, A. E. *et al.* Phosphatidylserine receptor BAI1 and apoptotic cells as new promoters of myoblast fusion. *Nature* **497**, 263-267 (2013).

19 Trivedi, P. & Hematti, P. Simultaneous generation of CD34+ primitive hematopoietic cells and CD73+ mesenchymal stem cells from human embryonic stem cells cocultured with murine OP9 stromal cells. *Experimental hematology* **35**, 146-154 (2007).

20 Kerppola, T. K. Visualization of molecular interactions by fluorescence complementation. *Nature reviews Molecular cell biology* **7**, 449-456 (2006).

21 Yilmaz, Y., Lazova, R., Qumsiyeh, M., Cooper, D. & Pawelek, J. Donor Y chromosome in renal carcinoma cells of a female BMT recipient: visualization of putative BMT–tumor hybrids by FISH. *Bone marrow transplantation* **35**, 1021-1024 (2005).

22 Alvarez-Dolado, M. *et al.* Fusion of bone-marrow-derived cells with Purkinje neurons, cardiomyocytes and hepatocytes. *Nature* **425**, 968-973, doi:10.1038/nature02069 (2003).

23 Croce, C. M. *et al.* Chromosomal location of the genes for human immunoglobulin heavy chains. *Proceedings of the National Academy of Sciences* **76**, 3416-3419 (1979).

24 Aguilar, P. S. *et al.* Genetic basis of cell–cell fusion mechanisms. *Trends in Genetics* **29**, 427-437 (2013).

25 Defendi, V., Ephrussi, B., Koprowski, H. & Yoshida, M. Properties of hybrids between polyoma-transformed and normal mouse cells. *Proceedings of the National Academy of Sciences* **57**, 299-305 (1967).

26 Erikson, J., Martinis, J. & Croce, C. M. Assignment of the genes for human lambda immunoglobulin chains to chromosome 22. *Nature* **294**, 173-175 (1981).

27 Schindelin, J. *et al.* Fiji: an open-source platform for biological-image analysis. *Nature methods* **9**, 676-682 (2012).

28 Kemp, K., Wilkins, A. & Scolding, N. Cell fusion in the brain: two cells forward, one cell back. *Acta neuropathologica* **128**, 629-638 (2014).

29 Vaupel, P. & Harrison, L. Tumor hypoxia: causative factors, compensatory mechanisms, and cellular response. *The oncologist* **9**, 4-9 (2004).

30 Greijer, A. & Van der Wall, E. The role of hypoxia inducible factor 1 (HIF-1) in hypoxia induced apoptosis. *Journal of clinical pathology* **57**, 1009-1014 (2004).

31 Mekler, L. [Hybridization of transformed cells with lymphocytes as 1 of the probable causes of the progression leading to the development of metastatic malignant cells]. *Vestnik Akademii meditsinskikh nauk SSSR* **26**, 80-89 (1970).

32 Özel, C. *et al.* Hybrid cells derived from breast epithelial cell/breast cancer cell fusion events show a differential RAF-AKT crosstalk. *Cell Communication and Signaling* **10**, 1 (2012).

33 Goldenberg, D. M., Pavia, R. A. & Tsao, M. C. In vivo hybridisation of human tumour and normal hamster cells. (1974).

34 Berndt, B. *et al.* Fusion of CCL21 non-migratory active breast epithelial and breast cancer cells give rise to CCL21 migratory active tumor hybrid cell lines. *PloS one* **8**, e63711 (2013).

35 Berndt, B., Zanker, K. S. & Dittmar, T. Cell fusion is a potent inducer of aneuploidy and drug resistance in tumor cell/normal cell hybrids. *Critical Reviews™ in Oncogenesis* **18** (2013).

36 Dittmar, T. *et al.* Characterization of hybrid cells derived from spontaneous fusion events between breast epithelial cells exhibiting stem-like characteristics and breast cancer cells. *Clinical & experimental metastasis* **28**, 75-90 (2011).

37 Lu, X. & Kang, Y. Efficient acquisition of dual metastasis organotropism to bone and lung through stable spontaneous fusion between MDA-MB-231 variants. *Proceedings of the National Academy of Sciences* **106**, 9385-9390 (2009).

38 J Yang, J. *et al.* P-glycoprotein and breast cancer resistance protein affect disposition of tandutinib, a tyrosine kinase inhibitor. *Drug metabolism letters* **4**, 202-212 (2010).

39 Yang, J. Y., Ha, S.-A., Yang, Y.-S. & Kim, J. W. p-Glycoprotein ABCB5 and YB-1 expression plays a role in increased heterogeneity of breast cancer cells: correlations with cell fusion and doxorubicin resistance. *BMC cancer* **10**, 388 (2010).

40 Mortensen, K., Lichtenberg, J., Thomsen, P. & Larsson, L.-I. Spontaneous fusion between cancer cells and endothelial cells. *Cellular and Molecular Life Sciences CMLS* **61**, 2125-2131 (2004).

41 Lu, X. & Kang, Y. Efficient acquisition of dual metastasis organotropism to bone and lung through stable spontaneous fusion between MDA-MB-231 variants. *Proceedings of the National Academy of Sciences* **106**, 9385 (2009).

42 Rappa, G., Mercapide, J. & Lorico, A. Spontaneous formation of tumorigenic hybrids between breast cancer and multipotent stromal cells is a source of tumor heterogeneity. *The American journal of pathology* **180**, 2504-2515 (2012).

43 Xu, M.-H. *et al.* EMT and acquisition of stem cell-like properties are involved in spontaneous formation of tumorigenic hybrids between lung cancer and bone marrow-derived mesenchymal stem cells. *PloS one* **9**, e87893 (2014).

44 Chakraborty, A. *et al.* Donor DNA in a renal cell carcinoma metastasis from a bone marrow transplant recipient. *Bone marrow transplantation* **34**, 183-186 (2004).

45 Lazova, R. *et al.* A melanoma brain metastasis with a donor-patient hybrid genome following bone marrow transplantation: first evidence for fusion in human cancer. *PLoS One* **8**, e66731 (2013).

46 Chakraborty, A. K. *et al.* Fusion hybrids with macrophage and melanoma cells up-regulate N-acetylglucosaminyltransferase V, β1-6 branching, and metastasis. *Cell growth and differentiation* **12**, 623-630 (2001).

47 Ramakrishnan, M., Mathur, S. R. & Mukhopadhyay, A. Fusion-derived epithelial cancer cells express hematopoietic markers and contribute to stem cell and migratory phenotype in ovarian carcinoma. *Cancer research* **73**, 5360-5370 (2013).

48 Fan, H. & Lu, S. Fusion of human bone hemopoietic stem cell with esophageal carcinoma cells didn't generate esophageal cancer stem cell. *Neoplasma* **61**, 540-545 (2013).

49 Stanbridge, E. J. Suppression of malignancy in human cells. *Nature* **260**, 17-20 (1976).

50 Harris, H. The analysis of malignancy by cell fusion. *Cancer Res* **48**, 3302-3306 (1988).

51 Zhao, M. *et al.* Mesenchymal stem cells in mammary adipose tissue stimulate progression of breast cancer resembling the basal-type. *Cancer biology & therapy* **13**, 782-792 (2012).

52 Karnoub, A. E. *et al.* Mesenchymal stem cells within tumour stroma promote breast cancer metastasis. *Nature* **449**, 557-563 (2007).

53 Liu, S. *et al.* Breast cancer stem cells are regulated by mesenchymal stem cells through cytokine networks. *Cancer research* **71**, 614-624 (2011).

54 Vignery, A. Macrophage fusion: are somatic and cancer cells possible partners? *Trends in cell biology* **15**, 188-193 (2005).

55 Podbilewicz, B. Virus and cell fusion mechanisms. *Annual review of cell and developmental biology* **30**, 111-139 (2014).

56 Pawelek, J. M. & Chakraborty, A. K. Fusion of tumour cells with bone marrow-derived cells: a unifying explanation for metastasis. *Nat Rev Cancer* **8**, 377-386 (2008).

57 Duelli, D. M. *et al.* A virus causes cancer by inducing massive chromosomal instability through cell fusion. *Current biology : CB* **17**, 431-437, doi:10.1016/j.cub.2007.01.049 (2007).

58 Vignery, A. Macrophage fusion: the making of osteoclasts and giant cells. *J Exp Med* **202**, 337-340, doi:10.1084/jem.20051123 (2005).

59 Pajcini, K. V., Pomerantz, J. H., Alkan, O., Doyonnas, R. & Blau, H. M. Myoblasts and macrophages share molecular components that contribute to cell–cell fusion. *The Journal of cell biology* **180**, 1005-1019 (2008).